UNIVERSITY OF SOUTHAMPTON

Body Forces in Particle Suspensions in Turbulence

by

Gabriel H. Amine-Eddine

Thesis for the degree of Doctor of Philosophy

January 2015

Dedicated to Mum, Dad, and my Brother.

UNIVERSITY OF SOUTHAMPTON

ABSTRACT

FACULTY OF ENGINEERING AND THE ENVIRONMENT

Thesis for the degree of Doctor of Philosophy

by Gabriel H. Amine-Eddine

The work contained within this thesis concerns the behaviour of poly-dispersed and electrically charged particles in turbulent flows. Fundamental investigation has considered effects of momentum two-way coupling between particles and turbulence within such scenarios, and practical investigation has examined the potential utilisation of charge on fuel droplets to improve pre-combustion spray dynamics internal to marine Diesel combustion engines.

A spectral formulation is derived for the mesoscopic Eulerian transport equation describing momentum and kinetic energy transport for mono-dispersed electrically charged particles suspended at isotropic or near-isotropic conditions. This spectral transport equation specifically takes into account momentum contributions from the random uncorrelated particle velocity field.

An in-house pseudo-spectral direct numerical simulation (DNS) code has been extended and used to numerically investigate high order spectral statistics associated with momentum and kinetic energy transport equations for homogeneous and isotropic turbulence with particulate suspensions. Key results show that poly-dispersity can reduce the attenuation level of turbulent kinetic energy relative to mono-dispersed suspensions at similar mass loading ratios. In addition, two-way coupled charged particle suspensions were found to exhibit in their mesoscopic spectra, large scale augmentation of kinetic energy and small scale attenuation of kinetic energy, analogous to the behaviour of turbulence spectra in the presence of polymer chain additives. Furthermore, in the presence of gravity, two-way coupled charged particle suspensions were found under certain conditions, to fall with a velocity slower than their own Stokes settling velocity.

A droplet charge-diameter distribution model suitable for attributing electrical charge to poly-dispersed droplets in electrostatically atomized dielectric liquid sprays, has successfully been validated against experimental data. A methodology has been developed that uses the charge-diameter distribution model to simulate and successfully predict characteristics of electrostatically atomized dielectric sprays for low pressure spray systems.

A computational methodology has also been developed, suitable for predicting the characteristics of high pressure electrostatically charged sprays. This methodology has also been validated against existing experimental data, and is found to be reliable at predicting secondary atomization processes for both uncharged and charged spray plumes at elevated injection conditions.

Declaration

The work in this thesis is based on research carried out at the Institute of Complex Systems Simulation, University of Southampton, England. No part of this thesis has been submitted elsewhere for any other degree or qualification and is all my own work unless referenced to the contrary in the text.

Acknowledgements

I would like to thank my supervisor Dr John Shrimpton for all his advice and guidance over the years. I would also like to thank Professor Seth Bullock, Professor Hans Fanghor, Dr Jason Noble, and Nicki Lewin from the Institute of Complex Systems Simulation for their support.

This work was supported by an EPSRC Doctoral Training Centre grant (EP/G03690X/1)

Contents

Nomenclature

Alphanumeric Symbols

$\mathscr{F}$	Fourier Transform
τ_j	Jet time-scale
C	Particle Concentration
C_D	Nozzle Co-Efficient of Discharge
C_r	Relative Velocity Magnitude
D	Diameter
$D(\kappa)$	Turbulent Energy Dissipation Spectra
D_{10}	Arithmetic Mean Droplet Diameter
D_{32}	Sauter Mean Droplet Diameter
d_{inj}	Diameter of Injector Orifice
D_{stable}	Stable droplet diameter
E	Electric Field
$E(\kappa)$	Turbulent Energy Spectra
E_c	Critical breakdown electric field strength
e_{rms}	Fluctuating Electric Field Magnitude
E_s	Electric field normal to surface
F^*	Effective force
f_D	Drag Correction Factor
g	Gravity
I	Imaginary Part
k	Turbulent Kinetic Energy
L_{11}	Longitudinal Integral Length Scale
L_c	Characteristic Fluid Length-Scale
l_f	Longitudinal Integral Length Scale
l_j	Jet breakup length
M	Mass
m	Mass
N	Number of Computational Nodes
N_c	Number of Computational Particles
N_F	Number of Forced Modes
N_p	Number of Real Particles
Oh	Ohnesorge number
p	Instantaneous Pressure
p'	Fluctuating Pressure
p^*	Modified Pressure
P_k	Production Rate of Turbulent Kinetic Energy
Q	Charge
Q_{ray}	Rayleigh charge limit
Q_V	Volumetric Charge Density

r	Radial Displacement if Cylindrical Co-ordinate System
r_{inj}	Radius of Injector Orifice
Re	Reynolds number
Re_λ	Taylor Reynolds Number
St_η	Stokes Number
t	Time
t_{bag}	Bag breakup time
t_b	Droplet breakup time
T_F	Forcing Time-Scale
t_{strip}	Strip breakup time
U	Mean Fluid Velocity (Axial if Cylindrical Co-ordinate System)
u	Instantaneous Fluid Velocity (Axial if Cylindrical Co-ordinate System)
u'	Fluctuating Fluid Velocity (Axial if Cylindrical Co-ordinate System)
U_c	Characteristic Fluid Velocity
U_i	Fluid Velocity
u_{rel}	Relative velocity magnitude
V	Volume
v	Radial Velocity
V_i	Particle Velocity
W_f	Weighting Factor
W_p	Statistical Weight
We	Weber number
x	Position
z	Axial Displacement if Cylindrical Co-ordinate System

Greek Symbols

β	Forcing Constant
Δ	Change in Quantity
δ_{ij}	Dirac-Delta Function
ϵ_r	Relative Permittivity
ϵ_0	Permittivity of free space
ϵ_{ijk}	Levi-Civita Psuedo Tensor
η	Kolmogorov Length-Scale
$\frac{\partial}{\partial t}$	Partial Derivative
$\frac{D}{Dt}$	Material Derivative
$\hat{\theta}$	Complex Random Vector
κ_{max}	Maximum Resolved Wavenumber
κ	Wavenumber
κ_0	Minimum Resolved Wavenumber
κ_F	Forcing Radius
κ_I	Ionic Mobility
λ	Taylor Length Scale
μ_{eff}	Effective viscosity
μ	Dynamic Viscosity
μ_t	Turbulent Viscosity
ν	Kinematic Viscosity
Ω	Squared Magnitude of Vorticity
ω_i	Vorticity
ϕ_m	Mass Loading Ratio
ϕ_v	Volume Fraction
ϕ	Scalar Quantity
ϕ_e	Voltage Potential
ρ	Density
σ	Surface Tension

σ^* Effective Surface Tension

σ_ε Prandtl Number Constant for Dissipation Rate

σ_F Forcing Amplitude

σ_k Prandtl Number Constant for Turbulent Kinetic Energy

τ Time-Scale

τ_η Kolmogorov Time-Scale

τ_e Eddy Turnover Time

θ Spray Angle

ε Energy Dissipation Rate

Abbreviations

ADF Angular Distribution Function

CFD Computational Fluid Dynamics

CFL Courant Freidricks Levy

CO Carbon Oxides

DNS Direct Numerical Simulation

EU European Union

FFT Fast Fourier Transform

HC Hydrocarbons

$JPDF$ Joint Probability Distribution Function

MEF Mesoscopic Eulerian Formalism

$MEPVF$ Mesoscopic Eulerian Particle Velocity Field

NO Nitrogen Oxides

NS Navier Stokes

$PISO$ Pressure Implicit Splitting of Operators

PM Particulate Matter

$QBVD$ Quasi-Brownian Velocity Distribution

$RANS$ Reynolds Averaged Navier-Stokes

RDF Radial Distribution Function

RUM Random Uncorrelated Motion

RUV Random Uncorrelated Velocity

Subscripts

f Fluid Phase

p Dispersed Phase

Superscripts

$*$ Non-Dimensional Quantity

$\hat{}$ Complex Variable

Mathematical Symbols

$\bar{}$ Time Average

$\dot{}$ Rate of Change

$\langle\,\rangle_{\mathscr{V}}$ Spatial Average

$\langle\rangle_{\mathscr{E}}$ Ensemble Average

$\langle\rangle_{\mathscr{F}}$ Favre Average

$\langle\rangle_{\mathscr{L}}$ Lagrangian Average

Chapter 1

Introduction

1.1 Motivation and Objectives

Dispersed multiphase flows are common in numerous engineering and practical applications. For fuel sprays internal to combustion engines, the efficient atomization, dispersion and evaporation is crucial for minimising specific fuel consumption and pollutant emissions (Jankowski et al. 2002; Nishad 2013; Karimi 2007). Within selective catalytic reduction (SCR) systems utilised in modern automotive engines, precise control of dispersed Ammonia within exhaust gas flow stream, is crucial for achieving a homogeneous reduction reaction with NOx, (Majewski W. 1996). Other examples include the control of liquid-gas phase synthesis of nano-particles in micro-reactors, (Zhao et al. 2011), and at environmental scales the phenomenon of collective nucleation, growth and transport of droplets within atmospheric clouds, (Devenish et al. 2012).

Frequently, dispersed multiphase flows are turbulent, and thus exhibit a wide range of interacting temporal and spatial scales. These flows look chaotic, yet they can also exhibit somewhat ordered behaviour. An example of such order is the phenomena of preferential concentration, where the combination of interacting temporal and spatial scales between particles and turbulence, promotes formation of particle clusters within low-vorticity and high strain-rate regions of the flow field. If the aim of the application is to sufficiently homogenise the dispersed phase present, utilising the nature of turbulence

itself, focus shifts towards quantifying the extra mechanical work required to mitigate effects of preferential concentration, and whether or not this mechanical work can be controlled using intrinsic physical properties of the dispersed phase itself. One proposed method is the utilisation of electrical charge, imparted to the spray at the point of injection, using a process known as charge injection, (Kelly 1984a). In essence, a semi-conducting liquid passes at high flow-rate between a high-voltage negatively charged electrode and an earthed atomizer body. Due to the semi-conducting properties of the liquid, it acts as a carrier of electrons, stripping them away from the electrode and convecting them downstream and out of the nozzle orifice before they have a chance to reach the earthed atomizer body. Since like charges repel one-another, subsequent spray droplets exhibit greater dispersal tendency, increased likelihood of droplet breakup due to reduced effective surface tension forces, aiding processes such as heat and mass transfer beneficial within many multiphase engineering applications.

Due to the complex nature of such physics, detailed insight into the mechanisms and dynamics present for an electrostatically dispersed spray and subsequent particle suspension can be simulated using computational fluid dynamics (CFD). The main advantage of utilizing CFD is the fact that quantities otherwise difficult to obtain experimentally can be extracted numerically with relative ease. For fundamental analysis, direct numerical simulation (DNS) offers an attractive option due to the accuracy of scales resolved, and the strong correlation with existing experimental data. Hence, DNS are typically known as "numerical" experiments. Ultimately, the aim of DNS is to help with the interpretation and discovery of physical phenomena, providing a source of reliable quantitative information and knowledge for the development and validation of models suitable for the everyday demands of modern engineers who tend to utilise Reynolds Averaged Navier Stokes (RANS) based CFD methods instead. Due to the tendency of RANS based CFD requiring far less effort time-wise to reach a solution compared to DNS based methods, it is often chosen by engineers for rapid prototyping, optimisation, and evaluation of engineering design solutions pertinent to a given application. However, the main concern in usage of RANS based CFD methods is the level of accuracy gleamed from simulations accounting for all important physics, whilst not resolving all relevant scales of the system. For example, take a dense poly-dispersed liquid spray injected into a turbulent gas

flow field. Due to the high density of liquid particles within the spray core, there is every reason to suggest a modification of underlying gas-phase turbulence, a mechanism that is known as two-way coupling. Typically, this modification is accounted for using source terms in governing transport equations, quantifying the changes experienced in local mass fraction and momentum coupling. Yet these source terms alone cannot correctly account for the energy modification of turbulence scales, (Boivin et al. 1998).

Therefore, utilising both DNS and RANS based CFD methods, this thesis aims to examine the different effects and phenomena associated with realistic electrically charged sprays and charged particle suspensions in turbulence, within the practical context of multiphase flow engineering application.

The work presented in this thesis is therefore limited in the sense that focus lies upon two underlying objectives;

1. To investigate the behaviour of two-way coupling between poly-dispersed particles in turbulence, charged particles in turbulence, and additionally charged particles falling under gravity in turbulence.

2. To examine the potential utilisation of electrical charge on fuel droplets, to improve the pre-combustion dynamics and characteristics of sprays internal to marine Diesel combustion engines.

1.2 Organisation of Thesis

This thesis consists of a further nine chapters as follows:

- Chapter 2 presents a short summary covering basic fundamentals of turbulence, and subsequently introduces the relevant research developments examining particle laden turbulence. A brief review is also presented covering the background of electrically charged spray systems, as well as the motivation behind usage of such technology towards specific practical engineering applications.

- Chapter 3 presents a summary of governing equations used for DNS investigations presented in this thesis, also introducing the Mesoscopic Eulerian Formalism, used to describe a dispersed particle phase in terms of an Eulerian set of transport equations.

- Chapter 4 presents a Fourier decomposition of governing equations, and lists the spectral energy transport equations for the fluid turbulence, mesoscopic particle phase, and electrical continuum phase.

- Chapter 5 introduces the pseudo-spectral DNS code and associated numerical methodology. Procedures used for simulation set-up and post-processing are also presented, along with benchmark validations performed against key literature in this research field.

- Chapter 6 presents the DNS investigation on the two-way coupling of poly-dispersed particles in isotropic turbulence.

- Chapter 7 presents the DNS investigation on the two-way coupling of charge mono-dispersed particles in isotropic, and near-isotropic turbulence for the case of suspensions accounting for gravity.

- Chapter 8 presents details of a 2D CFD code, tailored to simulate charged spray plumes pertinent to engineering applications. This chapter also presents a completed study on the validation of a droplet charge-diameter distribution model, with a procedure for simulating charged and electrostatically atomized low pressure liquid sprays.

- Chapter 9 extends on the work of chapter 7, and presents the validation of a procedure suitable for simulating high-pressure charged and electrostatically atomized liquid sprays, where secondary atomization plays a dominant role in the characteristics and dynamics of droplet deformation and breakup.

- Chapter 10 summarizes the conclusions from this thesis, and suggests potential avenues for further work in this research field.

Chapter 2

Literature Review

2.1 Introduction

The aim of this chapter is to outline key publications and notable advancements made in research carried out thus far in the field of turbulent dispersed multiphase flows, whilst providing a summary of key fundamental concepts to be revisited throughout later chapters of this thesis.

This chapter starts with a brief introduction to fundamental turbulence theory, then focuses on the physical behaviour of particle suspensions within homogeneous turbulence. This is followed by a brief summary regarding the potential application of electrically charged sprays to marine Diesel combustion engines, introducing the motivation and corresponding research developments within this specific applied field of engineering.

2.2 Background to Turbulence

Turbulence is difficult to describe due to the many physical characteristics and phenomena that it possesses. Turbulence has the ability of being able to transport and mix fluid much more effectively than a comparable laminar flow. An essential feature of turbulence is that it exhibits random behaviour, with the velocity field varying significantly and irregularly, both in position and time. Despite this irregularity, flow structures such

as eddies and vortices, emerge, evolve, and dissipate chaotically across a wide range of different length and time scales.

One non-dimensional parameter that characterises fluid flows is known as the Reynolds number Re, which describes the ratio of inertial to viscous forces within the flow field. The Reynolds number is defined by,

$$Re = \frac{U_c L_c}{\nu_f} \tag{2.1}$$

where U_c and L_c represent the characteristic velocity and length-scale of the flow, and ν_f the kinematic viscosity of the fluid respectively. With increasing Reynolds number as the fluctuations in fluid velocity intensify, non-linear fluid inertia assumes greater importance compared to viscosity. Flow instabilities then become responsible for the continued generation of turbulence, producing large scale unstable eddies that breakup, giving rise to smaller eddies that are also themselves unstable, and so on generating progressively smaller eddies until the molecular viscosity of the fluid takes over and becomes effective at dissipating kinetic energy of the smallest scale eddies. Turbulence is therefore intrinsically a dissipative phenomenon, that requires continual energy input at large scales in order to sustain itself. At sufficiently high Reynolds numbers due to the wide range of eddy lengths and time-scales present within the turbulent flow, directional biases of large scale eddies are lost as a result of the chaotic cascading of energy down to successively smaller eddies. Bearing this fact in mind, comes Kolmogorov's hypothesis of local isotropy that is, *"at sufficiently high Reynolds numbers, the small scale turbulent motions are statistically isotropic"*. In other words, statistics measured in any direction of the local flow field yield the same characteristics as statistics measured in different directions within that same local flow field. Furthermore, Kolmogorov's first similarity hypothesis states, *"that in every turbulent flow at sufficiently high Reynolds number, the statistics of the small scale motions have a universal form that is uniquely determined by ϵ and ν_f"*, where ϵ represents the rate of kinetic energy dissipation. The smallest of turbulence scales are typically referred to as the Kolmogorov length and time-scales defined by,

$$\eta = \left(\frac{\nu_f^3}{\epsilon}\right)^{1/4} \tag{2.2}$$

$$\tau_\eta = \left(\frac{\nu_f}{\epsilon}\right)^{1/2} \tag{2.3}$$

with the velocity of Kolmogorov scale eddies defined by,

$$u_\eta = (\epsilon\nu_f)^{1/4} \tag{2.4}$$

The largest scales of turbulence are determined by the characteristic dimensions of the flow itself, and may refer to either the size of domain that contains the flow, or the diameter of an object that resides within the flow. This length scale is referred to as the integral length scale l, and it is at this scale in which energy is supplied to turbulent fluctuations of the inertial subrange. With this comes Kolmogorov's second similarity hypothesis, which describes that at sufficiently high Reynolds numbers, statistics of scales within the range $l^{-1} \gg \kappa \gg \eta^{-1}$, are universally and uniquely determined by the scale κ and the rate of energy dissipation ϵ. In essence, this refers to the concept of energy cascade from the largest of scales l, to the smallest of scales η.

2.2.1 Homogeneous and Isotropic Turbulence

In this thesis, fundamental examination of turbulence is performed in a mathematically idealised scenario. This scenario is the concept of homogeneous and isotropic turbulence, whereby statistics of any spatially averaged quantity when taken along both translations and rotations of the reference frame do not change.

For homogeneous isotropic turbulence, the largest length scales may be calculated from a quantity known as the two-point correlation statistic. This measure quantifies the correlation between velocity components taken at two different spatial locations and is defined by,

$$R_{ij}(r, x_i, t) = \langle u_i(x_i + r, t) u_j(x_i, t) \rangle \tag{2.5}$$

where r is the spatial displacement and u_i the fluid velocity field vector. Subsequently, the longitudinal integral length scale may be calculated as the area under the R_{11} versus r curve such that,

$$L_{11}(x_i, t) = \frac{1}{R_{11}(0, x_i, t)} \int_0^\infty R_{11}(e_1 r, x_i, t) dr \tag{2.6}$$

where e_1 is the unit vector in the x_1 direction. The associated integral time-scale of isotropic turbulence, otherwise known as the eddy turnover time may then be defined as,

$$\tau_e = \frac{L_{11}}{u'} \tag{2.7}$$

with u' as the r.m.s turbulent fluctuating velocity. Conveniently, Taylor (1935) defined a Taylor length-scale,

$$\lambda_{11} = \sqrt{\frac{2 \langle u_1^2 \rangle}{\left\langle (\partial u_1 / \partial x_1)^2 \right\rangle}} \tag{2.8}$$

which represents an intermediate length scale between the Kolmogorov and integral length-scales of the turbulence. Essentially, the Taylor length-scale defines the scale at which viscous dissipation starts to affect turbulent eddies. Lastly, from the Taylor length-scale, an associated Taylor Reynolds number may be defined as,

$$Re_\lambda = \frac{u' \lambda_{11}}{\nu_f} \tag{2.9}$$

which similarly characterises the ratio of inertial to viscous forces, only this time for a homogeneous turbulent flow field.

2.3 Particle Laden Turbulence

In this section of the literature review, basic characteristics exhibited by particle suspensions within homogeneous turbulence are explained with reference to key literature research findings relevant to the scope and objectives set out for this thesis.

2.3.1 Regimes of Coupling Between Turbulence and Particles

Two dimensionless numbers, namely the volume fraction ϕ_v, and mass loading ratio ϕ_m are typically used to characterise the conditions of a dispersed phase of spherical particles.

$$\phi_v = \phi_m \frac{\rho_f}{\rho_p} \tag{2.10}$$

$$\phi_m = N_p \frac{\pi D^3}{6} \frac{1}{V} \frac{\rho_p}{\rho_f} \tag{2.11}$$

These numbers refer to a ratio of particle volume or mass, to the fluid volume or mass respectfully. One-way coupling occurs when both the volume fraction and mass loading ratios remain small, such that $\phi_v < 10^{-4}$ and $\phi_m < 10^{-2}$, and that the influence of particles on the overall characteristics of the fluid system remain negligible. On the other-hand for two-way coupling, defined by the limits $\phi_v < 10^{-4}$ and $\phi_m > 10^{-2}$, the influence of particles on the underlying turbulence becomes more important, (Elghobashi and Truesdell 1993; Boivin et al. 1998). Some of the classical DNS work done by such authors identified that dilute particle suspensions can exert enough force to significantly modify turbulence, resulting in the attenuation of large scales and the augmentation of small scales, as well as an increase in turbulent energy dissipation rate. For $10^{-1} > \phi_v > 10^{-4}$ and $\phi_m < 10^{-2}$, inter-particle collisions become increasingly relevant, and for $\phi_v > 10^{-1}$ the particle suspension is said to be dense with collisions dominating most of flow physics, (Poelma and Ooms 2006; Eaton 2009; Balachandar and Eaton 2010).

Focus in this thesis specifically considers dilute particle suspensions where two-way coupling plays a dominant role, and where multi-scale effects of particle clustering contribute to the modification of turbulence characteristics, via interference with cascading turbulent energy.

2.3.2 Discrete Particles and Two-way Coupling Physics

Lagrangian models typically used within DNS, are based on point-particle assumptions that do not take into account the boundary layer development at the surface of particles themselves. Due to this very reason, experimental work by Hwang and Eaton (2006a;b), found that the degree of turbulence attenuation caused by heavy particles, can in fact be much greater than that typically predicted by point-particle DNS methods. Ooms and Jansen (2000) aimed to resolve this issue by developing a finite-diameter particle model that takes into account detailed flow around particles, however significant deviations were found in the prediction of turbulence intensities compared to the point-particle model.

Only recently have DNS studies involving fully resolved particles with two-way coupling been completed (Corre et al. 2008; Homann and Bec 2010; Lucci et al. 2010). Yet computational cost was a notable factor restricting the total number of fully resolved particles that could actually be examined using such methods, adversely affected the quality of obtained statistics. To some extent, experiments of Tanaka and Eaton (2010) managed to avoid the issues associated with fully resolved particles, by instead using high resolution particle image velocimetry (PIV) measurements of particles and tracer flow. Their work focused on mechanisms surrounding how particles larger than Kolmogorov scale eddies affect small scale turbulent structures. Despite the fact that two-way coupled conditions existed in experiments, tracer measurements on surrounding gas phase turbulence showed that particles actually reduced kinetic energy in a local region around themselves, with no evidence suggesting that falling particles augment local turbulence due to suspected particle wake mechanisms.

Abdelsamie and Lee (2012) examined two-way coupling within the context of turbulence field zones, namely the eddy, stream, rotation and convergence zones classified

by Hunt et al. (1988). When clustered within convergence zones, particles were found to contribute a positive source of energy to the turbulence. This was due to relatively high particle velocities compared to slow moving fluid, whereby particles have to drag surrounding fluid along with themselves. Within streaming zones, particles were found to act as a negative sink of turbulent energy. This was due to the relatively high fluid velocity compared to slow moving particles whereby the fluid has to drag particles along instead. Within eddy and rotation zones, particles were found to positively contribute to the rotational velocity of those zones, sometimes resulting in enlargement of zone spatial extent. Abdelsamie and Lee (2013) also found an increased alignment between particles and surrounding fluid velocity vectors, attributed to the reduction in turbulence intensity, and decrease in effective particle Stokes number due to modified energy dissipation rate levels of the turbulence.

2.3.3 Particle Dispersion

Particle dispersion was first recognised through the early theory of Yudine (1959); Csanady (1963); Reeks (1977) and Wells and Stock (1983). Yudine (1959) were the first of such authors, who introduced the "crossing trajectories" effect, which predicts that in the presence of a drift velocity caused by an external body force such as gravity, a particle of finite inertia will disperse faster than a fluid particle. To show this statistically, Yudine (1959) noted that the auto-correlation co-efficient of a heavy particle's velocity, decreased faster in time than that of a tracer fluid particle. Csanady (1963) instead introduced the concept of a "continuity" effect, that describes how the dispersion of a particle taken in the direction of a drift velocity, can exceed the dispersion taken in directions normal to drift velocity. Lastly, Reeks (1977) introduced the concept of an "inertia" effect, that predicts how in the absence of external body forces, dispersion of heavy particles can also exceed dispersion of fluid particles. For all crossing trajectories, continuity and inertia effect's, greater dispersion corresponds to faster decay of the particle's velocity auto-correlation curve.

Squires and Eaton (1991a) were the first to use DNS of forced isotropic turbulence to look at effects of particle dispersion. They found that in the absence of a drift velocity, particle

dispersion was faster than fluid elements. This was attributed to particles losing their correlation with local regions of the flow much faster than particles acting as tracers, thus demonstrating the inertia effect. With the presence of a drift velocity, inertial particle dispersion was found to be greatest in directions parallel to the drift velocity than in directions normal to the drift velocity, thus demonstrating the continuity effect. Several other studies (Elghobashi and Truesdell 1992; Truesdell and Elghobashi 1994; Mashayek et al. 1997; Yang and Shy 2005; Parthasarathy and Faeth 2006; Wetchagarun and Riley 2010), have looked at statistical measures of particle dispersion, and for each attributed many observations due to either crossing trajectories, continuity, or inertia effects within the suspension.

2.3.4 The Phenomena of Preferential Concentration

It is well known that particles preferentially accumulate in regions of low vorticity and high strain rate, when the particle relaxation time-scale is similar to the Kolmogorov time-scale, (Squires and Eaton 1990; 1991b; Fessler et al. 1994). The particle Stokes number St_η is a parameter that characterises this ratio. The preferential accumulation of particles is explained by the role of intense eddy structures that sweep out heavy particles due to centrifugal effects, resulting in the accumulation of particles along the outer peripheries of high-vorticity regions. However, it has been suggested by many researchers (Chen et al. 2006; Yoshimoto and Goto 2007; Bec et al. 2007b; Goto and Vassilicos 2008), that this picture is not entirely valid for fully developed turbulence at high Reynolds numbers, when near-empty spaces for particles are also shown to appear throughout the turbulence even when $St_\eta > 1$. On this matter, Chen et al. (2006) examined 2D DNS of high Reynolds number turbulence and found that inertial particle clustering was correlated with the spatial clustering of zero-acceleration points, defined at the centre of, or between adjacent vortices that evolve with time-scales similar to those of surrounding vortices. Furthermore, Yoshimoto and Goto (2007) managed to quantify the multi-scale behaviour of clustering phenomena using a void fraction PDF measure. Yoshimoto and Goto (2007) found that this measure obeys a power law, reflecting evidence of self-similarity between particle clusters and inertial range eddies. Bec et al. (2007a), through

means of DNS performed at $Re_\lambda = 65$, 105 and 185, found that clustering of particles within inertial range eddies could also be characterised by a scale-dependent volume contraction rate, i.e. a measure of particle field compressibility. Bec et al. (2007a) went further by stating that the distribution of particles is characterised by voids spanning all scales of the turbulent flow, which through means of Voronoi analysis was later shown to be true (Monchaux et al. 2010; 2012). Goto and Vassilicos (2008) developed on the idea of zero-acceleration points and compressibility of the particle phase, to develop the concept of a sweep-stick mechanism applicable to 3D isotropic turbulence. Essentially, the sweeping process describes the transport of particles via the velocity of the fluid acceleration field, whereas the stick mechanism describes the tendency for heavy particles to stick with, and move at a similar velocity to zero acceleration points, whilst moving away from any non-zero acceleration regions of the field. The key discovery here was the fact that this type of clustering phenomena was found to be independent of particle Stokes number (Goto and Vassilicos 2008; Coleman and Vassilicos 2009).

2.3.5 Settling Behaviour of Particles Falling in Turbulence Under Gravity

Ferrante and Elghobashi (2003) briefly examined the effects of gravity for $St_\eta = 0.25$ particles in decaying near-isotropic turbulence, and found that the preferential sweeping of particles by vortical structures formed clusters only on the sides of structures rotating downwards towards gravity. They also determined that only the swept sides of these vortical structures would be subject to the majority of particle drag forces, resulting in localised drag force gradients and associated alignments of vorticity vectors with respect to horizontal component directions normal to gravity. Recent research by Dejoan and Monchaux (2013) showed that clusters also become more elongated towards the gravity direction. To quantify the settling behaviour of particles, Bosse et al. (2006) measured the deviation of averaged particle velocities to the Stokes settling velocity of a single particle defined by,

$$\Delta V_3 = -\overline{\langle V_{p,3} \rangle}_{\mathscr{L}} - U_p \tag{2.12}$$

with U_p defined by,

$$U_p = \tau_p g \left(1 - \frac{\rho_f}{\rho_p}\right) \tag{2.13}$$

Bosse et al. (2006) found velocity enhancements of $\Delta V_3/U_p = 0.18$ for their one-way coupled DNS studies, compared to $\Delta V_3/U_p = 0.13$ from equivalent experiments preformed by Yang and Shy (2005). Extending to two-way coupled studies, Bosse et al. (2006) found that velocity enhancement increased to $\Delta V_3/U_p = 0.38$, supporting earlier findings by Aliseda et al. (2002) who found that settling velocities of particles increased as the mass loading ratio of clusters increased. With regards to the effects of particle settling behaviour on turbulent kinetic energy spectra, Elghobashi and Truesdell (1993) were the first researchers who found evidence that in directions orthogonal to the gravity vector, a reverse energy cascade occurred from small to larger scales. This idea wasn't revisited again until Yang and Shy (2005), who detailed experiments investigating particle settling behaviour in stationary homogeneous and near-isotropic turbulence. Turbulent energy spectra was compared for three different $St_\eta = 0.36$, 1.0 and 1.9 cases, to that of an unladen turbulent flow. For $St_\eta = 0.36$ and 1.0 cases, the horizontal and vertical turbulent spectral kinetic energy components both showed clear evidence of a transition wave-number, whereby the energy of the laden flow started to become much greater than that of the unladen turbulent flow. For the $St_\eta = 1.9$ case, vertical component turbulent kinetic energy spectra showed augmentation occurring across the entire range of turbulence scales.

2.4 Application of Electrically Charged Spray Systems

As discussed earlier in section 1.1, this thesis proposes the question as to whether or not it is possible to improve turbulent multiphase mixing capability in marine Diesel engines, by adding electrical charge to dispersed phase particles. This section presents the motivation behind such a question, and summarises developments made in this specific field of applied engineering research.

2.4.1 Motivation

European Union directives regarding emissions legislation relate to measures to be taken, against air pollution by gases from internal combustion engines. Motivation behind such directives is to achieve levels of air quality that do not give rise to significant negative impacts on the environment. The need to reduce emissions of harmful air pollutants such as carbon oxides (CO), hydrocarbons (HC), Nitrogen oxides (NO) and particulate matters (PM) is outlined in these regulations. Currently, regulations have been adopted to limit the pollutant emissions from light and heavy duty road vehicles. Manufacturers must ensure that newly built engines comply with limitations set out regarding exhaust emissions from both petrol and Diesel internal combustion engines.[1][2] These limitations however have not yet been placed on engines used in the shipping industry. Since these limitations are due to become more stringent for manufacturers, a step change in technology is required. This step change is expected to yield significant implementation costs for redesigning engines, yet will increase research and development of advanced technical solutions in order to meet legislation requirements. Motivation therefore stems from two main factors as follows; Firstly, compliance to EU emissions legislation requires cost effective means by which manufacturers can improve and advance combustion technology. Secondly, the greater cost of fuel prices creates an incentive for shipping operators to find more economical engines that offer greater mileage per gallons than counterparts. Engine manufacturers are therefore forced to compete, and develop the cheapest and most economical engineering solutions for their product lines.

2.4.2 Background to Charge Injection Technology

Charge injection is a process whereby a semi-conducting dielectric liquid is forced within an atomizer, to pass between a negative high voltage electrode typically at 2-10kV, and an earthed body of a nozzle consisting of a small outlet orifice. Above a certain threshold

[1]Proposal for a Directive of the European Parliament and of the Council amending Directive 97/68/EC as regards the provisions for engines placed on the market under the flexibility scheme SEC(2010)828 SEC(2010)829

[2]Council Directive 88/436/EEC of 16 June 1988 amending Directive 70/220/EEC on the approximation of the laws of the Member States relating to measures to be taken against air pollution by gases from engines of motor vehicles (Restriction of particulate pollutant emissions from Diesel engines)

voltage applied to the electrode, the process of charge injection occurs whereby electrons are effectively stripped from the electrode and "injected" into the liquid (Kelly 1984a;b; 1990; 1994). Before electrons have a chance to reach the earthed body of the nozzle, they are convected along with the bulk liquid flow through the nozzle outlet orifice and into the spray. The electrical performance for such a device is typically measured by the amount of spray specific charge delivered, and is denoted by Q_v with units of C/m^3. The spray specific charge is determined from the measured current contained in the spray, and the volumetric liquid flow-rate form the nozzle. The greater the level of Q_v, the more primary atomization and dispersal of liquid within the spray occurs. Another measure of performance stems from the electrical efficiency of the atomizer device, which is simply the ratio of spray current I_S to the total current injected I_T within the nozzle itself. The difference between the spray and total current injected is termed the leakage current I_L, which quantifies the number of electrons that pass to the atomizer body and then to the earth. The reader is referred to a comprehensive review of Shrimpton (2009) for a detailed look into the physical principles and theoretical work relating to charge injection systems.

2.4.3 Research Developments in Charge Injection Technology

Electrostatic atomization of conducting and semi-conducting liquid sprays is now well established in many industrial and engineering processes, e.g. non-impact printing (Agui and Nakajima 1977), and pollution abatement, (Ahmed and Balachandran 1991). It has been suggested by Shrimpton and Kourmatzis (2009), that charging of electrically insulating fuels can offer significant benefits to both small, and large combustion engines. With potential improvement in primary and secondary atomization mechanisms, spray dispersal, lack of droplet coalescence, and the possibility to control combustion kinetics, existing combustion technology can be advanced to provide better fuel economy whilst simultaneously reducing the level of pollutant emissions. Usage of charge injection for improved combustion of different fuels has already been given focus by several researchers (Shrimpton 1995; Yule et al. 1995; Rigit 2003; Ergene et al. 2010). These developments

are becoming increasingly pertinent to optimizing combustion applications within aeronautical, automotive and marine sectors, where a need exists to achieve greater energy efficient methods within fuel atomization (Kourmatzis et al. 2011). This objective requires deep understanding of the multiphase dynamics that occur within such charged fuel spray applications. There is also great importance placed on the control and optimisation of problem variables, such as the spray specific charge, flow rate, nozzle geometry and orifice diameters, which all have an impact upon spray atomization performance (Shrimpton and Yule 1999; Shrimpton 2003; Shrimpton and Yule 2004).

Kwack et al. (1989) and Bankston et al. (1988) were some of the first authors in this field to investigate electrostatic dispersion of Diesel fuel jets at high back pressures typical to Diesel combustion engines of that era. However, the charge injection atomizer used for such experiments was a "spray triode" type design which over the more recent decades worth of work in this field has been outdated by far better atomizer designs, as far as the injected level of spray charge is concerned (Shrimpton and Yule 1999; Rigit and Shrimpton 2006).

Modern day high pressure fuel injectors benefit sprays by reducing the size of droplets via the mechanisms associated with secondary atomization. It has been suggested by Anderson et al. (2007) that these high pressure spray systems can be downsized to operate at lower pump pressures, thereby reducing the energy needed to operate, yet achieve the same spray performance to that of a high pressure spray pump using the principle of charge injection. On this matter, Ergene et al. (2011); Kourmatzis et al. (2011) managed to achieve spray specific charges of up to $6.7 C/m^3$ at high hydrodynamic pressures ranging 7-35 *bar*. They determined that all the potential benefits discussed earlier in this section, with regards to improved mechanisms of fuel breakup, atomization, and dispersal can be achieved to good effect.

It should be noted that although the concept of electrostatic charge injection is applied here with the motivation to improve pre-combustion behaviour of fuel sprays, all the ideas and potential benefits offered by this technology can be applied to other practical engineering challenges, such as chemical spray reactors in food processing and pharmaceutical industries.

2.5 Summary

The purpose of this chapter was to provide a review of fundamental concepts relating to turbulent dispersed multiphase flow, as well as introduce the idea of applying electrically charge to dispersed particle suspensions. The important conclusions taken from this chapter can be summarised as follows;

- A level of uncertainty exists with regards to the ability of the point-particle framework to correctly account for two-way coupling physics occurring locally around realistic particles of finite diameter. Whilst this issue cannot be avoided due to the nature of the point-particle framework itself, the specific methodology that accounts for particle momentum transfer back to the fluid is something that shall be examined later in section 5.4.2 of this thesis.

- The specific question of how the additional electrical body forces acting on particles increase or decrease the level of momentum two-way coupling at different scales of the turbulence, as well as what qualitative effect charged particles have on settling velocity enhancement in the presence of gravity, is something that remains unanswered in previous research. These questions shall be examined in Chapter 7.

- Whilst two-way coupling has been studied extensively for mono-dispersed turbulent particle suspensions, very little attention has been given to poly-dispersed suspensions. Most multiphase flows of an industrial nature contain poly-dispersed suspensions, yet the two-way coupling effect that such suspensions have on turbulence remains unknown. The added complexity of having poly-dispersed particles with different characteristic time-scales, collectively interacting with different length scales of the turbulence is something that shall be examined in Chapter 6.

- With regards to the application of electrically charged spray systems, two prerequisites are required in order to successfully start examining the potential improvements of electrostatic charge on pre-combustion spray dynamics internal to Diesel combustion engines. Firstly, a validated Lagrangian-Eulerian based CFD

methodology is required such that the dynamics of low-pressure electrostatically charged dielectric liquid sprays can successfully be predicted. Secondly, a suitable procedure for predicting high-pressure electrostatically atomized spray behaviour that takes into account the additional physics associated with secondary atomization is also required. Both of these pre-requisites shall be examined in Chapters 8 and 9 of this thesis respectively.

Chapter 3

Governing Equations (Spatial Form)

3.1 Overview

The aim of this chapter is to provide a source of reference for all governing equations used throughout the DNS investigations presented in this thesis.

The first section of this chapter presents the Navier-Stokes equations for a pure and incompressible fluid. Simplifications are subsequently applied to yield the general and physical rotational form suitable for homogeneous and isotropic turbulent flow fields. Lastly, the Reynolds stress and kinetic energy transport equations are presented.

The second section of this chapter presents the governing equations of motion for the dispersed particle phase. The procedure used to transform Lagrangian information to Eulerian spatial information is introduced, followed by a summary of the mesoscopic Eulerian formulation used to describe the particle phase dynamics via a set of Eulerian transport equations.

The third section of this chapter introduces the governing equations describing the electrical continuum phase, and briefly discusses how the electrical phase behaves for a turbulent charged particle suspension.

3.2 The Equations of Fluid Motion

Starting with the continuity and Navier-Stokes equations for a pure and incompressible fluid, fluctuating equations for conservation of mass and momentum are given by,

$$\frac{\partial u_i'}{\partial x_i} = 0 \tag{3.1}$$

$$\frac{\partial u_i'}{\partial t} + u_j' \frac{\partial u_i'}{\partial x_j} = -\frac{1}{\rho_f}\frac{\partial p'}{\partial x_i} + \nu_f \frac{\partial^2 u_i'}{\partial x_j \partial x_j} - \frac{1}{\rho_f} f_i' + a_i' \tag{3.2}$$

where ρ_f represents the fluid density and $\nu_f = \mu_f/\rho_f$ the kinematic viscosity of the fluid respectively. Here f_i' represents the dispersed phase two-way coupling source term with contributions from either drag f_i^d, or electrical body forces f_i^d, and a_i' the artificial forcing acceleration required to prevent decay of the turbulence within a homogeneous and isotropic flow field. The material derivative which appears on the LHS of equation (3.2) represents the time rate of change of momentum, for a fluid element subjected to a time and spatially dependent velocity field as it moves in the co-ordinate system defined by x_i.

3.2.1 Treatment of the Discrete Phase Momentum Source Term

Treatment of the discrete phase source term present in equation (3.2), requires first a Lagrangian to Eulerian transformation of information. This is performed using a nearest-node projection scheme, (Kaufmann et al. 2008). For a general uppercase Lagrangian variable Z, the nearest-node scheme may be written as,

$$z(x_i, t) = \frac{1}{(\Delta x)^3} \sum_{n=1}^{N_p} Z^{(n)}(X_i, t)\delta(x_i - X_i^{(n)}) \tag{3.3}$$

where the interface between the discrete Lagrangian particle and Eulerian continuum phase is represented by the vectorial Dirac delta function $\delta(x_i - X_i^{(n)})$, with Z being

a vector or scalar dispersed phase quantity. The choice of projection method used for DNS investigations presented in this thesis is discussed further in section 5.4.

Subsequently, the contribution from drag on the two-way coupling source term present in equation (3.2), is defined by,

$$f_i^d(x_i,t) = \frac{1}{(\Delta x)^3}\sum_{n=1}^{N_p}\frac{M_p}{\tau_p}\left(u_i(X_i,t) - V_i^{(n)}\right)\delta(x_i - X_i^{(n)}) \tag{3.4}$$

and the contribution from electrical Lorentz forces is defined by,

$$f_i^e(x_i,t) = \frac{1}{(\Delta x)^3}\sum_{n=1}^{N_p} Q_p e_i(X_i,t)\delta(x_i - X_i^{(n)}) \tag{3.5}$$

Together, equations (3.4) and (3.5) contribute to the total force exerted by N_p particles per unit volume of fluid such that,

$$f_i(x_i,t) = f_i^d(x_i,t) + f_i^e(x_i,t) \tag{3.6}$$

It should be noted that the mass loading ratio ϕ_m defined by equation (2.11), describing the ratio between the total mass of particles to the total mass of fluid within a given volume dimension, is automatically computed when substituting equations (3.4) and (3.5), in the Navier-Stokes momentum equation given by (3.2).

3.2.2 The Reynolds Stress and Kinetic Energy Transport Equations

In this section, transport equations for the fluctuating turbulent Reynolds stresses and the fluctuating turbulent kinetic energy are derived. These transport equations are valid specifically for a homogeneous and isotropic turbulent flow field. Homogeneous flows are defined as flows whose statistical properties are invariant under translations of the reference frame. Isotropic flows extend to flows whose statistical properties are invariant under both translations *and* rotations of the reference frame, in other words there are zero spatial gradients for any spatially averaged quantity.

Starting from the transport equation for fluctuating momentum u_i' given by (3.2), multiplying by u_j' gives,

$$u_j'\frac{\partial u_i'}{\partial t} + u_j'u_k'\frac{\partial u_i'}{\partial x_k} = -\frac{1}{\rho_f}u_j'\frac{\partial p'}{\partial x_i} + \nu_f u_j'\frac{\partial^2 u_i'}{\partial x_k \partial x_k} - \frac{1}{\rho_f}u_j' f_i' + u_j' a_i' \tag{3.7}$$

Similarly, multiplying a corresponding transport equation for u_j' with u_i' gives,

$$u_i'\frac{\partial u_j'}{\partial t} + u_i'u_k'\frac{\partial u_j'}{\partial x_k} = -\frac{1}{\rho_f}u_i'\frac{\partial p'}{\partial x_j} + \nu_f u_i'\frac{\partial^2 u_j'}{\partial x_k \partial x_k} - \frac{1}{\rho_f}u_i' f_j' + u_i' a_j' \tag{3.8}$$

Summation of equations (3.7) and (3.8) together, utilising identities,

$$\frac{\partial u_i'u_j'}{\partial t} = u_i'\frac{\partial u_j'}{\partial t} + u_j'\frac{\partial u_i'}{\partial t} \tag{3.9}$$

$$\frac{1}{2}\frac{\partial u_i'u_j'u_k'}{\partial x_k} = u_j'u_k'\frac{\partial u_i'}{\partial x_k} + u_i'u_k'\frac{\partial u_j'}{\partial x_k} \tag{3.10}$$

and,

$$\frac{\partial^2 u_i'u_j'}{\partial x_k \partial x_k} = 2\frac{\partial u_i'\partial u_j'}{\partial x_k \partial x_k} + u_i'\frac{\partial^2 u_j'}{\partial x_k \partial x_k} + u_j'\frac{\partial^2 u_i'}{\partial x_k \partial x_k} \tag{3.11}$$

an ensemble average denoted by $\langle\rangle_{\mathscr{E}}$ (see appendix A), is then taken across terms to yield a transport equation for the turbulent fluctuating Reynolds stresses.

$$\begin{aligned}\frac{\partial \left\langle u_i'u_j'\right\rangle_{\mathscr{E}}}{\partial t} + \frac{1}{2}\frac{\partial \left\langle u_i'u_j'u_k'\right\rangle_{\mathscr{E}}}{\partial x_k} = &-\frac{1}{\rho_f}\left\langle u_j'\frac{\partial p'}{\partial x_i} + u_i'\frac{\partial p'}{\partial x_j}\right\rangle_{\mathscr{E}} + \nu_f\frac{\partial^2 \left\langle u_i'u_j'\right\rangle_{\mathscr{E}}}{\partial x_k \partial x_k} \\ &-2\nu_f\left\langle \frac{\partial u_i'\partial u_j'}{\partial x_k \partial x_k}\right\rangle_{\mathscr{E}} - \frac{1}{\rho_f}\left\langle u_j' f_i' + u_i' f_j'\right\rangle_{\mathscr{E}} + \left\langle u_j' a_i' + u_i' a_j'\right\rangle_{\mathscr{E}}\end{aligned} \tag{3.12}$$

Since the flow is both homogeneous and isotropic, assuming ergodicity (see section A.6), allows one to replace ensemble averages with spatial averages denoted by $\langle\rangle_{\mathscr{V}}$. Subsequently, second terms on both the LHS and RHS of equation (3.12) go to zero. This yields a simplified transport equation for the turbulent Reynolds stresses.

$$\frac{\partial \left\langle u_i' u_j' \right\rangle_{\mathscr{V}}}{\partial t} = -\frac{1}{\rho_f} \left\langle u_j' \frac{\partial p'}{\partial x_i} + u_i' \frac{\partial p'}{\partial x_j} \right\rangle_{\mathscr{V}} - 2\nu_f \left\langle \frac{\partial u_i' \partial u_j'}{\partial x_k \partial x_k} \right\rangle_{\mathscr{V}} - \frac{1}{\rho_f} \left\langle u_j' f_i' + u_i' f_j' \right\rangle_{\mathscr{V}} + \left\langle u_j' a_i' + u_i' a_j' \right\rangle_{\mathscr{V}} \tag{3.13}$$

The first term on the LHS of equation (3.13), represents the time-rate of change of the Reynolds stresses. On the RHS of equation (3.13), the first term represents the velocity-pressure gradients within the flow field, the second term represents the viscous dissipation tensor, and the third and fourth terms represent the two-way coupling source, and artificial forcing acceleration terms respectively. Particular note should be made to the fact that forcing energy is now an explicit function of the local fluid velocity field.

To derive a transport equation for the turbulent kinetic energy defined as $k = \frac{1}{2} \langle u_i' u_i' \rangle_{\mathscr{V}}$, one can take half the trace of equation (3.12) letting $j = i$ to yield,

$$\frac{\partial \frac{1}{2} \langle u_i' u_i' \rangle_{\mathscr{V}}}{\partial t} = -\nu_f \left\langle \frac{\partial u_i' \partial u_i'}{\partial x_j \partial x_j} \right\rangle_{\mathscr{V}} - \frac{1}{\rho_f} \langle u_i' f_i' \rangle_{\mathscr{V}} + \langle u_i' a_i' \rangle_{\mathscr{V}} \tag{3.14}$$

Here the sub-script notation k is replaced by j for readability. Again since only homogeneous and isotropic flows are considered, there is no velocity-pressure gradient term appearing in equation (3.14).

3.2.3 The Non-Linear Term and its Rotational Form

It should be noted, that the non-linear term appearing in equation (3.2) is presented in its convective form, and not the physical rotational form. The physical rotational form has been shown beneficial for numerical integration, in the sense that it conserves

more kinetic energy (Hussaini 1987; Layton et al. 2009), and is cheapest to compute numerically compared to its convective, divergence and skew-symmetric counterpart forms. To yield the physical rotational form for equation (3.2), one may use the identity,

$$u'_j \frac{\partial u'_i}{\partial x_j} = \epsilon_{ijk}\omega'_j u'_k + \frac{\partial}{\partial x_i}\left(\frac{1}{2}u'_j u'_j\right) \tag{3.15}$$

Here the Levi-Civita tensor ϵ_{ijk} is defined as $+1$ for even permutations of $(1,2,3)$, -1 for odd permutations of $(1,2,3)$, and 0 if any index is repeated. The first term on the RHS of equation (3.15) represents the non-linear cross product of vorticity and velocity fluctuations such that,

$$\epsilon_{ijk}\omega'_j u'_k \equiv (\omega' \times \mathbf{u}') \tag{3.16}$$

where the fluctuating vorticity vector ω' is computed by taking the curl of the fluctuating velocity field vector, expressed as,

$$\omega'_i = \epsilon_{ijk}\frac{\partial u'_k}{\partial x_j} \tag{3.17}$$

The LHS of equation (3.15) represents the convective form of the non-linear fluctuating velocities and the last term on the RHS of equation (3.15) represents the change of the fluid kinetic energy per unit mass of fluid. Subsequently, by substituting equation (3.15) into equation (3.2) one derives,

$$\frac{\partial u'_i}{\partial t} = -\epsilon_{ijk}\omega'_j u'_k - \frac{\partial p^*}{\partial x_i} + \nu_f \frac{\partial^2 u'_i}{\partial x_j \partial x_j} - \frac{1}{\rho_f} f'_i + a'_i \tag{3.18}$$

Noting that the treatment of the last term appearing in equation (3.15) has now become part of the modified pressure in the form $p^* = p'/\rho_f + \frac{1}{2}u_i'^2$.

3.3 The Equations of Particle Motion

In this section the dispersed particle phase equations for homogeneous and isotropic flows are introduced. For DNS investigations presented in this thesis, a point force approximation is used model the dispersed phase. This typically assumes that the diameter of a real particle is much smaller than the smallest scales of turbulence such that $D \ll \eta$. If conditions of the dispersed phase require significantly large particle diameters, based on the analysis of Ling et al. (2013), the condition of $D/\eta \ll 1$ may be relaxed up to $D/\eta = \sqrt{18\delta}$ with $\delta \approx 5\%$, before point-particle assumptions become invalidated. Nevertheless, the material density of particles is assumed to be much larger than the density of the fluid, such that $\rho_p \gg \rho_f$. This allows us to neglect buoyancy, added mass, Basset history, and pressure gradient forces from the full particle equations of motion (Maxey and Riley 1983).

The position and velocity for a real particle is then calculated using the following ordinary differential equations,

$$\frac{\mathrm{d}X_i^{(n)}}{\mathrm{d}t} = V_i^{(n)} \tag{3.19}$$

$$\frac{\mathrm{d}V_i^{(n)}}{\mathrm{d}t} = \frac{1}{\tau_p}(U_i - V_i^{(n)}) + \frac{Q_p}{M_p}E_i + g_i \tag{3.20}$$

Here $V_i^{(n)}$ and $X_i^{(n)}$ are the instantaneous Lagrangian velocity and position of the n^{th} particle respectively, recalling that uppercase variables denote a Lagrangian quantity. The first and second terms on the RHS of equation (3.20) represent the body forces due to drag with the fluid where $U_i = u_i(X_i^{(n)}, t)$ is the fluid velocity seen at the particles position, and electrical body forces experienced by a particle of charge Q_p and mass M_p in the presence of an electric field $E_i = e_i(X_i^{(n)})$ at the particle position. Here both the fluid velocity and electric field seen by the particle, is calculated using interpolation from solutions known at the nearest surrounding eight grid nodes from the particle using a 2nd-order accurate polynomial (Ferziger and Perić 1996). Lastly, the third term on the RHS of equation (3.20) represents the acceleration of the particle due to gravity,

typically taken as $g_i = -9.81\delta_{i3}$. The particle relaxation time τ_p is modelled using the non-linear modified Stokes drag law given by,

$$\tau_p = \frac{\rho_p D^2}{18\mu_f} \frac{1}{f_D} \tag{3.21}$$

Assuming Stokes flow conditions where $f_D = 1$, equation (3.21) simplifies to provide a straightforward approximation for the characteristic particle relaxation time. In equation (3.21), D is the diameter of the particle, and f_D the drag correction factor using the Schiller and Naumann (1933) model defined as,

$$f_D = 1 + 0.15 Re_p^{0.687} \tag{3.22}$$

This model is valid up to a particle Reynolds number of $Re_p \leq 1000$, where Re_p is defined as,

$$Re_p = \frac{|(U_i - V_i)|\, D}{\nu_f} \tag{3.23}$$

The ratio of the characteristic particle relaxation time to characteristic fluid time-scale defines the particle Stokes number. Typically for turbulent flows, the characteristic fluid time-scale used to define the particle Stokes number is the Kolmogorov time-scale τ_η.

$$St_\eta = \frac{\tau_p}{\tau_\eta} \tag{3.24}$$

If $St_\eta \ll 1$ then the particle will follow the turbulent flow like a tracer. But if $St_\eta > 1$, the particle will remain relatively unaffected by the flow acting somewhat ballistically. Most importantly, the Stokes number characterises the majority of dispersed particle phase behaviour.

3.3.1 The Mesoscopic Eulerian Formalism

The Mesoscopic Eulerian Formalism (MEF) originally presented by Février et al. (2005), is based on the presumed chaotic behaviour of inertial particles interacting with a given carrier-fluid realization denoted by $\mathscr{H}_f$. The goal is to separately account for the correlated mesoscopic particle velocity field shared by all particles and affected via interaction with the turbulence, and a spatially uncorrelated velocity contribution which may be characterized by Eulerian fields of particle velocity moments. The formalism considers a large number of particle phase realizations denoted by $\mathscr{H}_p$, that differ slightly with initial conditions such as position and velocity, yet yield the same statistics over a sufficiently large finite period of time for a given carrier-fluid realization. The MEF is used to investigate properties of statistically stationary particle-laden isotropic turbulence.

For a general local and instantaneous mesoscopic quantity $\tilde{z}_p(x_i,t)$, the contracted notation is introduced, whereby $\tilde{z}_p(x_i,t) = \langle z_p(t)|\mathscr{H}_f\rangle_{\mathscr{E}}$ represents an ensemble averaged quantity conditioned on a single carrier fluid flow realisation. Here it should be noted that the overbar $\tilde{}$, represents a quantity derived from the mesoscopic field.

First, the velocity of a particle n located at point X_i at time t, may formally be expressed in terms of an instantaneous mesoscopic Eulerian particle velocity component $\tilde{v}_i(X_i,t)$, and a random uncorrelated velocity component $\delta V_i^{(n)}(X_i,t)$, otherwise more commonly referred to as the random uncorrelated motion (RUM).

$$V_i^{(n)}(X_i,t) = \tilde{v}_i(X_i,t) + \delta V_i^{(n)}(X_i,t) \tag{3.25}$$

The first term on the RHS of equation (3.25) stems from the mesoscopic Eulerian particle velocity field (MEPVF), a field shared by all particles that accounts for all scale interactions with the entire spectrum of fluid turbulent motions. The second term on the RHS of equation (3.25) is associated with each particle separately, and is simply the vector difference in velocity between the Lagrangian particle and the mesoscopic Eulerian particle velocity seen by the particle. To some extent, the distribution of $\delta V_i^{(n)}(X_i,t)$ satisfies the assumption of molecular chaos, hence it is referred to in literature as the

quasi-brownian velocity distribution (QBVD). Statistical properties of the QBVD are such that the ensemble average of $\delta V_i^{(n)}(X_i, t)$, for all particle phase realisations conditioned on a given carrier fluid realisations equal zero. i.e. $\langle \delta V_i(t) | \mathscr{H}_f \rangle_{\mathscr{E}} = 0$.

3.3.1.1 Numerical Approximation

Using Eulerian-Lagrangian DNS, one may compute approximations to the MEF using local cell volume averages at a given time t for relevant dispersed phase quantities. With this approximation, each computational particle represents a single particle phase realisation $\mathscr{H}_p$, and each local cell volume surrounding an Eulerian grid node corresponds to a single carrier fluid realisation $\mathscr{H}_f$.

The local cell volume average used for MEF approximation is equivalent to a spatial filtering procedure, where Lagrangian quantities are projected onto an Eulerian grid. The appropriate choice of local cell size used for volume averaging requires consideration of both spatial and statistical error. Spatial error occurs due to the fact that computational particles themselves are not at grid nodes where MEF approximations are evaluated at. Hence any spatial gradients that exist within local scales smaller than the cell size are filtered. Statistical error on the other-hand is due to the fact that only a finite number of computational particles exist within the local cell volume itself, and as the grid is refined, fewer and fewer computational particles are available for accurate MEF approximations. The compromise between spatial and statistical accuracy can be characterised using the mean expected error E, (Schmidt 2006; Bartlett 1963), which for a single dimension using the nearest-node scheme can be defined as follows,

$$E \approx \sqrt{\frac{f}{l n_c} + \frac{1}{4}\frac{l^4}{144}\left(\frac{\mathrm{d}^2 f}{\mathrm{d}x^2}\right)^2} \tag{3.26}$$

Here, f represents the information contribution to the mesoscopic Eulerian grid node, l represents the length of the nearest-node kernel support, which is equal to $\Delta x/2$, and n_c the represents the number of computational particles encompassed within the bounds of the support itself. The first term under the radical of equation (3.26) represents statistical error, and the second term represents spatial error. One can interpret from

equation (3.26), that statistical error decreases with an increase in number of computational particles, up until a point whereby the spatial error starts to dominate (assuming that spatial resolution Δx remains a constant). Whilst the spatial error term may dominate for this type of scenario, there is no change in its magnitude, thus no adverse effect on the quality of dispersed phase information projected to the Eulerian grid. Due to the fact that spatial resolution appears within the denominator of the statistical error term, increasing grid refinement whilst keeping the number of computational particles constant will increase statistical error, (Schmidt 2006; Bartlett 1963). On the otherhand, increasing coarseness of the grid also results in an increase of spatial error. As a consequence, there is an optimal spatial resolution whereby the mean expected error of the scheme is at a minimum.

For convenience in this work, MEF approximations are evaluated at nodes of the computational grid used to directly resolve the Navier-Stokes momentum equations on, using a cell volume with dimensions of $(\Delta x)^3$ centred on the computational grid nodes themselves. Subsequently, a single carrier fluid realisation $\mathscr{H}_f$ is directly resolved without any approximation. Based on the previous considerations regarding the compromise between statistical and spatial error, one must subsequently ensure that the number of computational particles residing within cell volumes is sufficiently high enough. This issue is investigated further in section 5.4.2 of this thesis.

Nevertheless, to compute an approximation to the MEPVF, knowledge of the local and instantaneous mesoscopic particle number density is required. Since this is a scalar quantity, one may substitute $Z_\phi = 1$ in equation (3.3) to yield,

$$\tilde{n}_p(x_i, t) \approx \frac{1}{(\Delta x)^3} \sum_{n=1}^{N_p} \delta(x_i - X_i^{(n)}) \tag{3.27}$$

Subsequently, one may then compute the local and instantaneous mesoscopic particle velocity, by substituting $Z_i = V_i$ in (3.3) and normalising by the local and instantaneous mesoscopic particle number density.

$$\tilde{v}_i(x_i,t) \approx \frac{1}{\tilde{n}_p(x_i,t)} \left(\frac{1}{(\Delta x)^3} \sum_{n=1}^{N_p} V_i^{(n)}(X_i,t)\delta(x_i - X_i^{(n)}) \right) \tag{3.28}$$

Utilising equation (3.25) allows one to subsequently compute the quantity $\tilde{v}_i(X_i,t)$, and also the quantity $\delta V_i^{(n)}(X_i,t)$. From this information it is then possible to characterise the QBVD for a given carrier-fluid realisation, and associated random uncorrelated velocity (RUV) field using,

$$\langle \delta V_i(t) | \mathscr{H}_f \rangle_{\mathscr{E}} \approx \frac{1}{\tilde{n}_p(x_i,t)} \left(\frac{1}{(\Delta x)^3} \sum_{n=1}^{N_p} \delta V_i^{(n)}(X_i,t)\delta(x_i - X_i^{(n)}) \right) \tag{3.29}$$

Similarly, higher order moments such as the mesoscopic kinetic stress tensor of the RUM can be computed using,

$$\langle \delta V_i(t)\delta V_j(t) | \mathscr{H}_f \rangle_{\mathscr{E}} \approx \frac{1}{\tilde{n}_p(x_i,t)} \left(\frac{1}{(\Delta x)^3} \sum_{n=1}^{N_p} \delta V_i^{(n)}\delta V_j^{(n)}(X_i,t)\delta(x_i - X_i^{(n)}) \right) \tag{3.30}$$

and also the third-order moment of the RUM using,

$$\langle \delta V_i(t)\delta V_j(t)\delta V_k(t) | \mathscr{H}_f \rangle_{\mathscr{E}} \approx \frac{1}{\tilde{n}_p(x_i,t)} \left(\frac{1}{(\Delta x)^3} \sum_{n=1}^{N_p} \delta V_i^{(n)}\delta V_j^{(n)}\delta V_k^{(n)}(X_i,t)\delta(x_i - X_i^{(n)}) \right) \tag{3.31}$$

At this point it should be reminded that quantities computed usign equations (3.27)-(3.31), are local and instantaneous to the computational cell volumes of the macroscopic system used for averaging. Hence, they represent a mesoscopic characterisation of particle phase properties.

3.3.1.2 Eulerian Transport Equations for the Mesoscopic Particle Phase

Eulerian transport equations for the mesoscopic particle phase can be derived following the procedure outlined by Février et al. (2005). For a dispersed phase subjected to drag,

electrical, and gravitational body-forces, the local and instantaneous transport equations for the mesoscopic particle number density and mesoscopic particle velocity are given by,

$$\frac{\partial \tilde{n}_p}{\partial t} + \frac{\partial \tilde{n}_p \tilde{v}_i}{\partial x_i} = 0 \tag{3.32}$$

$$\frac{\partial \tilde{n}_p \tilde{v}_i}{\partial t} + \frac{\partial \tilde{n}_p \tilde{v}_i \tilde{v}_j}{\partial x_j} = \frac{\tilde{n}_p}{\tau_p}(u_i - \tilde{v}_i) + \tilde{n}_p \frac{Q_p}{m_p} e_i + \tilde{n}_p g_i - \frac{\partial \tilde{n}_p \delta\tilde{\sigma}_{p,ij}}{\partial x_j} \tag{3.33}$$

In equation (3.33), $\delta\tilde{\sigma}_{p,ij}(x_i,t) = \langle \delta V_i(t)\delta V_j(t)|\mathscr{H}_f\rangle_{\mathscr{E}}$ represents the mesoscopic kinetic stress tensor of the RUM, noting its equivalent approximation given by (3.30). At the second order, a transport equation for mesoscopic kinetic stress tensor is given by,

$$\frac{\partial \tilde{n}_p \delta\tilde{\sigma}_{p,ij}}{\partial t} + \frac{\partial \tilde{n}_p \delta\tilde{\sigma}_{p,ij}\tilde{v}_k}{\partial x_k} = -2\frac{\tilde{n}_p}{\tau_p}\delta\tilde{\sigma}_{p,ij} - \tilde{n}_p \delta\tilde{\sigma}_{p,jk}\frac{\partial \tilde{v}_i}{\partial x_k} - \tilde{n}_p \delta\tilde{\sigma}_{p,ik}\frac{\partial \tilde{v}_j}{\partial x_k} - \frac{\partial \tilde{n}_p \delta\tilde{\xi}_{p,ijk}}{\partial x_k} \tag{3.34}$$

where $\delta\tilde{\xi}_{p,ijk}(x_i,t) = \langle \delta V_i(t)\delta V_j(t)\delta V_k(t)|\mathscr{H}_f\rangle_{\mathscr{E}}$ represents the third-order moment of the RUM, noting also its equivalent approximation given by (3.31). The first term on the RHS of equation (3.34) represents the dissipation of the RUM stresses by the fluid drag. Second and third terms on the RHS of equation (3.34) represent production of RUM by mesoscopic velocity field gradients.

Subsequently, by taking the trace of equation (3.34) letting $j = i$ and dividing by two, one may obtain a transport equation describing the RUM kinetic energy, i.e. $\delta\tilde{\theta}_p = \delta\tilde{\sigma}_{p,ii}/2$.

$$\frac{\partial \tilde{n}_p \delta\tilde{\theta}_p}{\partial t} + \frac{\partial \tilde{n}_p \delta\tilde{\theta}_p \tilde{v}_j}{\partial x_j} = -2\frac{\tilde{n}_p}{\tau_p}\delta\tilde{\theta}_p - \tilde{n}_p \delta\tilde{\sigma}_{p,ij}\frac{\partial \tilde{v}_i}{\partial x_j} - \frac{1}{2}\frac{\partial \tilde{n}_p \delta\tilde{\xi}_{p,iij}}{\partial x_j} \tag{3.35}$$

3.3.1.3 Mean Kinetic Energy Transport Equations for the MEPVF and QBVD

In order to understand the energy exchange interactions between the MEPVF and the QBVD, a macroscopic viewpoint of mesoscopic particle phase characteristics must instead be taken. Firstly, macroscopic particle phase quantities can be obtained by taking a density-weighted average (see appendix A.4), of mesoscopic particle phase quantities using the mesoscopic particle number density $\tilde{n}_p$ as the weighting factor. The density-weighted average is taken over an ensemble of carrier-fluid realisations $\mathscr{H}_f$ that contribute to the macroscopic turbulent flow field[1].

For a general mesoscopic variable $\tilde{g}$, this average is defined by,

$$\langle \tilde{g} \rangle_{\mathscr{F}} = \frac{\langle \tilde{n}_p(x_i,t)\tilde{g}(x_i,t) \rangle_{\mathscr{E}}}{\langle \tilde{n}_p(x_i,t) \rangle_{\mathscr{E}}} \tag{3.36}$$

where the notation $\langle . \rangle_{\mathscr{F}}$ is used to indicate the density-weighted average.

To subsequently derive a transport equation for mean mesoscopic kinetic energy, one can multiply equation (3.33) by $\tilde{v}_i$, and take the density-weighted ensemble average across terms to yield,

$$\begin{aligned} n_p \frac{\partial \tilde{q}_p^2}{\partial t} + n_p \langle \tilde{v}_i \rangle_{\mathscr{E}} \frac{\partial \tilde{q}_p^2}{\partial x_i} = -\frac{\partial}{\partial x_j}\left[n_p \langle \tilde{v}_i' \delta\tilde{\sigma}_{p,ij} \rangle_{\mathscr{F}} + \frac{1}{2} n_p \left\langle \tilde{v}_i' \tilde{v}_i' \tilde{v}_j' \right\rangle_{\mathscr{F}} \right] \\ + \frac{n_p}{\tau_p}(q_{fp} - 2\tilde{q}_p^2) + n_p \frac{Q_p}{m_p} q_{pe} - n_p \left\langle \tilde{v}_i' \tilde{v}_j' \right\rangle_{\mathscr{F}} \frac{\partial \langle \tilde{v}_i \rangle_{\mathscr{E}}}{\partial x_j} + n_p \left\langle \delta\tilde{\sigma}_{p,ij} \frac{\partial \tilde{v}_i'}{\partial x_j} \right\rangle_{\mathscr{F}} \end{aligned} \tag{3.37}$$

Here the mean mesoscopic particle number density is defined by, $n_p = \langle \tilde{n}_p(x_i,t) \rangle_{\mathscr{E}}$, distinguishing the fact that the mean of the mesoscopic particle number density distribution within a statistically stationary macroscopic system equals a constant.

In equation (3.37), the mean mesoscopic kinetic stress tensor $\left\langle \tilde{v}_i' \tilde{v}_j' \right\rangle_{\mathscr{F}}$ is defined by,

[1] In this case represented by the DNS domain itself

$$\left\langle \tilde{v}_i' \tilde{v}_j' \right\rangle_{\mathscr{F}} = \frac{\left\langle \tilde{n}_p(x_i,t)\tilde{v}_i'(x_i,t)\tilde{v}_j'(x_i,t) \right\rangle_{\mathscr{E}}}{\langle \tilde{n}_p(x_i,t) \rangle_{\mathscr{E}}} \tag{3.38}$$

Also in equation (3.37), the quantities $\tilde{q}_p^2$, q_{fp} and q_{pe} are introduced, representing respectively the mean mesoscopic particle kinetic energy defined by,

$$\tilde{q}_p^2 = \frac{1}{2} \langle \tilde{v}_i' \tilde{v}_i' \rangle_{\mathscr{F}} = \frac{1}{2} \frac{\langle \tilde{n}_p(x_i,t)\tilde{v}_i'(x_i,t)\tilde{v}_i'(x_i,t) \rangle_{\mathscr{E}}}{\langle \tilde{n}_p(x_i,t) \rangle_{\mathscr{E}}} \tag{3.39}$$

the mean kinetic energy exchange between the turbulent fluid velocity and the mesoscopic particle velocity field defined by,

$$q_{fp} = \langle u_i' \tilde{v}_i' \rangle_{\mathscr{F}} = \frac{\langle \tilde{n}_p(x_i,t) u_i'(x_i,t)\tilde{v}_i'(x_i,t) \rangle_{\mathscr{E}}}{\langle \tilde{n}_p(x_i,t) \rangle_{\mathscr{E}}} \tag{3.40}$$

and the mean kinetic energy exchange between mesoscopic particle velocity field and the electrical Lorentz force field defined by,

$$q_{pe} = \langle \tilde{v}_i' e_i \rangle_{\mathscr{F}} = \frac{\langle \tilde{n}_p(x_i,t)\tilde{v}_i'(x_i,t) e_i(x_i,t) \rangle_{\mathscr{E}}}{\langle \tilde{n}_p(x_i,t) \rangle_{\mathscr{E}}} \tag{3.41}$$

A transport equation for the mean RUM kinetic energy can also be derived, by setting $i = j$ and taking a density-weighted ensemble average across terms present in equation (3.34),

$$\begin{aligned} n_p \frac{\partial \delta q_p^2}{\partial t} + n_p \langle \tilde{v}_i \rangle_{\mathscr{E}} \frac{\partial \delta q_p^2}{\partial x_i} = & -\frac{\partial}{\partial x_j} \left[\frac{1}{2} n_p \left\langle \delta \tilde{\xi}_{p,iij} \right\rangle_{\mathscr{F}} + n_p \left\langle \tilde{v}_j' \delta \tilde{\theta}_p \right\rangle_{\mathscr{F}} \right] \\ & - \frac{n_p}{\tau_p} 2\delta q_p^2 - n_p \langle \delta \tilde{\sigma}_{p,ij} \rangle_{\mathscr{F}} \frac{\partial \langle \tilde{v}_i \rangle_{\mathscr{E}}}{\partial x_j} - n_p \left\langle \delta \tilde{\sigma}_{p,ij} \frac{\partial \tilde{v}_i'}{\partial x_j} \right\rangle_{\mathscr{F}} \end{aligned} \tag{3.42}$$

Here the mean RUM stress tensor $\langle \delta \tilde{\sigma}_{p,ij} \rangle_{\mathscr{F}}$ is defined by,

$$\langle \delta \tilde{\sigma}_{p,ij} \rangle_{\mathscr{F}} = \frac{\langle \tilde{n}_p(x_i,t) \delta \tilde{v}_i(x_i,t) \delta \tilde{v}_j(x_i,t) \rangle_{\mathscr{E}}}{\langle \tilde{n}_p(x_i,t) \rangle_{\mathscr{E}}} \tag{3.43}$$

and the mean RUM kinetic energy δq_p^2 defined by,

$$\delta q_p^2 = \left\langle \delta\tilde{\theta}_p \right\rangle_{\mathscr{F}} = \frac{\left\langle \tilde{n}_p(x_i,t)\delta\tilde{\theta}_p(x_i,t) \right\rangle_{\mathscr{E}}}{\langle \tilde{n}_p(x_i,t) \rangle_{\mathscr{E}}} \tag{3.44}$$

Together, equations (3.44) and (3.39) contribute to the total macroscopic kinetic energy per unit mass of the particle phase defined by,

$$q_p^2 = \tilde{q}_p^2 + \delta q_p^2 \tag{3.45}$$

Taking into account the statistical properties of a stationary homogeneous and isotropic turbulent flow field, invoking the ergodic hypothesis (see appendix A.6), allows one to replace ensemble averages with equivalent spatial averages taken with a frame of reference following that of the mean flow. Subsequently, equations (3.37) and (3.42) can be simplified further to yield,

$$n_p \frac{\partial \tilde{q}_p^2}{\partial t} = \frac{n_p}{\tau_p}(q_{fp} - 2\tilde{q}_p^2) + n_p \frac{Q_p}{m_p} q_{pe} - n_p \tilde{\epsilon}_p \tag{3.46}$$

and,

$$n_p \frac{\partial \delta q_p^2}{\partial t} = -\frac{n_p}{\tau_p} 2\delta q_p^2 + n_p \tilde{\epsilon}_p \tag{3.47}$$

where the dissipation of the mesoscopic field has been introduced in the form,

$$\tilde{\epsilon}_p = -\left\langle \delta\tilde{\sigma}_{p,ij} \frac{\partial \tilde{v}_i'}{\partial x_j} \right\rangle_{\mathscr{F}} \tag{3.48}$$

Lastly, it should be noted that for particle suspensions within a turbulent flow field there exists a dominant transfer of energy from the MEPVF to the QBVD. Hence, $\tilde{\epsilon}_p$ is termed a sink of mesoscopic kinetic energy within equation (3.46), and a source of quasi-Brownian kinetic energy within equation (3.47).

3.4 Equations for an Electrical Lorentz Force Field

For an electrically charged non-uniform particle suspension present within a turbulent fluid flow field, an electric field describing Lorentz forces present between all charged particles of the system exists. The electric field may be treated as a continuum, whose properties depend entirely upon the spatial distribution of charged particles within the suspension.

To determine the electric field, it is first necessary to account for the non-uniformity of electrically charged particles by computing the continuous Eulerian charge distribution throughout the suspension. To achieve this, one computes the local charge density within a cell volume $(\Delta x)^3$ centred about each Eulerian grid node within the DNS domain. This is achieved using the nearest-node scheme described earlier in section 3.2.1, and defined by equation (3.3). Applying Gauss's theorem and Poisson's equation towards this Eulerian charge distribution, the scalar electric voltage potential ϕ_e, and electric field vector e_i may be computed throughout the entire DNS domain.

$$\frac{\partial e_i}{\partial x_i} = -\frac{\partial^2 \phi_e}{\partial x_i^2} = \frac{\rho_Q}{\epsilon_r \epsilon_0} \tag{3.49}$$

Here, $\epsilon_0 = 8.854 \times 10^{-12}\ F/m$ represents the electrical permittivity of free space, ϵ_r the relative permittivity of the continuum, and ρ_Q the local charge density. Notably this method assumes that the Lorentz force due to the nearest particle is small compared to the effect of all particles within the suspension combined (Karnik 2010). This is verified by characterising the electrical length scale x_E defined by,

$$x_E = \frac{q_p}{4\pi \epsilon_0 e_{rms}} \tag{3.50}$$

where q_p is the charge present on a single particle and e_{rms} the fluctuating electric field magnitude. The assumption of a continuum approximation for an electrical Lorentz force field remains valid if charged particles are separated by a distance greater than the electrical length scale.

Chapter 4

Governing Equations (Spectral Form)

4.1 Overview

Before the spectral space transformations for governing equations are presented, it is necessary to define how domain variables are transformed from real space to spectral space and vice versa. Starting with the continuous forward and inverse transforms for 1D and 3D decompositions, simplifications required for defining discrete forward and inverse Fourier transforms over arbitrary domain sizes are introduced. Lastly, spectral equations for the turbulent fluid phase, mesoscopic particle phase, and electrical continuum phase are subsequently presented, along with a summary respective spectral energy transport equations.

The reason for presenting spectral equations at this point is to clarify the spectral forms of terms present within fluid, mesoscopic particle, and electrical continuum phase energy transport equations. These spectral terms characterise the energy behaviour, and provide insight on the relative magnitude and direction of energy transfer across phases in the presence of two-way coupling, across a specified range of resolved turbulent scales. Important terms will first be identified here, and examined in detail later within the context of DNS investigations presented in chapters 6 and 7.

4.2 The Forward and Inverse Fourier Transform

The forward Fourier transform is a function that allows spatially periodic signals in the spatial domain (real space), to be expressed in terms of signals in the frequency domain (spectral space). For spatially continuous and periodic functions in 1D this forward Fourier transform may be written as follows.

$$\hat{\phi}(\kappa) \equiv \mathscr{F}\left\{\phi(x)\right\} = \int_{-\infty}^{\infty} \phi(x) \exp^{-2\pi I \kappa x}\, dx \tag{4.1}$$

Here, ϕ and $\hat{\phi}$ represent signals in real and spectral space respectively, with κ representing the wavenumber, x the spatial position of the signal, and I as the imaginary componant. The inverse Fourier transform performs the exact opposite operation, and allows signals in spectral space to be expressed in terms of signals in real space.

$$\phi(x) \equiv \mathscr{F}^{-1}\left\{\hat{\phi}(\kappa)\right\} = \int_{-\infty}^{\infty} \hat{\phi}(\kappa) \exp^{2\pi I \kappa x}\, d\kappa \tag{4.2}$$

In 3D, forward and inverse transforms are given by,

$$\hat{\phi}(\kappa_1, \kappa_2, \kappa_3) = \int_{-\infty}^{\infty}\int_{-\infty}^{\infty}\int_{-\infty}^{\infty} \phi(x_1, x_2, x_3) \exp^{-2\pi I[\kappa_1 x_1 + \kappa_2 x_2 + \kappa_3 x_3]}\, dx_1 dx_2 dx_3 \tag{4.3}$$

and,

$$\phi(x_1, x_2, x_3) = \int_{-\infty}^{\infty}\int_{-\infty}^{\infty}\int_{-\infty}^{\infty} \hat{\phi}(\kappa_1, \kappa_2, \kappa_3) \exp^{2\pi I[\kappa_1 x_1 + \kappa_2 x_2 + \kappa_3 x_3]}\, d\kappa_1 d\kappa_2 d\kappa_3 \tag{4.4}$$

Fourier transforms are well suited to periodic signals, and since all DNS of turbulence presented in this thesis are homogeneous, they are also by definition periodic. Thus it is suitable to represent the flow field in terms of a discrete Fourier series approximation

that assume 2π spatial periodicity. For 1D cases, an arbitrary physical quantity ϕ may be represented as a discrete truncated Fourier series with N wave-numbers such that,

$$\phi(x_n) = \sum_{m=-\frac{N}{2}+1}^{N/2} \hat{\phi}(\kappa_m) \exp^{I\kappa_m x_n} \tag{4.5}$$

with Fourier amplitudes,

$$\hat{\phi}(\kappa_m) = \frac{1}{N} \sum_{n=0}^{N-1} \phi(x_n) \exp^{-I\kappa_m x_n} \tag{4.6}$$

The wave-number κ is now a function of node positions x_n, with grid spacings Δ such that,

$$x_n = n\Delta \tag{4.7}$$

and,

$$\kappa_m = \frac{2\pi m}{N\Delta} \tag{4.8}$$

with sequences $n = 0, 1, ..., N-1$ and $m = -\frac{N}{2}, ..., -1, 0, 1, ..., \frac{N}{2}$ defined for node positions and wave-numbers respectively. It should be noted at this point that the domain can be of any arbitrary size depending on grid spacings used. In 3D, equations (4.5) and (4.6) become,

$$\phi(x_n, x_o, x_p) = \sum_{m=-\frac{N_x}{2}+1}^{N_x/2} \sum_{l=-\frac{N_y}{2}+1}^{N_y/2} \sum_{k=-\frac{N_z}{2}+1}^{N_z/2} \hat{\phi}(\kappa_m, \kappa_l, \kappa_k) \exp^{I[\kappa_m x_n + \kappa_l x_o + \kappa_k x_p]} \tag{4.9}$$

and,

$$\hat{\phi}(\kappa_m, \kappa_l, \kappa_k) = \frac{1}{N_x N_y N_z} \sum_{n=0}^{N_x-1} \sum_{o=0}^{N_y-1} \sum_{p=0}^{N_z-1} \phi(x_n, x_o, x_p) \exp^{-I[\kappa_m x_n + \kappa_l x_o + \kappa_k x_p]} \tag{4.10}$$

respectively. Here N_x, N_y and N_z represent the number of computational domain nodes used for evaluation of the flow field. Lastly, similar definitions to equations (4.7) and (4.8) exist for x_o, x_p and κ_l, κ_k.

In order to compute the discrete Fourier transform, the fast Fourier transform (FFT) algorithm of Cooley and Tukey (1965) is used. The FFT algorithm reduces the number of operations required to naively compute the discrete Fourier transform (DFT) from $O(N^2)$ down to $O(N \log N)$. The motivation being using FFT's for DNS of turbulence stems from the fact that in addition to them being fast numerically, convergence associated with usage of the spectral method itself comes with infinite-order accuracy (Gottlieb and Orszag 1977).

4.3 Spectral Equations for the Fluid Turbulence

To derive the spectral space equations for the fluid turbulence, a Fourier transform operation of terms present in equation (3.18) is performed. Noting that the Fourier transformation of the time derivative yields,

$$\mathscr{F}\left\{\frac{\partial u_i'}{\partial t}\right\} = \frac{\partial \hat{u}_i}{\partial t} \tag{4.11}$$

and a transformation of the spatial derivatives yields,

$$\mathscr{F}\left\{\frac{\partial p^*}{\partial x_i}\right\} = I\kappa_i \hat{p}^* \tag{4.12}$$

allows one to re-write equations (3.1) and (3.2) as,

$$\kappa_i \hat{u}_i = 0 \tag{4.13}$$

$$\frac{\partial \hat{u}_i(\kappa)}{\partial t} = -I\kappa_l \left(\delta_{ik} - \frac{\kappa_i \kappa_k}{\kappa^2}\right) \sum_{\kappa'} \hat{u}_k(\kappa')\hat{u}_l(\kappa - \kappa') - \nu_f \kappa^2 \hat{u}_i(\kappa) - \hat{f}_i(\kappa) + \hat{a}_i(\kappa) \quad (4.14)$$

Here the identity $I^2 = -1$ is introduced within the viscous dissipation term.

4.3.1 Spectral Energy Transport Equations

To obtain the evolution equation for the turbulent kinetic energy spectra, one simply multiplies each term in equation (4.14) by the complex conjugate of $\hat{u}_i(\kappa)$, where $\hat{u}_i^*(\kappa) \equiv \hat{u}_i(-\kappa)$).

By summing the real parts in remaining terms, over spherical shells of radius κ and thickness $\delta\kappa = 1$[1], the time rate of change of turbulent kinetic energy, non-linear energy transfer rate, and the energy dissipation rate spectra may be computed. These three quantities are given by equations (4.15), (4.16) and (4.17) respectively.

$$\frac{\partial E_{ii}(\kappa)}{\partial t} = \frac{\partial}{\partial t} \sum_{\kappa \leq |\kappa| < \kappa+1} \frac{1}{2} \left[\hat{u}_i^*(\kappa)\hat{u}_i(\kappa)\right] \quad (4.15)$$

$$T_{ii}(\kappa) = -\sum_{\kappa \leq |\kappa| < \kappa+1} \kappa_l \left(\delta_{ik} - \frac{\kappa_i \kappa_k}{\kappa^2}\right) \mathrm{Im}\left\{\sum_{\kappa'} \hat{u}_k(\kappa')\hat{u}_l(\kappa - \kappa')\hat{u}_i^*(\kappa)\right\} \quad (4.16)$$

$$D_{ii}(\kappa) = 2\nu_f \sum_{\kappa \leq |\kappa| < \kappa+1} |\kappa|^2 \frac{1}{2} \left[\hat{u}_i^*(\kappa)\hat{u}_i(\kappa)\right] \quad (4.17)$$

For the spectral two-way coupling source term, calculated as $\mathrm{Re}\left\{\hat{u}_i^*(\kappa)\hat{f}_i(\kappa)\right\}$, it should be stressed that two sub-components exist. The first component characterising the fluid-to-particle energy exchange rate due to drag has spectra defined by,

[1]Typically for a shell of thickness $\delta\kappa = 1$, there is a sufficient quantity of wave-number modes to provide reliable enough statistics in terms of the energy states for different scales of turbulent motion. However, since there is a non-uniform distribution of wave-number modes across spherical shells, the total energy contained within each band must be normalised by the number of modes present within each band.

$$\Pi_{ii}(\kappa) = -\sum_{\kappa \leq |\kappa| < \kappa+1} \mathrm{Re}\left\{\hat{u}_i^*(\kappa)\hat{f}_i^d(\kappa)\right\} \tag{4.18}$$

Here the term $\hat{f}_i^d(\kappa) = \mathscr{F}\left[f_i^d(x_i,t)\right]$ represents the Fourier transform of equation (3.4). In a similar manner, the second component characterising the fluid-to-electrical energy exchange rate due to Lorentz force interactions has spectra defined by,

$$\Sigma_{ii}(\kappa) = -\sum_{\kappa \leq |\kappa| < \kappa+1} \mathrm{Re}\left\{\hat{u}_i^*(\kappa)\hat{f}_i^e(\kappa)\right\} \tag{4.19}$$

Here, the term $\hat{f}_i^e(\kappa) = \mathscr{F}\left[f_i^e(x_i,t)\right]$ represents the Fourier transform of equation (3.5).

In equations (4.18) and (4.19), a negative energy exchange rate indicates that energy is moving *from* the fluid, to either the particle phase via drag, or electrical continuum phase via Lorentz force interactions respectively. Whereas a positive energy exchange rate indicates that energy is moving *to* the fluid, from either the particle phase or electrical continuum phase respectively. The dependency of spectral two-way coupling terms on wavenumber bands identifies the range of turbulence scales whereby the transfer of energy occurs.

The evolution equation for turbulent kinetic energy spectra is subsequently defined by,

$$\frac{\partial E(\kappa)}{\partial t} = A(\kappa) + T(\kappa) - D(\kappa) + \Pi(\kappa) + \Sigma(\kappa) \tag{4.20}$$

Here, $A(\kappa)$ is the artificial spectral forcing term required to maintain a statistically stationary turbulent flow field, and is defined by,

$$A(\kappa) = \sum_{\kappa \leq |\kappa| < \kappa+1} \mathrm{Re}\left\{\hat{u}_i^*(\kappa)\hat{a}_i(\kappa)\right\} \tag{4.21}$$

where $\hat{a}_i(\kappa)$ represents the complex artificial forcing term (see section 5.2.2).

4.3.2 The Spectral Rotational Form

To derive the spectral space equivalent for the rotational form of the Naiver-Stokes momentum transport equation, one can simply perform a Fourier transformation of equation (3.18) to give,

$$\frac{\partial \hat{u}_i}{\partial t} = -\epsilon_{ijk}\mathscr{F}\left\{\omega_j' u_k'\right\} - I\kappa_i \hat{p}^* + \nu_f I^2 \kappa^2 \hat{u}_i - \hat{f}_i(\kappa) + \hat{a}_i(\kappa) \tag{4.22}$$

noting that $I^2 = -1$. Examining the spectral form of the continuity equation provides us with the interpretation that in order to ensure a divergent free condition, the velocity vector in spectral space, $\hat{u}_i$ must be orthogonal to the wave-vector κ_i. Using this condition and taking the dot product of κ_i with the momentum equation (4.22), allows one to re-write the pressure term in its spectral space form,

$$\hat{p}^* = I\frac{\kappa_i}{\kappa^2}\left(\epsilon_{ijk}\mathscr{F}\left\{\omega_j' u_k'\right\}\right) \tag{4.23}$$

with $\kappa^2 = \kappa_i \kappa_i$. Substitution of equation (4.23) back into the equation (4.22) then yields,

$$\frac{\partial \hat{u}_i}{\partial t} = -\epsilon_{ijk}\mathscr{F}\left\{\omega_j' u_k'\right\} + \frac{\kappa_i}{\kappa^2}\left[\kappa_l \cdot \epsilon_{lmn}\mathscr{F}\left\{\omega_m' u_n'\right\}\right] - \nu_f \kappa^2 \hat{u}_i - \hat{f}_i + \hat{a}_i \tag{4.24}$$

Equation (4.24) now represents the time-integrateable spectral formulation, for the Navier-Stokes momentum equation presented in its physical rotational form.

4.4 Spectral Equations for the Mesoscopic Particle Phase

Starting from the transport equation for the mesoscopic particle number density given by equation (3.32), assuming a statistically stationary flow field one may assume that the average time rate of change for the mesoscopic particle number density to be zero, when measured relative to the scales of turbulent motion we want to characterise. This allows us to neglect the time derivative present in equation (3.32), and subsequently simplify equation (3.33) by dividing with $\tilde{n}_p$, and assuming both homogeneity and ergodicity of the flow field.

A Fourier transformation of remaining terms may then be taken to yield the spectral evolution equation for the MEPVF,

$$\frac{\partial \hat{v}_i(\kappa)}{\partial t} = \frac{1}{\tau_p}\widehat{(u_i - \tilde{v}_i)}(\kappa) + \frac{Q_p}{M_p}\hat{e}_i(\kappa) - I\kappa_j \widehat{\delta\tilde{\sigma}}_{p,ij}(\kappa) \tag{4.25}$$

noting the last term appearing in equation (4.25) defining the spectral spatial derivative of the mesoscopic kinetic stress tensor of the RUM.

4.4.1 Spectral Energy Transport Equations

In a similar manner to deriving the evolution equation for the turbulent kinetic energy spectra as noted in section 4.3.1, one can also derive the evolution equation for the mesoscopic particle phase spectra, by multiplying terms present in equation (4.25) by the complex conjugate of $\hat{v}_i(\kappa)$, where $\hat{v}_i^*(\kappa) \equiv \hat{v}_i(-\kappa)$).

By summing the real parts in remaining terms, over spherical shells of radius κ and thickness $\delta\kappa = 1$, the time rate of change of particle kinetic energy may be defined by,

$$\frac{\partial E_{p,ii}(\kappa)}{\partial t} = \frac{\partial}{\partial t} \sum_{\kappa \leq |\kappa| < \kappa+1} \frac{1}{2} \left[\hat{v}_i^*(\kappa)\hat{v}_i(\kappa)\right] \tag{4.26}$$

The particle-to-fluid energy exchange rate is then defined by,

$$\Pi_{p,ii}(\kappa) = \sum_{\kappa \leq |\kappa| < \kappa+1} \mathrm{Re}\left\{ \hat{f}_i^d(\kappa) \hat{v}_i^*(\kappa) \right\} \tag{4.27}$$

where the term $\hat{f}_i^d(\kappa) = \mathscr{F}\left[f_i^d(x_i, t) \right]$ represents the Fourier transform of equation (3.4).

Furthermore, the particle-to-electrical energy exchange rate is defined by,

$$\Sigma_{p,ii}(\kappa) = \sum_{\kappa \leq |\kappa| < \kappa+1} \mathrm{Re}\left\{ \hat{f}_i^e(\kappa) \hat{v}_i^*(\kappa) \right\} \tag{4.28}$$

where the term $\hat{f}_i^e(\kappa) = \mathscr{F}\left[f_i^e(x_i, t) \right]$ represents the Fourier transform of equation (3.5).

Lastly, the particle-to-RUM energy exchange rate is defined by,

$$\Lambda_{ii}(\kappa) = \sum_{\kappa \leq |\kappa| < \kappa+1} \mathrm{Im}\left\{ \kappa_j \widehat{\delta\tilde{\sigma}}_{p,ij}(\kappa) \hat{v}_i^*(\kappa) \right\} \tag{4.29}$$

The spectral space energy balance equation for the mesoscopic particle phase may then be defined as,

$$\frac{\partial E_p(\kappa)}{\partial t} = \Pi_p(\kappa) + \Sigma_p(\kappa) - \Lambda(\kappa) \tag{4.30}$$

where, for first and second terms on the RHS of equation (4.30), a positive energy exchange rate indicates that energy is moving *to* the particle phase, *from* either the fluid or electrical continuum phases respectively. Whereas a negative energy exchange rate indicates that energy is moving *from* the particle phase *to* either the fluid or electrical continuum phases respectively. For the last term on the RHS of equation (4.30), a negative energy exchange rate indicates that energy is moving *to* the particle phase from the RUV field, whereas a positive energy exchange rate indicates that energy is moving *from* the particle phase *to* the RUV field. Lastly, one may also define the scale dependent kinetic energy spectra for the RUV field, which shall henceforth be referred to as the RUM kinetic energy spectra.

$$\delta E_{p,ii}(\kappa) = \sum_{\kappa \leq |\kappa| < \kappa+1} \frac{1}{2} \left[\delta \hat{\tilde{v}}_i^*(\kappa) \delta \hat{\tilde{v}}_i(\kappa) \right] \tag{4.31}$$

4.5 Spectral Equations for an Electrical Lorentz Force Field and Voltage Potential

Spectral equations for the electric field may be derived by taking a 3D Fourier transformation of equation (3.49) to yield,

$$I \kappa_i \hat{e}_i = -I^2 \kappa^2 \hat{\phi}_e = \mathscr{F} \left\{ \frac{\rho_Q}{\epsilon_r \epsilon_0} \right\} \tag{4.32}$$

By simple re-arrangement of terms relating the electric field to the domain charge density, and noting that $I^2 = -1$, one subsequently obtains,

$$\kappa_i \hat{e}_i - \left(-I \mathscr{F} \left\{ \frac{\rho_Q}{\epsilon_r \epsilon_0} \right\} \right) = 0 \tag{4.33}$$

Furthermore, the electric field must be divergence free, in the sense the electric field vector must be orthogonal to the wave-number κ such that,

$$\hat{e}_i = \hat{e}_i - \frac{\kappa_i}{\kappa^2} \cdot \left[\kappa_j \hat{e}_j - \left(-I \mathscr{F} \left\{ \frac{\rho_Q}{\epsilon_r \epsilon_0} \right\} \right) \right] \tag{4.34}$$

To derive a spectral equation for the voltage potential, equation (4.33) may be used to compute,

$$\hat{\phi}_e = \frac{\mathscr{F} \left\{ \frac{\rho_Q}{\epsilon_r \epsilon_0} \right\}}{\kappa^2} \tag{4.35}$$

Lastly, by taking inverse Fourier transforms of equations (4.34) and (4.35), one subsequently obtains solutions for the real-space electric field and scalar voltage potentials throughout the computational domain.

4.5.1 Spectral Energy Transport Equations

The spectral energy content throughout the electrical continuum phase may be defined as,

$$\Xi_{ii}(\kappa) = \sum_{\kappa \leq |\kappa| < \kappa+1} \frac{1}{2} \left[\hat{e}_i^*(\kappa) \hat{e}_i(\kappa) \right] \tag{4.36}$$

For a statistically stationary isotropic turbulent suspension containing electrically charged particles, the rate of change of electrical energy is zero. This is because the electric field and energy contained within, is defined instantaneously by the spatial distribution of particles throughout the suspension. If equally charged mono-dispersed particles are placed in a perfect lattice arrangement, the Eulerian space charge density and electric field would be uniform throughout the domain. Hence, there would be no electrical energy, nor voltage potential present. In reality however, drag forces from the surrounding fluid turbulence would act to move particles away from this perfect lattice-like arrangement. With turbulent mixing of charged particles, and the multi-scale clustering effects exhibited by particles in the presence of turbulence (Karnik and Shrimpton 2008; Scott et al. 2009; Karnik 2010), one would expect to see scale dependent states of energy for the electrical continuum. Equation (4.36) characterises this scale dependent electrical energy, but provides no information regarding the sources of electrical energy for these scales. However, the latter information can be ascertained by examining the spectral fluid-to-electrical, and particle-to-electrical energy exchange rate source terms given by equations (4.19), and (4.28) respectively.

Chapter 5

The Pseudo-Spectral DNS Code

5.1 Introduction

The DNS code used for this thesis was originally developed by Scott (2006), and later extended by Karnik (2010) for use in both their respective PhD theses. Various procedural modifications and additions have been made to this inherited code, as part of work required for this thesis, the functionalities of which have been stated and summarized below.

- Ability to track Lagrangian fluid and inertial particles for examination of turbulence in relation to stochastic based Langevin models and full Lagrangian methodology.
- Ability to compute spectral statistics for drag and electrical two-way coupling source terms, as well as ability to compute all component and total spectral energy quantities relevant to MEF analysis of the discrete particle phase.
- Ability to examine two-way coupling in the presence of gravity, via implementation of a negative force on the fluid to balance the net weight of falling particles exerting downward motion on the fluid.

- Implementation of a linear nearest neighbour, 3-point standard, smooth and Gaussian delta functions relevant for the analysis on Lagrangian to Eulerian information transfer and numerical two-way coupling methodology.

5.2 Numerical Method

The DNS code follows from the same pseudo-spectral method developed by Orszag and Patterson (1972) for homogeneous isotropic turbulence and later extended by Rogallo (1981) for flows such as irrotational strain, shear, rotation and relaxation towards isotropy. In the pseudo-spectral approach, linear terms are solved in spectral space whereas non-linear terms are solved in physical space, with Fast Fourier Transforms used to transform field information between the two space domains (Cooley and Tukey 1965). However, evaluating non-linear terms in real space and subsequent transformation to spectral space introduces aliasing errors, which can be eliminated using a variety of methods such as partial or full phase shifting, truncation, or by solving instead a skew-symmetric form of non-linear terms. The DNS code used in this thesis uses a simple truncation scheme that zeros wavenumber mode interactions outside a given range, resulting in a maximum wavenumber of $\kappa_{max} = N/3$, where N is the number of computational nodes in a single dimension.

The DNS code uses an Eulerian-Lagrangian approach, whereby the Navier-Stokes fluid phase equations are solved directly using the discrete Fourier collocation method, and the particle phase solved for via integration of simplified Lagrangian particle equations of motion. The code is based on the incompressible Navier-Stokes equations in the physical rotational form, (see equation (3.18) in section 3.2.3), which has been shown to be the most stable form for conserving kinetic energy during numerical simulations, (Hussaini 1987).

5.2.1 Fluid Field Initialisation

The velocity field is initialised in Fourier Space using the method described in Rogallo (1981), which is designed to satisfy continuity and to conform to a pre-specified energy

spectrum. The initial velocity field is not an exact solution to the Navier-Stokes equations, but it is instead designed to be similar in form to a fully developed turbulent flow. This is necessary otherwise significant computational effort is required to reach a fully developed solution. For a complex velocity vector $\hat{u}_i(\kappa_i)$ located at a discrete wavenumber node denoted by κ_i, each component of the fluid velocity is defined using,

$$\hat{u}_i(\kappa_i) = \left(\frac{\alpha|\kappa|\kappa_2 + \beta\kappa_1\kappa_3}{|\kappa|\sqrt{\kappa_1^2+\kappa_2^2}}, \frac{\beta\kappa_2\kappa_3 + \alpha|\kappa|\kappa_1}{|\kappa|\sqrt{\kappa_1^2+\kappa_2^2}}, -\frac{\beta\sqrt{\kappa_1^2+\kappa_2^2}}{|\kappa|} \right) \tag{5.1}$$

where complex co-efficients α and β are random both in amplitude and phase such that,

$$\alpha = \left(\frac{E(\kappa)}{4\pi\kappa^4} \right)^{1/2} \exp^{I\theta_1} \cos(\phi) \tag{5.2}$$

$$\beta = \left(\frac{E(\kappa)}{4\pi\kappa^4} \right)^{1/2} \exp^{I\theta_2} \sin(\phi) \tag{5.3}$$

with θ_1, θ_2, and ϕ being normally distributed random numbers in the interval 0 to 2π. The pre-specified energy spectrum $E(\kappa)$ is defined from the model by Sullivan et al. (1994) given as,

$$E(\kappa) = \frac{u_0}{4\pi}\kappa^4 \exp\left(-\frac{2\kappa^2}{\kappa_p^2} \right) \tag{5.4}$$

where u_0 is the energy magnitude and κ_p the peak wavenumber location of the energy spectrum.

5.2.2 Artificial Forcing

To allow for statistically stationary turbulence without decay of the energy spectrum, an input of energy at large scales is required to balance the dissipation occurring at the smallest of scales. This is achieved by using an artificial forcing scheme developed by Eswaran and Pope (1988), implemented by adding an extra source term to the Navier-Stokes momentum equation in spectral form as follows.

$$\frac{\partial \hat{u}_i(\kappa_i, t)}{\partial t} = \hat{a}_i^{NS}(\kappa_i, t) + \hat{a}_i^{F}(\kappa_i, t) \tag{5.5}$$

Here $\hat{a}_i^{NS}(k_i, t)$ represents all the spatial terms in the Navier-Stokes equations. The artificial forcing term $\hat{a}_i^{F}(\kappa_i, t)$, is specified as a complex, vector-valued Uhlenbeck-Ornstein stochastic process defined by a forcing amplitude σ_f and forcing time-scale T_L.

$$\hat{b}_i(\kappa_i, t + \Delta t) = \hat{b}_i(\kappa_i, t)\left(1 - \frac{\Delta t}{T_f}\right) + \hat{\theta}_i\left(\frac{2\sigma_f^2 \Delta t}{T_f}\right)^{1/2} \tag{5.6}$$

Equation (5.6) represents a vector of three independent complex stochastic processes. Each vector component of $\hat{\theta}_i$ conforms to a Gaussian distribution with zero mean and unit variance. Continuity is enforced by the projection of $\hat{b}_i(\kappa_i, t)$ onto the plane normal to κ_i as follows.

$$\hat{a}_i^{F}(\kappa_i, t) = \hat{b}_i(\kappa_i, t)\left(\delta_{ij} - \frac{\kappa_i \kappa_j}{|\kappa|}\right) \tag{5.7}$$

The objective of the forcing scheme is to achieve a desired Taylor Reynolds number Re_λ, and Kolmogorov length scale η, which satisfies the requirements of good small scale resolution, i.e. $\kappa_{max}\eta > 1.5$ (Yeung and Pope 1989). The predicted one-way coupled Taylor Reynolds number can then be estimated from the empirical relation,

$$Re_\lambda \approx \frac{8.5}{(\eta\kappa_0)^{5/6}\, N_F^{2/9}} \tag{5.8}$$

Where κ_0 is the minimum wavenumber resolved for in isotropic simulations. Due to appropriate choice of domain size, $\kappa_0 = 1$. N_F represents the number of wavenumber modes subjected to artificial forcing, which is determined via the non-dimensional wavenumber forcing radius K_f. For all DNS investigations presented in this thesis, a value of $K_f = 2\sqrt{2}$ is used, resulting in $N_F = 92$ forced modes. Inevitably, the artificial forcing introduces numerical artefacts within large scales of turbulent motion. To reduce numerical artefacts of forcing at large scales, ideally one would use a small forcing

radius. However, spatially averaged flow quantities show strong fluctuations in time if the number of forced modes is too small, (Wang and Maxey 1993). Ideally, the value of N_F should represent a compromise between these two considerations.

From equation (5.6), forcing is governed by the forcing amplitude σ_f, and the forcing time-scale T_F. Together these parameters define the non-dimensional forcing dissipation ϵ^* as follows,

$$\epsilon^* \equiv \sigma_f^2 T_F \tag{5.9}$$

To estimate σ_f and T_F, choices for the kinematic viscosity ν_f and non-dimensional forcing time-scale T_F^*, are first required. The non-dimensional forcing time-scale is defined as,

$$T_F^* \equiv T_F \epsilon^{*1/3} \kappa_0^{2/3} \tag{5.10}$$

and the non-dimensional forcing dissipation ϵ^*, can be estimated using the following empirical relation,

$$\epsilon \equiv \frac{4\epsilon^* N_F}{1 + T_F^* N_F^{1/3}/\beta} \tag{5.11}$$

where $\beta = 0.8$ is a constant (Eswaran and Pope 1988), and ϵ estimated from equation (2.2). For all DNS investigations presented in this thesis, a non-dimensional forcing time-scale of $T_F^* = 0.15$ is chosen. Subsequently, the forcing amplitude σ_f and the forcing time-scale T_F can be obtained using equations (5.9) and (5.10) respectively. Depending on the size of the DNS domain used for resolving the turbulence, different forcing amplitudes and time-scale parameters are required. For all 64^3 DNS simulations presented in this thesis, a forcing amplitude and time-scale of $\sigma_f = 0.212$ and $T_F = 0.321$ is used.

5.2.3 Time Advancement

Time is advanced within the DNS code using the low-storage, third-order Runge-Kutta scheme of Williamson (1980) as follows,

$$\begin{aligned} G1 &= F(U_n, t_n) \\ U_2 &= U_1 + \frac{1}{3}\Delta t G1 \\ G2 &= -\frac{5}{9}G1 + F(U_2, t_n + \frac{1}{3}\Delta t) \\ U_3 &= U_2 + \frac{15}{16}\Delta t G2 \\ G3 &= -\frac{153}{128}G2 + F(U_3, t_n + \frac{3}{4}\Delta t) \\ U_{n+1} &= U_3 + \frac{8}{15}\Delta t G3 \end{aligned} \tag{5.12}$$

Essentially for each time-step, the solution is advanced using three different smaller time-steps, designed to accurately resolve any sudden changes within the underlying partial differential equations describing the turbulence. To ensure accuracy of Lagrangian velocity and trajectory solutions, positions and velocities are time-advanced in the same manner to that of the turbulence. Critically, the timestep Δt is adjusted dynamically during simulation such that,

$$\Delta t = CFL \frac{\min(\Delta_x, \Delta_y, \Delta_z)}{\max(|u_1| + |u_2| + |u_3|)} \tag{5.13}$$

using a Courant Freidricks Levy (CFL) number of $CFL = 0.75$.

5.3 Simulation Setup and Post-Processing Procedures

The aim of this section is to provide details on; a) how physical conditions are specified for DNS simulations presented in this thesis, b) how simulations are performed in terms of requirements needed to obtain stationary statistics for turbulence and dispersed phase quantities, and c) how various measures of preferential concentration that are presented in later chapters 6 and 7, are numerically computed.

5.3.1 Procedure for Specifying Physical Conditions of One and Two-way Coupled DNS Investigations

Here the calculation procedure for defining physical conditions of the dispersed particle phase for subsequent DNS investigations presented in chapters 6 and 7 is presented.

The calculation procedure first assumes that Kolmogorov length η, and Kolmogorov time-scale τ_η variables have been obtained from a pre-existing DNS of statistically stationary isotropic turbulence, without the presence of any two-way coupled dispersed phase suspension. Given these known quantities for η and τ_η, the procedure used to calculate realistic dispersed phase conditions for particle suspensions is as follows;

1. For each target Stokes number St_η value, using the known τ_η from a pre-existing DNS simulation, one computes the required particle time-scale τ_p of the suspension using equation (3.24).

2. From the particle time-scale τ_p, assuming Stokes flow conditions where $Re_p \ll 1$, and choosing a realistic value for material particle density ρ_p, one may subsequently compute the required diameter D for real particles of the suspension using equation (3.21).

3. At this stage, one checks the validity of using the point-particle approximation for modelling real particles, recalling from section 3.3 that the dispersed phase must satisfy $D \ll \eta$, or if absolutely necessary relaxed up to $D/\eta = \sqrt{18\delta}$ with $\delta \approx 5\%$, (Ling et al. 2013).

4. For one-way coupled simulations, given the particle diameter D, one chooses the total number of computational particles N_c to be tracked within the DNS. Subsequently, one may calculate the volume fraction ϕ_v and mass loading ratio ϕ_m of the suspension according to equation (2.11), and ensure that the limits $\phi_v < 10^{-4}$ and $\phi_m < 10^{-2}$ are obeyed.

5. For two-way coupled simulations one requires $\phi_v < 10^{-4}$ and $\phi_{mv} > 10^{-2}$. Given the particle diameter D, the total number of computational particles N_c, and a target mass loading ratio ϕ_m, one calculates the desired statistical weight W_p to be assigned per computational particle according to equation (C.2). For further discussion regarding the physical significance of statistically weighted computational particles, see appendix C.

Following the procedure outlined above, it was convenient prior to performing DNS investigations presented in this thesis to document a data matrix of prospective DNS runs. These data matrix tables are included in appendix B for reference.

5.3.2 Procedure for Obtaining Stationary Statistics within DNS Investigations

In order to obtain an initial statistically stationary turbulence state ready for release of particle suspensions, turbulence is initialised, maintained and advanced according to the procedures outlined in section 5.2. Following initialization of the turbulence, the simulation is evolved until statistics of basic quantities such as the turbulent kinetic energy k, energy dissipation rate ϵ, and turbulence intensity u' reach a stationary state, i.e. their time rate of change equals zero. Typically, the simulation needs to evolve for a sufficiently high number of large scale eddy turnover times before this state is reached. Once a statistically stationary state has been reached, the current DNS code records the state of both fluid and particle phase information to appropriate dump files, ready for restart and collection of statistics for any subsequent DNS run. For spectral statistics, averaging must typically be performed for at least 30 large scale eddy turnover times,

due to the requirement of sampling a sufficiently large number of spectral energy states for each wave-number band in order to get quality statistics.

5.3.3 Preferential Concentration Measures

In this subsection typical measures of preferential accumulation are introduced, some of which shall be used and referenced back to in chapters 6 and 7 of this thesis.

5.3.3.1 The Number Density-Enstrophy Correlation Measure of Scott et al. (2009)

The first measure introduced is the number density-enstrophy correlation (ND-E), denoted by $\langle n'e' \rangle_{\mathscr{V}}$, which specifically measures the correlation between deviation of local enstrophy, e', and deviation of local particle number density, n', within the turbulence. In order to calculate $\langle n'e' \rangle_{\mathscr{V}}$, the DNS domain is first subdivided into small volumetric bins. For convenience, the bins used for this correlation statistic are equivalent to the control volumes of cells within the DNS domain. Subsequently for each volumetric bin, the deviation of local number density relative to the average in the domain is computed via,

$$n' = \frac{n - \langle n \rangle_{\mathscr{V}}}{\langle n \rangle_{\mathscr{V}}} \tag{5.14}$$

and the deviation of local enstrophy relative to the average in the domain is computed via,

$$\Omega' = \frac{\Omega - \langle \Omega \rangle_{\mathscr{V}}}{\langle \Omega \rangle_{\mathscr{V}}} \tag{5.15}$$

In equations (5.14) and (5.15), the local particle number density n is the number of particles Np within a control volume of size $(\Delta x)^3$, and local enstrophy computed as the square magnitude of vorticity such that $\Omega = |\omega_i|^2$ with vorticity ω computed according to form given by equation (3.17).

5.3.3.2 The D Measure of Fessler et al. (1994)

Another preferential accumulation statistic is the D measure, first used by Fessler et al. (1994) to characterise the non-homogeneous distribution of particles within a turbulent channel flow. To compute the D measure, the domain is first divided in small bins of uniform dimension[1]. The following step then counts the number of bins that contain a certain number of particles C, at which point the probability of finding bins that contain C particles, $P_m(C)$, is calculated by,

$$P_m(C) = \frac{N_b(C)}{N_b} \tag{5.16}$$

where $N_b(C)$ is the number of bins that contain C particles and N_b the total number of bins used for sampling. For a uniform distribution of particles, the number of particles in each bin would simply be $\lambda = N_p/N_b$. Subsequently, the difference between a measured particle distribution and a uniform particle distribution can be quantified via,

$$\sigma_m^2 = \sum_{C=0}^{N_p} (C-\lambda)^2 P_m(C) \tag{5.17}$$

In an analogous manner, the difference between a random (Poission) distribution of particles and a uniform particle distribution can be quantified via,

$$\sigma_p^2 = \sum_{C=0}^{N_p} (C-\lambda)^2 P_p(C) \tag{5.18}$$

with the probability of finding bins with C particles for a random distribution, $P_p(C)$, defined as,

$$P_p(C) = \frac{\exp^{-\lambda}\lambda^C}{C!} \tag{5.19}$$

[1]It should be noted that the D measure is dependent on the bin-size used for sampling, hence the most appropriate presentation of the measure is in the form of non-dimensional bin-size versus D. One may then characterise the location of the peak in D, and the location along non-dimensional bin size at which the peak occurs.

Lastly, the D measure may then be computed using the formula,

$$D = \frac{\sigma_m - \sigma_p}{\lambda} \tag{5.20}$$

with σ_m and σ_p computed from equations (5.17) and (5.18) respectively.

5.3.3.3 The Radial Distribution Function

The radial distribution function (RDF) measure has been used by previous researchers to estimate the effect of clustering on frequency of inter-particle collisions (Sundaram and Collins 1997; Reade and Collins 2000), as well as to simply quantify the behaviour of preferential concentration of particles at different Stokes numbers (Scott et al. 2009; Karnik 2010). The RDF measure quantifies the separation between particle pairs within a suspension, and is defined by,

$$g(r) = \frac{P_r/\Delta V_r}{P/V} \tag{5.21}$$

where P_r is the number of particle pairs separated by the distance $r \pm 0.5\Delta r$ and ΔV_r the volume of the shell of thickness Δr located at radius r. In addition, $P = N_p(N_p - 1)/2$ is the total number of possible particle pairs in the suspension and V is the total volume of the DNS domain. The RDF can be interpreted at the probability of finding particle pairs with a given radial separation distance, and for a uniform particle distribution, $g(r)$ is unity. Values for $g(r)$ that exceed unity are indicators of accumulation at that length scale. For all RDF statistics presented in this thesis, the length scale r is made non-dimensional by the Kolmogorov length scale η. Subsequently, the size of particle clusters can be estimated from the non-dimensional length scale where the RDF becomes less than unity. It should be noted that care must be taken whilst choosing the bin size of the RDF. If Δr is too large, then the RDF statistic will fail to capture any underlying structure within the suspension, whilst if Δr is too small, the quality of statistics at small scales may diminish as a result of reduced particle number density at those small scales within the suspension. For all RDF statistics reported in this thesis, a non-dimensional

bin-size of $\Delta\eta_{(\phi_m=0)}$ is used. Lastly, during the numerical procedure which computes $g(r)$, it is also possible to compute the mean distance to closest particle defined by $\langle D_{sep} \rangle_{\mathscr{L}}$. This quantity is obtained by keeping track of the minimum distance between particle pairs during each particle pair evaluation within the RDF computation.

5.3.3.4 The Voronoi Measure of Monchaux et al. (2010)

Voronoi diagram analysis of preferential concentration is one of the more recent additions to the repertoire of tools used to quantify clustering within particle suspensions, and was first introduced by Monchaux et al. (2010). Essentially, the Voronoi diagram is a way of decomposing 2D or 3D domain space into independent cells that contain a single particle. One Voronoi cell is defined as the ensemble of arbitrary points in space, that are closer to a particle than any other. The segments of the Voronoi diagram are all points in the plane that are equidistant to two nearest particles, and the Voronoi cell vertices are the points equidistant to three (or more) particles. The core implementation of Voronoi tessellation pre-exists within the commercial MATLAB® code environment and is computationally efficient in terms of its methodology. However, the numerical procedure for computing Voronoi volume PDF statistics in 3D space requires a little extra work as follows;

1. Given a set of N_c computational particle co-ordinates X_i, utilise the MATLAB® `voronoin` function to return all vertices and cells of the corresponding Voronoi diagram.

2. Ensure that the bounds for Voronoi cells are entirely enclosed within the $(2\pi)^3$ domain. This eliminates any infinitely bounded cells from being included in subsequent PDF statistics.

3. For finite bounded Voronoi cells, utilise the MATLAB® `convhulln` function to compute the corresponding volumes for those cells.

4. Use the dataset of Voronoi cell volumes to compute the Voronoi volume PDF statistics.

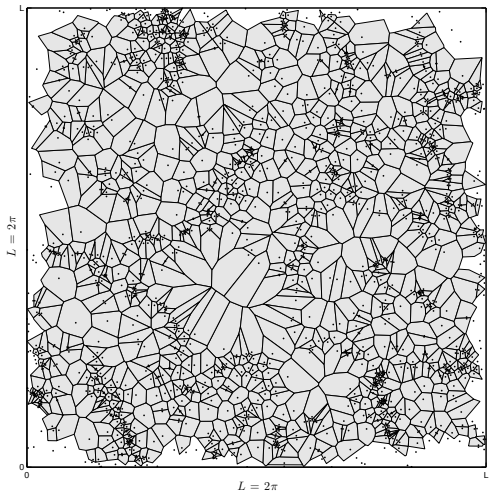

FIGURE 5.1: Plot showing a computed 2D Voronoi diagram, for an arbitrary slice of a down-sampled particle suspension, where $St_\eta \approx 1$. Cells at the edge of the 2π domain are infinitely bounded and have been removed appropriately.

It should be noted that the quality of Voronoi volume PDF statistics diminishes for large values of Voronoi cell volumes. This is a side effect of reduced statistical sample size for voids that are present between particles in a given suspension. One way to eliminate this undesirable aspect, is to perform the Voronoi analysis over many independent particle suspension ensembles for a given flow field.

Nevertheless, given Voronoi volume PDF statistics for an arbitrary suspension of particles, one may compare the Voronoi volume PDF for a given particle suspension, to the PDF of a random Poission distribution of particles. Conveniently, the PDF of a random Poission distribution of particles in 3D space may be described via the model function (Ferenc and Néda 2007), defined by,

$$f_{3D}(x) = \frac{3125}{24} x^4 \exp^{-5x} \tag{5.22}$$

where x is the normalised Voronoi volume $\mathcal{V}^{3D}$ defined by,

$$\mathcal{V}^{3D} = \frac{\mathcal{V}}{\langle \mathcal{V} \rangle_{\mathscr{L}}} \tag{5.23}$$

Lastly, the two curve intersections of measured Voronoi volume PDF statistics, with the model function allow one to quantify the Voronoi clustering dimension $\mathcal{V}_c^{3D}$ and the Voronoi void space dimension $\mathcal{V}_v^{3D}$.

5.4 DNS Code Validation

The current DNS code was previously validated during the work of Scott (2006) and Karnik (2010). Scott (2006) compared the turbulent kinetic energy spectra from decaying isotropic turbulence simulations to spectra obtained from experiments performed by Comte-Bellot and Corrsin (1971), who looked at the behaviour of grid-generated turbulence downstream within a wind tunnel. Karnik (2010) also compared statistics from stationary isotropic turbulence simulations, to those performed by previous authors Overholt and Pope (1996) and Yeung et al. (2006). Excellent agreement to previous works was found by both authors Scott (2006) and Karnik (2010).

One can therefore justify that the code has been sufficiently validated from the perspective of statistics generated solely from turbulence. However, an integral part of the DNS work presented in this thesis, specifically relates to the behaviour of two-way coupling between particles and turbulence. It is therefore necessary to validate the physical behaviour exhibited by particles in turbulence, as well as the specific methodology regarding how two-way coupling is numerically implemented within the current DNS code.

This section is split into three parts; the first which validates the behaviour of one-way coupled particles in turbulence at different Stokes numbers against results of Karnik (2010), the second which evaluates different numerical schemes used for momentum transfer from the discrete particle phase to the fluid continuum phase, and the third which validates two-way coupling behaviour within the current DNS code against results of Boivin et al. (1998).

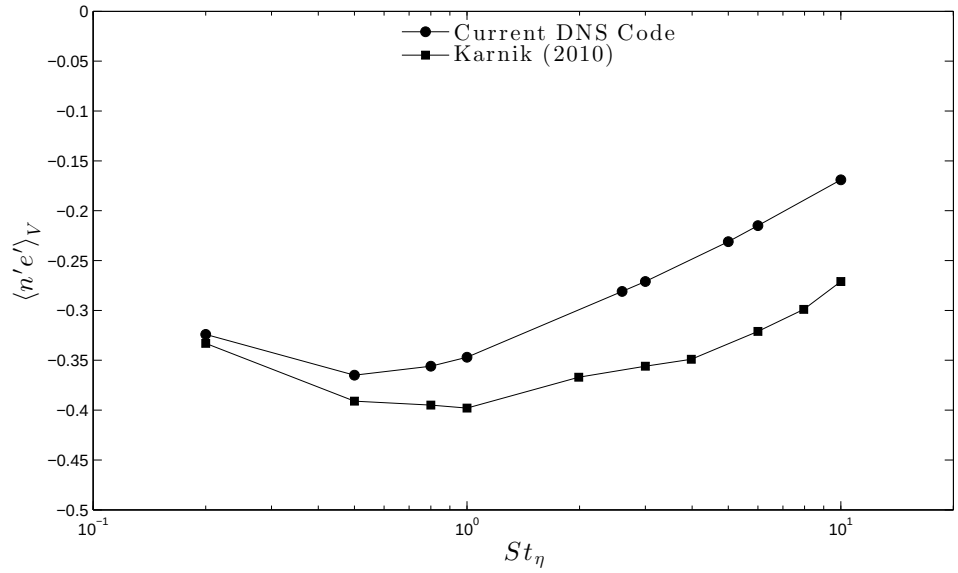

FIGURE 5.2: Plot showing the ND-E correlation $\langle n'e' \rangle_{\mathscr{V}}$, for one-way coupled particles at different Stokes numbers computed using the current DNS code, compared to results of Karnik (2010). Results were both computed for a 64^3 DNS domain at $Re_\lambda \approx 45$

5.4.1 One-Way Coupled Validation of Preferential Concentration Behaviour Against Results of Karnik (2010)

The purpose of this particular validation section is to ensure that the behaviour exhibited by particles of different Stokes numbers is correctly captured within the current DNS code.

For validation results presented here, statistics were obtained from a set of one-way coupled 64^3 DNS runs, performed at Taylor Reynolds number of $Re_\lambda \approx 45$, for a range of different particle Stokes numbers. Details regarding the dispersed phase parameters used for these runs are contained in tables B.1 and B.2 of appendix B.

Figure 5.2 compares the ND-E correlation computed for one-way coupled particles across a range of different Stokes numbers using the current DNS code, to the results of Karnik (2010). Whilst there is slight deviation and weaker correlation between results of the current DNS code and those of Karnik (2010), across both profiles the ND-E correlation shows a characteristic minima near a Stokes number of unity, which indicates the tendency of particles with a Stokes number of unity to preferentially accumulate in regions of low-vorticity and high strain rate (Scott et al. 2009; Karnik 2010). The difference

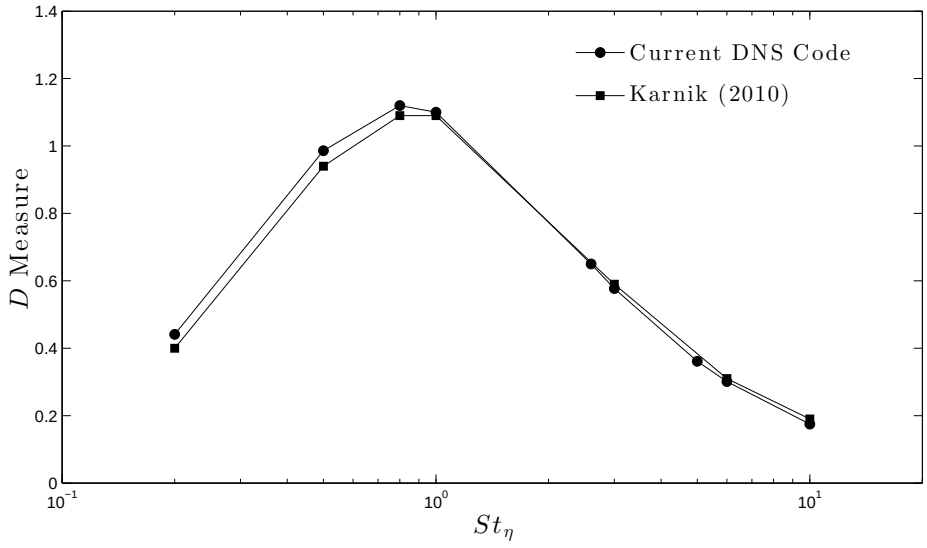

FIGURE 5.3: Plot showing the D measure, for one-way coupled particles at different Stokes numbers computed using the current DNS code, compared to results of Karnik (2010). Results were both computed for a 64^3 DNS domain at $Re_\lambda \approx 45$

between the two ND-E correlation profiles can be attributed to the fact that the number of computational particles used to compute the correlation for this validation, was increased by two orders of magnitude in order to increase the statistical accuracy of the particle number density spatial distribution (see section 3.3.1.1), compared to the 10^5 computational particles used by Karnik (2010). The increase in smoothness of the mesoscopic particle number density distribution corresponds to an increase in the quality of statistical moments computed for the ND-E correlation.

Figure 5.3 compares the peak D measure statistic, computed for one-way coupled particles across a range of different Stokes numbers using the current DNS code, to the results of Karnik (2010). Excellent agreement to the results of Karnik (2010) can be seen, with the D measure showing a characteristic peak near a Stokes number of unity.

5.4.2 Evaluation of Two-Way Coupling Numerical Schemes

As discussed previously in section 3.2.1, numerical treatment of the discrete phase source term within the Navier-Stokes equation is designed to encompass the physics associated with two-way coupling of particle momentum with the fluid. However, the choice of numerical scheme used for such treatment remains open for debate. Various authors

have examined the errors associated with different back-projection methods (Boivin et al. 1998; Garg et al. 2007; Kaufmann et al. 2008; Ling et al. 2010), yet few have looked specifically at the impact of such methods on resolved kinetic energy spectra. For this reason, tests have been performed to demonstrate the advantages of various back-projection schemes, and the effects that certain schemes have on two-way coupling with resolved scales of turbulent motion.

To evaluate this two-way coupling methodology, 10^7 particles were randomly placed throughout a 64^3 computational domain for which a DNS of isotropic turbulence was evolved to reach a statistically stationary state. For an initially random particle distribution, approximately ≈ 38 computational particles exist within each cell volume, thereby minimizing the impact of any statistical error. The turbulent velocity field information is subsequently interpolated to particle positions using a second order accurate polynomial, and then projected back from each particle using various methods, onto the grid nodes used originally for resolving the turbulence via DNS. It should be noted that spectral energies associated with aliased modes of the DNS (whether from the resolved or back-projected spectra), are not included in the analysis due to the de-aliasing scheme employed. Lastly, the turbulent kinetic energy spectrum obtained post back-projection is then compared to the spectrum obtained directly from the fully resolved DNS.

The delta functions used for back-projection in this validation are summarized below for reference, along with a description of the linear particle-neighbouring-nodes (PNN) projection method.

- Standard 3-point delta function of Roma et al. (1999).

$$\phi(x) = \begin{cases} \frac{1}{3}(1 + \sqrt{1 - 3|x|^2}), & |x| \leq 0.5 \\ \frac{1}{6}(5 - 3|x| - \sqrt{1 - 3(1 - |x|)^2}), & 0.5 < |x| \leq 1.5 \\ 0, & |x| > 1.5 \end{cases}$$

- Smoothed 3-point delta function of Yang et al. (2009).

$$\phi(x) = \begin{cases} \frac{3}{4} - |x|^2, & |x| \leq 0.5 \\ \frac{9}{8} - \frac{3}{2}|x| + \frac{1}{2}|x|^2), & 0.5 < |x| \leq 1.5 \\ 0, & |x| > 1.5 \end{cases}$$

- 3-point Gaussian delta function, (Kaufmann et al. 2008).

$$\phi(x) = \frac{(2\Delta)^3}{\mathrm{erf}(\sqrt{6})^3} \left(\frac{6}{\pi\Delta^2}\right)^{3/2} \exp\left(-\frac{6|x|^2}{\Delta^2}\right)$$

- Nearest-node scheme.

$$\phi(x) = \begin{cases} 1, & |x| \leq 0.5 \\ 0, & |x| > 0.5 \end{cases}$$

- Linear PNN method.

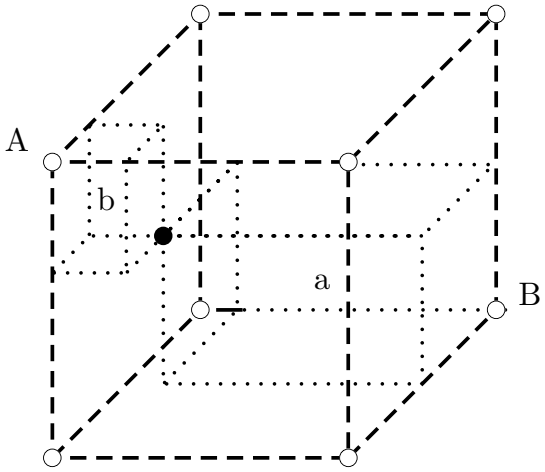

FIGURE 5.4: Illustration showing how the linear PNN method calculates the weighting of particle information to cell corner nodes.

For the linear PNN method in 3D, each cell corner node receives a fraction of stored particle information, proportional to the volume between the particle and the diagonally opposite node, divided by the total volume of the cell. An illustration of this method

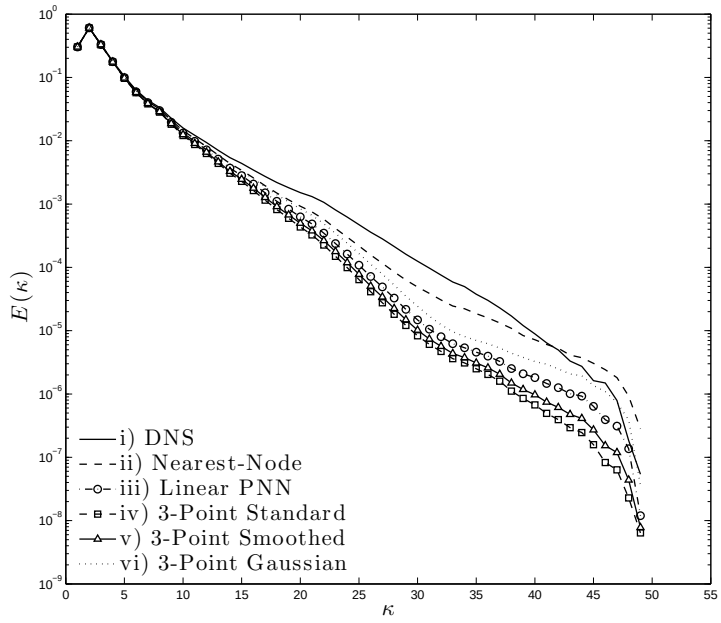

FIGURE 5.5: Figure showing the turbulent energy spectra present for one realization of a statistically stationary flow at zero mass loading ratio, where i) corresponds to the spectra of the DNS prior the interpolation to 10^7 random particle locations, ii) corresponds to the spectra obtained after back projection using a nearest-node scheme, iii) a linear PNN method, iv) a standard 3-point delta function (Roma et al. 1999), v) a smoothed 3-point delta function (Yang et al. 2009), and vi) a 3-point Gaussian delta function (Kaufmann et al. 2008).

is shown in figure 5.4, where node A (shown in white) receives a fraction of the total information from the particle (shown in black), based on the ratio of volume a, divided by the total volume of the cell.

Figure 5.5 shows that at small scales, usage of the Gaussian function yields back-projected spectra with the closest agreement to the resolved kinetic energy spectra of the DNS. However, for intermediate transfer scales of the turbulence the Gaussian function does not perform as well. Instead, the closest agreement in spectra for intermediate transfer scales is provided by the nearest-node scheme. Surprisingly, the linear PNN function is not as good at retaining spectral energies as the nearest-node scheme, nor is it as good as the Gaussian function. The linear PNN function does however retain greater spectral kinetic energy than the standard and smoothed 3-point delta functions. Between the standard and smoothed 3-point delta functions, it is the latter of the two which performs the best.

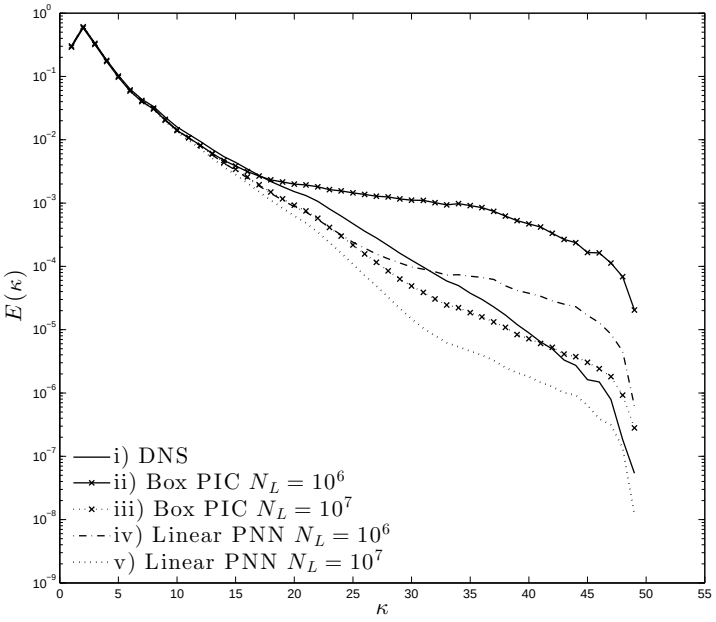

FIGURE 5.6: Figure showing the turbulent energy spectra present for one realization of a statistically stationary flow at zero mass loading ratio, where i) corresponds to the resolved spectra of the DNS, ii) corresponds to the spectra obtained after back projection using the nearest-node scheme from 10^6 computational particles, and iii) using the same nearest-node scheme with 10^7 computational particles, iv) using the linear PNN method with 10^6 computational particles and v) using the linear PNN method with 10^7 computational particles.

Notably, it was the linear PNN function in the work of Boivin et al. (1998) which was suggested as being more able to capture the resolved spectra of the DNS, yet this suggestion was also made noting the fact that decreased particle sample size leads to statistical error. The results shown in figure 5.6 confirm instead, that the nearest-node scheme is more accurate than the linear PNN scheme. This is due to the fact that increasing the number of statistical particles per cell from ≈ 3.8 to 38, increases both the accuracy and correlation with resolved DNS spectra for the nearest-node scheme, unlike the linear PNN scheme where this is clearly not the case.

In order to quantify the accuracy of back-projection schemes examined, the root total sum of squares error (RSSE) is measured between the spectra obtained post back-projection $E^{\phi(x)}(\kappa)$, to the fully resolved turbulent kinetic energy spectra $E^*(\kappa)$, of the DNS. In simple terms, this measure quantifies how accurate back-projection methods are at retaining information from the resolved turbulence velocity field. This measure is defined as follows,

Method	$\langle N_c \rangle$ per cell	RSSE	% of resolved kinetic energy accounted for
3-Point Standard	38	0.0195	95.50
3-Point Smoothed	38	0.0171	96.00
Gaussian	38	0.0072	98.16
Linear PNN	38	0.0129	96.89
Nearest-Node	38	0.0069	98.26
Linear PNN	3.8	0.0078	98.10
Nearest-Node	3.8	0.0383	95.75

TABLE 5.1: Percentage summaries of resolved kinetic energies accounted for using various back projection methods at increased (top), and reduced (bottom) averaged computational particle sample size count per computational cell.

$$RSSE = \left[\sum_{\kappa}^{\kappa_{max}} \left(E^{*}(\kappa) - E^{\phi(x)}(\kappa) \right)^2 \right]^{1/2} \tag{5.24}$$

where smaller values indicate closer agreement to resolved spectra and larger values indicating greater disagreement. Calculated values from tested back-projection methods are summarized in table 5.1, along with a percentage measure comparing the total kinetic energy accounted for using various back projection methods to the total kinetic energy of the resolved turbulent velocity field.

Table 5.1 shows that when 10^7 computational particles are present within the DNS, the nearest-node projection scheme outperforms all other methods by being able to capture 98.26% of the total resolved turbulent kinetic energy, with an improvement in RSSE of approximately 4.2% over its nearest rival the Gaussian function, and 46.5% over the linear PNN function. When 10^6 computational particles are present within the DNS, using the linear PNN method yields a RSSE with approximately the same magnitude as the Gaussian function for 10^7 computational particles. However, as discussed earlier in this section, increasing the statistical sample size leads to an increase in RSSE for the linear PNN method, indicating that the close match to DNS spectra is more a result of statistical error, rather than something intrinsic to the physical reality of two-way coupling.

Clearly, a trade-off exists between the different projection methods used, and the scales for which one wishes to resolve two-way coupling physics to a high degree of accuracy for. Whilst numerical schemes are conservative by design in terms of the total information retained during forwards and backwards projection to and from particles, spatial error as

a result of projection from the particle positions in unavoidable. Nevertheless, usage of the nearest-node scheme for DNS investigations presented in this thesis is justified due to the superiority seen with retaining information during back projection over alternative schemes.

5.4.3 Two-Way Coupled Validation Against Results of Boivin et al. (1998)

For DNS investigations presented in this thesis, it is important for two-way coupling in the current DNS code to behave in a manner that agrees well with existing literature research. For purposes of this validation, the DNS work of Boivin et al. (1998) is chosen as the baseline for comparison.

For the DNS code runs presented by Boivin et al. (1998), 96^3 collocation points were used with a forcing radius $\kappa_F = \sqrt{8}$, a forcing time-scale of $T_F = 1.4$, and a forcing variance of $\sigma^2 = 0.033$. The maximum wave-number resolved in simulations was $\kappa_{max} = \sqrt{2}N/3$, along with a CFL number of 0.5 to ensure accurate resolution of small scales and minimise time-stepping errors. The kinematic viscosity used was $\nu = 0.015m^2/s$. With regards to the particle phases examined in the study of Boivin et al. (1998), three populations with time-scales in the order the Kolmogorov, Taylor and Eulerian time-scales of the unloaded reference turbulence were investigated, each for mass loading ratios of $\phi_m = 0.0$, $\phi_m = 0.2$, $\phi_m = 0.5$ and $\phi_m = 1.0$. Furthermore, 96^3 computational particles were tracked each with a statistical weight, calculated based on the mass loading ratio constraints investigated. Once particles were released, the simulation was evolved for an additional period of time such that a statistically stationary state was achieved, allowing both fluid and particle phases to adapt to the new two-way coupled conditions of the flow field.

First it was necessary to achieve single-phase turbulence that was statistically stationary, and representative of initial conditions obtained by Boivin et al. (1998) prior to addition of a two-way coupled particle suspension. A comparison of basic turbulence statistics obtained from such validation is shown in table 5.2, with DNS statistics from

	Re_λ	$\kappa_{max}\eta$	k	ε	l_f/l_g	τ_e	τ^ε	τ_λ	τ_η
Boivin et al. (1998)	62	1.26	7.00	5.7	1.98	0.43	1.23	0.32	0.051
Current DNS Code	61	1.28	6.54	5.21	1.97	0.47	1.25	0.33	0.053
% Uncertainty	-1.6	1.6	-6.6	-8.6	-0.5	9.3	1.6	3.1	3.9

TABLE 5.2: Summary of single-phase turbulence statistics obtained from current DNS code, compared against those from table 1 of Boivin et al. (1998).

the single-phase run agreeing well with those from Boivin et al. (1998), with percentage uncertainties ranging between 0.5-9.3%.

With regards to the two-way coupling validation of the current DNS code against results of Boivin et al. (1998), only a select few parameters were changed. Firstly the total number of computational particles tracked was increased from 96^3 up to 10^7, in order to reduce the statistical error and increase the accuracy of momentum transfer from particles to the fluid. Secondly the choice of back projection scheme was changed from the linear PNN to the nearest-node scheme.

Figure 5.7 compares the ratio of turbulent kinetic energy between loaded and unloaded turbulence, between results computed via the current DNS code and those of Boivin et al. (1998). For the current DNS code as mass loading increases, the largest attenuation of turbulent kinetic energy is seen from particles with time-scales in the order of the Kolmogorov time-scale. Attenuation is the least for particles with time-scales in the order of the Eulerian integral time-scale. Generally, the same qualitative trend of increasing turbulent kinetic energy attenuation is seen with increasing mass loading ratio for both the current DNS code, and results of Boivin et al. (1998).

For the ratio of turbulent energy dissipation rate between loaded and unloaded turbulence, figure 5.8 shows qualitative trends similar to the results of Boivin et al. (1998), with a decrease in energy dissipation rate for loaded turbulence and increasing mass loading ratio. Strong agreement is shown between the current DNS code and Boivin et al. (1998), for particles with time-scales in the order of the Taylor time-scale. For a mass loading ratio of $\phi_m = 1.0$, the energy dissipation rate is the greatest in loaded turbulence for particles with time-scales in the order of the Kolmogorov time-scale, and the least for particles with time-scales in the order of the Taylor time-scale.

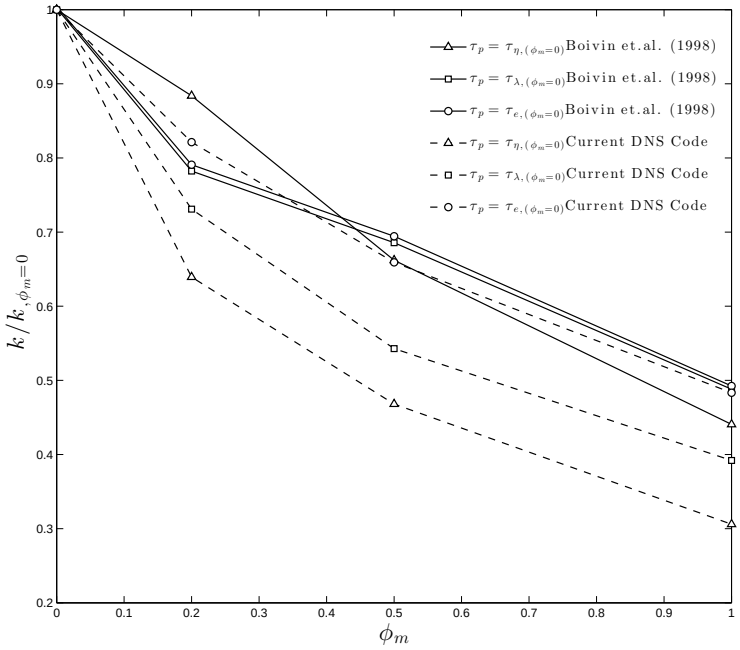

FIGURE 5.7: Comparison of turbulent kinetic energy ratios between loaded and unloaded turbulence, between current DNS code and results of Boivin et al. (1998).

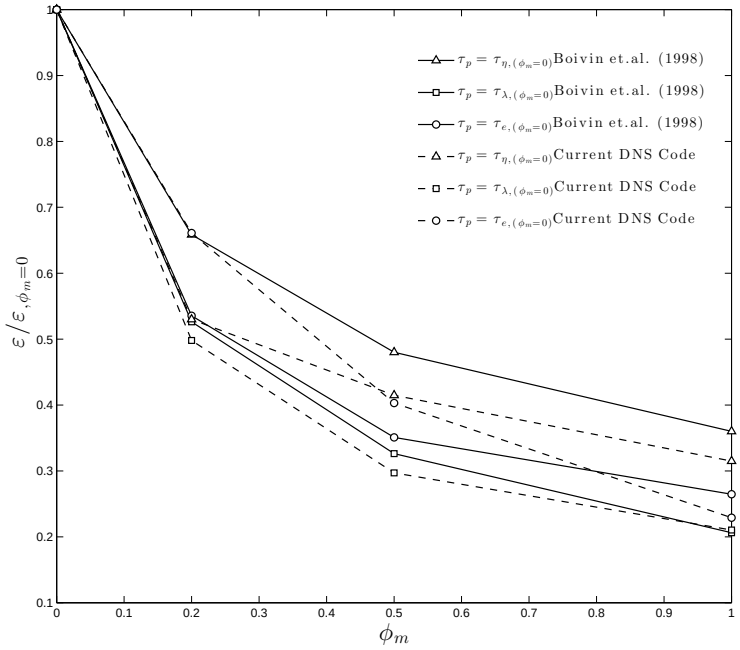

FIGURE 5.8: Comparison of turbulent dissipation rate ratios between loaded and unloaded turbulence, between current DNS code and results of Boivin et al. (1998).

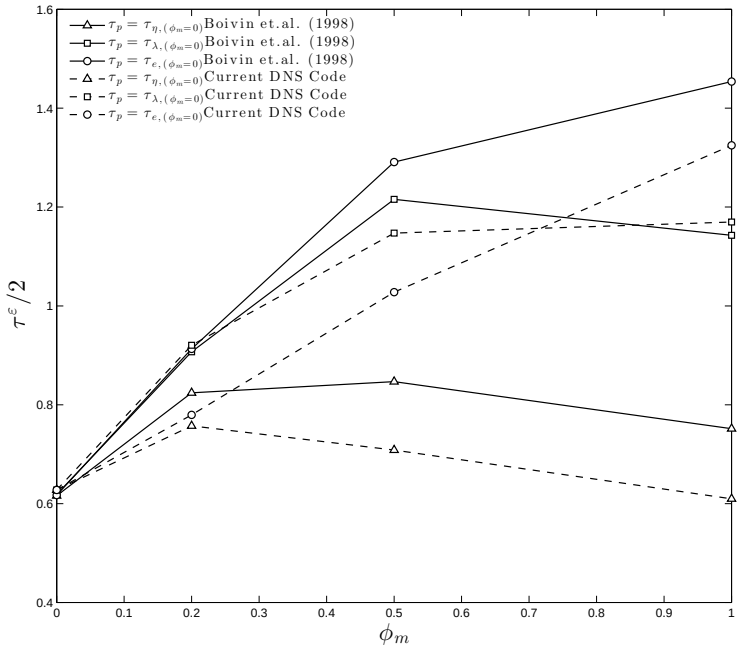

FIGURE 5.9: Comparison of Eulerian time macro-scale between loaded and unloaded turbulence, between current DNS code and results of Boivin et al. (1998).

For a final comparison of two-way coupling between results of the current DNS code and Boivin et al. (1998), the Eulerian time macro-scale τ^{ε}, computed as the ratio between turbulent kinetic energy and energy dissipation rate, is shown in 5.9. Results from the current DNS code shows that the Eulerian time macro-scale increases with increasing mass loading ratio, eventually reaching a maximum that occurs for larger ϕ_m with increasing particle time-scale in agreement with the results of Boivin et al. (1998).

Whilst the presented comparisons show that two-way coupling behaves in a consistent manner with previous research, there exits discrepancies in the values reported for the turbulent kinetic energy, energy dissipation rate, and Eulerian time macro-scales. For both sets of results one would expect to see a monotonic decrease for turbulent kinetic energy and energy dissipation rate profiles with increasing mass loading ratio, and relative consistency in magnitude of profile attenuation for variation in particle relaxation time-scales. Whilst the former hypothesis appears to be true, the latter hypothesis is only partially fulfilled due to the crossover seen in some profiles at fixed mass loading ratios. Possible causes for these discrepancies are discussed as follows.

One cause for uncertainty is the periods used for time averaging of statistics. Boivin et al. (1998) noted that after an initial development period allowing for production of turbulent energy and viscous dissipation to reach equilibrium, statistics were averaged over a further period of $7\tau_e$ eddy turnover times. In section 5.3.2 it was noted that time-averaging required at least $30\tau_e$ eddy turnover times before statistics became sufficiently stationary. Whilst this requirement was ensured for the current DNS code comparisons with Boivin et al. (1998), results suggest that best-practice time-averaging periods need to be extended significantly. Ideally, simulations need to evolve for a period long enough such that variation in quantities of interest reach statistical convergence. This is complicated by the fact that artificial forcing of turbulence is pseudo-random and a function of the turbulence state itself (see equation (4.21)). Consequently, any numerical artefacts appearing in large scales of turbulent motion must also reach statistical convergence. One must also consider that the state of turbulence at any period during its evolution, is dependant on the conditions at start of simulation. In the numerical sense, initial conditions encompass the pseudo-random construction of turbulence during fluid field initialisation, the turbulence state at the point when particles are released in the flow field, as well as the position of particles themselves upon release. Differences regarding initial conditions are therefore significant between simulations performed using the two codes.

With regards to the different numerical methods used between the current DNS code comparisons and Boivin et al. (1998), the first difference considered is the numerical scheme used for two-way coupling of particles to the fluid. However, this was intended due to the advantages seen regarding retention of information during backwards projection (see section 5.4.2). Secondly, the current DNS code uses 10^7 computational particles compared to only 96^3 computational particles used in Boivin et al. (1998). This yields an average of ≈ 11 and 1 computational particles per Eulerian grid cell respectively. More importantly, this assumes that particles are homogeneously distributed throughout the DNS domain whereas in practice this is rarely ever the case. As a consequence, there is a difference between the smoothness of the particle number density field, and a subsequent difference in how momentum two-way coupling is applied from the particles to the fluid. There is also a difference in the time integration scheme used between the current

DNS code and Boivin et al. (1998). Specifically, the current DNS code uses the low-storage, third-order Runge-Kutta scheme of Williamson (1980), whereas Boivin et al. (1998) utilises a second-order Runge-Kutta scheme. As a consequence, solutions to the fluid turbulence and Lagrangian particles are solved with different orders or accuracy.

In summary, there are several differences that exist between the current DNS code and the code used by Boivin et al. (1998). It is perhaps of no surprise then that differences exist between results computed using the two codes. Considering all the above aforementioned factors, results from Boivin et al. (1998) are perhaps not the most suitable of choices for validating two-way coupling behaviour against. Nevertheless, it would be preferable in future work to validate the behaviour of two-way coupling with more suitable experimental data, such as that published within the work of Hwang and Eaton (2006a;b).

Chapter 6

DNS Investigations: Two-Way Coupling of Poly-Dispersed Particles

6.1 Overview

Typically, multiphase flows in reality consist of particle populations with a wide range of sizes, shapes and mass properties. Populations such as these are defined as being poly-dispersed. Yet as research stands currently, there are few published studies that examine the effects of poly-dispersity on two-way coupling. Furthermore, no study to date has examined two-way coupling effects of poly-dispersed suspensions within a stationary isotropic turbulent flow field. What remains unanswered, is whether or not poly-dispersity exhibits two-way coupling behaviour, that reflects the cumulative contribution of momentum transfer from individual particle size classes that make up the poly-dispersity themselves.

The aim of this chapter therefore, is to examine two-way coupling effects that poly-disperse suspensions exhibit across different scales of the turbulence, and compare the

scale dependent contributions of two-way coupling momentum transfer between individual particle size classes within a poly-dispersed suspension and equivalent mono-dispersed suspensions, within the same turbulent flow field.

6.2 Objectives

The primary objective of this chapter is to identify any unique differences in two-way coupling behaviour with turbulence, between a poly-dispersed suspension of particles and mono-dispersed suspensions that reflect the individual particle size class properties that make up the poly-dispersity. Secondary objectives for this chapter consist of; a) identifying differences in poly-dispersed two-way coupling behaviour for suspensions where the average Stokes number is less than or greater than unity, reflecting the tendency of the suspension to behave like tracer or ballistic particles respectively, b) identifying the behaviour of the particle-to-RUM energy exchange rate spectra, for tracer-like and ballistic-like poly-disperse suspensions, and c) identifying if there are any differences in the behaviour of preferential concentration measures and statistics for different suspension types.

6.3 Organisation

Section 6.4 presents a brief summary of past research that has examined poly-dispersed particle suspensions within isotropic turbulence. Section 6.5 presents details on how the poly-dispersed simulations are defined, along with details on how the individual particle size classes of the poly-dispersed suspensions are compared numerically with equivalent mono-dispersed suspensions. Section 6.6 presents the results from subsequent DNS investigations, and lastly section 6.7 presents a summary on main conclusions of this chapter.

6.4 Background

For turbulence and poly-dispersed particles, most DNS work undertaken in the past has been limited in the sense that only the interaction of the fluid upon the particle phase is considered. In an attempt to characterise the segregation of poly-dispersed particle populations, Calzavarini et al. (2008) examined DNS results from one-way coupled turbulence at Taylor Reynolds numbers of $Re_\lambda = 70$ and $Re_\lambda = 180$, introducing a statistical measure to quantify the segregation degree between two particle populations of different relative densities and Stokes numbers. This measure was found to saturate to a constant value, approximately twice that of the Taylor length scale, a peculiar observation that was suggested to be a possible indicator of an intrinsic property for the underlying turbulence, emerging only when particles are strongly clustered. More recently, Kondaraju et al. (2011) examined two-way coupling of poly-dispersed particles in a decaying field of isotropic turbulence. They specified the poly-dispersity by assigning two particle size classes, each with a unique Stokes number, but with identical mass loading ratio contribution. In total, three poly-dispersed particle populations were examined, made up from contributions of $St_\eta = 3.2$, 6.4 and 12.8 particles. The time evolution of the turbulent kinetic energy, particle drag energy, viscous dissipation, and decay rate of turbulence quantified as the time rate-of-change of turbulent kinetic energy, was examined. Kondaraju et al. (2011) found that whilst the decay rate of turbulence was faster for increasing particle Stokes number in mono-dispersed suspensions, poly-dispersed suspensions exhibited even faster decay rates, seemingly proportional to an increase in the average Stokes number of the poly-dispersed suspension itself. To characterise this behaviour, Kondaraju et al. (2011) defined a scale dependent effective viscosity that provided to some extent, a physical measure to the interactions occurring between poly-dispersed suspensions and specific scales of the turbulence. This effective viscosity measure was found to be greater for poly-dispersed flows than it was for mono-dispersed flows. This suggests that in reality, poly-dispersity within a turbulent multiphase flow can potentially have a negative impact on the mixing capability of the flow itself.

6.5 Dispersed Particle Phase Set-up

In this study, two poly-dispersed suspensions were specified with the aim that either tracer-like, or ballistic-like behaviour of particles would be present. For this to be the case, particle size classes that made up the poly-dispersity were chosen based on Stokes numbers that were either less than unity, or greater than or equal to unity respectively. Using table 6.1 as reference to clarify how poly-dispersity within simulations are defined, poly-dispersed suspension A) contains three unique particle size classes Aa), Ab) and Ac). Whilst each of the three unique particle size classes contribute to poly-dispersity within a single two-way coupled simulation, three additional mono-dispersed simulations are performed, where each mono-dispersed suspension of particles reflects the same properties of the corresponding particle size class. The objective here is to quantify across all resolved scales of the turbulence, the individual two-way coupling contributions for each particle size class present within a poly-dispersed suspension of particles. Statistics associated with two-way coupling from individual size classes are isolated from the poly-dispersed suspension during runtime of the DNS, without affecting the actual two-way coupling associated with the poly-dispersity itself. Direct comparison is therefore made between 10^7 computational particles from each mono-dispersed suspension, to 10^7 computational particles from each size class within poly-dispersed suspensions. This minimises the statistical error associated with sampling reduced number of computational particles (see section 5.4.2).

For all simulations reported in this study, the material density chosen for particles is $\rho_p = 11300 kg/m^3$. In addition, to ensure the point-particle assumptions remain valid for simulations presented in this chapter, the ratio of $D/\eta_{(\phi_m=0.0)}$ was computed for all suspensions. Computed ratios for poly-dispersed suspensions A) and B), ranged between $0.02 < D/\eta < 0.04$ and $0.04 < D/\eta < 0.1$ respectively, indicating that the Lagrangian point-particle framework for simulating particles remains valid.

Particle Phase DNS Parameters			Unloaded	A	Aa	Ab	Ac	B	Ba	Bb	Bc
Dispersed Type	k	m^2/s^2	-	Poly	Mono	Mono	Mono	Poly	Mono	Mono	Mono
Average Stokes Number	$\left\langle N_p^{(i)} St_{\eta,(\phi_m=0)}^{(i)} \right\rangle_{\mathscr{L}}$	-	-	0.35	0.2	0.5	0.8	1.84	1.0	3.0	6.0
Mass Loading Ratio	ϕ_m	-	-	0.9	0.2	0.5	0.2	0.9	0.2	0.5	0.2
Average Diameter	$\left\langle N_p^{(i)} D^{(i)} \right\rangle_{\mathscr{L}}$	(μm)	-	893.2	697.6	1103.1	1395.3	2014.0	1560.0	2701.9	3821.1
Statistical Weight per Computational Particle	W_p	-	-	-	2.469	1.562	0.309	-	0.221	0.106	0.015[a]
No. Computational Particles Tracked	$N_c \times 10^6$	-	-	30	10	10	10	30	10	10	10
Turbulence Statistics			Unloaded	A	Aa	Ab	Ac	B	Ba	Bb	Bc
Turbulent Kinetic Energy	k	m^2/s^2	6.69	4.28	4.74	3.24	4.63	4.45	4.7	3.44	5.08
Dissipation Rate	ϵ	m^2/s^3	6.1	3.59	4.22	2.86	3.54	2.90	3.5	2.12	3.55
Turbulence Intensity	$u' = (2k/3)^{1/2}$	m/s	2.11	1.69	1.78	1.47	1.75	1.72	1.77	1.51	1.84
Longitudinal Integral Length-scale	$l = \frac{3}{4k}\int_0^{\kappa_{\max}} \frac{E(\kappa)}{\kappa} d\kappa$	m	0.33	0.35	0.34	0.35	0.35	0.36	0.36	0.37	0.36
Eddy Turnover Time	$\tau_e = l/u'$	s	0.16	0.21	0.19	0.24	0.20	0.21	0.2	0.25	0.19
Turbulent Length-scale	$L_e = \frac{k^{3/2}}{\epsilon}$	m	2.84	2.47	2.45	2.04	2.81	3.24	2.91	3.01	3.23
Taylor Length-scale	$\lambda = \left(\frac{10\nu_f k}{\epsilon}\right)^{1/2}$	m	0.52	0.55	0.53	0.53	0.57	0.62	0.58	0.64	0.6
Kolmogorov Length-scale	$\eta = \left(\frac{\nu_f^3}{\epsilon}\right)^{1/4}$	m	0.04	0.046	0.044	0.048	0.046	0.048	0.046	0.052	0.046
Kolmogorov Time-scale	$\tau_\eta = \left(\frac{\nu_f}{\epsilon}\right)^{1/2}$	s	0.064	0.084	0.077	0.094	0.084	0.093	0.085	0.11	0.085
Taylor Reynolds Number	$Re_\lambda = \frac{u'\lambda}{\nu_f}$	-	44.24	36.98	37.69	31.31	40.12	42.57	41.02	38.6	44.11
Turbulence Reynolds Number	$Re_L = \frac{k^2}{\epsilon\nu_f}$	-	293.48	204.10	212.96	146.82	242.22	273.14	252.46	223.28	290.78
Dispersed Phase Statistics			Unloaded	A	Aa	Ab	Ac	B	Ba	Bb	Bc
Mean Particle Kinetic Energy	$\frac{1}{N_p}\sum_{i=1}^{N_p} \frac{1}{2} M_p^{(i)} V_i^2$	$kg\ (\times 10^{-3})$	-	0.022	0.006	0.016	0.043	0.232	0.058	0.156	0.499
Mean Relative Velocity Magnitude	$\lvert U_i - V_i \rvert$	m/s	-	0.307	0.155	0.211	0.415	0.915	0.486	0.653	1.281
Mean Distance to Closest Particle	$\langle D_{sep} \rangle_{\mathscr{L}} / \bar{\eta}$	-	-	1.81	1.96	1.63	1.51	1.74	1.47	1.50	1.90
Voronoi Clustering Dimension	$\mathcal{V}_c^{3D}$	-	-	0.59	0.66	0.57	0.53	0.56	0.51	0.54	0.60
Voronoi Void Space Dimension	$\mathcal{V}_v^{3D}$	-	-	1.92	1.89	1.92	2.03	1.96	1.99	2.08	1.97

TABLE 6.1: Summary of particle phase DNS parameters, along with recorded mean turbulence and dispersed phase statistics taken for poly-dispersed and relevant mono-dispersed DNS investigations. Superscript $^{(i)}$ where $i = 1$, 2, or 3, corresponds to the size classes present within a given suspension.

[a]The reader is referred to Appendix C regarding potential limitations of saturating the DNS flow field by a large number of computational particles with $W_p \ll 1$.

6.6 Results

In this section results are presented from the study focused on the two-way coupling of poly-dispersed particle suspensions within isotropic turbulence. For selected results, direct comparison is made between mono-dispersed suspensions and the equivalent size classes isolated from the corresponding parent poly-dispersed suspension.

6.6.1 Basic Turbulence and Dispersed Phase Statistics

Table 6.1 summarises basic turbulence and dispersed phase statistics collected via DNS, comparing cases involving two-way coupled mono and poly-dispersed suspensions to that of an unloaded reference DNS case.

With the behaviour of turbulence statistics in table 6.1, one can see a significant reduction in turbulent kinetic energy when moving from unloaded to loaded turbulence in agreement with the results of Boivin et al. (1998) and the validations presented earlier in section 5.4 of this thesis. Reduction in turbulent kinetic energy appears to be greater for poly-dispersed suspension A) than poly-dispersed suspension B), which may be attributed to the presence of greater clustering tendency of particles. Surprisingly, the turbulent kinetic energy present in A) and B) poly-dispersed simulations that both have a mass loading ratio of $\phi_m = 0.9$, is greater than the turbulent kinetic energy present in mono-dispersed simulations Ab) and Bb), that instead have mass loading ratios of $\phi_m = 0.5$. This somewhat contradicts the idea that increased turbulence attenuation occurs for increased mass loading ratios. Whilst this idea may be true for mono-dispersed simulations, it is clearly not the case for poly-dispersed simulations. With regards to the dissipation rate, again there is reduction when moving from unloaded to loaded turbulence, and an associated increase for poly-dispersed simulations A) and B) compared to mono-dispersed simulations Ab) and Bb). Similar behaviour is also observed for turbulence intensity, turbulent length scale, as well as Taylor and turbulence Reynolds numbers. Little change is observed for computed Longitudinal integral length scales, albeit a slight increase in value when moving from unloaded to loaded turbulence.

Examining dispersed phase statistics in table 6.1, poly-dispersed suspensions appear to have greater mean particle kinetic energies than their respective dominant size class (with respect to mass loading ratio), mono-dispersed suspensions. The mean particle kinetic energies for poly-dispersed suspensions are also less than their larger Stokes number size class mono-dispersed suspensions. Similar behaviour is also observed for mean relative velocity magnitudes. Interestingly, the mean distance to closest particle measure for poly-dispersed suspension A) appears to be biased towards a value greater than that computed for mono-dispersed suspension Ab), and less than the measure computed for mono-dispersed suspension Aa). On the other-hand for poly-dispersed suspension B), the mean distance to closest particle appears biased towards a values greater than mono-dispersed suspension Bb), and less than the measure computed for mono-dispersed suspension Bc). This implies that the presence of poly-dispersity can bias the de-clustering tendency of particles, depending on whether or not particle size classes within the poly-dispersed suspension have Stokes numbers less than or greater than unity.

6.6.2 Spectral Turbulence Statistics

6.6.2.1 Turbulent Kinetic Energy and Dissipation Rate Spectra

Figure 6.1 shows the turbulent kinetic energy spectra from poly-dispersed simulations A) and B), as well as mono-dispersed simulations Aa)-Bc) and Ba)-Bc) defined in table 6.1. For poly-dispersed simulation A), where $\langle St_\eta \rangle_{\mathscr{L}} < 1$, the kinetic energy spectra shows a characteristic attenuation of large scale energy and a slight augmentation of small scale energy beyond the crossover wave-number compared to the unloaded reference DNS case, in agreement with known behaviour of two-way coupled particles in turbulence (Elghobashi and Truesdell 1993; Boivin et al. 1998).

Despite having a larger mass loading ratio, the attenuation of large scale energy for poly-dispersed simulation A), does not appear to be as much as the attenuation seen for the mono-dispersed Ab) simulation. In fact the attenuation level at large scales is roughly

the same order of magnitude as the two $\phi_m = 0.2$, Aa) and Ac) mono-dispersed simulations. With regards to the augmentation at small scales for poly-dispersed suspension A), only a slight increase in turbulent kinetic energy is observed above the unloaded reference DNS case. Furthermore, the augmentation exhibited by poly-dispersed suspension A), remains less than the augmentation observed for the mono-dispersed Ab) suspension. For poly-dispersed simulation B), there is a clear attenuation of turbulent kinetic energy across all scales of turbulent motion compared to the unloaded reference DNS case. For large scales of turbulent motion, the attenuation exhibited in simulation B) is greater than the $\phi_m = 0.2$ mono-dispersed simulations Ba) and Bc), yet less than the attenuation level exhibited in simulation Bb) that has $\phi_m = 0.5$. At small scales the attenuation exhibited by poly-dispersed simulation B), is greater than the the attenuation of mono-dispersed simulation Ba) and Bb), yet less than the high Stokes number Bc) suspension. To summarize, these observations provide further evidence to the idea discussed in section 6.6.1, that turbulence modulation for poly-dispersed suspensions is not as dependent on the mass loading ratio, as one would typically expect to be the case for mono-dispersed suspensions.

Since the dissipation spectra is directly related to the turbulent kinetic energy spectra in terms of its mathematical definition, the effects discussed previously regarding the attenuation and augmentation characteristics between poly-dispersed simulations, corresponds directly with the energy dissipation rate characteristics shown in figure 6.2.

6.6.2.2 Transfer Spectra

Examining the transfer spectra between the two poly-dispersed suspensions provides some insight on the energy cascade processes occurring within the turbulence, and the effect that poly-dispersity and two-way coupling has on such processes. In essence, the transfer spectra is simply a measure quantifying the scale dependent correlation between turbulent velocity, and the turbulent Reynolds stresses. The non-linear terms present within the Navier-Stokes equations leads to a cascading transfer of energy, to progressively smaller scales of turbulent motion until viscosity takes hold. In figure 6.3, $\bar{T}(\kappa)$ quantifies the magnitude of energy transferred through the scales of turbulent motion

into wave-number κ. One can see that the modification of turbulence by the presence of particles, leads to a change in the magnitude of energy transferred, a process complicated further by the poly-dispersity, with different particle size classes interacting, extracting and supplying energy to different scales of turbulent motion. In figure 6.3, the transfer spectra between the two poly-dispersed simulations shows a negative correlation at large scales of turbulent motion, and a positive correlation across transfer scales, tending to zero with increasing wave-number. The negative correlation is due to effects from the stochastic forcing scheme, and the positive correlation is mainly due to cascading transfer mechanisms of energy moving from larger eddies to progressively smaller eddies within the turbulence. Since unloaded turbulence contains the greatest total kinetic energy compared to any two-way coupled turbulence cases, the magnitude of the transfer spectra remains the greatest compared to any loaded mono or poly-dispersed turbulence simulations. Unfortunately, no other discernible impact of poly-dispersity on the transfer spectra can be seen.

6.6.2.3 Fluid-to-Particle Energy Exchange Rate Spectra

Figure 6.4 illustrates the fluid-to-particle energy exchange rate due to drag. The negative spectral correlation corresponds to a transfer of energy *from* the fluid *to* the particle phase, whereas a positive spectral correlation indicates a transfer of energy *from* the particle phase back *to* the fluid. This correlation can be interpreted as the tendency for fluid velocity vectors to orient themselves with the direction of particle motion when positive, and against the direction of particle motion when negative. For poly-dispersed suspension A), there is a significant transfer of energy from the fluid to the particle phase occurring at large scales, nearly as much as the energy transfer for the mono-dispersed Ab) suspension, despite the Ab) suspension having smaller mass loading ratio. The same observation can be said for poly-dispersed suspension B), where the fluid-to-particle energy transfer is nearly as much as the mono-dispersed Bb) suspension. With regards to the rate of energy transfer back to the fluid for poly-dispersed suspension A), the transfer is similar in magnitude compared to the mono-dispersed Aa) suspension, apart from a slight shift towards higher wave-numbers before the positive transfer of energy

occurs. For poly-dispersed suspension B), the change to a positive energy transfer back to the fluid is seen at greater wave-numbers than those observed for suspension A), yet is as most comparable in magnitude to the energy transfer rate of the mono-dispersed Bc) suspension. Figure 6.4 also shows that the rate of energy transfer back to the fluid at small scales is much greater for the tracer-like $\langle St_\eta \rangle_{\mathscr{L}} < 1$ poly-dispersed suspension A), than it is for the more ballistic-like $\langle St_\eta \rangle_{\mathscr{L}} > 1$ poly-dispersed suspension B). An interesting observation can also be seen whilst comparing the mono-dispersed fluid-to-particle energy exchange rate spectra, to the spectra of size classes isolated from poly-dispersed suspensions A) and B). For suspension A), the fluid-to-particle energy transfer rate for each isolated size class is reduced significantly, compared to equivalent mono-dispersed suspensions. The same can be said for isolated size classes within poly-dispersed suspension B). This evidence supports further the fact that poly-dispersity has non-trivial effect upon the two-way coupling energy transfer processes within turbulence.

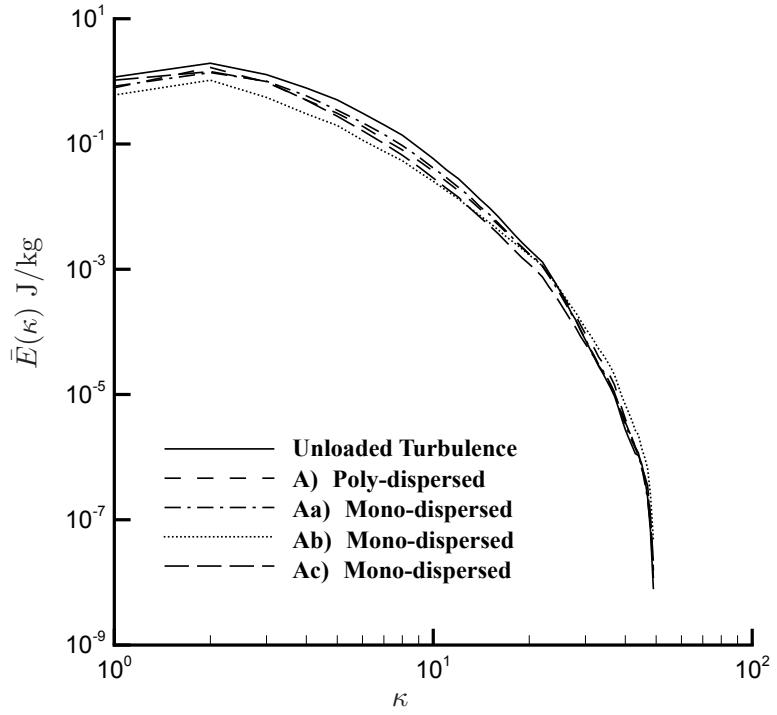

(a)

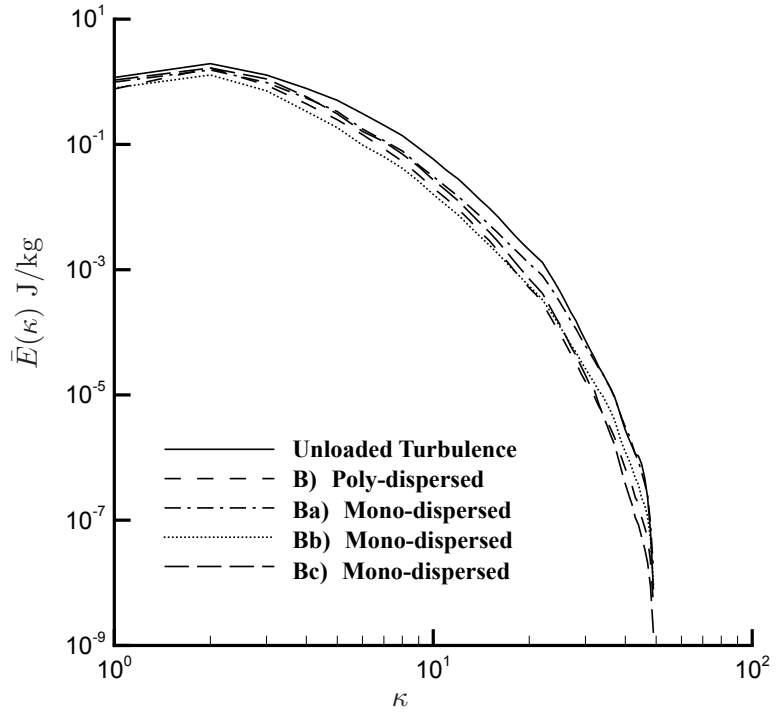

(b)

FIGURE 6.1: Spectrum of the Turbulent Kinetic Energy defined by equation (4.15) for; a) Poly-Dispersed Group A where $\langle St_\eta \rangle_{\mathscr{L}} < 1$, and b) Poly-Dispersed Group B where $\langle St_\eta \rangle_{\mathscr{L}} > 1$

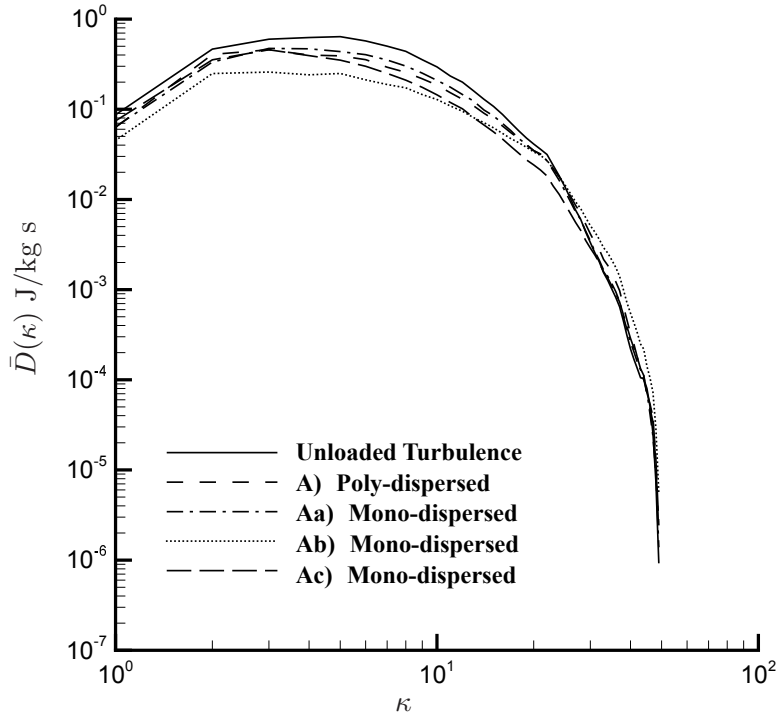

(a)

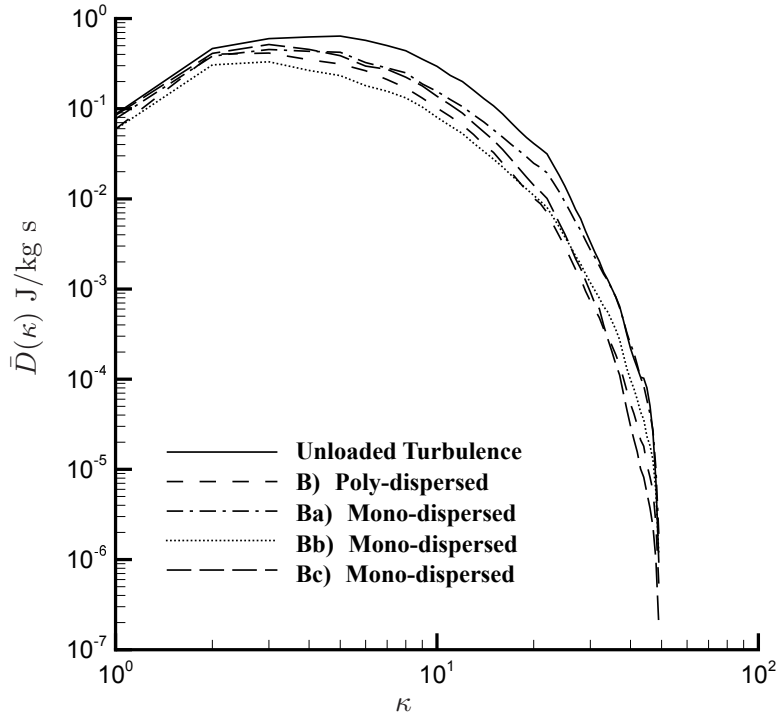

(b)

FIGURE 6.2: Spectrum of the Kinetic Energy Dissipation Rate defined by equation (4.17) for; a) Poly-Dispersed Group A where $\langle St_\eta \rangle_{\mathscr{L}} < 1$, and b) Poly-Dispersed Group B where $\langle St_\eta \rangle_{\mathscr{L}} > 1$

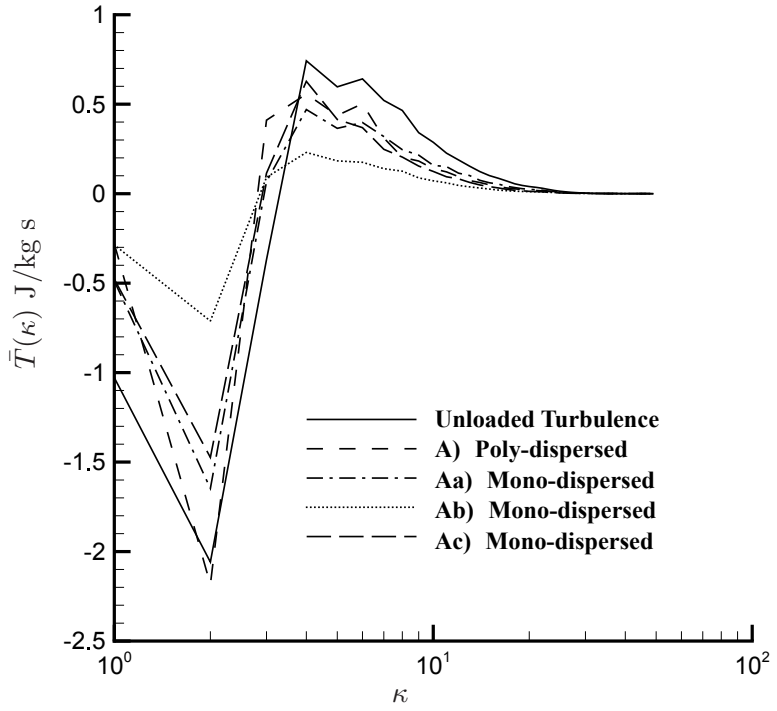

(a)

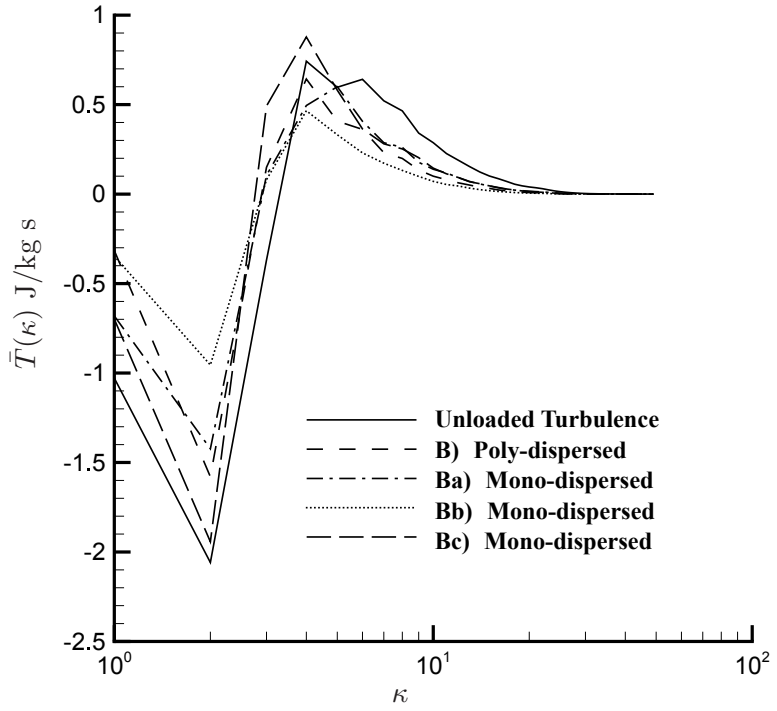

(b)

FIGURE 6.3: Transfer Spectra defined by equation (4.16) for; a) Poly-Dispersed Group A where $\langle St_\eta \rangle_{\mathscr{L}} < 1$, and b) Poly-Dispersed Group B where $\langle St_\eta \rangle_{\mathscr{L}} > 1$

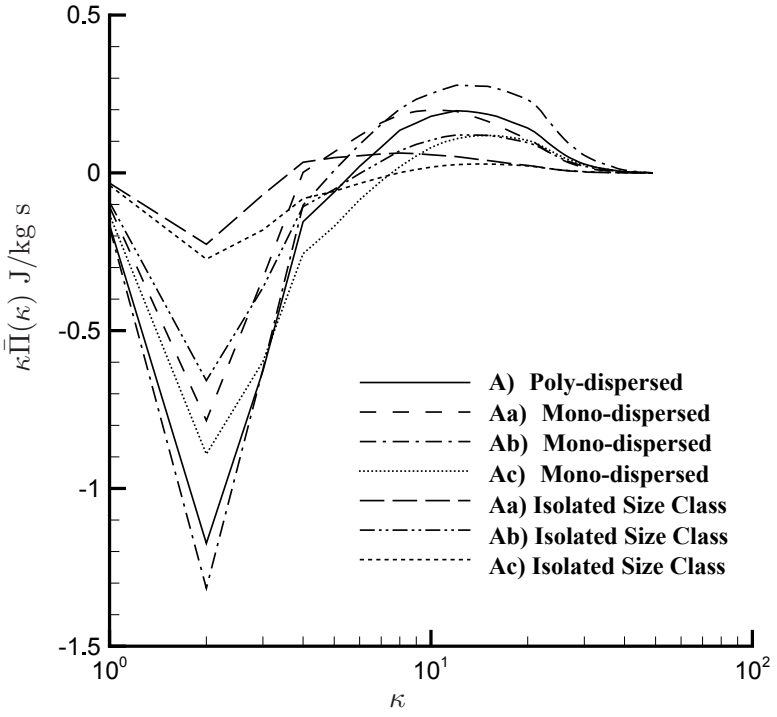

(a)

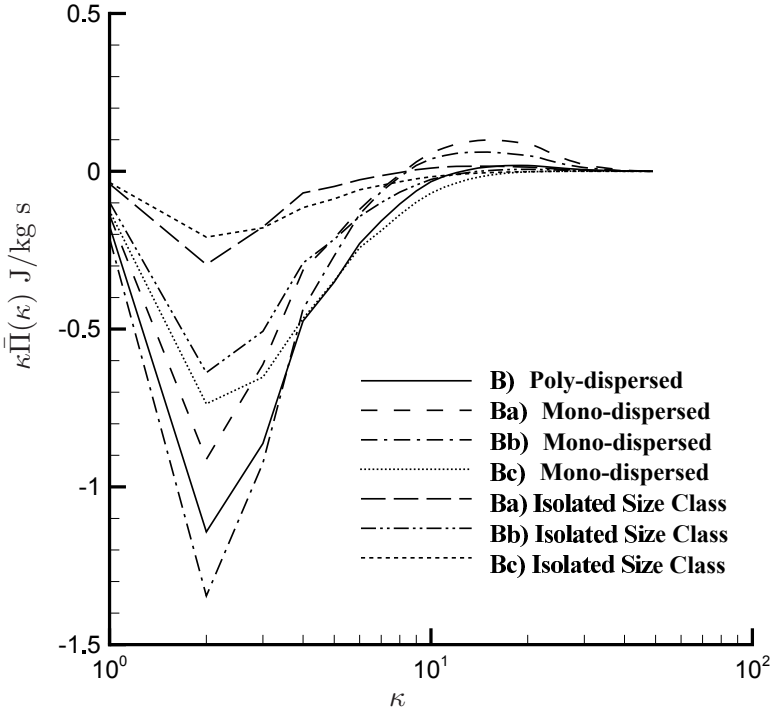

(b)

FIGURE 6.4: Fluid-to-Particle Energy Exchange Rate Spectra defined by equation (4.18) for; a) Poly-Dispersed Group A where $\langle St_\eta \rangle_{\mathscr{L}} < 1$, and b) Poly-Dispersed Group B where $\langle St_\eta \rangle_{\mathscr{L}} > 1$

6.6.3 Spectral Particle Phase Statistics

6.6.3.1 Particle Phase Mesoscopic Kinetic Energy Spectra

Figure 6.5 illustrates the scale dependent mesoscopic energy content of the particle phase suspensions listed in table 6.1. Comparing the mesoscopic energy spectra for both poly-dispersed suspensions A) and B), particles present in the largest scales of turbulent motion contain the greatest kinetic energy compared to particles that are present in the smallest scales of turbulent motion. This is to be expected since the largest scales of turbulent motion are transferring their momentum to the particle phase as indicated by the negative fluid-to-particle energy exchange rate spectra shown in figure 6.4. For poly-dispersed suspension A), the large scale kinetic energy has the same magnitude of kinetic energy as the isolated Aa) size class, and nearly the same level of kinetic energy as the mono-dispersed Aa) suspension. Compared to the other isolated size classes, the magnitude of kinetic energy for poly-dispersed suspension A) is much larger. This observation suggests that at large scales, the majority of poly-dispersed particle phase kinetic energy is actually coming from the movement of particles within the isolated Aa) size class. This is supported further with the evidence seen at small scales, whereby the kinetic energy for poly-dispersed suspension A) has nearly the same magnitude as the isolated Aa) size class, whilst isolated size classes Ab) and Ac) have small scale kinetic energies that are much larger.

For poly-dispersed suspension B), the kinetic energy present at large scales is greater than any of its mono-dispersed or isolated size classes. This suggests that the kinetic energy of the poly-dispersed particle phase at large scales is predominantly from the collective motion of all size classes that are present within. At small scales, the kinetic energy present in poly-dispersed suspension B) has nearly the same magnitude as the the isolated Bc) size class. This suggests that at small scales, the majority of poly-dispersed kinetic energy is actually coming from the movement of particles within the isolated Bc) size class. It should be noted that whilst isolated size classes Ba) and Bc) have kinetic energies greater than isolated size class Bc), the greater presence of Bc) size

class particles at small scales will bias kinetic energies of the poly-dispersed suspension to be smaller and comparable in magnitude.

6.6.3.2 Particle-to-Fluid Energy Exchange Rate Spectra

Figure 6.6 illustrates the scale dependent particle-to-fluid energy exchange rate due to drag. As documented in section 4.3.1, a positive spectral correlation indicates that the particle phase is receiving energy from the fluid whereas a negative spectral correlation indicates that energy is moving from the particle phase back to the fluid. At large scales, both poly-dispersed suspensions A) and B) receive the greatest energy from the fluid phase compared to their respective size classes, with poly-dispersed suspension A) receiving more energy from the turbulence than poly-dispersed suspension B). This makes sense from a theoretical standpoint, since particles with Stokes numbers less than unity behave more like tracers and are more responsive to changes in direction within the surrounding fluid, whereas particles with Stokes numbers greater than unity behave in a ballistic manner, and are less responsive to changes in direction within the surrounding fluid.

With regards to the mono-dispersed and isolated size classes, it is the isolated size classes that receive less turbulent energy as part of a poly-dispersed suspension, than compared to mono-dispersed counterparts. This behaviour indicates that kinetic energy from the fluid is being distributed amongst size classes within the poly-dispersed suspension, and hence size classes would not receive as much kinetic energy as they normally would when present as a mono-dispersed suspension in turbulence.

Across the transfer scales of the turbulence between wave-numbers $\kappa \approx 4$ and $\kappa \approx 20$, it is immediately apparent that a non-trivial behaviour is observed for both poly-dispersed suspensions with regards to the energy transfer from the particle phase back to the fluid. For poly-dispersed suspension A), the rate of energy exchange from the particle phase back to the fluid remains greater than all isolated size classes. For those same isolated size classes, the rate of energy transfer back to the fluid is significantly diminished compared to mono-dispersed counterparts. For suspension B), the rate of energy transfer back to the fluid is delayed to slightly smaller scales within the transfer range at $\kappa \approx 6$.

A surprising observation is that poly-dispersed suspension B) has a negative spectral correlation between wave-numbers $\kappa \approx 10$ and $\kappa \approx 20$, that is smaller in magnitude compared to the isolated Bb) size class, whilst larger in magnitude to Ba) and Bc) size classes. This is despite the fact that poly-dispersed suspension B) has a mass loading ratio of $\phi_m = 0.9$, compared to the Bb) size class that has a mass loading ratio of $\phi_m = 0.5$. Again, this suggests that for particle size classes with Stokes number greater than unity, there may be a situation that as one size class gives back energy to the fluid at a given scale of turbulence, that same energy may immediately be given back to another size class of the suspension, at the same or similar scales within the turbulence.

6.6.3.3 Particle-to-RUM Energy Exchange Rate Spectra

Figure 6.7 shows the particle-to-RUM energy exchange rate spectra, defined by equation (4.29), for particle phase suspensions listed in table 6.1. As documented in section 4.4.1, a positive spectral correlation indicates a transfer of kinetic energy from the mesoscopic particle phase to the RUM, whereas a negative spectral correlation indicates a transfer of kinetic energy from the RUM to the mesoscopic particle phase. Evidently, there is a distinctive difference in behaviour between the two poly-dispersed particle suspensions. Is appears that the particle-to-RUM energy exchange rate spectra for poly-dispersed suspension A) exhibits a 'saddle' like behaviour. A positive energy exchange from the mesoscopic field to the RUM is seen at large scales of turbulent motion, and across transfer scales between wave-numbers $\kappa \approx 3 - 10$, there is a negative transfer of energy from the RUM back to the mesoscopic phase. Beyond wave-number $\kappa \approx 10$, there is a positive transfer of energy from the mesoscopic to RUM that reaches a maximum at around $\kappa \approx 12$, before diminishing to zero up to the smallest scales of resolved turbulent motion. For poly-dispersed suspension B), an entirely different behaviour is observed. A positive transfer of energy occurs from the mesoscopic to RUM at large scales of turbulent motion, that decreases steadily to zero with increasing wave-number up to the smallest scales of resolved turbulent motion. There is no negative transfer of energy occurring from the RUM to mesoscopic, neither is there the presence of a saddle like profile in the spectra for the poly-dispersed suspension. However, for isolated size classes

and mono-dispersed suspensions, there is still evidence of a saddle like behaviour within the spectra, the only difference being that the transfer of energy from the mesoscopic to RUM dominates at large scales of the saddle. With regards to differences between mono-dispersed suspensions and isolated size classes, it appears that within the saddle part of the spectra, i.e. the intermediate transfer scales, the two isolated $\phi_m = 0.2$ Aa) and Ac) size classes transfer more energy from their RUM to mesoscopic fields, than their mono-dispersed counterparts. Only the $\phi_m = 0.5$ Ab) sub-population transfers less energy than its mono-dispersed counterpart. The opposite is seen at smaller scales beyond the saddle maxima at $\kappa \approx 12$, where the Aa) and Ac) isolated size classes now transfer less energy from the mesoscopic to their RUM fields than their mono-dispersed counterparts. Additionally, the isolated Ab) size class now transfers more energy from mesoscopic to RUM than its mono-dispersed counterpart. For isolated Ba) and Bc) size classes, the energy exchange from the mesoscopic to RUM at large scales remains less than mono-dispersed counterparts, whilst the isolated Bb) size class exceeds the energy exchange from the mesoscopic to RUM of its mono-dispersed counterpart. The same behaviour remains true within the saddle like region of the spectra.

Collectively, all these observations discussed suggest a distinctive change in energy transfer behaviour. This behaviour appears to be scale dependent, with $\langle St_\eta \rangle_{\mathscr{L}} < 1$ suspensions more sensitive to intermediate transfer and dissipative scales of the turbulence, and $\langle St_\eta \rangle_{\mathscr{L}} > 1$ suspensions instead more sensitive to inertial and intermediate transfer scales of the turbulence.

6.6.3.4 RUM Kinetic Energy Spectra

Figure 6.8 illustrates the RUM kinetic energy spectra for particle phase suspensions listed in table 6.1. Since the RUM spectra is intrinsically linked to the mesoscopic energy spectra via the particle-to-RUM energy exchange rate spectra discussed previously in section 6.6.3.3, the same qualitative findings to those of the mesoscopic kinetic energy spectra may also be found. The only difference is a distinctive bump exhibited in the RUM kinetic energy at small scales, most likely caused by the sudden increase in mesoscopic to RUM energy transfer at small scales discussed previously in section 6.6.3.3.

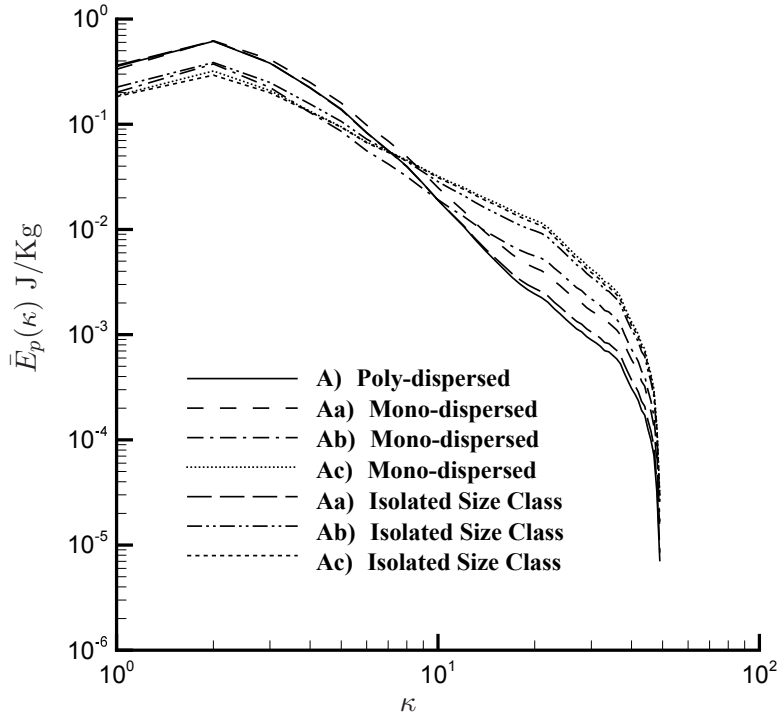

(a)

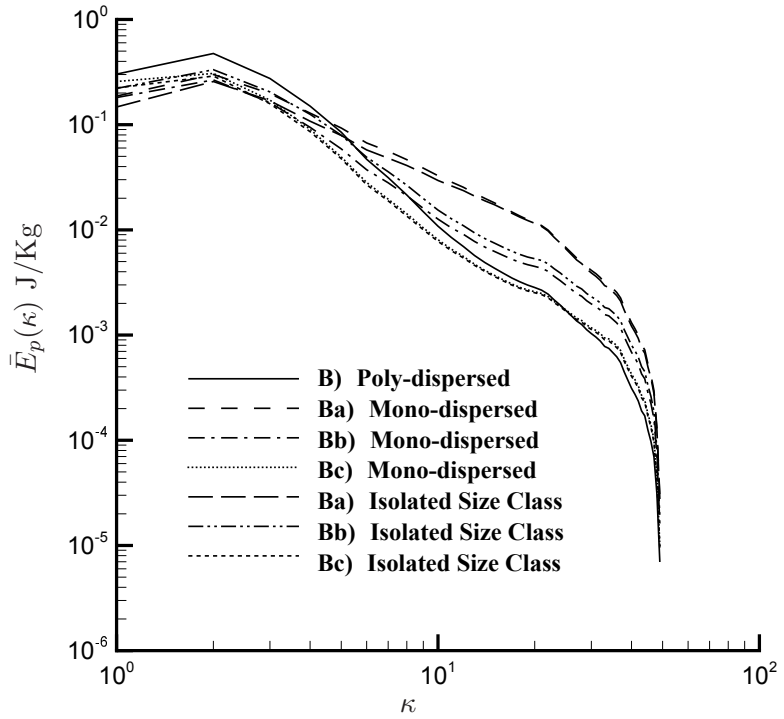

(b)

FIGURE 6.5: MEPVF Spectra defined by equation (4.26) for; a) Poly-Dispersed Group A where $\langle St_\eta \rangle_{\mathscr{L}} < 1$, and b) Poly-Dispersed Group B where $\langle St_\eta \rangle_{\mathscr{L}} > 1$

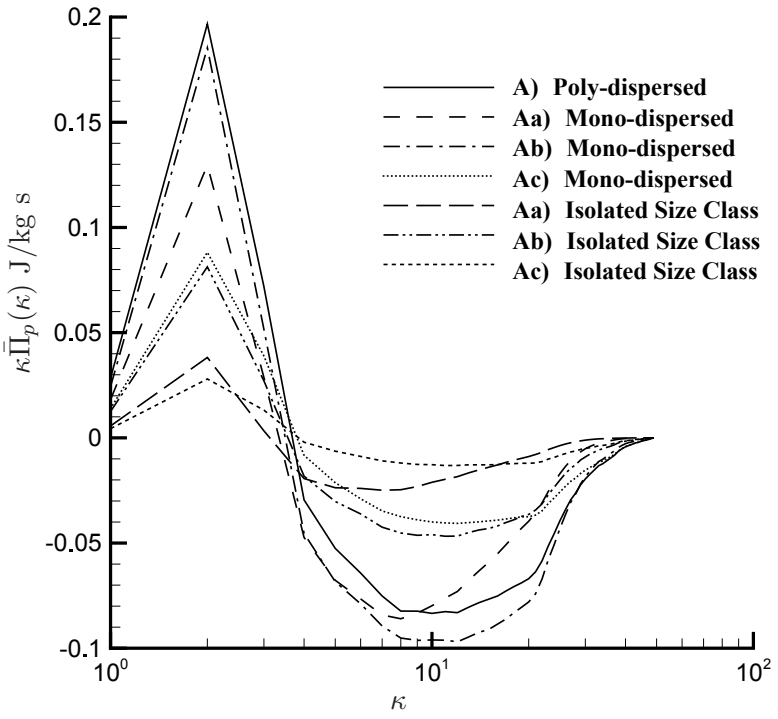

(a)

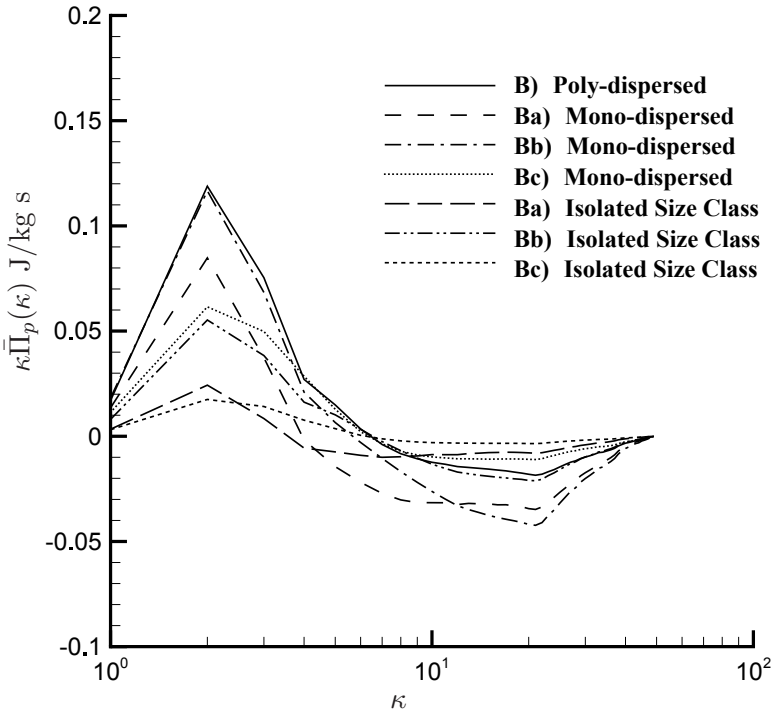

(b)

FIGURE 6.6: Particle-to-Fluid Energy Exchange Rate Spectra defined by equation (4.27) for; a) Poly-Dispersed Group A where $\langle St_\eta \rangle_{\mathscr{L}} < 1$, and b) Poly-Dispersed Group B where $\langle St_\eta \rangle_{\mathscr{L}} > 1$

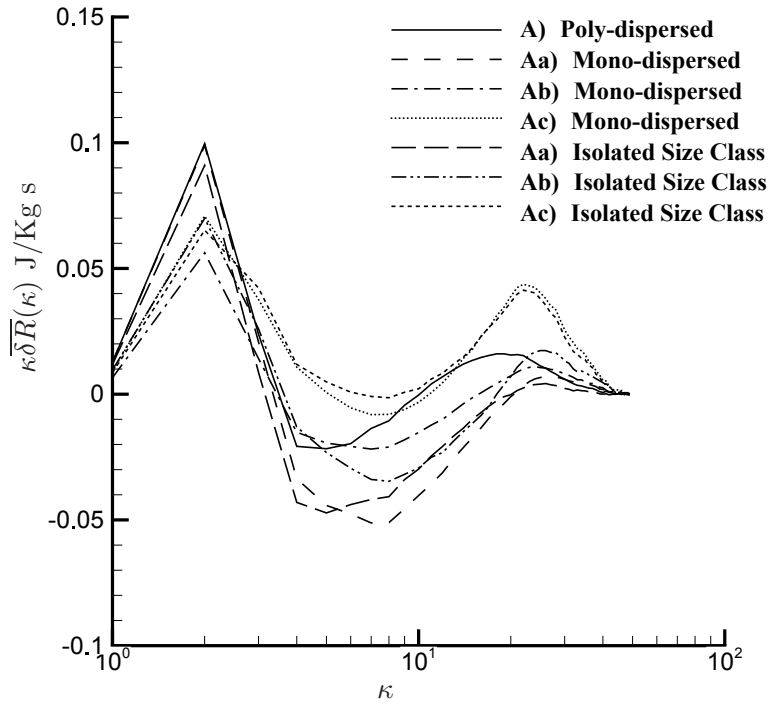

(a)

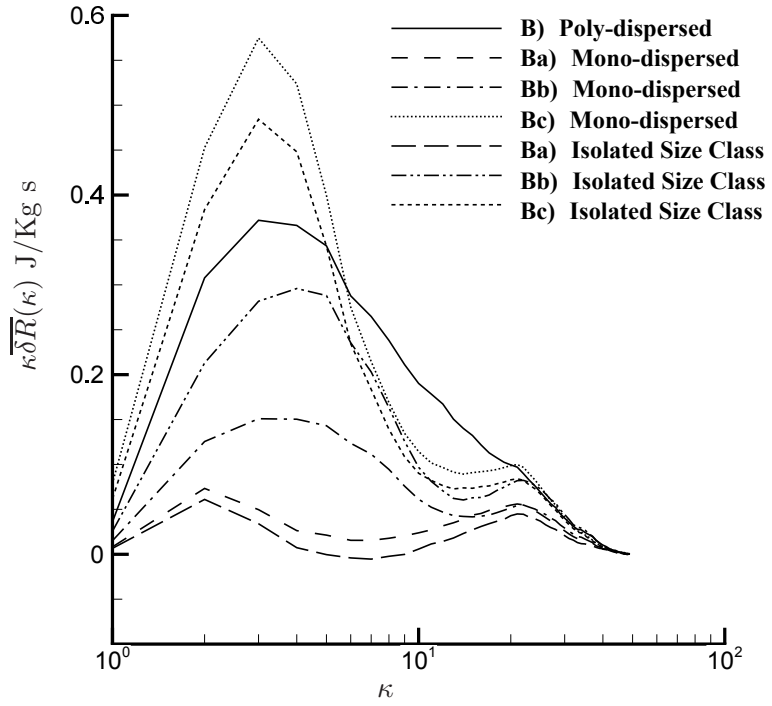

(b)

FIGURE 6.7: Particle-to-RUM energy exchange rate spectra defined by equation (4.29) for; a) Poly-Dispersed Group A where $\langle St_\eta \rangle_{\mathscr{L}} < 1$, and b) Poly-Dispersed Group B where $\langle St_\eta \rangle_{\mathscr{L}} > 1$. Negative values represent the transfer of energy from the RUM to mesoscopic field, whereas positive values represent the transfer of energy from the mesoscopic to RUM field.

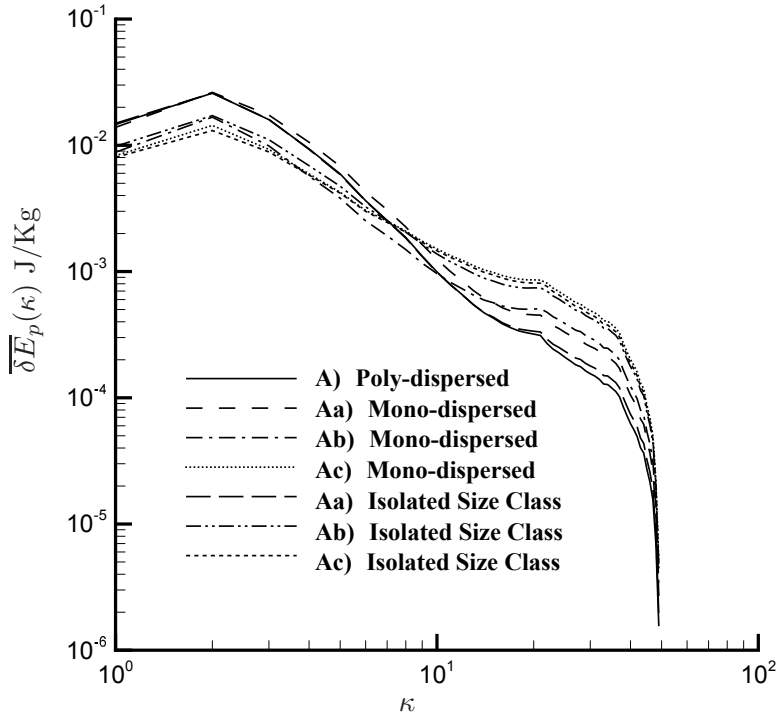

(a)

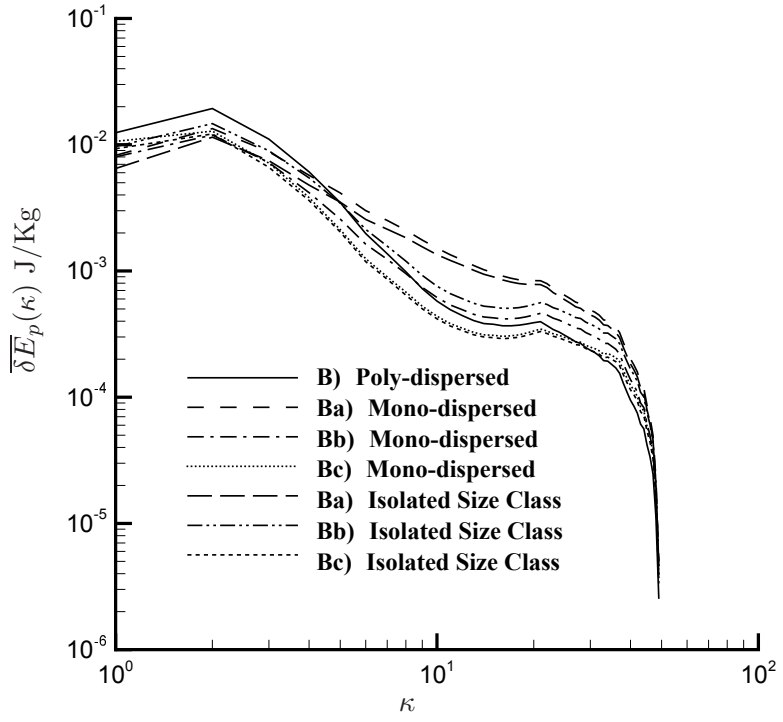

(b)

FIGURE 6.8: RUM kinetic energy spectra defined by equation (4.31) for; a) Poly-Dispersed Group A where $\langle St_\eta \rangle_{\mathscr{L}} < 1$, and b) Poly-Dispersed Group B where $\langle St_\eta \rangle_{\mathscr{L}} >$ 1

6.6.4 Preferential Concentration Statistics

Figure 6.9 presents D measures computed for poly-dispersed and associated mono-dispersed suspensions, which as discussed in Scott et al. (2009), characterises the deviation of the observed particle distribution from a perfectly random Poisson distribution. Firstly, the D measures for mono-dispersed suspensions Aa)-c) increase with the increase in particle Stokes number. Interestingly enough, the D measure for poly-dispersed suspension A) has nearly the same characteristic shape as the D measure for the mono-dispersed suspension Ab), despite having a greater mass loading ratio. For mono-disperse suspensions Ba)-c), the D measures instead decrease in their magnitude with the increase in particle Stokes number of the suspension. Furthermore, the D measure for poly-dispersed suspension B) remains slightly greater in magnitude compared to the mono-dispersed Bc) suspension, yet smaller in magnitude compared to mono-dispersed suspensions Ba) and Bb). Lastly, the D measure for poly-dispersed suspension A) achieves slightly higher magnitudes compared to suspension A).

Figure 6.10 illustrates the 3D RDFs for poly-dispersed and mono-dispersed suspensions listed in table 6.1. In a similar fashion to the D measure, the RDFs for mono-disperse populations Aa)-c), show an increase in magnitude at small separation distances, with an associated increase in particle Stokes number. For mono-disperse populations Ba)-c), RDFs instead show a decrease in magnitude with increasing Stokes number. With regards to the RDFs for poly-dispersed suspensions A) and B), behaviour is similar to what was observed for D measures discussed previously. The RDF for suspension Ba) achieves the highest $g(r)$ magnitude compared to all other poly and mono-dispersed suspensions, mainly due to the fact that the suspension has a Stokes number of unity, where preferential concentration is known the be significant. For RDFs of poly-dispersed suspensions A) and B), both have very similar profiles with suspension B) achieving slightly higher magnitudes for $g(r)$ compared to suspension A), an observation also seen within computed D measure profiles.

Figure 6.11 illustrates PDFs of the normalised Voronoi volumes and compares them against a model PDF function that describes a 3D random Poisson distribution. The key difference between PDF $\mathcal{V}^{3D}$ measures compared to other D and RDF measures,

is the ability to characterise both particle clusters and void spaces present within the suspension. The two intersections with the model 3D RPP profile provide an indication as to the length scales at which particle clusters and voids begin to form, relative to a 3D random Poisson distribution of particles. With regards to the characteristics of particle clusters between cases, it appears that mono-disperse suspensions Aa)-c) demonstrate an increasing likelihood of particle clustering with increasing Stokes number towards unity. Conversely, for mono-disperse suspensions Ba)-c), there is a decreasing likelihood of particle clustering with increasing Stokes number beyond unity. For poly-dispersed suspensions A) and B), the observed behaviour of clustering at small scales is consistent with that characterised by corresponding D and 3D RDF measures. Moreover, the characteristics of voids is rather obscured by the diminishing quality of statistics in the right-side tails of normalised Voronoi volume PDFs. This is attributed to lack of statistical convergence for observed voids within a given particle suspension. Nonetheless, the location of $\mathcal{V}_v^{3D}$ appears consistent across all poly-dispersed, and mono-dispersed suspensions listed in table 6.1.

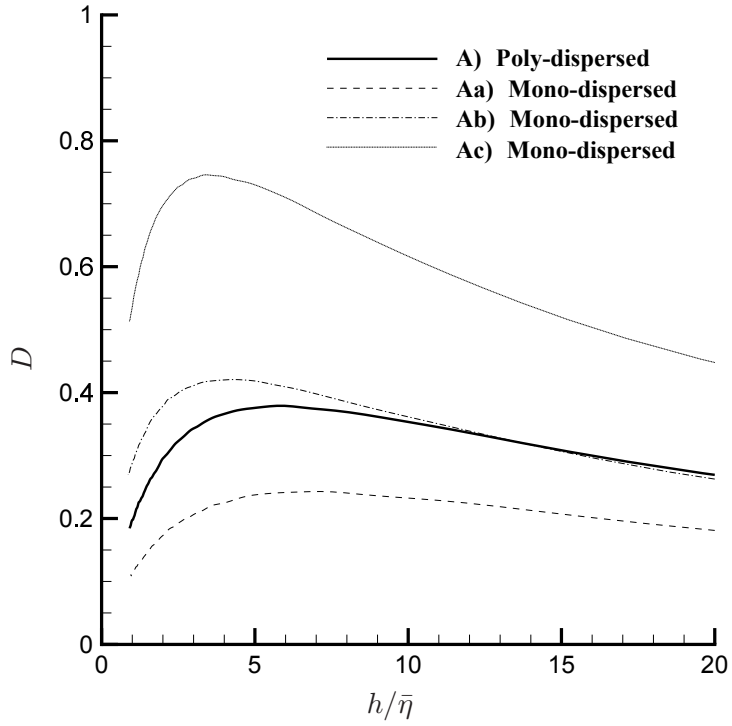

(a)

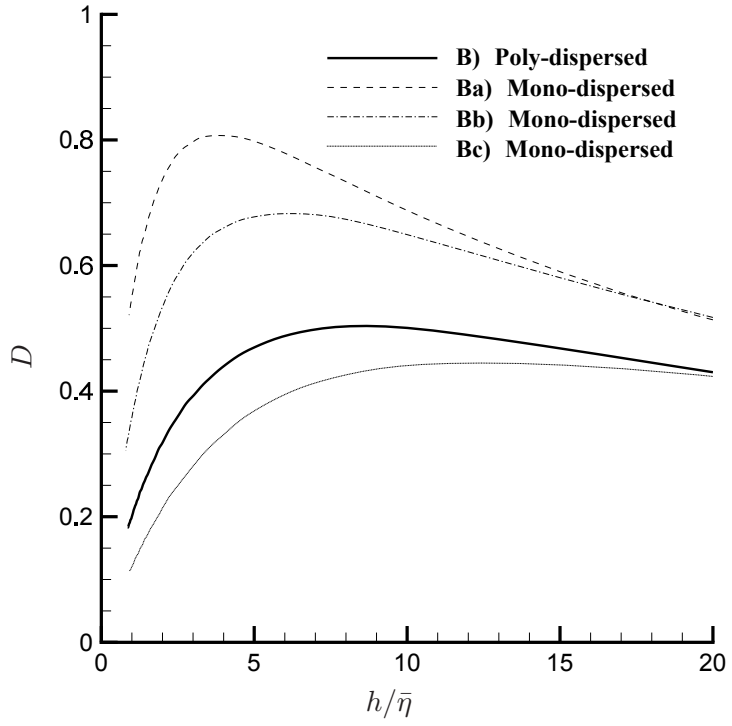

(b)

FIGURE 6.9: Dependence of D measure on non-dimensional bin-size, $h/\bar{\eta}$, for; a) Poly-Dispersed Group A where $\langle St_\eta \rangle_{\mathscr{L}} < 1$, and b) Poly-Dispersed Group B where $\langle St_\eta \rangle_{\mathscr{L}} > 1$.

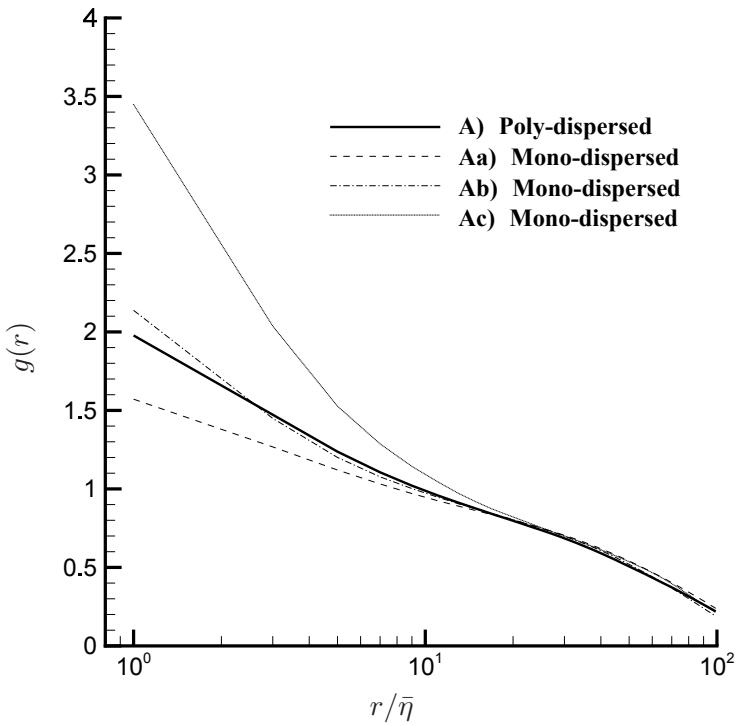

(a)

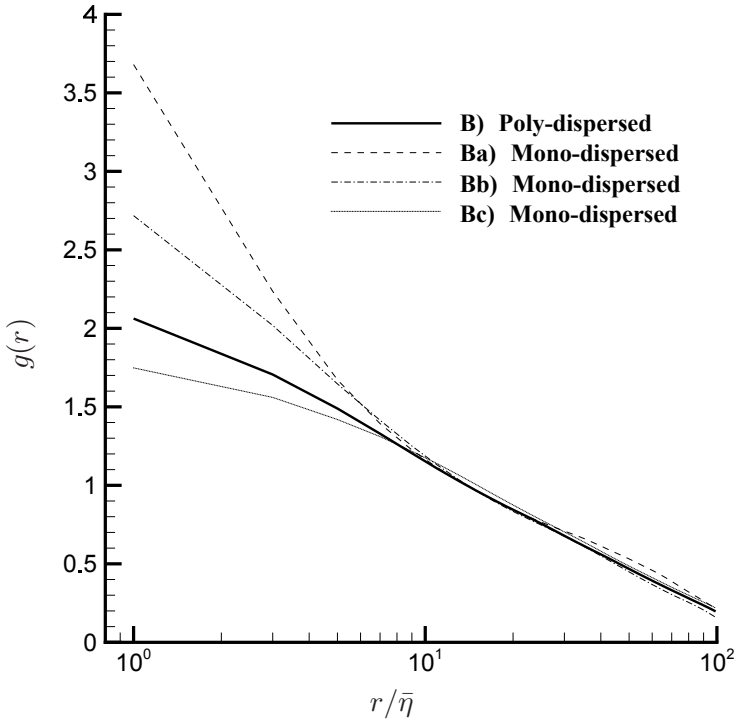

(b)

FIGURE 6.10: 3D radial distribution functions for; a) Poly-Dispersed Group A where $\langle St_\eta \rangle_{\mathscr{L}} < 1$, and b) Poly-Dispersed Group B where $\langle St_\eta \rangle_{\mathscr{L}} > 1$.

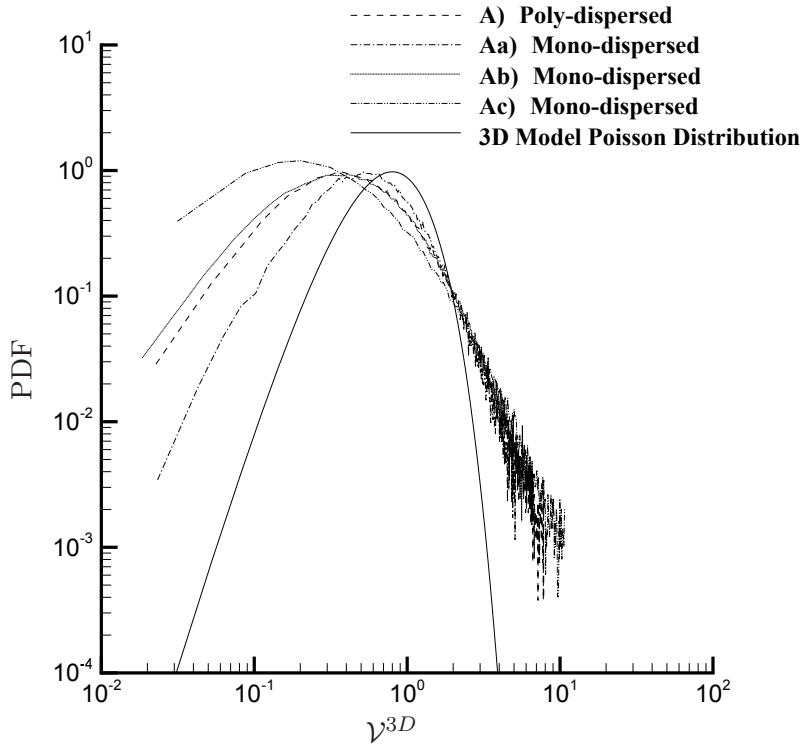

(a)

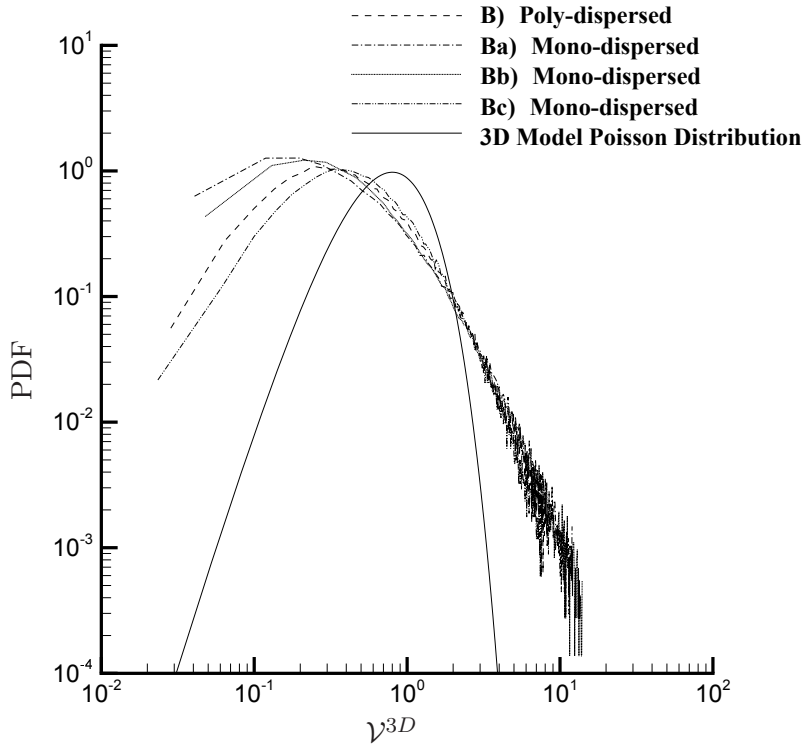

(b)

FIGURE 6.11: Normalised Voronoi Volume PDFs for; a) Poly-Dispersed Group A where $\langle St_\eta \rangle_{\mathscr{L}} < 1$, and b) Poly-Dispersed Group B where $\langle St_\eta \rangle_{\mathscr{L}} > 1$. The model corresponds to that of a 3D random Poisson distribution given by the function, $f_{3D}(x) = \frac{3125}{24} x^4 \exp^{-5x}$, (Ferenc and Néda 2007).

6.7 Summary

- DNS investigations have shown that a poly-dispersed suspension, two-way coupled with turbulence at a high mass loading ratio, can attenuate turbulent kinetic energy less so than a mono-dispersed suspension two-way coupled with turbulence at a smaller mass loading ratio, even when such a mono-dispersed suspension is present as a size class within the poly-dispersed suspension.

- It has also been found that the presence of two sub-populations with an individual mass loading ratio of $\phi_m \approx 0.2$, can counteract the level of turbulent kinetic energy attenuated by a dominant particle size class with an individual mass loading ratio of $\phi_m \approx 0.5$. This is strictly valid in the scenario when the two non-dominant $\phi_m \approx 0.2$ size classes reside either side of the dominant size class in terms of Stokes number.

- Particle kinetic energies of poly-dispersed particle suspensions appear to have a negative skewness towards the particle kinetic energy of the largest mass loading ratio size class.

- Investigations have also shown that the magnitude of energy exchange occurring from a $\langle St_\eta \rangle_{\mathscr{L}} < 1$ poly-dispersed particle suspension to intermediate transfer and small scales of turbulence, remains less than the energy exchange that occurs for a $\langle St_\eta \rangle_{\mathscr{L}} > 1$ poly-dispersed particle suspension. Furthermore, a distinctive behavioural change in particle-to-RUM energy exchange rate is observed between a $\langle St_\eta \rangle_{\mathscr{L}} < 1$ and $\langle St_\eta \rangle_{\mathscr{L}} > 1$ poly-dispersed particle suspension.

- With regards to particle clustering phenomena, the dependence of D measure on non-dimensional particle bin size profiles for $\langle St_\eta \rangle_{\mathscr{L}} < 1$ poly-dispersed particle suspensions, appear to be biased towards the profile of the smallest Stokes number size class. Whereas for $\langle St_\eta \rangle_{\mathscr{L}} > 1$ poly-dispersed particle suspensions, D measure profiles appear to be biased towards the largest Stokes number size class. Since particles are least clustered when Stokes numbers are farthest away from unity,

one can conclude that it is favourable to have a poly-dispersed particle suspension rather than a mono-dispersed suspension, when one aims to maximise the homogeneity of a dispersed particle phase within a turbulent flow field.

Chapter 7

DNS Investigations: Two-Way Coupling of Mono-Dispersed Particles Under Electrical and Gravitational Body Forces

7.1 Introduction

As discussed earlier in section 2.3 of this thesis, the majority of research that exists on two-way coupling focuses on the physics of energy exchange between turbulence and dispersed phase particles that are uncharged. In this chapter, two-way coupling for electrically charged particles in turbulence is examined instead. To consider realistic charged particle suspensions, this chapter also examines scenarios that include the presence of gravitational body force.

7.2 Hypothesis and Overview

Firstly, one may recall from section 5.4.1 that the rate of energy exchange between turbulence and particles, depends locally on the mass loading ratio present within the fluid, which in turn depends on the clustering tendency of particles within the suspension. To consider an electrically charged particle suspension, Coulomb's law states that the magnitude of electrostatic force between two charged particles is directly proportional to the product of their charges and inversely proportional to the square of the distance between them. One would therefore expect that Coulomb repulsion forces present between particles in a given suspension, would act to mitigate any clustering tendency (Karnik and Shrimpton 2008). If the clustering tendency within a two-way coupled charged particle suspension is reduced, one should also expect that two-way coupling behaviour should change as well.

To consider the effects of gravity for uncharged particle suspensions, one may recall from section 2.3.5 that gravity acts to pull particles unidirectionally in a collective downwards motion. Both continuity, and crossing trajectories effects discussed in section 2.3.3 of this this thesis, are phenomenon associated with such a scenario. For two-way coupled suspensions, any particle clusters that fall under gravity are also known to increase the tangential velocity of turbulent vortices in the direction of gravity (Ferrante and Elghobashi 2003). If one now considers the scenario whereby the falling two-way coupled particle suspensions are also electrostatically charged, what remains unknown is the effect that charge has on the behaviour of particle settling and associated two-way coupling.

The aim of this chapter therefore, is to examine what effect charge has on two-way coupling for particle suspensions within turbulence, in both non-gravity and gravity scenarios. This chapter also aims to answer the question, of whether or not one can use such knowledge to beneficial advantage in suitable multiphase engineering applications.

7.3 Objectives

The primary objective is to identify any unique differences in physical behaviour between one-way coupled, two-way coupled, uncharged and charged particle suspensions within turbulence without the presence of gravity. A detailed analysis of spectral turbulence and dispersed phase statistics should give insight to the range of scales for which two-way coupling interaction is modified between dispersed, fluid, and electrical continuum phases. Extension of the spectral analysis for a two-way coupled scenario that includes the presence of gravity will also give further insight into the practical behaviour of charge particle suspensions within realistic scenarios. Secondary objectives of this chapter are to examine real space and spectral RUM statistics associated with the particle phase in order to identify any inherent properties associated with a two-way coupled electrically charged particle suspension within turbulence.

7.4 Organisation

Section 7.5 presents a summary of previous research that has specifically examined electrically charged particle suspensions within isotropic turbulence. Section 7.6 presents details on how the electrically charged particle suspension are defined along with clarification on how to specify realistic dispersed phase conditions that don't violate any key assumptions. Section 6.6 then presents results from DNS investigations, and lastly section 7.8 presents a summary on key findings of this chapter.

7.5 Background

Very little research has specifically looked at the behaviour of charged particle suspensions in isotropic turbulence. The limited work published by researchers Alipchenkov et al. (2004) and Lu et al. (2010) provided some insight on the theoretical foundations to describe, via RDF based models, charged particle dispersion characteristics in isotropic turbulence. Typically, RDF based models are used to estimate the effects of particle clustering on collision frequencies, as they characterise the probability of finding particle

pairs for a given radial separation distance. Alipchenkov et al. (2004) developed foundations for one such model, specifically governing the formation of clusters for charged particle suspensions within an isotropic turbulent flow field. This model was derived by taking into consideration the balances between turbophoretic forces that describe the tendency of particles to migrate towards one another due to centrifugal interaction with turbulent eddies, diffusion forces that smooth the distribution of particles throughout the turbulence, Coulomb repulsion forces between pairwise particles, and the effective Coulomb force of interaction between all remaining particles throughout the suspension. Lu et al. (2010) extended this work, excluding interactions beyond pairwise particles, but instead providing a complete model for charged particle RDFs with experimentally fitted parameters. This complete model is described by,

$$g(r) = c_0 \left(\frac{\eta}{r}\right)^{c_1} \exp\left[-c_2 St_\eta \left(\frac{E_{charge}}{E_{turb}}\right)\left(\frac{\eta}{r}\right)^3\right] \tag{7.1}$$

where c_0 and c_1 are dimensionless fitting parameters. Here c_2 is taken either as a fitted parameter, or equal to $\frac{2}{3B_{n1}}$ where B_{n1} is the dimensionless co-efficient for turbulent diffusivity with the theoretical constant $B_{n1} = 0.0926$, (Chun et al. 2005). The Electrical-Kolmogorov energy ratio E_{charge}/E_{turb}, otherwise known as the Coulomb number, is a key parameter characterising the relative strength of electrical and turbulent fluid energy uniquely between two particles at Kolmogorov scale separation distances.

$$\frac{E_{charge}}{E_{turb}} = \frac{Q_p^2}{4\pi\epsilon_0 M_p \eta} \Big/ \left(\frac{\eta}{\tau_\eta}\right)^2 \tag{7.2}$$

DNS validation of the model developed by Lu et al. (2010) was achieved by Karnik (2010), who found reasonable agreement to results albeit with a slight increased over-prediction in probability for decreasing particle separation distances. This is most likely attributed to the unresolved sub-grid scale Coulomb repulsion forces between particles within the DNS. In addition to the work on validating RDFs, Karnik (2010) examined the effects of electrical charge on the phenomenon of preferential accumulation within one-way coupled turbulence, identifying that under certain conditions preferential accumulation can be suppressed. To characterise this behaviour, Karnik (2010) defined an

electrical settling velocity v_c, representing the terminal velocity attained by a particle due to the influence of a specified electric field.

$$v_c = \tau_p e_{rms} \frac{Q_p}{M_p} \tag{7.3}$$

Subsequently, a non-dimensional electrical settling velocity was defined as such,

$$v_c^* = \frac{v_c}{u_{rms}} \tag{7.4}$$

with u_{rms} representing the fluctuating fluid velocity of the turbulence. It should be noted that e_{rms} appearing in equation (7.3) represents the fluctuating electric potential within the domain, and is a quantity that can only be obtained from a DNS of turbulence that has included the presence of electrically charged particles. To ascertain indication to the likely behaviour of v_c^*, such as an increase or decrease in value from a known priori level, one may use basic turbulence measures of Kolmogorov length and time-scales, along with specified particle properties that include material density, diameter and particle charge, to compute the parameter E_{charge}/E_{turb} using equation (7.2).

Previous work by Karnik (2010) identified specific values for v_c^*, where for one-way coupled charged particle suspensions, electrical body forces on particles start to exceed body forces arising due to drag with the fluid. It remains unclear however, whether or not v_c^* characteristics extend to two-way coupled charged particle suspensions, since u_{rms} and subsequently e_{rms} is likely to change due to modification of the underlying turbulence. Nevertheless, one can hypothesise an alteration of fluid-to-particle and particle-to-fluid coupling dynamics, unique to the scales of turbulence and the ratio of electrical-to-drag body forces present within the suspension.

7.6 Dispersed Particle Phase Set-up

In this section, details of simulation parameters used for investigating two-way coupling in charged particle suspensions are provided.

As discussed in sections 2.3.1 and 2.3.4, modification of turbulence is observed most for a mono-dispersed $St_\eta = 1.0$ particle suspension at high mass loading ratios typically at $\phi_m \approx 1.0$. With the added physics associated with electrical charge on particles, these values should offer the greatest potential for establishing what effect on two-way coupling charged particle suspensions have, within an isotropic turbulent flow field. For this reason, a target Stokes number of unity was chosen for all particle suspensions examined in this study and all suspensions were defined with a mass loading ratio of $\phi_m = 1.0$.

It should also be stressed, that properties of the dispersed phase examined in this study were chosen to reflect conditions one would find within a hypothetical electrically charged particle suspension. Such suspension could exist if a liquid fuel spray was electrostatically injected internal within a combustion chamber. Based on the fact that droplets created via the electrostatic atomization process itself, are limited in practice to typically 80% of the Rayleigh limit defined by,

$$Q_{ray} = 4\pi\sqrt{0.5\sigma\epsilon_0 D^3} \tag{7.5}$$

particles within suspensions of this study are charged accordingly such that $Q_p = 0.8Q_{ray}$. Surface tension is taken as $\sigma = 0.028N/m$ to reflect a value typical of liquid fuel oil. However, it should be noted that one of the key objectives of this chapter is to investigate the difference exhibited in behaviour of two-way coupling, when the ratio of electrical to drag body forces within the charged particle suspension is either less than or greater than unity. Due to the difficulty in maintaining dispersed phase conditions suitable for the latter scenario, the material surface tension of particles was found to be the only free parameter available for change to maintain a fixed particle Stokes number

of unity. Surface tension for the latter scenario investigations was therefore taken as $\sigma = 0.303N/m$.

As discussed earlier in chapters 5.4.2 of this thesis, 10^7 computational particles were tracked to minimise statistical errors associated with the two-way coupling scheme and improve the quality of computed mesoscopic Eulerian particle phase statistics. In order to compute the total volumetric charge density within the domain, one may use the following equation,

$$Q_V = \frac{Q_p W_p N_c}{(2\pi)^3} \tag{7.6}$$

where W_p is a quantity computed using the procedure outlined in section 5.3.1. Parameter values subsequently defined for this chapter's DNS investigations are listed in table 7.1 for reference.

7.7 Results

In this section, results from the study focused on the two-way coupling of charged particle suspensions within isotropic turbulence are presented. Simulations have been performed both with and without incorporating the effects of gravity, with the latter scenario focused on the anisotropic change to two-way coupling contributions between the dispersed particle, fluid and electrical continuum phases present within the system.

7.7.1 Basic Turbulence and Dispersed Phase Statistics

Table 7.1 summarises basic turbulence statistics collected via DNS, comparing two-way coupled uncharged and charged particle suspensions to that of a one-way coupled turbulent flow. Comparing unloaded reference DNS statistics to those of case D) containing a two-way coupled uncharged particle suspension, there is a significant reduction seen for the turbulent kinetic energy and dissipation rate, in agreement with previous research of

Boivin et al. (1998), and corresponding validations presented in section 5.4.3. Comparing two-way coupled charged particle suspensions cases E) and F), with the uncharged suspension case D), increases in turbulent kinetic energy and intensity are observed with an increase in F_{elec}/F_{drag} ratio. This behaviour suggests that electrical body forces between particles are reducing local clustering within the suspension, thereby decreasing local mass loading ratios, and subsequently reducing the amount of energy extracted from the turbulence by particles.

For case E) where $F_{elec}/F_{drag} < 1$, the energy dissipation rate decreases temporarily whilst the turbulent kinetic energy continues to increase relative to the uncharged suspension. For case F) where $F_{elec}/F_{drag} > 1$, the dissipation rate remains comparable to the uncharged suspension yet the turbulent kinetic energy continues to increase further. Whilst the increase in turbulent kinetic energy is no enough to recover the levels of turbulent kinetic energy present in an unloaded suspension, the behaviour seen here highlights the potential benefit for having practical suspensions where $F_{elec}/F_{drag} > 1$. Essentially, if $F_{elec}/F_{drag} > 1$ for a given practical multiphase suspension, less input energy would be required at large scales to maintain levels of turbulent kinetic energy as high as possible for an identically yet uncharged suspension where energy dissipation rate levels of the underlying turbulence remain comparable in magnitude.

For dispersed particle phase statistics, the mean particle kinetic energies for one-way and two-way coupled suspensions without gravity appear to increase for increasing F_{elec}/F_{drag} ratio. This increase suggests that particles encounter more energetic scales of the turbulence when charged, compared to when uncharged. Therefore, particles receive more kinetic energy from the fluid at those scales which subsequently increases their velocities. This is confirmed by the mean relative velocity magnitude between fluid and particles, which decreases for increasing F_{elec}/F_{drag} ratio of the suspension, and occurs when particles are both one-way and two-way coupled to the turbulence. Both the increase in mean distance to closest particle, and Voronoi clustering dimension parameters for increasing F_{elec}/F_{drag} ratio, confirms that inter-particle spacing within the charged suspension increases compared to uncharged suspensions.

Particle Phase DNS Parameters			A	B	C	D	Dg	E	Eg	F	Fg
Coupling Type	-	-	One-way Coupling			Two-way Coupling					
Gravity Present	-	-	no	no	no	no	yes	no	yes	no	yes
Material Density	ρ_p	kg/m^3	735	735	735	735	735	735	735	735	735
Particle Diameter	D	mm	6.116	6.116	6.116	6.116	6.116	6.116	6.116	6.116	6.116
Statistical Weight per Computational Particle	W_p	-	-	-	-	0.282	0.282	0.282	0.282	0.282	0.282
Charge per Particle	Q_p	nC	0.0	1.693	5.576	0.0	0.0	1.693	1.693	5.576	5.576
Domain Charge Density	Q_V	$\mu C/m^3$	0.0	19.23	28.6	0.0	0.0	19.23	19.23	28.6	28.6
Turbulence Statistics			Reference DNS $\phi_m = 0$			D	Dg	E	Eg	F	Fg
Turbulent Kinetic Energy	k	m^2/s^2	6.69			2.18	2.16	2.21	2.14	2.27	2.23
Dissipation Rate	ϵ	m^2/s^3	6.1			1.98	1.90	1.86	1.68	1.99	1.80
Turbulence Intensity	$u' = (2k/3)^{1/2}$	m/s	2.11			1.20	1.20	1.21	1.19	1.23	1.22
Longitudinal Integral Length-scale	$l = \frac{3}{4k}\int_0^{\kappa_{\max}} \frac{E(\kappa)}{\kappa} d\kappa$	m	0.33			0.36	0.37	0.35	0.36	0.34	0.35
Eddy Turnover Time	$\tau_e = l/u'$	s	0.16			0.30	0.31	0.29	0.30	0.28	0.29
Turbulent Length-scale	$L_e = \frac{k^{3/2}}{\epsilon}$	m	2.84			1.63	1.67	1.77	1.86	1.72	1.85
Taylor Length-scale	$\lambda = \left(\frac{10\nu_f k}{\epsilon}\right)^{1/2}$	m	0.52			0.52	0.53	0.55	0.57	0.53	0.55
Kolmogorov Length-scale	$\eta = \left(\frac{\nu_f^3}{\epsilon}\right)^{1/4}$	m	0.04			0.053	0.054	0.054	0.055	0.053	0.054
Kolmogorov Time-scale	$\tau_\eta = \left(\frac{\nu_f}{\epsilon}\right)^{1/2}$	s	0.064			0.11	0.12	0.12	0.12	0.11	0.12
Taylor Reynolds Number	$Re_\lambda = \frac{u'\lambda}{\nu_f}$	-	44.24			25.25	25.58	26.47	27.02	26.26	27.18
Turbulence Reynolds Number	$Re_L = \frac{k^2}{\epsilon\nu_f}$	-	293.48			96.0	98.22	105.03	109.04	103.58	110.51
Dispersed Phase Statistics			A	B	C	D	Dg	E	Eg	F	Fg
Mean Particle Kinetic Energy	$\frac{1}{N_p}\sum_{i=1}^{N_p} \frac{1}{2} M_p^{(i)} V_i^2$	$kg\ m^2/s^2$ $(\times 10^{-3})$	0.324	0.353	0.795	0.100	0.115	0.126	0.140	0.294	0.317
Electrical To Drag Body-Force Ratio	F_{elec}/F_{drag}	-	-	0.47	0.72	-	-	0.85	0.28	1.22	0.37
Electrical To Gravitational Body-Force Ratio	F_{elec}/F_{grav}	-	-	-	-	-	-	-	0.30	-	0.40
Gravitational To Drag Body-Force Ratio	F_{grav}/F_{drag}	-	-	-	-	-	0.93	-	0.93	-	0.94
Coulomb Number	$\frac{E_{charge}}{E_{turb}} = \frac{Q_p^2}{4\pi\epsilon_0 M_p \eta} / \left(\frac{\eta}{\tau_\eta}\right)^2$	-	-	0.018	0.09	-	-	0.025	0.024	0.122	0.131
R.M.S Electric Field	e_{rms}	kgm/s^3A $(\times 10^5)$	-	3.52	3.60	-	-	1.93	1.84	1.77	1.70
Electrical Settling Velocity	$v_c^* = \frac{v_c}{u_{rms}}$	-	-	0.19	0.30	-	-	0.19	0.18	0.25	0.80
Electrical Length Scale	$x_E = \frac{q_p}{4\pi\epsilon_0 e_{rms}}$	m $(\times 10^{-5})$	-	4.33	13.92	-	-	7.90	8.27	28.34	29.53
Mean Relative Velocity Magnitude	$\lvert U_i - V_i \rvert$	m/s	0.75	0.724	0.671	0.224	0.623	0.215	0.617	0.201	0.597
Particle Settling Velocity	U_p/u_η	-	-	-	-	-	1.330	-	1.306	-	1.323
Settling Velocity Enhancement	$\Delta V_3/U_p$	-	-	-	-	-	0.054	-	0.011	-	-0.042
Mean Distance to Closest Particle	$\langle D_{sep} \rangle_{\mathscr{C}} / \bar{\eta}$	-	1.60	2.08	2.20	1.45	-	1.68	-	1.76	-
Voronoi Clustering Dimension	$\mathcal{V}_c^{3D}$	-	0.49	0.62	0.65	0.57	-	0.60	-	0.63	-
Voronoi Void Space Dimension	$\mathcal{V}_v^{3D}$	-	2.07	1.95	1.91	1.99	-	1.82	-	0.63	-

TABLE 7.1: Summary of turbulence and particle phase statistics for investigations on two-way coupling of charged particle suspensions. Particle phase parameters are set based on a target Stokes number of unity $St_\eta = 1.0$, for an unloaded turbulence simulation at a Taylor Reynolds number of $Re_\lambda = 44.24$. The $D/\eta_{(\phi_m=0.0)}$ ratios for cases A)-D) and E)-F), are 0.16 and 0.35 respectively. Case names post-fixed with a small letter 'g' denote the presence of gravity at $-9.81\ m/s^2$ acting on the suspension. For cases C), F) and Fg) the surface tension is taken as $\sigma = 0.303N/m$.

7.7.1.1 Effects of Gravity on Basic Turbulence and Dispersed Phase Statistics

With regards to the two-way coupled particle phase statistics and the effect of gravity on measured quantities, computed mean particle kinetic energies appear greater for suspensions Dg), Eg) and Fg) than equivalent suspensions that do not take into account gravity. Notably, the effect of gravity within charged particle suspensions leads to a decrease in F_{elec}/F_{drag} ratios. Whilst the electrical-to-gravitational body force F_{elec}/F_{grav} ratios increase when moving from case Eg) to Fg) due to increased charge on particles within the suspension, the ratio remains small compared to the ratio of gravitational-to-drag body forces present.

It may appear that gravity reduces some of the beneficial effects in two-way coupled suspensions associated with F_{elec}/F_{drag} ratios that exceed unity, however examining two-way coupled turbulence statistics for cases Dg), Eg) and Fg) shows that this is definitely not the case, since Taylor Reynolds numbers are larger than equivalent simulations that do not take into account effects of gravity. This occurs despite a slight reduction in both turbulent kinetic energy and energy dissipation rate, yet the increase observed for computed Taylor length scales indicates that the magnitude of reduction for dissipation rate is actually greater than the magnitude of turbulent kinetic energy reduction, hence the increase in Taylor and turbulent Reynolds numbers.

With regards to the settling velocity enhancements exhibited across suspensions Dg), Eg) and Fg), one can see that the settling velocity enhancement $\Delta V_3/U_p$ defined by equation (2.13), is negative for the larger charge density Fg) suspension than compared to positive settling velocity enhancements computed for uncharged Dg) and charged Eg) suspensions. This suggests that particles charged to a sufficiently high enough level can fall at a velocity slower than their Stokes settling velocity.

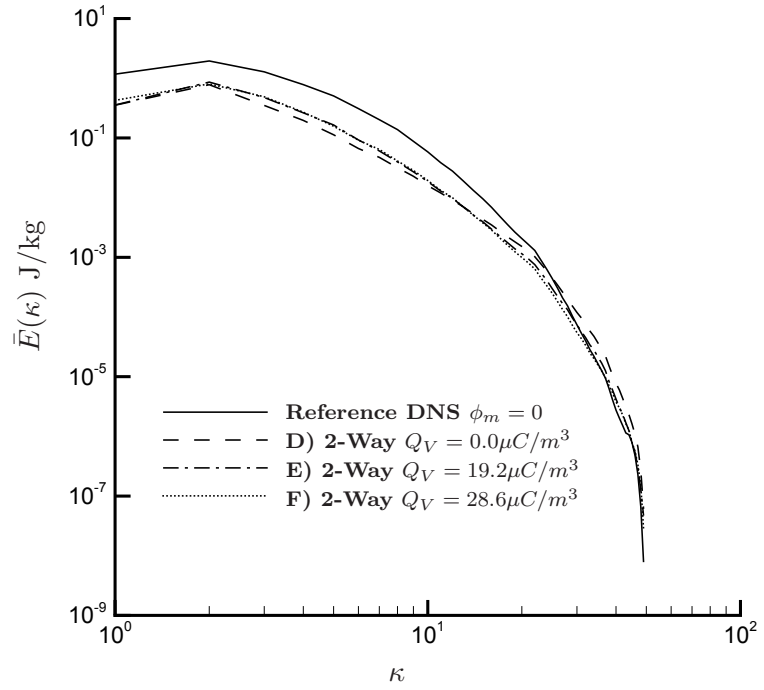

FIGURE 7.1: Figure comparing turbulent kinetic energy spectra defined by equation (4.15) for cases D)-F) of table 7.1.

7.7.2 Spectral Turbulence Statistics

7.7.2.1 Turbulent Kinetic Energy and Dissipation Rate Spectra

Comparing the kinetic energy spectra between uncharged one-way and two-way coupled cases A) and D) respectively, figure 7.1 shows that two-way coupling leads to a characteristic attenuation of large scale energy, and an augmentation of small scale energy in agreement with previous research (Elghobashi and Truesdell 1993; Boivin et al. 1998). Comparing the spectra between two-way coupled uncharged case D), and charged cases E) and F), charged particles appear to attenuate large scales of the turbulence less so than uncharged particles, relative to the turbulence spectra for one-way coupled cases. In addition, small scales of the turbulence appear to be less augmented for charged particle suspensions than for uncharged suspensions. Another way to interpret this behaviour, is that two-way coupled charged particle suspensions augment large scales of turbulence more so than two-way coupled uncharged suspensions, whilst small scale augmentation of energy is suppressed for charged particle suspensions. Dissipation rate

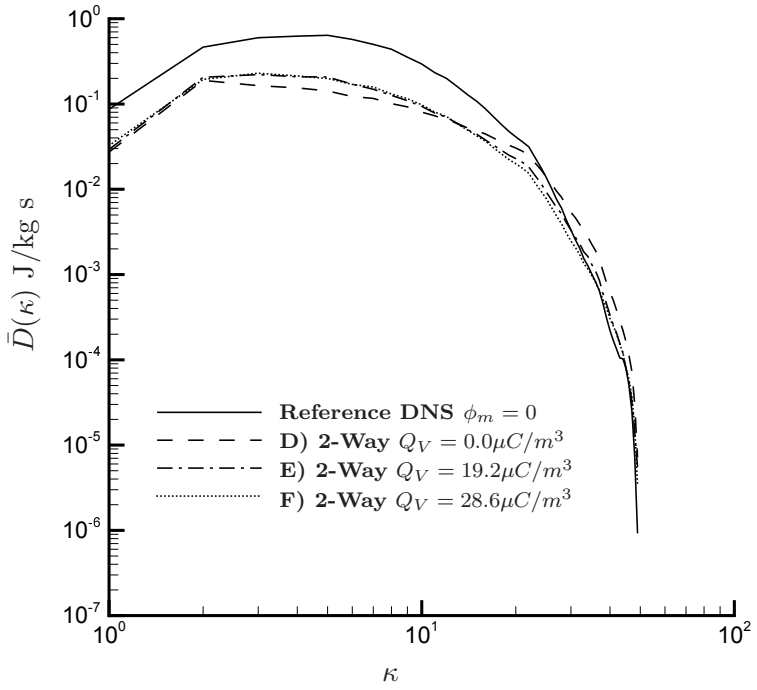

FIGURE 7.2: Figure comparing turbulent energy dissipation rate spectra defined by equation (4.17) for cases D)-F) of table 7.1

spectra is also shown in figure 7.2, and due to the direct relationship to turbulent kinetic energy spectra, similar qualitative observations between cases can be seen.

7.7.2.2 Transfer Spectra

With regards to the transfer spectra shown in figure 7.3, one can see that for charged two-way coupled suspensions E) and F), the energy transfer rate through scales of the turbulence is greater than for the uncharged D) suspension. This is most likely a consequence of the reduced attenuation of large scale turbulent kinetic energy from charged two-way coupled suspensions, discussed previously in section 7.7.2.1.

7.7.2.3 Fluid-to-Particle and Fluid-to-Electrical Energy Exchange Rate Spectra

Figure 7.4a shows that there is transfer of energy *from* the fluid *to* the particle phase via drag occurring at large scales. This energy exchange appears to be greater for the

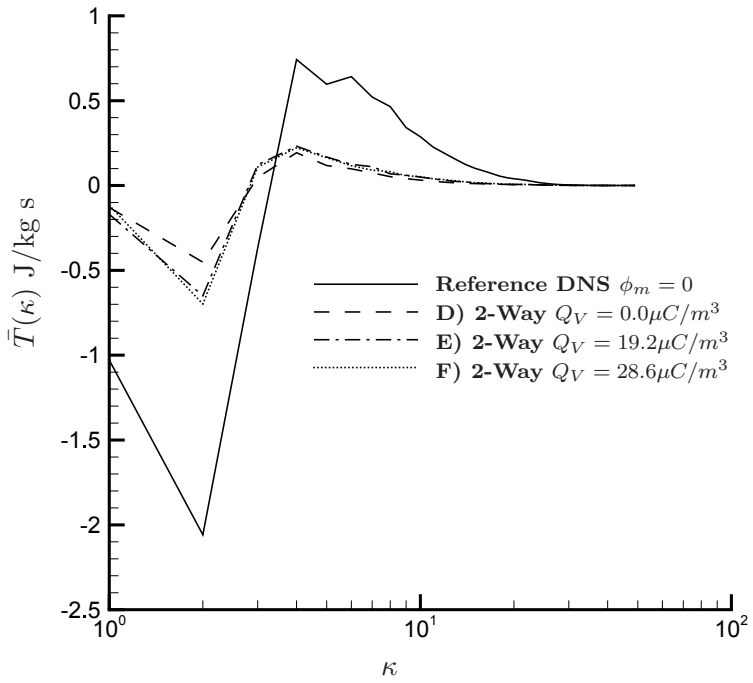

FIGURE 7.3: Figure comparing the energy transfer spectra defined by equation (4.16) for cases D)-F) of table 7.1.

uncharged particle suspension than it does for the charged suspension. Furthermore, it appears that the change from a negative to positive energy exchange rate back to the fluid, occurs earlier at higher wave-numbers for the charged particle suspension than it does for the uncharged suspension. As scales become smaller, the energy exchange rate back to the fluid becomes greater for the uncharged particle suspension than it does for the charged suspension. Nevertheless, it is apparent that the total energy exchange rate from and to the fluid at large and small scales respectively, is dominated by the energy exchange rate due to drag. Figure 7.4b shows that at large scales of the turbulence, the energy exchange rate *from* the fluid *to* the electrical phase is at most $\approx 7\%$ of the total energy exchange rate. Whereas at smaller scales, the energy exchange rate to the fluid from the electrical phase is at most $\approx 27\%$ of the total energy exchange rate. This suggests that charged particles have a greater influence on the fluid-to-electrical energy exchange rate when present at small scales of turbulent motion than when present at large scales.

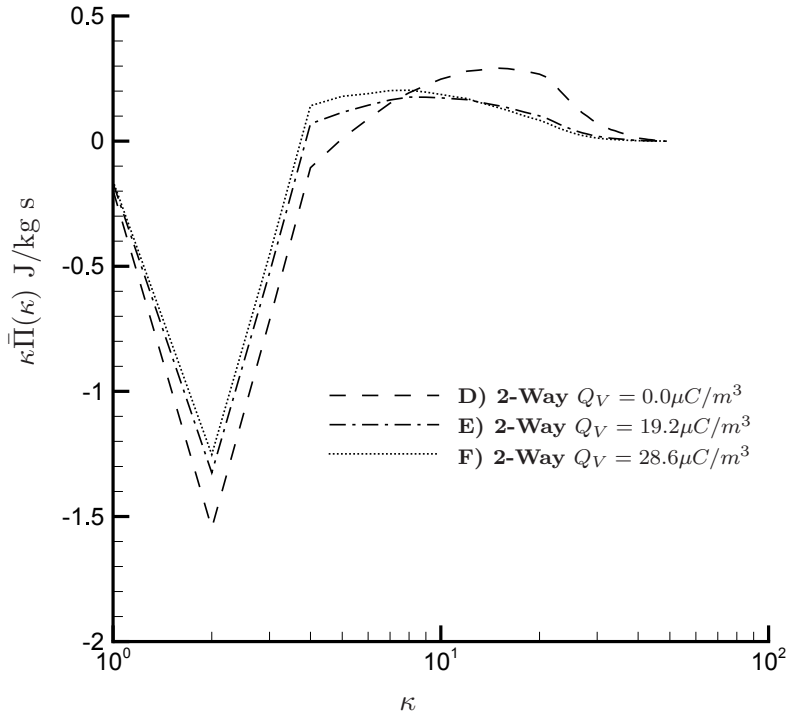

(a)

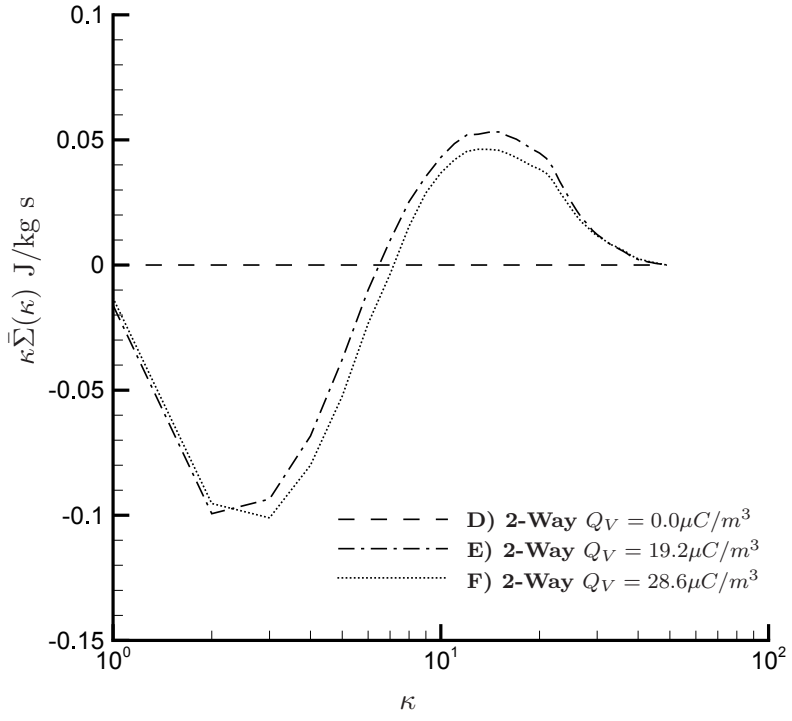

(b)

FIGURE 7.4: Spectrum of; a) fluid-to-particle energy exchange rate due to drag defined by equation (4.18), and b) fluid-to-electrical energy exchange rate defined by equation (4.19), for cases D)-F) of table 7.1.

7.7.3 Spectral Particle Phase Statistics

7.7.3.1 Particle Phase Mesoscopic Kinetic Energy Spectra

Figure 7.5 shows the spectral mesoscopic kinetic energy content for particle phase suspensions listed in table 7.1. The mesoscopic kinetic energy spectra characterises the energy of particles whilst they are present within different scales of turbulent motion. Examining this particular spectral quantity allows for much deeper insight into the behaviour of particles when suspended in turbulence. To this matter, the mesoscopic kinetic energy spectra for the one-way coupled uncharged particle suspension case A), shows that at large scales particles have much more kinetic energy than they do at small scales. This behaviour is to be expected since particles gain their momentum predominantly from the large inertial scale eddies of the turbulence. However, one can see from figure 7.5, that when the particle suspension becomes charged, the the large scale mesoscopic kinetic energy becomes augmented whilst at small scales the mesoscopic kinetic energy becomes attenuated. This behaviour is most pronounced for case C), where a greater F_{elec}/F_{drag} ratio is present. The same qualitative observations can be seen in the mesoscopic kinetic energy spectra between two-way coupled suspensions D), E) and F), with the only quantitative difference being the decrease in magnitude of spectrum for a given wave-number band.

7.7.3.2 RUM Kinetic Energy Spectra

In figure 7.6, the scale dependent RUM energy content of the particle phase suspensions listed in table 7.1 are compared. Qualitative observations are similar to those found within the mesoscopic energy spectra discussed previously in section 7.7.3.1. However, one can also see evidence of a slight 'bump' in the small scale RUM energy spectra, which appears to attenuate more as the particle suspension becomes increasingly charged.

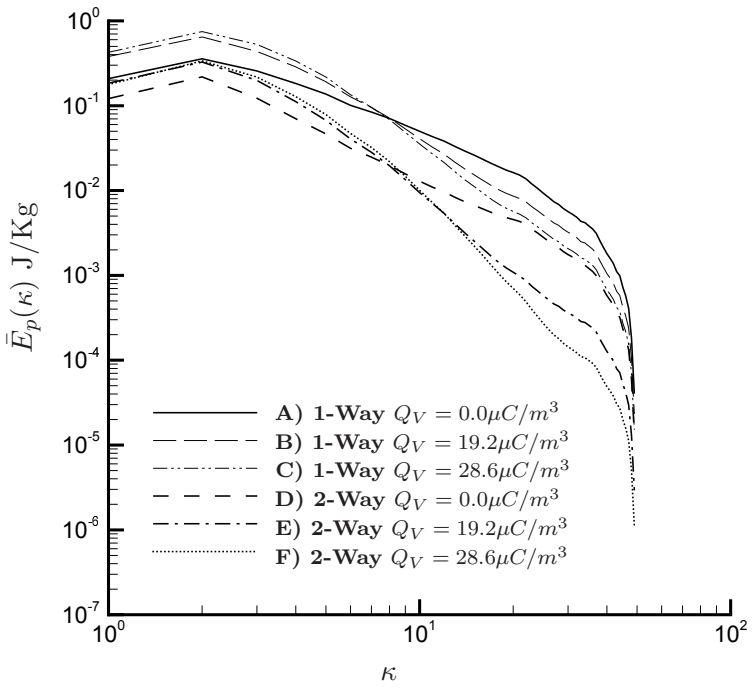

FIGURE 7.5: Figure comparing the mesoscopic particle phase kinetic energy spectra defined by equation (4.26) between cases A)-F) of table 7.1

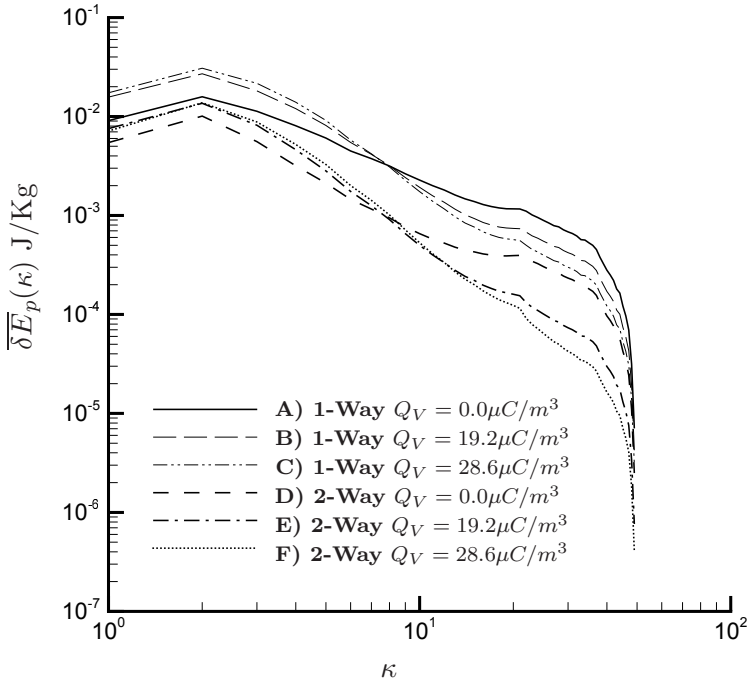

FIGURE 7.6: Figure comparing the RUM kinetic energy spectra defined by equation (4.31) between cases A)-F) of table 7.1

7.7.3.3 Particle-to-Fluid and Particle-to-Electrical Energy Exchange Rate Spectra

In figures 7.7a and 7.7b, the particle-to-fluid and particle-to-electrical energy exchange rate spectra is compared for two-way coupled cases D), E) and F).

For the particle-to-fluid energy exchange rate spectra shown in figure 7.7a, a positive transfer of energy to the particle phase from the fluid may be observed at large scales. The magnitude of this energy exchange remains roughly the same irrespective as to whether particles are charged or not. At $\kappa \approx 4$, the change to a negative particle-to-fluid energy exchange rate shows that energy is now moving from the particle phase back to the fluid, and between wave-numbers $4 < \kappa < 14$, charged particles transfer a greater amount energy back to the fluid than compared to uncharged particles. The opposite is true for wave-numbers $\kappa > 14$, where greater energy is transferred back to the fluid at smaller scales by uncharged particles than charged particles. This behaviour appears more pronounced for increasing F_{elec}/F_{drag} ratio of the suspension. Beyond, $\kappa > 20$, effects of viscous dissipation begin to take hold where a gradual diminishing of the energy exchange rate back to the fluid can be seen.

In figure 7.7b, a positive particle-to-electrical energy exchange rate occurs at large scales which shows energy is moving *from* the electrical continuum *to* the particle phase. This positive energy exchange rate corresponds to a positive correlation between the electric field and the particle velocity vectors, indicating that particles are predominantly pushed via the electrical body forces, into scales that are slightly smaller. At the onset of change between a positive and negative energy exchange rate occurring at $\kappa \approx 3$, there is a noticeable delay for case F) towards smaller scales of the turbulence, than compared to case E). This suggests a dependency on the F_{elec}/F_{drag} ratio for charged suspensions, regarding the ability of large scale eddies to push particles from regions of high electric potential to regions of low electric potential. Between wave-numbers $3 < \kappa < 26$, a negative particle-to-electrical energy exchange rate is observed, indicating that energy is now being supplied to the electrical continuum from the particles. This negative particle-to-electrical energy exchange rate shows a greater magnitude for case F), which

has a larger F_{elec}/F_{drag} ratio compared to case E). At wave-number $\kappa \approx 30$, there is also a surprising change from a negative to positive energy exchange rate, occurring earlier for case F) than for case E). This indicates that at small scales, there is a transfer of energy from the electrical continuum to the particle phase. This behaviour is most likely caused via the high frequency small scale eddies, attempting to sweep particles together to form clusters, whilst being prevented from doing so, by the subsequent increase in Coulomb repulsion forces generated between particles. In summary, analysis of figure 7.7b, shows that both large scale eddies and small scale eddies of turbulence, have the ability to induce dispersed phase motion within electrically charged particle suspensions.

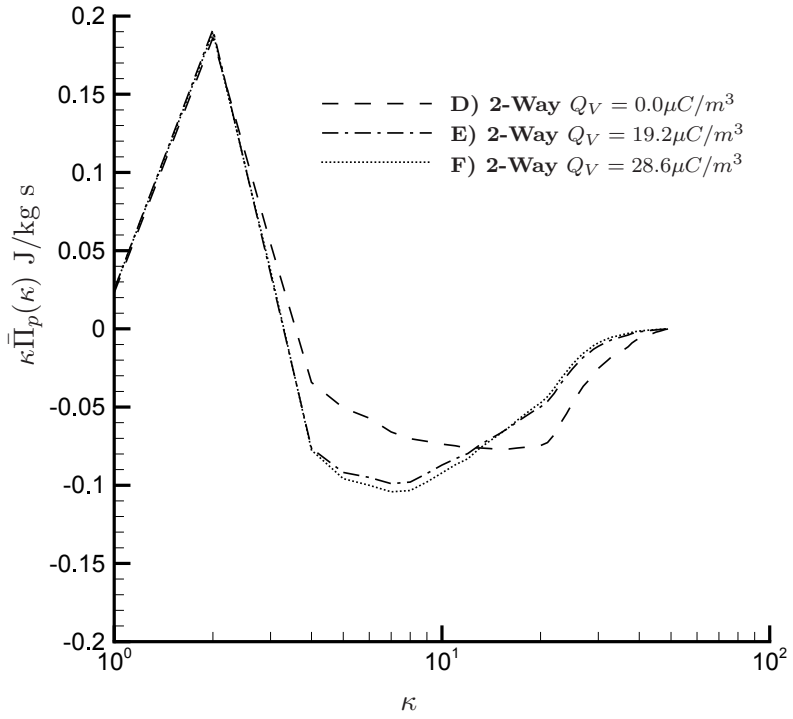

(a)

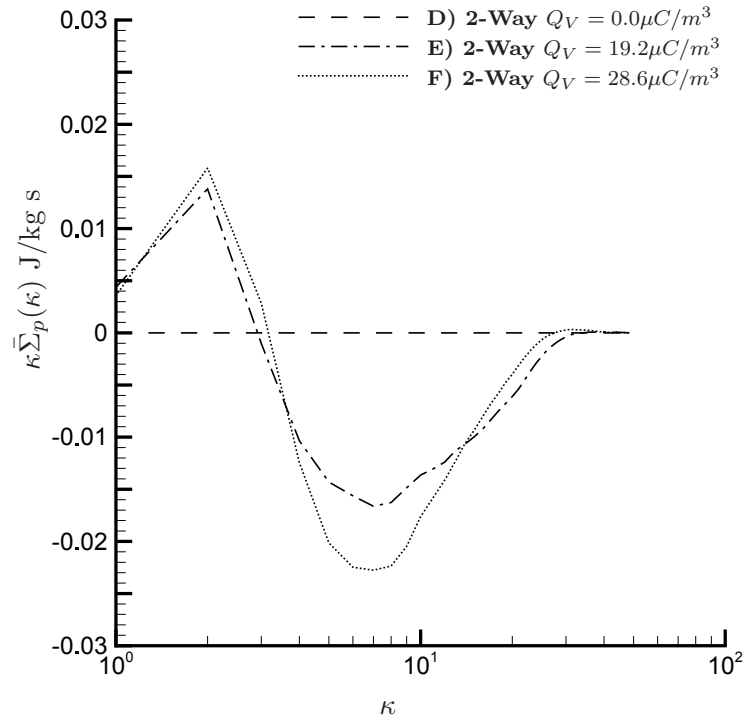

(b)

FIGURE 7.7: Spectrum of; a) particle-to-fluid energy exchange rate due to drag defined by equation (4.27), and b) particle-to-electrical energy exchange rate defined by equation (4.28), for cases D)-F) of table 7.1.

7.7.3.4 Particle-to-RUM Energy Exchange Rate Spectra

One may recall from section 4.4.1, that the spectral energy transport equation for the particle phase contains a particle-to-RUM energy exchange rate term that describes the rate of energy exchange between the mesoscopic particle velocity field, and the quasi-Brownian velocity distribution of the particle phase. The energy exchange rate spectra associated with this term is presented in figure 7.8. Firstly, the particle-to-RUM energy exchange rate spectrum for cases A)-C) shows a general positive transfer of energy from the mesoscopic particle phase to the RUM[1]. One can see that effect of charge on a one-way coupled turbulent suspension, augments the transfer of energy from the mesoscopic to RUM at large scales, and attenuates the transfer of energy from the mesoscopic to RUM at small scales. This effect is more pronounced the greater the F_{elec}/F_{drag} ratio of the suspension. The behaviour seen for two-way coupled cases D)-F) appears entirely different, with the positive transfer of energy from the mesoscopic to RUM being significantly smaller than what was observed for cases A)-C), and for a small band of wave-numbers within transfer scales, there exists a negative energy exchange rate indicating the transfer of energy from RUM to mesoscopic. This negative transfer of energy remains short lived, reverting back to a positive transfer that increases up to a maxima of $\kappa \approx 21$ for case D), and earlier at $\kappa \approx 15$ for cases E)-F) respectively. For smaller wave-numbers beyond this maxima, the positive energy exchange rate declines steadily up to the cut-off wave-number of the DNS.

[1]This does not exclude the possibility of transfer of energy from the RUM to mesoscopic, but more that it characterises only the dominant direction of energy transfer. It should also be noted that the kinetic energy spectra associated with one-way coupled cases A)-C) remains identical, without any effect of turbulence modification seen.

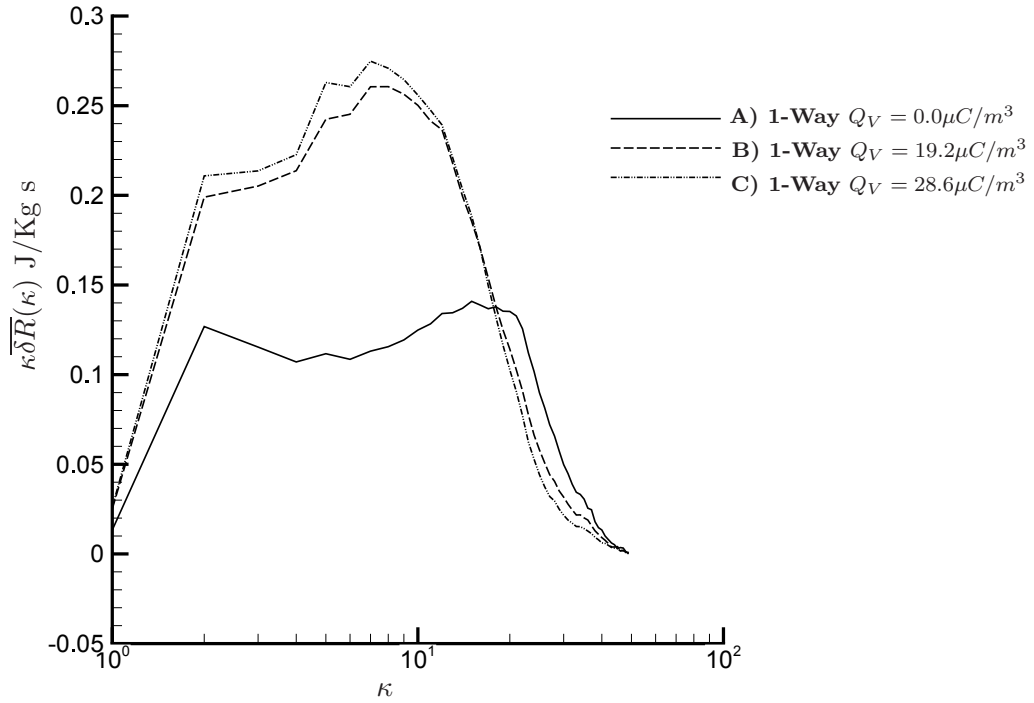

(a)

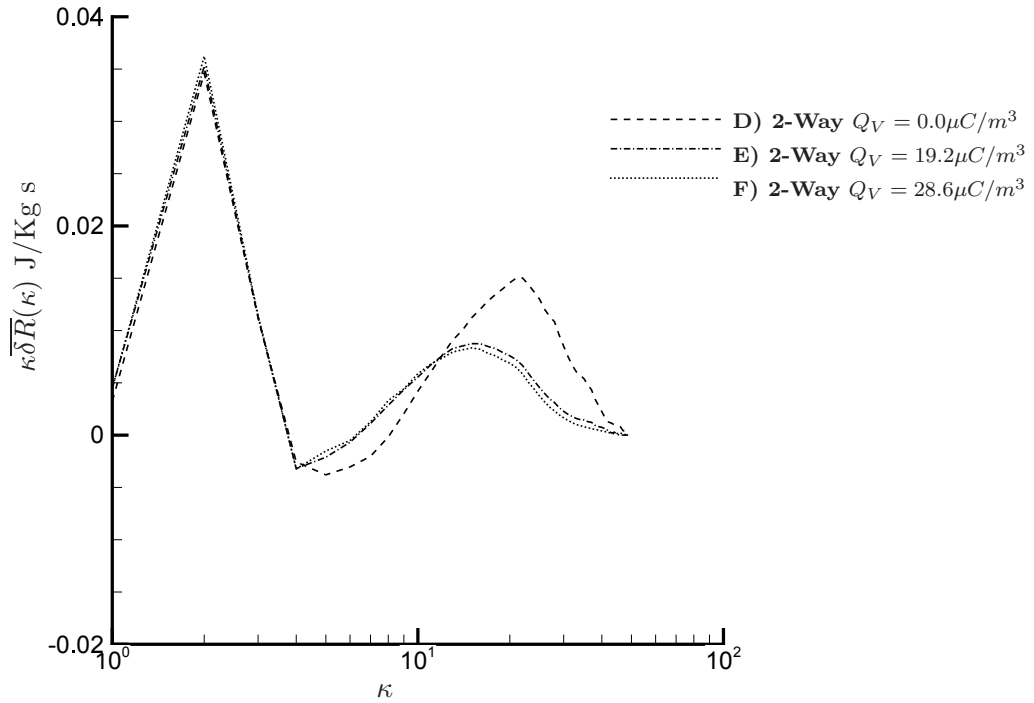

(b)

FIGURE 7.8: Spectrum of the particle-to-RUM energy exchange rate spectra defined by equation (4.29) for; a) One-way coupled cases A)-C), and b) Two-way coupled cases D)-F), of table 7.1. Negative values represent the transfer of energy from the RUM to mesoscopic field, whereas positive values represent the transfer of energy from the mesoscopic to RUM field.

Real-Space RUM Source PDF Statistics

Whilst the particle-to-RUM energy exchange rate spectra provides information about the scale dependent transfer of energy, it is also useful to examine PDFs of the quasi-Brownian kinetic energy source term, i.e. $-n_p \left\langle \delta\tilde{\sigma}_{p,ij} \frac{\partial \tilde{v}_i'}{\partial x_j} \right\rangle_{\mathscr{F}}$, which appears explicitly within the transport equation for mesoscopic kinetic energy given by 3.46, as well as the transport equation for mean RUM kinetic energy given by 3.47.

In figure 7.9, computed PDFs for the quasi-Brownian kinetic energy source term of cases A)-F) listed in table 7.1, are centred at approximately zero, with a slight positive skewness towards the left. This means that local energy exchanges between the MEPVF and RUM occur in both directions, with a predominant transfer of energy occurring from the MEPVF to the RUM as indicated by the large probability in positive values for quasi-Brownian kinetic energy source, compared to smaller probability for negative values. For both one-way and two-way coupled charged particle suspensions, PDF tails of the quasi-Brownian kinetic energy source term, decreases with larger F_{elec}/F_{drag} ratio of the suspension.

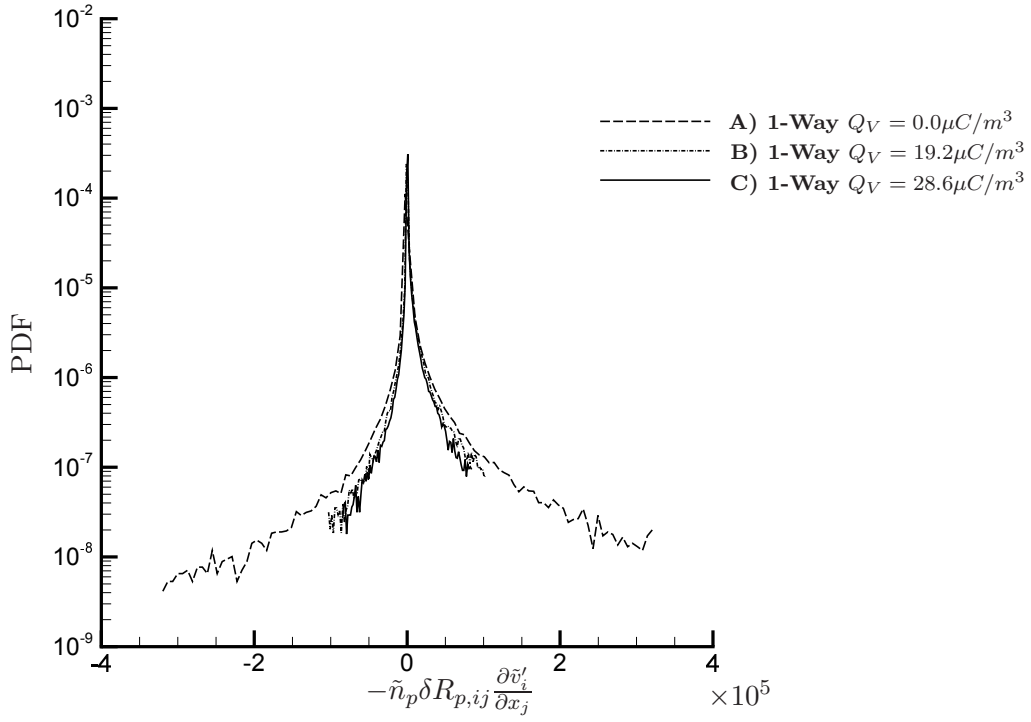

(a)

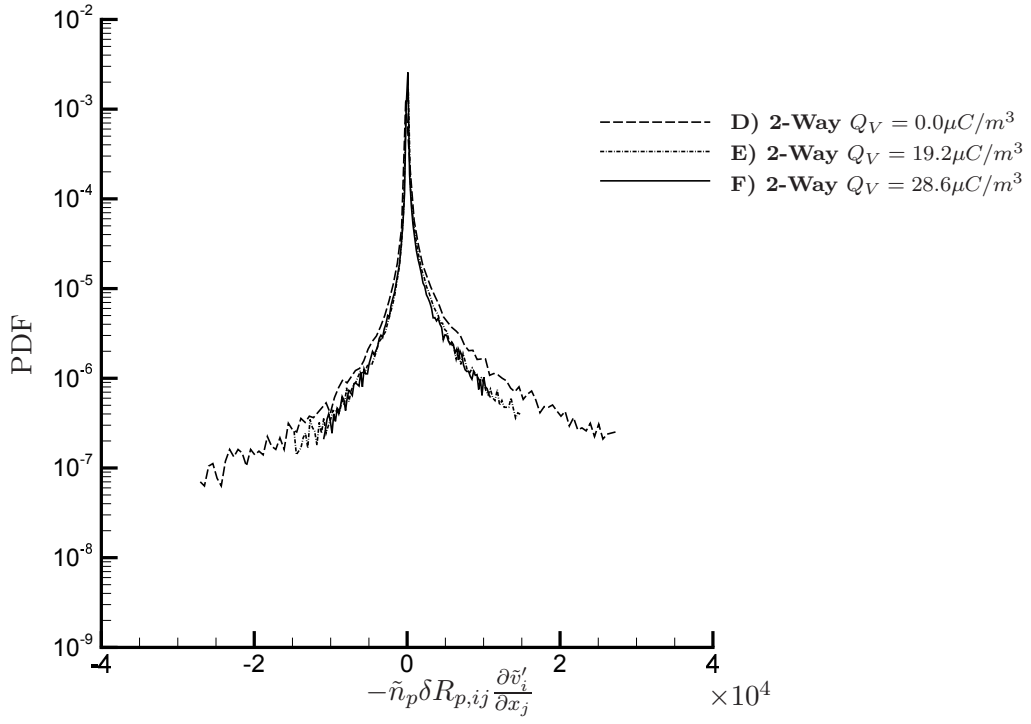

(b)

FIGURE 7.9: PDFs of the quasi-Brownian kinetic energy source term defined in equations (3.46) and (3.47) for; a) One-way coupled cases A)-C), and b) Two-way coupled cases D)-F), of table 7.1. Negative values represent the transfer of energy from the RUM to mesoscopic field, whereas positive values represent the transfer of energy from the mesoscopic to RUM field.

7.7.4 Electrical Energy Spectra

Figure 7.10 presents the electrical energy spectra for the charged particle phases case E) and F). The electrical energy spectra is observed to be greatest at large scales and smallest at dissipative scales of the turbulent motion. One can see that the shape of the electrical energy spectra reflects to some extent the shape of the turbulent kinetic energy spectra. Subtle differences can be seen between cases E) and F), where at the largest scales of turbulent motion for wave-numbers $\kappa < 4$, the electrical energy for case F) is slightly less than the electrical energy for case E). For wave-numbers $\kappa > 4$ the energy content for case F) is marginally greater than case E).

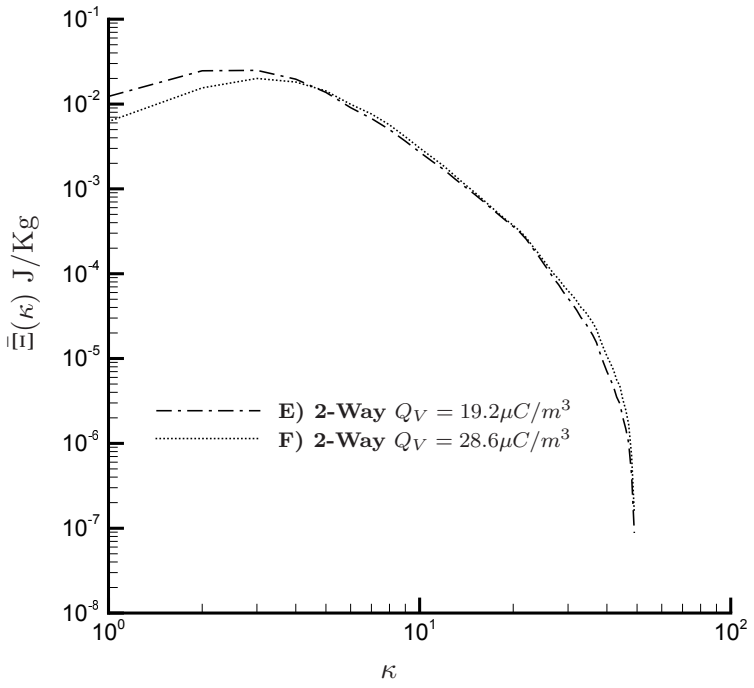

FIGURE 7.10: Figure comparing the electrical energy spectra defined by equation (4.36), between cases E)-F) of table 7.1

7.7.5 Preferential Concentration Statistics

In figure 7.11, D measure profiles are shown for cases A)-F) listed in table 7.1. As discussed in section 5.3.3.2, the D measure helps to characterise the non-homogeneous distribution of particles within a suspension, relative to a random distribution of particles. Comparing the one-way coupled uncharged case A) suspension, with the uncharged two-way coupled case D) suspension, one can see that the effect of two-way coupling, reduces the preferential concentration behaviour exhibited by the suspension. This is most likely due to the Kolmogorov time-scale of the fluid increasing slightly in the presence of the two-way coupled suspension, which subsequently reduces the effective particle Stokes number of the suspension. This results in slightly less preferential accumulation occurring compared to one-way coupled suspensions, as indicated by smaller magnitudes for D measure profiles across two-way coupled suspensions D)-F). With regards to the effects of particle charge on D measure profiles, greater F_{elec}/F_{drag} ratio of the suspension leads to a reduction in D measure magnitudes. This occurs for both one-way, and two-way coupled charged particle suspensions. The only difference regarding D measures between one-way and two-way coupled suspensions, is the fact that for one-way coupled suspensions A)-C), profiles all show a single distinctive peak at small $h/\bar{\eta}$, whereas only the uncharged two-way coupled suspension exhibits such a peak. Two-way coupled charged particle suspensions instead show an extended plateau-like D measure profile, suggesting similarity to that of a random particle distribution,i.e. a more homogeneous distribution, as indicated by the uniquely zero and flat D measure profile.

In figure 7.12, 3D RDF profiles are presented for cases A)-F) listed in table 7.1. The uncharged two-way coupled particle suspension case D), exhibits a large probability of finding particle pairs at separation distances of $\approx 10\bar{\eta}$. This appears to increase with further reduction in separation distances. For charged particle suspensions, RDF profiles for cases E) and F) both remain below that of case D), showing that the probability of finding particle pairs at smaller separation distances, diminishes for charged particle suspensions due to the increase in Coulomb repulsion forces. Similar qualitative observations can be seen for the one-way coupled particle suspensions A)-C). One would expect that the presence of charge would introduce a length scale below which inertial clustering

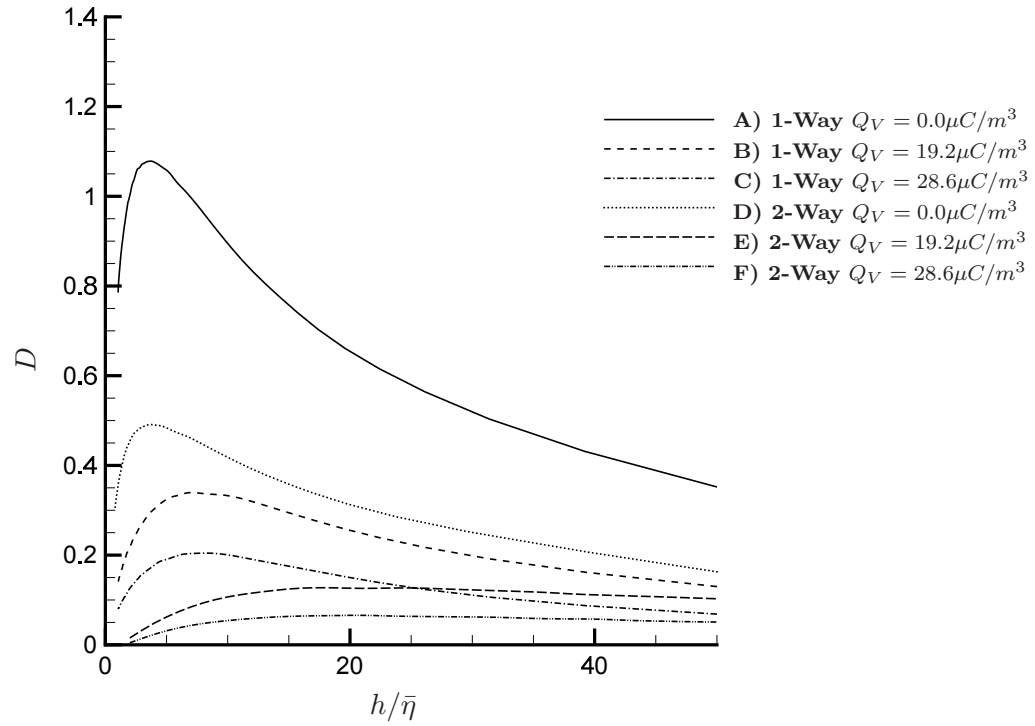

FIGURE 7.11: Dependence of D measure on non-dimensional bin-size, $h/\bar{\eta}$, for cases A)-F) of table 7.1.

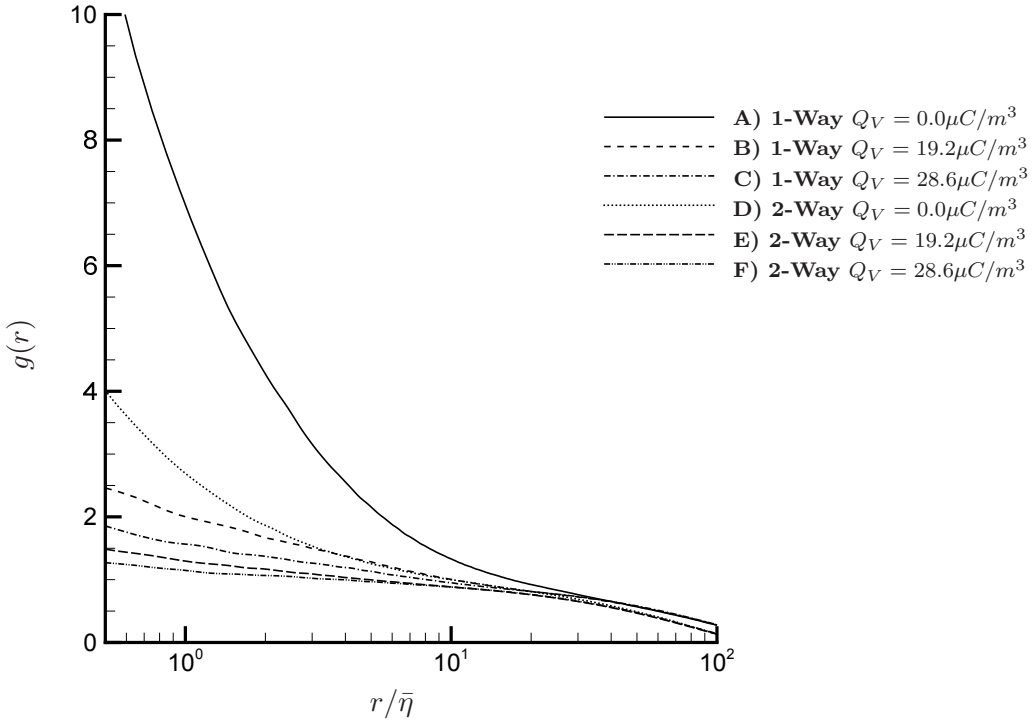

FIGURE 7.12: 3D radial distribution functions for cases A)-F) of table 7.1.

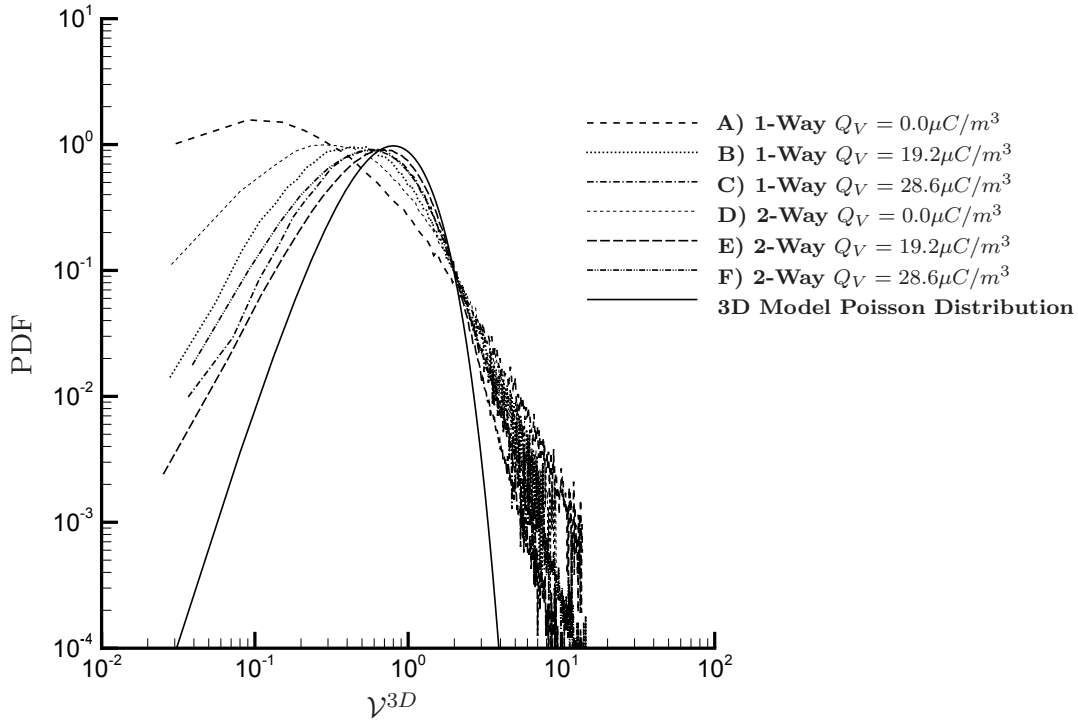

FIGURE 7.13: Normalised Voronoi Volume PDFs for cases D-F of table 7.1. The model corresponds to that of a 3D random Poisson distribution given by the function, $f_{3D}(x) = \frac{3125}{24}x^4 \exp^{-5x}$, (Ferenc and Néda 2007).

is suppressed in accordance with Lu et al. (2010), thereby leading to a diminishing probability of finding particle pairs for small separation distances. However, findings from Lu et al. (2010) were based on analysis of suspensions where $E_{charge}/E_{turb} = 2$, whereas for all charged suspensions examined in this study from table 7.1, the E_{charge}/E_{turb} ratio defined by equation 7.2 remains $\ll 1$, . Nevertheless, from this ratio one can deduce that at Kolmogorov scales there is still enough turbulent energy to try and attempt to force particles close to one another, which from earlier discussion in section 7.7.3.3, is why positive particle-to-electrical energy exchange rate is seen at small scales.

In figure 7.13 the normalised Voronoi volume PDFs are presented for suspensions A)-F) of table 7.1. The Voronoi PDF for two-way coupled suspension D) deviates significantly from the model PDF of a random 3D Poisson distribution. For the two-way charged particle suspension E), the PDF appears to compresses inwards from the tail extremes, resembling closer the form of a random 3D Poisson distribution. As one would expect, this compression effect is most pronounced for charged suspension F) with the greatest

F_{elec}/F_{drag} ratio. Similar qualitative observations can bee seen across one-way coupled suspension A)-C).

7.7.6 Effects of Gravity on the Two-Way Coupling Energy Exchange between Dispersed, Fluid and Electrical Continuum Phases

In this section, focus extends to examine the behaviour of gravity on the directional energy exchange rates, between two-way coupled particle suspensions, turbulence, and the electrical continuum phases.

In figures 7.14a and 7.14b, the directional fluid-to-particle and fluid-to-electrical energy exchange rates respectively are shown. For the uncharged case Dg) suspension, in the x_2 direction normal to gravity, there is a characteristic transfer of energy from the fluid to the particle phase at large scales of turbulent motion, and a transfer of energy back to the fluid at smaller scales of motion for wave-numbers $\kappa > 5$. However, in the x_3 direction parallel to gravity, only a narrow range of large scales actually transfer energy to the particle phase. In fact, a significant proportion of the energy exchange rate parallel to gravity experiences a positive energy exchange rate from the particle phase to the fluid. This shows that particles within the suspension are acting to pull the fluid downwards due to dominant effects of drag.

With regards to the effects of particle charge on the directional fluid-to-particle energy exchange rate spectra, it appears that for increasing suspension charge densities, the magnitude of the energy exchange rate from the particle phase back to the fluid occurring at intermediate transfer scales decreases in the direction parallel to gravity. However, in the direction normal to gravity, increasing the suspension charge density yields spectra with a greater magnitude of positive energy exchange rate back to the fluid. At smaller wave-numbers beyond $\kappa \approx 10$, very little discernible impact between charged suspensions can be seen, yet the magnitude of the energy exchange back to the fluid from the particle phase is significantly attenuated compared to what is observed for the uncharged case Dg) suspension.

With regards to the fluid-to-electrical energy exchange rate spectra shown in figure 7.14b, a negative transfer of energy from the fluid to the electrical phase occurs at large scales of turbulent motion. The effect of increasing suspension charge density leads to a greater magnitude of energy exchange rate, and similarly greater magnitudes attained for the x_3 direction parallel to gravity compared to the x_2 direction normal to gravity. For intermediate transfer scales of turbulent motion, it appears that in the parallel direction to gravity, a greater magnitude of energy back to the fluid from the electrical continuum occurs for the smaller charge density case Eg) suspension. This is most likely due to its increased clustering tendency relative to the larger charge density case Fg) suspension.

Figure 7.15a illustrates the directional particle-to-fluid energy exchange rate spectra, showing that for the uncharged case Dg) suspension in the x_3 parallel direction to gravity, a significant amount of energy is lost from the particle phase back to the fluid, across most inertial and transfer scales of the turbulence. However, for wave-numbers beyond $\kappa \approx 13$, it appears that particles gain some energy from the fluid in the parallel direction to gravity, as indicated by a slight positive particle-to-fluid energy exchange rate. For charged cases Eg) and Fg) suspensions, this positive energy exchange rate disappears completely, and is neither present within the directional spectra normal to gravity for the uncharged case Dg) suspension. Between wave-numbers $4 < \kappa < 10$, the directional spectra's parallel to gravity for charged suspensions appear to have greater magnitudes in negative energy exchange rate compared to the directional x_2 spectra's normal to gravity. This shows that particles transfer more energy to the fluid in directions parallel to gravity than compared to directions normal to gravity. However, it is noticeable that case Eg), which has the smallest charge density present within the suspension, transfers more energy back to the fluid in the parallel direction to gravity than compared to the larger charge density Fg) suspension. Again this is most likely due to charged particles disrupting their own settling behaviour by residing in different scales of the turbulent non-resonant with their own characteristic time-scales, and falling at a speed slower than their Stokes settling velocity. This corroborates the earlier findings made in section 7.7.1.1, whereby the settling velocity enhancement for the larger charge density Fg) suspension, was negative compared to positive settling velocity enhancements for uncharged Dg), and charged Eg) suspensions. For wave-numbers beyond $\kappa \approx 10$, little

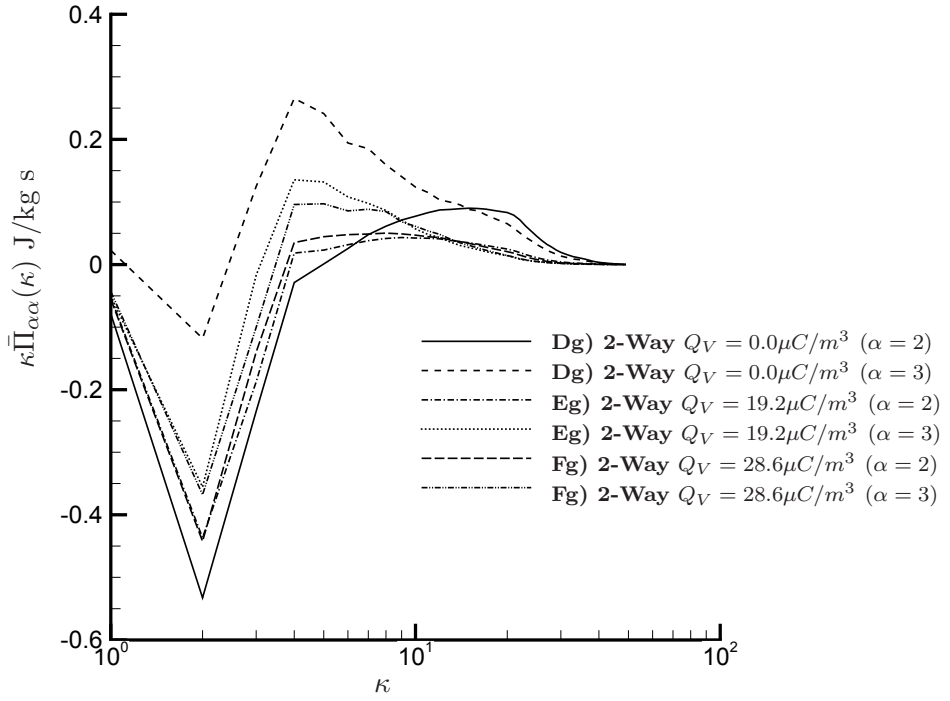

(a)

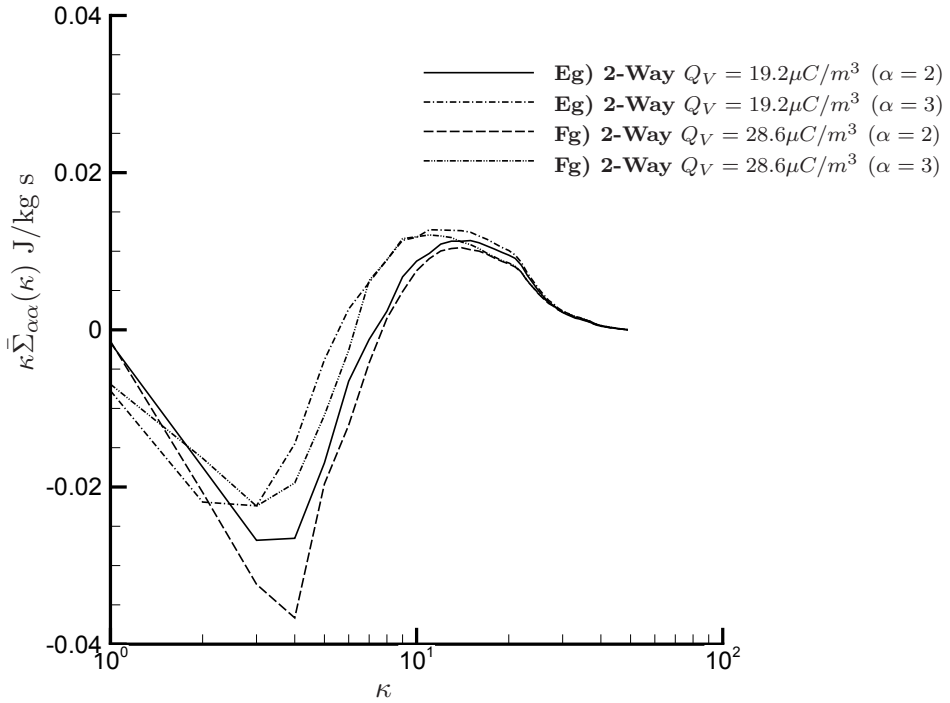

(b)

FIGURE 7.14: Spectrum of; a) fluid-to-particle energy exchange rate due to drag, and b) fluid-to-electrical energy exchange rate.

difference in energy exchange rate can be seen between charged suspensions. However it appears that directional spectra's normal to gravity for case Eg) and Fg) suspensions, slightly exceed the negative transfer of energy back to the fluid compared to x_3 directional spectra's parallel to gravity. This suggests that for a certain range of turbulence scales, charged particles transfer the same proportion of kinetic energy back to fluid in parallel and normal directions to gravity.

Figure 7.15b shows the directional particle-to-electrical energy exchange rate spectra for charged suspensions Eg) and Fg). At large scales of the turbulence, particles tend to receive energy from the electrical continuum. At intermediate transfer scales of the turbulence, particles tend to give back energy to the electrical continuum, more so for the larger charge density case Fg) suspension, and also more so in the x_3 direction parallel to gravity compared to the x_2 direction normal to gravity. At small scales, around a wave-number $\kappa \approx 11$, a positive energy exchange rate from the electrical continuum to the particle phase can be seen. This appears to be more prominent for the larger charge density case Fg) suspension than case Eg), yet more in the x_2 direction normal to gravity compared to the x_3 direction parallel to gravity. These observations suggest a strong interplay between the directional characteristics of particle phase dynamics and the two-way coupling interactions within the electrical continuum at certain scales of turbulent motion.

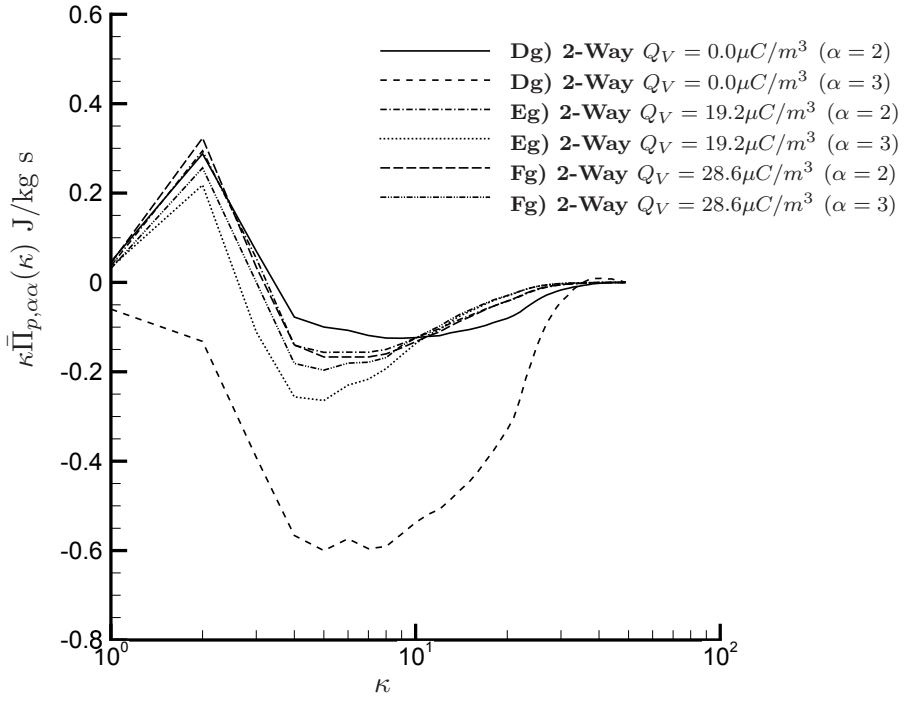

(a)

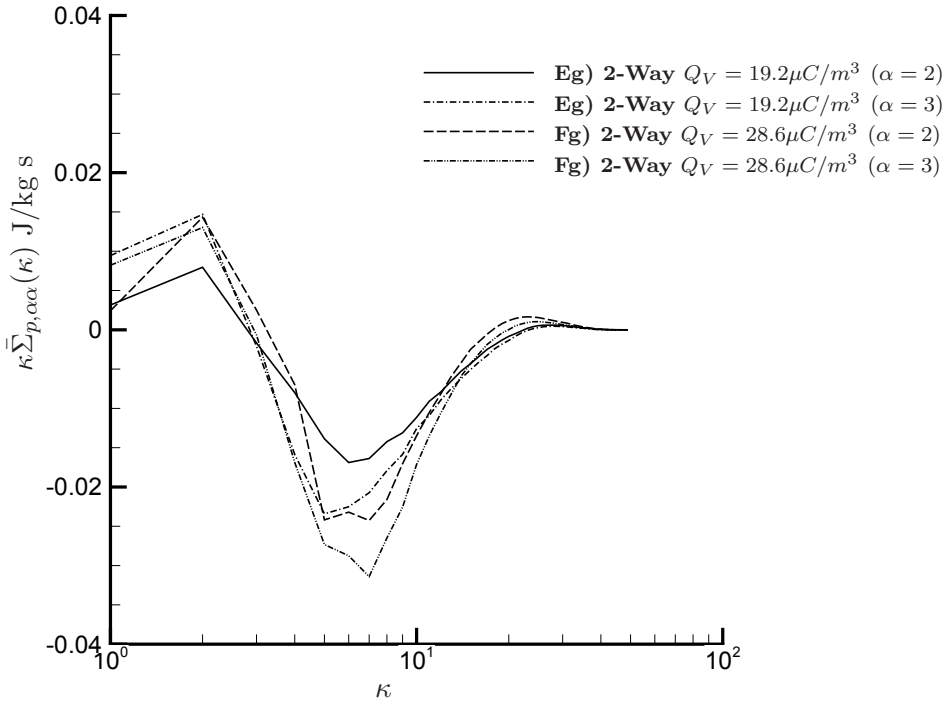

(b)

FIGURE 7.15: Spectrum of; a) particle-to-fluid energy exchange rate due to drag, and b) particle-to-electrical energy exchange rate.

7.8 Summary

- Investigations showed that the ratio of particle kinetic energy to turbulent kinetic energy, increased as the level of charge density increased within the suspension. It was also found that the relative velocity magnitude between particles and the fluid decreased as suspensions became charged, occurring despite an increase in turbulent kinetic energy. This suggests particles increase their velocities, most likely due to the combined effect of electrical body forces pushing particle into regions of faster moving fluid compared to low vorticity high strain rate regions, and the induced motion from fluctuations in the electric field due to the collective motion of particles within the suspension.

- The mean distance to closest particle was found to increase with increasing F_{elec}/F_{drag} ratio of the suspension, coinciding with increased spatial homogeneity of particles indicated by D measures, RDF measures, as well as Voronoi clustering measures. The Voronoi clustering dimension was found to increase whilst the Voronoi void space dimension decreased, for increasing F_{elec}/F_{drag} ratio of the suspension. This highlighted the fact that charged particles reside more in turbulence scales that are non-resonant with their own characteristic time-scales.

- Settling velocity statistics for the charged suspension with the greatest charge density, showed negative values compared to the lesser charged and uncharged particle suspension. This shows that particles if sufficiently charged, can fall at a rate slower than their own Stokes settling velocities. It is likely that the decrease in settling velocity enhancement is a direct result of particles having to work their way *through* turbulent vortices, rather than *past* them as would typically be the case for uncharged particle suspensions.

- The presence of electrical charge on particles within a two-way coupled mono-dispersed suspension, was found to attenuate levels of turbulent kinetic energy relative to kinetic energy of a one-way coupled turbulent flow, less so than an

uncharged particle suspension. Furthermore, the augmentation of small scale turbulence two-way coupled charged particle suspensions was not as much as the augmentation observed for the uncharged particle suspension.

- At low wave-number transfer scales of the turbulence, charged particle suspensions were found to have greater energy exchange rate back to the fluid than compared to the uncharged particle suspension. On the other-hand for high wave-number transfer scales of the turbulence, the positive exchange of energy from particles back to the fluid was greater for the uncharged particle suspension than for charged suspensions.

- The exchange of energy between the fluid and electrical continuum was found to be negative at large scales of turbulent motion indicating a transfer of energy from the fluid to electrical continuum, and positive at small scales of turbulent motion corresponding to a transfer of energy from the electrical continuum back to the fluid.

- Considering the exchange of energy between the charged particle suspension and the electrical continuum, investigations showed an increase in positive energy exchange for increasing F_{elec}/F_{drag} ratio. At intermediate scales of turbulence, the energy exchange was found to be negative showing that particles supply energy to the electrical continuum at those scales. At the smallest scales of turbulence, a small positive contribution to particle kinetic energy was visible, indicating that charged particles at certain small scales of turbulence have a slight tendency to follow the direction of local electric field vectors, thereby receiving energy from the electrical continuum at those scales.

- PDFs of local quasi-Brownian kinetic energy sources within the turbulence, were found to be suppressed in variance more so for charged suspensions than uncharged suspensions. The level of variance suppression was found to increase slightly for increasing F_{elec}/F_{drag} ratio of the suspension. Furthermore, spectral analysis of the quasi-Brownian kinetic energy source term, identified a distinctive change in behaviour observed between one-way and two-way coupled suspensions.

- Investigations found that the mesoscopic kinetic energy spectra for charged particle suspensions exhibited augmentation at large scales, and attenuation at small scales compared to mesoscopic kinetic energy spectra for uncharged particle suspensions. Surprisingly, this behaviour is similar to the behaviour observed when polymer concentrations are added to the fluid, and augmentation of large scale turbulent energy is observed along with attenuation of small scale energy Robert (2010). Analogous to the concept of drag reduction by polymers and the increased efficiency of turbulent fluid transportation, addition of electrical charge to particle suspensions within turbulent flows promotes dispersed phase transportation.

- With regards to the behaviour of two-way coupled uncharged and charged particle suspensions settling under the presence of gravity, the component energy exchange rate from the particle phase back to the fluid shows similar behavioural trends to that of suspensions without gravity, with the exception being a slight increase in magnitude of energy exchange occurring in the direction parallel to the gravity vector and a slight decrease in magnitude of energy exchange occurring in directions perpendicular to the gravity vector respectively.

Chapter 8

Validating a Droplet Charge-Diameter Distribution Model

8.1 Overview

Thus far in this thesis, research has concentrated on the fundamental interactions of poly-dispersed and charged point-particles, two-way coupled with an idealised turbulent flow. This necessitates both geometrical and Reynolds number constraints which preclude predictions relevant to typical engineering applications. In the remainder of this thesis, focus shifts towards the practical simulation of electro-statically atomized dielectric liquid sprays.

Therefore, the aim in this chapter is to validate a droplet charge-diameter (Q-D) distribution model suitable for generating reliable charged spray predictions.

8.2 Objectives

The primary objective for this chapter is to make use of recently available experimental data concerning the droplet charge-diameter JPDF, to define the accuracy in which

charged plumes of electrically insulating liquids such as hydrocarbon fuels may be predicted. Once this is achieved, the validated model can be applied to the scenario of a charged high pressure spray system that involves further consideration of secondary atomization.

8.3 Organisation

Section 8.4 discusses the governing equations for the Eulerian phase including details of turbulence model employed and details on computing the electric field across the domain. Brief details are also presented covering governing equations for the discrete particle phase. Section 8.5 presents the numerical implementation of these governing equations and discusses the general properties and features of the finite volume method used for subsequent simulations. Lastly, section 8.6 presents the completed study on the validation of droplet diameter-charge distributions in electrostatically atomized dielectric liquid sprays

8.4 Governing Equations

8.4.1 Eulerian Phase

The CFD code uses a 2D axisymmetric cylindrical co-ordinate system, where z and r denotes the axial and radial co-ordinates, along with u and v denoting the axial and radial velocities respectively. Due to the relatively high gas velocity at the atomizer orifice, the Eulerian phase can be modelled using the unsteady Reynolds-averaged Navier-Stokes (RANS) equations. To derive the unsteady RANS equations, instantaneous flow variables such as velocity u, are decomposed into mean U and fluctuating u' components. Inserting decomposed variables into instantaneous momentum equations and time averaging across terms to separate out mean flow components, a set of Reynolds-averaged conservation equations for mass and momentum are thus derived.

These unsteady 2D RANS equations, for an incompressible flow using an axi-symmetric cylindrical co-ordinate system are as follows;

Continuity equation

$$\frac{\partial U}{\partial z} + \frac{1}{r}\frac{\partial}{\partial r}(rV) = S_{m,d} \tag{8.1}$$

z-Momentum

$$\rho_f\left(\frac{\partial U}{\partial t} + \frac{\partial}{\partial z}(UU) + \frac{1}{r}\frac{\partial}{\partial r}(rVU)\right) = -\frac{\partial P}{\partial z} + \frac{1}{r}\frac{\partial}{\partial r}\left(r\mu_f\left(\frac{\partial U}{\partial r} + \frac{\partial V}{\partial z}\right) - r\rho_f\overline{u'v'}\right) + \frac{\partial}{\partial z}\left(2\mu_f\frac{\partial U}{\partial z} - \rho_f\overline{u'u'}\right) + S_{u,d} \tag{8.2}$$

r-Momentum

$$\rho_f\left(\frac{\partial V}{\partial t} + \frac{\partial}{\partial z}(VU) + \frac{1}{r}\frac{\partial}{\partial r}(rVV)\right) = -\frac{\partial P}{\partial r} + \frac{1}{r}\frac{\partial}{\partial r}\left(2r\mu_f\frac{\partial V}{\partial r} - r\rho_f\overline{v'v'}\right) + \frac{\partial}{\partial z}\left(\mu_f\left(\frac{\partial U}{\partial r} + \frac{\partial V}{\partial z}\right) - \rho_f\overline{u'v'}\right) - 2\mu_f\frac{V}{r^2} + S_{v,d} \tag{8.3}$$

To compute all mean flow properties of the flow under consideration, there needs to be a prescription for computing the Reynolds stresses $\overline{u'u'}$, $\overline{v'v'}$ and $\overline{u'v'}$ such that the mean flow equations become closed. Closure of the RANS equations can be achieved through use of the κ-ε model of Launder and Spalding (1972). This model follows from the Boussinesq hypothesis, that each of the Reynolds stresses can be linked to the corresponding mean rate of strain by the turbulent eddy viscosity μ_t. These Reynolds stresses are listed as follows.

$$-\rho_f\overline{u'u'} = 2\mu_t\frac{\partial U}{\partial z} - \frac{2}{3}\rho_f k \tag{8.4}$$

$$-\rho_f\overline{v'v'} = 2\mu_t\frac{\partial V}{\partial r} - \frac{2}{3}\rho_f k \tag{8.5}$$

$$-\rho_f\overline{u'v'} = \mu_t\left(\frac{\partial V}{\partial z} + \frac{\partial U}{\partial r}\right) \tag{8.6}$$

Substituting the equations (8.4)-(8.6) into the RANS equations yields for the axial momentum,

$$\rho_f\left(\frac{\partial U}{\partial t} + \frac{\partial(UU)}{\partial z} + \frac{1}{r}\frac{\partial(rVU)}{\partial r}\right) = -\frac{\partial P}{\partial z} + \frac{1}{r}\frac{\partial}{\partial r}\left(r(\mu_f+\mu_t)\left(\frac{\partial U}{\partial r} + \frac{\partial V}{\partial z}\right)\right) + \frac{\partial}{\partial z}\left(2(\mu_f+\mu_t)\frac{\partial U}{\partial z} - \frac{2}{3}\rho_f k\right) + S_{u,d} \tag{8.7}$$

and for the radial momentum,

$$\rho_f\left(\frac{\partial V}{\partial t} + \frac{\partial(UV)}{\partial z} + \frac{1}{r}\frac{\partial(rVV)}{\partial r}\right) = -\frac{\partial P}{\partial r} + \frac{1}{r}\frac{\partial}{\partial r}\left(2r(\mu_f+\mu_t)\frac{\partial V}{\partial r} - \frac{2}{3}\rho_f k\right) + \frac{\partial}{\partial z}\left((\mu_f+\mu_t)\left(\frac{\partial V}{\partial z} + \frac{\partial U}{\partial r}\right)\right) - 2(\mu_f+\mu_t)\frac{V}{r^2} + S_{v,d} \tag{8.8}$$

Equations for the turbulent kinetic energy k and the energy dissipation rate ε may then be written as follows,

k-Equation

$$\rho_f\left(\frac{\partial k}{\partial t} + \frac{\partial(Uk)}{\partial z} + \frac{1}{r}\frac{\partial(rVk)}{\partial r}\right) = \frac{\partial}{\partial z}\left((\mu_f + \frac{\mu_t}{\sigma_k})\frac{\partial k}{\partial z}\right) + \frac{1}{r}\frac{\partial}{\partial r}\left(r(\mu_f + \frac{\mu_t}{\sigma_k})\frac{\partial k}{\partial r}\right) + P_k - \rho_f\varepsilon + S_{k,d} \tag{8.9}$$

ε-Equation

$$\rho_f\left(\frac{\partial\varepsilon}{\partial t}+\frac{\partial(U\varepsilon)}{\partial z}+\frac{1}{r}\frac{\partial(rV\varepsilon)}{\partial r}\right)=\frac{\partial}{\partial z}\left((\mu_f+\frac{\mu_t}{\sigma_\varepsilon})\frac{\partial\varepsilon}{\partial z}\right)+\frac{1}{r}\frac{\partial}{\partial r}\left(r(\mu_f+\frac{\mu_t}{\sigma_\varepsilon})\frac{\partial\varepsilon}{\partial r}\right)$$
$$+c_{\varepsilon1}\frac{\varepsilon}{k}P_k-c_{\varepsilon2}\rho_f\frac{\varepsilon^2}{k}+S_{\varepsilon,d} \quad (8.10)$$

The production rate P_k, which appears in equations (8.9) and (8.10) may be given by,

$$P_k=\mu_t\left(\left(\frac{\partial U}{\partial r}+\frac{\partial V}{\partial z}\right)^2+2\left(\frac{\partial U}{\partial z}\right)^2+2\left(\frac{\partial V}{\partial r}\right)^2+2\left(\frac{V}{r}\right)^2\right) \quad (8.11)$$

Model constants are then, $\sigma_\varepsilon = 1.22$, $\sigma_k = 1.0$, $c_{\varepsilon1} = 1.44$, $c_{\varepsilon2} = 1.92$ where $\mu_t = c_\mu\rho_f k^2/\varepsilon$ with $c_\mu = 0.09$, (Launder and Spalding 1972).

Since the CFD code models the charged spray, knowledge of the electric field throughout the domain is required. This is determined from the Eulerian based calculation of the voltage distribution Φ according to,

$$E_z=-\frac{\partial\Phi}{\partial z}, E_r=-\frac{\partial\Phi}{\partial r} \quad (8.12)$$

Subsequently the Poisson equation defining the voltage distribution throughout the domain has the form of,

$$\frac{1}{r}\frac{\partial}{\partial r}\left(r\frac{\partial\Phi}{\partial r}\right)+\frac{\partial^2\Phi}{\partial z^2}=-\frac{Q_V}{\epsilon_0} \quad (8.13)$$

where ϵ_0 is the permittivity of free space. The RHS of (8.13) is the interphase source term arising from the particle charge. Particle charge is held on Lagrangian droplets and is mapped onto the Eulerian grid by summing the charge present within in each computational cell. Here it assumed that the total droplet charge in each cell is uniformly distributed throughout the cell volume. This avoids the expensive requirement to calculate the $O(N_d^2)$ electrical body forces between each and every other spray droplet

within the domain. The volumetric charge density Q_V, is found by dividing the total charge in the computational cell by its volume.

8.4.2 Discrete Phase

The method used to model the spray is the Discrete Droplet Model (DDM) of Watkins (1989) and the presence of liquid droplets within the Eulerian cell volume is accounted for using a void fraction variable following the procedure of Amsden et al. (1985). Spray is modelled using a Lagrangian assumption so for each computational parcel of droplets, the motion can be described in an axi-symmetric cylindrical manner to equations (3.19) and (3.20) introduced earlier in section 3.3.

Taking the axial droplet momentum as an example,

$$\frac{\mathrm{d}Z_d}{\mathrm{d}t} = U_d \tag{8.14}$$

$$\frac{\mathrm{d}U_d}{\mathrm{d}t} = \frac{1}{\tau_d}(u(Z_d, R_d) + U_d) + \frac{Q_d}{m_d}E_z(Z_d, R_d) + g \tag{8.15}$$

Here U_d represents the droplet velocity, m_d the droplet mass and τ_d the characteristic droplet timescale in the same fashion to equation (3.21). The second term on the RHS of (8.15) represents the forces due to the electric field interpolated to the droplets location. To account for the influence of gas-phase turbulence on the movement of droplets, the instantaneous Eulerian phase velocity seen by the droplet $u(Z_d, R_d)$, consists of a mean U and fluctuating u' component, randomly sampled from a Gaussian distribution of the turbulent kinetic energy described by Gosman and Ioannides (1981). Specific to the CFD code used for investigations presented in this chapter, the drag correction factor appearing in (3.21) is defined using the empirical correlation of Putnam (1961).

$$f_D = 1 + \frac{Re_d^{2/3}}{6} \tag{8.16}$$

This correlation is valid in the region $Re_d \leq 800$ where Re_d is defined as the droplet Reynolds number as according to equation (3.23).

8.4.2.1 Discrete Phase Source Terms

The source term $S_{m,d}$ that appears on the RHS of (8.1) represents inter-phase mass transfer, however since evaporation from liquid droplets is not considered in this thesis, this source term is neglected such that $S_{m,d} = 0$.

Momentum is coupled between liquid droplets and the gas phase via source terms $S_{u,d}$ and $S_{v,d}$ that appear on the RHS of equations (8.7) and (8.8) respectively. Taking the axial momentum coupling as an example we have,

$$S_{u,d} = -\frac{m_d}{\Delta t_f}\left(\frac{\sum_k N_{d,k}[U_{d,k}^{n+1} - U_{d,k}^{n}]}{\Delta V_{cell}}\right) \tag{8.17}$$

Here, equation (8.17) represents the net change in axial momentum, imparted to the gas phase from k droplets that reside within a given control volume ΔV_{cell}, for a given time-period Δt_f, with initial and final axial velocities denoted by superscripts n and $n+1$.

Since closure of the momentum transport equations requires second order equations for turbulent kinetic energy k, and its rate of dissipation ε, one must also consider the phenomenon of two-way coupling and its impact on gas phase turbulence quantities. Following derivation of the turbulent kinetic energy transport equation, the unclosed discrete phase source term is thus given by,

$$S_{k,d} = \overline{uS_{u,d}} - U\overline{S_{u,d}} + \overline{vS_{v,d}} - V\overline{S_{v,d}} \tag{8.18}$$

First and third terms on the RHS of equation (8.18) represent unclosed correlations between the instantaneous gas velocities, and the net change in droplet momentum coupling for axial and radial directions respectively. For both these terms, one may account for the instantaneous gas phase velocity $u(Z_d, R_d)$ seen by the droplet using the

eddy interaction model of Gosman and Ioannides (1981). Taking the first term as an example we have,

$$\overline{uS_{u,d}} = -\frac{m_d}{\Delta t_f \Delta V_{cell}} \sum_k N_{d,k}[(u(Z_d, R_d)U_{d,k})^{n+1} - (u(Z_d, R_d)U_{d,k})^n] \tag{8.19}$$

Subsequently, second and fourth terms on the RHS of equation (8.18) can instead be computed directly from solutions to the mean axial and radial momentum transport equations.

The final source term that requires closure is the discrete phase source for turbulent kinetic energy dissipation rate defined by,

$$S_{\varepsilon,d} = 2\mu_f \left[\overline{\frac{\partial u'}{\partial r} \frac{\partial S'_{u,d}}{\partial r}} + \overline{\frac{\partial v'}{\partial r} \frac{\partial S'_{v,d}}{\partial r}} \right] \tag{8.20}$$

where terms on the RHS of equation (8.20) represent contributions to kinetic energy dissipation rate from inter-phase momentum transport, (Shuen 1983). For closure of equation (8.20) in a manner consistent with conventional k-ε turbulence models (Lain and Sommerfeld 2003), the discrete phase source term for energy dissipation rate is assumed to vary proportionally with $S_{k,d}$ such that,

$$S_{\varepsilon,d} = c_{\varepsilon 3} \frac{\varepsilon}{k} S_{k,d} \tag{8.21}$$

with the model constant taken as a typical value of $c_{\varepsilon 3} = 1.87$, (Shuen 1983; Shuen et al. 1985; Fan et al. 1997; Chrigui 2005). Lain and Sommerfeld (2003) discusses the implications of such closure, stating that the constant $c_{\varepsilon 3}$ is not universal, but depends instead most likely on the particle concentration and diameter. Furthermore, Lain and Sommerfeld (2003) noted that negative values for $c_{\varepsilon 3}$ are necessary to represent the effect of particles whereby they act as a source of energy dissipation rate.

Nevertheless, in context of charged spray experiments examined throughout subsequent chapters of this thesis, the effect of modelling source terms $S_{k,d}$ and $S_{\varepsilon,d}$ near the atomizer nozzle exit orifice, and within the downstream spray core region must be evaluated.

Near the atomizer nozzle exit orifice, the magnitude of source terms from discrete phase droplets are typically small compared to the levels of turbulent kinetic energy production induced via momentum shear between the injected bulk liquid velocity of the jet and the surrounding gas. If one now considers the spray region further downstream axial and radially from the atomizer nozzle exit orifice, due to increasing spray droplet dispersal, the volume fraction ratio within the spray subsequently decreases. Based on these facts, source terms $S_{k,d}$ and $S_{\varepsilon,d}$ are neglected from analysis in subsequent chapters.

8.5 Numerical Method

8.5.1 Eulerian Phase

The CFD code used to simulate the charged spray was originally developed as part of theoretical, computational and experimental studies on mechanisms governing electrostatic atomization of hydrocarbon oils, (Shrimpton 1995). The code solves equations for the Eulerian gas phase and electric field using a finite volume method, with an upwind/central differencing hybrid scheme on a back-staggered orthogonal cylindrical mesh (Versteeg and Malalasekera 1995). For a staggered mesh, scalar variables such as pressure, temperature and density are evaluated at nodal points, represented at cell centres, and considered uniform throughout the control volume. The non-iterative pressure implicit splitting of operator (PISO) scheme of Issa (1986) is used to solve the coupled pressure and momentum fields in the domain, with the pressure reference location taken to be at the furthest grid cell away from the strongest changes in velocity. An iterative scheme is used at each time-step for solution of the Poission voltage field throughout the domain. Control volumes used for the velocity and electric field components are different to those used for scalar variables, with details illustrated in Figure 8.1. Neighbouring control volumes are designated N, S, E and W and values at cell boundaries are represented by n, s, e and w respectively.

Time was discretised using a first order fully implicit scheme, with the time-step calculated automatically prior to each time advancement according to,

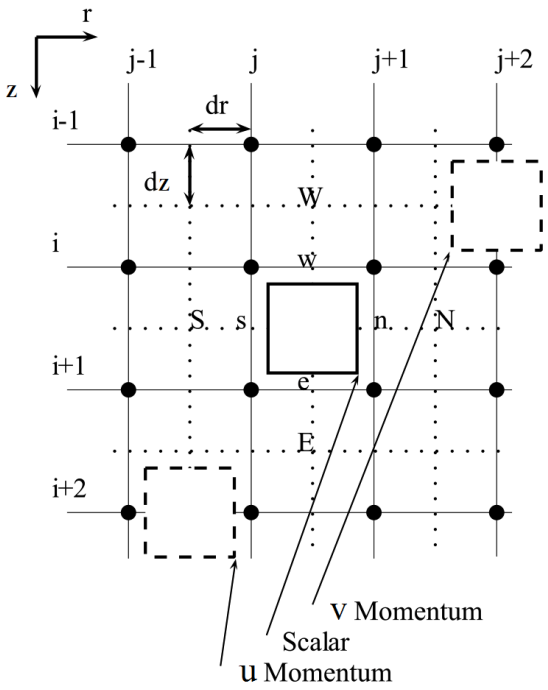

FIGURE 8.1: Control Volume Nomenclature

$$\Delta t_f = C_1 \times min(\frac{\Delta z}{U}, \frac{\Delta r}{V}, \frac{\Delta z}{U_d}, \frac{\Delta r}{V_d}) \tag{8.22}$$

where Δz and Δr are the control volume dimensions in the axial and radial directions respectively. The minimization operation is applied over all control volumes and drops for each time-step. The constant $C_1 = 0.1$, is the assumed fraction of the Courant cell condition.

8.5.2 Discrete Phase

8.5.2.1 Time Integration of Particles

The discrete phase time-step for each droplet parcel Δt_d is defined as an integer fraction of $\Delta t_f / \tau_d$. The number of integrations required for equation (8.15) is therefore,

$$N_{\Delta t_d} = INT\left(\frac{\Delta t_f}{\tau_d}\right) \tag{8.23}$$

This ensures that droplet trajectories are correctly resolved using the time discretization scheme.

8.5.2.2 Interpolation of Variables to Particle Locations

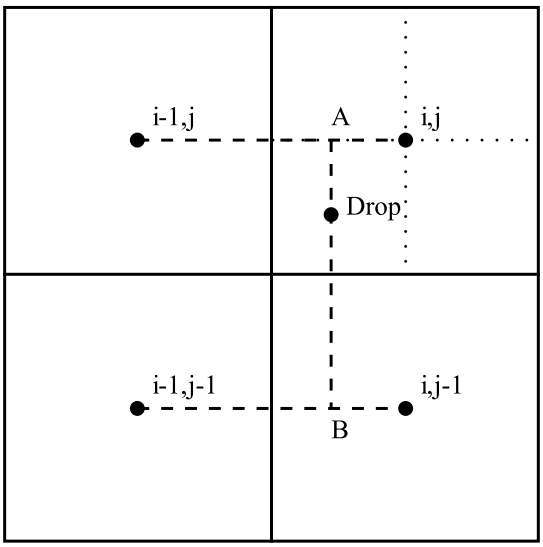

FIGURE 8.2: Interpolation Diagram and Nomenclature

Interpolation of cell variables follows a linear approach and figure 8.2 provides a diagram illustrating how variables such as the fluid velocity are mapped to particle locations. Here, the scalar variable φ is defined, and momentum variables are analogous. Firstly, the quadrant of the control volume for which the particle resides within is identified. The closest four control volume node points are then used for the interpolation. Secondly, the scalar values at perpendicular intersections A and B are calculated according to,

$$\varphi_A = \varphi_{i-1,j} + (\varphi_{i,j} - \varphi_{i-1,j}) \frac{z_{drop} - z^{(c)}_{i-1,j}}{dz_{i,j} + dz_{i,j}} \tag{8.24}$$

$$\varphi_B = \varphi_{i-1,j-1} + (\varphi_{i,j-1} - \varphi_{i-1,j-1}) \frac{z_{drop} - z^{(c)}_{i-1,j}}{dz_{i,j} + dz_{i,j}} \tag{8.25}$$

Here $dz_{i,j}$ and $dr_{i,j}$ represent the axial and radial cell dimensions for a cell with indexes i, j. Lastly, using the scalar values calculated at the intersections A and B, the scalar value at the particle location is then calculated using,

$$\varphi_{drop} = \varphi_B + (\varphi_A - \varphi_B)\frac{r_{drop} - r^{(c)}_{i,j-1}}{dr_{i,j} + dr_{i,j-1}} \tag{8.26}$$

8.5.3 Mesh Details and Boundary Conditions

The properties of the computational domain used for charged spray simulations of this study, are critical in terms of the accuracy required to resolve the physics likely to occur within practical charged spray applications. A domain with grid cells too large could adversely affect the way gas velocities and electric fields are computed during simulation, which in turn could adversely affect the way computed spray droplets disperse throughout the domain volume. Nevertheless, a trade off exists between the quality of domain and the speed at which the simulation can perform. This section presents details on the chosen spatial discretization and boundary conditions used for spray simulations presented henceforth in this thesis.

8.5.3.1 Spatial Discretization

Nodes are concentrated uniformly in the region close to the atomizer, indicated (A) in figure 8.3. In this region one can expect the largest gradients to be present for gas velocities and the electric field. For the rest of the domain, indicated (B) in figure 8.3, nodes are placed in an ordered but non-uniform manner with a placement expansion factor of ≈ 1.2 that was shown to aid numerical convergence during solution of domain variables, (Shrimpton 1995).

8.5.3.2 Boundary Conditions

At the spray axis, $r = 0$, zero normal gradients are imposed for all variables apart from the radial velocity which is specified as zero. Region (2) represents the earthed nozzle body of the atomizer, defined as a solid internal zone with voltage fixed to zero along with no-slip boundary conditions imposed along its walls. This region acts as a perfect sink for the discrete phase mass, charge and momentum with no droplets rebounding or shattering. A constant pressure boundary is applied for the free boundaries denoted

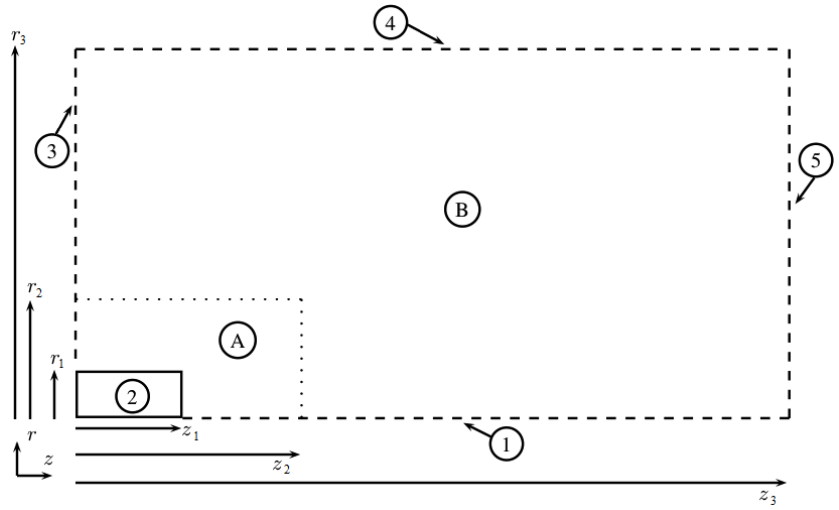

FIGURE 8.3: Boundary conditions, nomenclature and mesh details listed in table 8.3

(3) and (4) in figure 8.3. Boundary (5) is also defined as a constant pressure boundary however the voltage at this boundary is fixed to zero. This is because the sprays of Shrimpton and Yule (1999) were performed above an earthed Faraday cage and similarly sprays of Rigit and Shrimpton (2009) were performed above an earthed set of electrode rings. The inclusion of boundary conditions representing the earthed nozzle, Faraday cage and electrode rings were found to be critical in terms of obtaining physically realistic conditions to corresponding charged spray experiments.

8.6 Background

Due to complex dynamics of primary and secondary atomization present in electrostatically atomized sprays, the initial charge and droplet diameter distributions characterising such sprays are difficult to define from a deterministic approach. The main difficulty is determining the individual charge-to-mass ratio for droplets in these sprays. It is possible to directly sample discrete droplets from the spray plume, (Polat et al. 2000; Kulon et al. 2003). However this method can only be performed at the spray edge where samples collected are usually too few for reliable statistics and do not represent the whole of the spray. Indirect methods on the other-hand attempt to recover the charge-to-mass ratio from observed trajectory information integrated over the whole spray. However,

major assumptions are required to specify local electric fields and gas velocities at droplet locations throughout the spray, (Rigit and Shrimpton 2009).

8.6.1 Summary of Experiments Performed by Rigit and Shrimpton (2009) and Shrimpton and Yule (1999)

In previously published literature of Rigit and Shrimpton (2009), data from charged hydrocarbon spray experiments of Rigit (2003) was used to estimate via an indirect method, the charge-diameter (Q-D) joint probability density functions (JPDF) across four sprays. For these sprays, mean spray specific charges ranged from $1.2 - 3.16 C/m^3$, and injection velocities ranged $10 - 15 m/s$, using orifice diameters $\leq 254 \mu m$. A summary of spray conditions used in these experiments is shown in table 8.1. For these experiments, individual droplet charges were estimated by utilising a phase Doppler anemometry (PDA) measurement system in conjunction with a purpose built collection system that could simultaneously measure the spray current and mass flow rate, between sets of annular electrode rings situated at the base of the spray plume. Further details on this method may be found in Rigit (2003).

Spray	Ref.	Fluid Type	d_{inj} (μm)	U_{inj} (m/s)	$\dot{m}$ (kg/s)	Q_v (C/m^3)	v'_d (m/s)	l_j (mm)	$\theta/2$ (deg)
(i)	(A)	Calibration Diesel	254	10	0.4115	1.13	0.21	11.76	8
(ii)	(A)	Calibration Diesel	140	10	0.1304	2.25	0.23	6.22	14
(iii)	(A)	Calibration Diesel	140	15	0.1875	2.67	0.28	7.56	16
(iv)	(A)	Calibration Diesel	116	15	0.1253	3.16	0.27	6.25	17
(v)	(B)	Kerosene	250	10	0.39	1.2	0.69	3.67	15
(vi)	(B)	Kerosene	250	34	1.3025	1.8	1.04	8.16	7

TABLE 8.1: Spray operating conditions and test cases of interest along with additional parameters. All experiments were performed at standard room temperature conditions. Refs, (A);Rigit and Shrimpton (2009) and (B);Shrimpton and Yule (1999)

Shrimpton and Yule (1999) also investigated charged hydrocarbon spray characteristics and published details on three experiments with different spray operating conditions. Relevant to this study were the two PDA measured experiments, utilising nozzle orifice diameters of $250 \mu m$ with flow rates of $0.5 ml/s$ and $1.67 ml/s$, achieving mean spray specific charges of $1.2 C/m^3$ and $1.8 C/m^3$ respectively. A summary of these sprays are also shown in table 8.1. In these experiments, the spray was captured using a single electrically isolated metal drum which measured the current from the charges carried

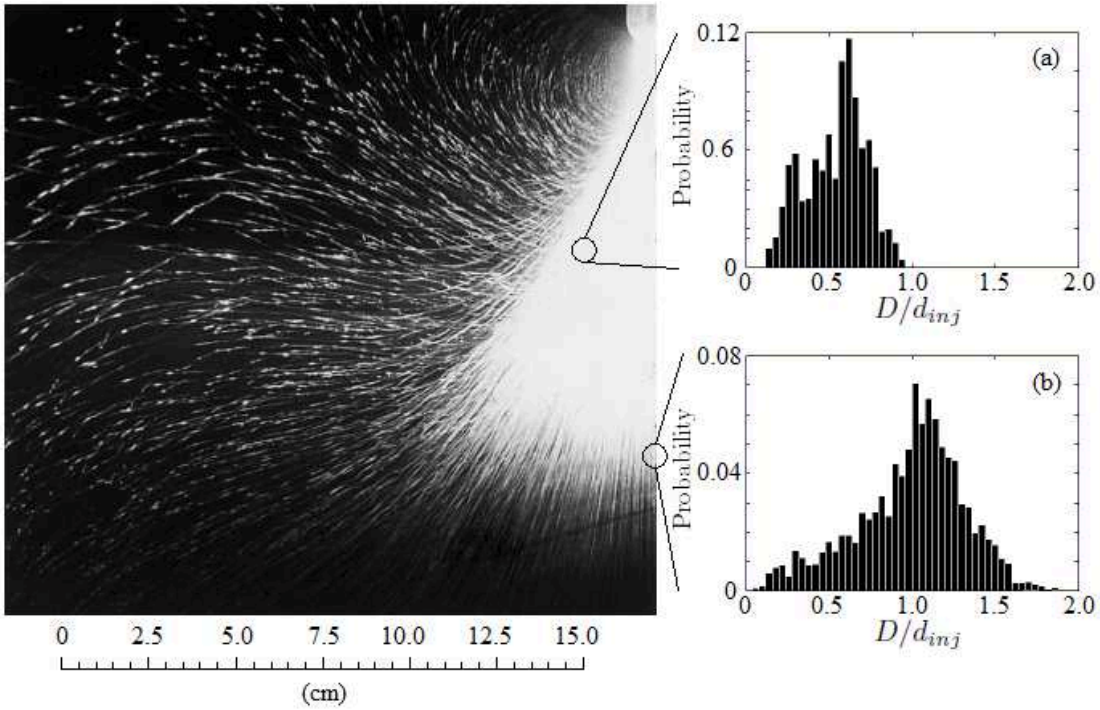

FIGURE 8.4: Photograph of the free spray, $\dot{m} = 0.39 \times 10^{-3} kg/s$, $Q_v = 1.20 C/m^3$, $d_{inj} = 250 \mu m$ of Shrimpton and Yule (1999), showing corresponding droplet diameter PDFs at indicated sample locations; (a) $z/d_{inj} = 240$, $r/d_{inj} = 80$, (b) $z/d_{inj} = 480$, $r/d_{inj} = 0$

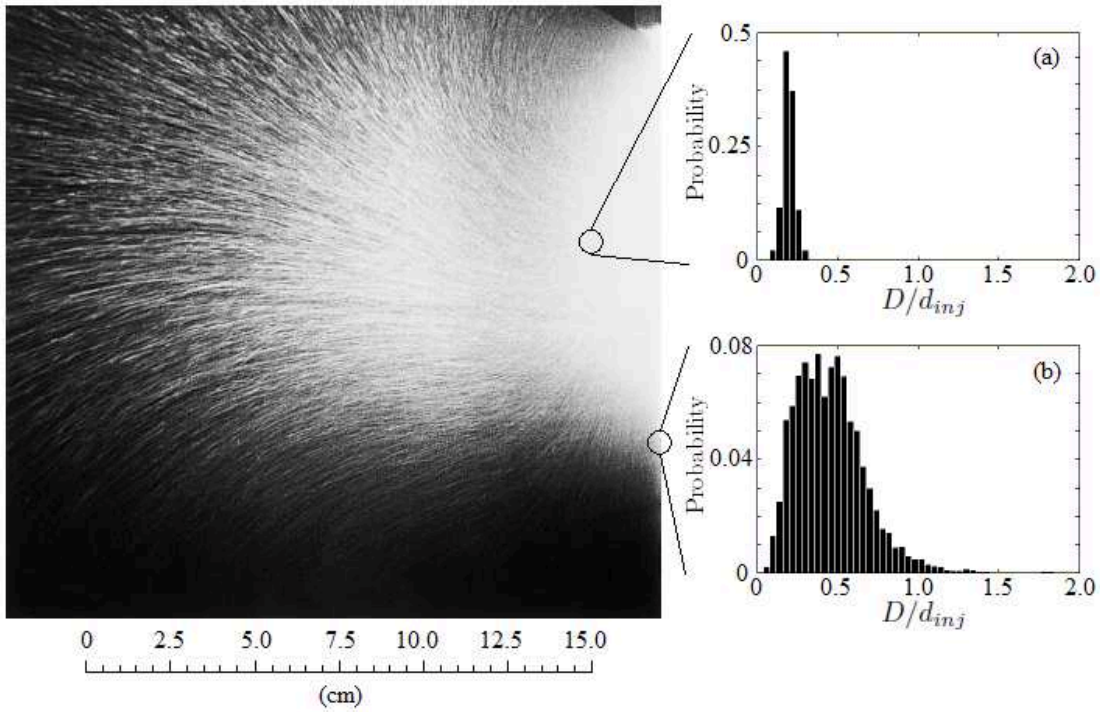

FIGURE 8.5: Photograph of the free spray, $\dot{m} = 1.30 \times 10^{-3} kg/s$, $Q_v = 1.80 C/m^3$, $d_{inj} = 250 \mu m$ of Shrimpton and Yule (1999), showing corresponding droplet diameter PDFs at indicated sample locations; (a) $z/d_{inj} = 240$, $r/d_{inj} = 80$, (b) $z/d_{inj} = 480$, $r/d_{inj} = 0$

by the spray. With the PDA measurements, Shrimpton and Yule (1999) presented detailed information on the spray structure, highlighting the spatial variations regarding arithmetic mean droplet diameters as well as the axial and radial droplet velocity profiles throughout the spray. Figures 8.4 and 8.5 show the free spray dynamics of these two experiments respectively. Comparison of the photography obtained using a laser sheet and $1s$ camera exposure, clearly shows a significant increase in radial droplet dispersal for the case with larger spray charge density. Also included in figures 8.4 and 8.5 are selected PDFs, constructed from PDA measurement data at identical spatial locations taken from the spray plume. These show how a polysized spray is generated with observed radial stratification of mean droplet diameter with larger, high inertia droplets populating more of the spray core. These PDFs also demonstrate how the increase in spray charge density at elevated injection velocities leads to smaller droplet diameters throughout the spray plume.

Property	**Kerosene** (A)	**Calibration Diesel** (B)
Density, kgm^{-3}	730	815
Dynamic Viscosity, $kgm^{-1}s^{-1}$	0.000838	0.002608
Surface Tension, Nm^{-1}	0.022	0.025
Relative Permittivity	1.99	2.20
Molecular Weight, $kgmol^{-1}$	0.142	0.180
Critical Pressure, MPa	2.16	2.46
Critical Temperature, K	617.0	569.4
Freezing Temperature, K	243.15	239.15
Specific Gas Constant, $Jkg^{-1}K^{-1}$	58.437	46.18

TABLE 8.2: Properties of liquids at $293K$ unless otherwise stated. Refs, (A);Brunner (1988); Shrimpton (2009) and (B);Shrimpton and Rigit (2006); Crowley et al. (1990); Bakar et al. (2008)

8.7 Modelling Jet Breakup

To develop a reliable and general injection procedure that can replicate the post-primary atomization dynamics of charged dielectric liquid hydrocarbon sprays, two major challenges are faced. The first is the assignment of charge to individual droplets, and the second being the droplets initial $f(Z_d, R_d, U_d, V_d; t = 0)$ distribution which is governed by jet break-up dynamics. The aim of this section is to establish these protocols and

ensure accurate simulation of electrically charged sprays of electrically insulating liquids. With regards to the second challenge, the process of injecting droplets has been designed to take into account some of the unique characteristics of the charged liquid jet break-up.

The introduction of electric charge to a dielectric liquid jet has been observed to decrease the stability of the jet surface, (Gomez 1994). Overall, this leads to smaller mean droplet diameters, smaller mean jet breakup lengths and larger spray cone angles with an increase of space charge induced repulsion. Shadow spark photography from experimental studies (Shrimpton 1995), and more recently from DNS studies of (van Poppel 2010), have revealed that ligament structures can extend radially and can persist typically up to many orifice diameter magnitudes downstream from the atomizer prior to producing droplets. As a starting point, the mean jet break-up length l_j may therefore be characterised using the following empirical equations, (Shrimpton and Yule 2001).

$$l_j = U_{inj}\tau_j \tag{8.27}$$

$$\tau_j = \frac{\epsilon_0\epsilon_r}{\kappa Q_V} \tag{8.28}$$

The mean liquid injection velocity at the atomizer orifice is represented by U_{inj} and the characteristic time t_j represents the time required for a charged fluid element to travel from the centre of the liquid jet to the surface. The ionic mobility κ_I is inversely proportional to the liquid dynamic viscosity, and from Walden (1906) is calculated as,

$$\kappa_I = A\mu^{-1} \tag{8.29}$$

Crowley et al. (1990) and Adamczewski (1969) suggest a typical value of $A = 2.0\times10^{-11}$ and Ergene et al. (2010) suggests a typical value of $A = 3.0\times10^{-11}$. From more recently collated experimental data available from literature, summarized in figure 8.6, A was calculated to be approximately $\approx 4\times10^{-11}$. Using this constant, it was found that

for sprays with low specific charges and injection velocities, the break-up lengths tend to be over-predicted for small orifice diameters, whereas for larger orifice diameters, the break-up lengths are under-predicted. For sprays where a high specific charge is present, only a small amount of deviation from the mean trend was found, and since sprays of interest are limited to high specific charges, one can justify use of the general model shown in equations (8.27), (8.28) and (8.29). Taking the permittivity of free space as $\epsilon_0 = 8.854 \times 10^{-12} F/m$, and using the liquid properties of kerosene and calibration Diesel from table 8.2, the mean jet break-up length for all simulated sprays of interest may be calculated.

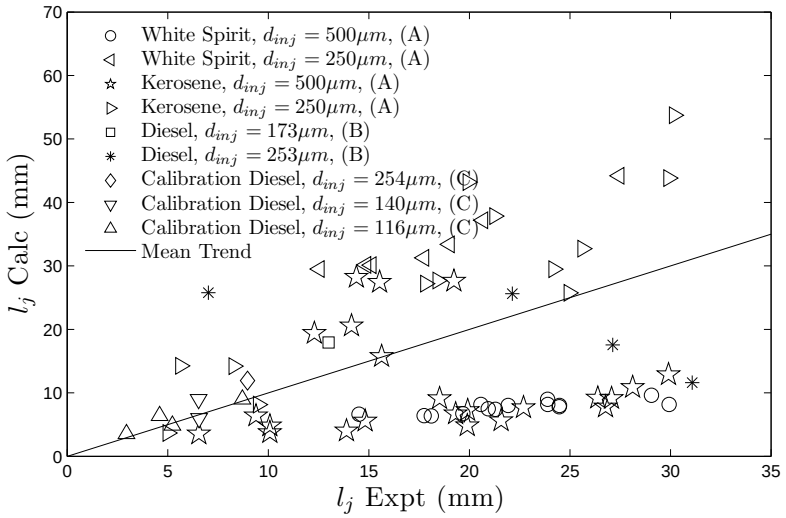

FIGURE 8.6: The calculated breakup length versus experimental breakup length for White spirit, Kerosene, Diesel and Calibration Diesel and with data organised according to the orifice diameters used in experiments. Refs, (A);Shrimpton (1995), (B);Malkawi (2009), (C);Rigit (2003)

Since the primary jet breakup location is known, one can move on to the modelling of primary atomization from ligaments transported downstream from the atomizer and their subsequent breakup into droplets. First, to mimic the random nature of ligament formation from the primary jet break-up, one may assume that the initial axial displacement of ligaments in normally distributed with a standard deviation equal to $1/3^{rd}$ of, and about the mean jet breakup length calculated from earlier. Since the CFD code models discrete droplets rather than physical structures such as ligaments, these jet breakup mechanisms may be represented by a numerical injection procedure for droplets. The numerical implementation is as follows.

At the start of each time-step Δt, the axial and radial displacement of injected droplets are specified according to equations (8.30) and (8.31) where $f(0)$ represents the value of $f(t)$ at $t = 0$.

$$Z_d(0) = l_j \left(1 + \frac{1}{3} RAN_G\right) \tag{8.30}$$

$$R_d(0) = r_{inj} \times RAN_U \tag{8.31}$$

Here r_{inj} represents the radius of the atomizer orifice, RAN_G a random number taken from a Gaussian distribution with zero mean and unit variance and RAN_U a uniform random number in the interval 0 to 1. Droplet velocities at the start of the current time-step are then specified by mean and fluctuating components of the injection conditions according to equations (8.32) and (8.33).

$$U_d(0) = U_{inj} \tag{8.32}$$

$$V_d(0) = V_{inj} + V' \times |RAN_G| \tag{8.33}$$

Here it is assumed that the initial axial velocity of droplets is equal to the bulk mean injection velocity U_{inj} at the atomizer orifice plane with the mean radial component $V_{inj} = 0$. The fluctuating radial velocity component V' is calculated using equation (8.34) where the half spray cone angle $\theta/2$ is taken from experimental measurements of primary atomization including ligament creation and break-up. Values for $\theta/2$ and V' are listed in table 8.1. The factor of two shown in equation (8.34), appears because one assumes that the spray angle of droplets is normally distributed with a 95% confidence interval that droplets fall within the first two quartiles of the normal distribution.

$$\tan(\theta/2) = \frac{2V'}{U_{inj}} \tag{8.34}$$

As it would be physically unrealistic to expect k numbers of parcels to be injected at the same time within a given interval, a uniformly distributed random injection time in the range ($0.05 < RAN_U < 0.95$) of Δt is used to modify the initial position of the droplets. Following a modified injection time, the displacement is then specified according to equations (8.35) and (8.36).

$$Z_d(RAN_U \Delta t) = Z_d(0) + U_d(0) \times RAN_U \Delta t \tag{8.35}$$

$$R_d(RAN_U \Delta t) = R_d(0) + V_d(0) \times RAN_U \Delta t + \left(\frac{Z_d(RAN_U \Delta t)}{U_d(0)} \times V_d(0) \right) \tag{8.36}$$

The second term in equation (8.36) represents the radial displacement of a droplet, formed from the break-up of a parent ligament that is travelling radially with a velocity of $V_d(0)$. Here it is assumed that the initial radial velocity of the droplet is the same as its parent ligament upon break-up. The third term in equation (8.36) represents the additional radial displacement of the droplet, after it has travelled a distance of $Z_d(RAN_U \Delta t)$ downstream, starting from an initial radial displacement with an initial velocity of $V_d(0)$.

8.8 Injection Conditions for Droplet Diameters, Masses and Charges

Following on from the jet breakup modelling, all that remains is defining the droplet properties that govern all subsequent dynamics occurring throughout the sprays evolution during simulation. The three most important parameters to this aspect are the diameters, masses and charges of injected droplets. These parameters are intrinsically linked with one another and must remain linked from a numerical standpoint to conserve liquid mass and charge injected into the domain.

8.8.1 Initial Droplet Diameters and Masses

In each of the experimental sprays presented in Rigit and Shrimpton (2006) and Shrimpton and Yule (1999), data from many PDA measurement locations was used to construct a composite PDF of droplet diameter for the whole of the spray. Since each PDA measurement volume represents a different sized control volume of the experimental domain, there exists a possibility that data acquired is inconsistent at some locations. PDA measurements are therefore control volume and acquisition time weighted in order to obtain a true composite droplet diameter PDF of the spray plume. Figure 8.7 shows these PDFs for all experimental sprays listed in table 8.1. Results show a bimodal, two-peak distribution of droplet diameters for sprays (i)-(v), whereas for spray (vi), only a heavily skewed, uni-modal, single-peak distribution is evident. Due to the higher injection velocity present in the latter spray, the aerodynamic disturbance experienced by droplets in the sprays is increased. This increase is associated with shorter breakup time-scales and explains why smaller satellite droplets are abundantly present in spray (vi).

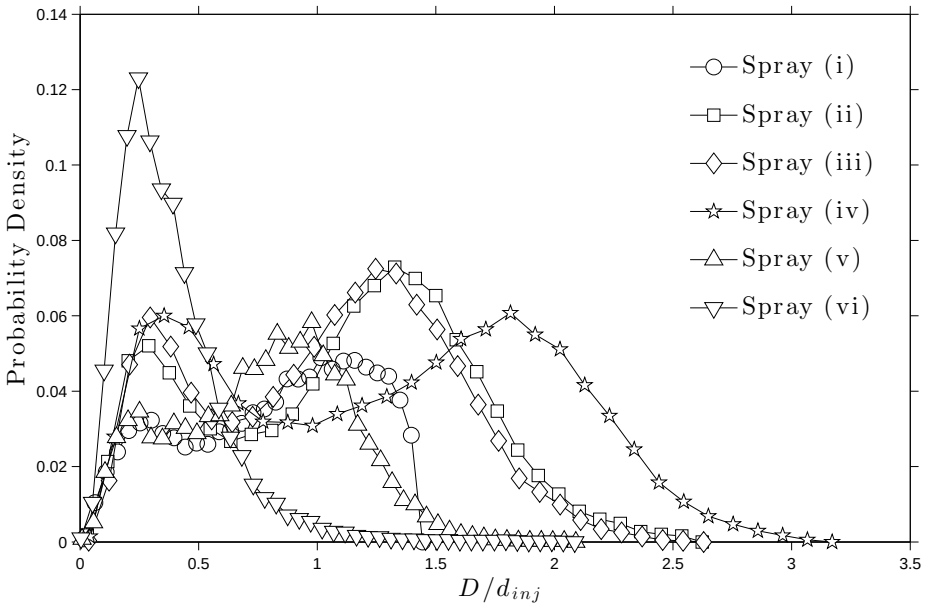

FIGURE 8.7: Composite droplet diameter PDFs for experimental sprays shown in table 8.1.

For each parcel of droplets injected during a given time-step, the droplet's diameter D_k, is chosen randomly with equal probability from the distributions summarised in figure 8.7. For the total mass injected per time-step per radian $\frac{\dot{m}\Delta t}{2\pi}$, conservation is ensured by

assigning a certain number of identical droplets to each parcel injected, whilst ensuring that the relative number of droplets contained in the set of parcels injected during that time-step, obeys the droplet diameter PDF constraint.

8.8.2 Initial Droplet Charges

For the experimental sprays (i)-(iv) of table 8.1, the relationship between droplet charge and diameter was quantified by using PDA measurements in conjunction with spatially resolved distributions of mass and charge flux to obtain a JPDF of droplet charge versus diameter. Figures 8.8 and 8.9 summarize these results in terms of estimated mean and r.m.s droplet charge as a fraction of the Rayleigh limit, for each droplet diameter class. It should be noted that due to fewer samples of droplets with diameters $D/d_{inj} > 1.5$, the estimated mean droplet charge in this region must be viewed with some caution. Data suggests that the additional charge density for more highly charged sprays is accommodated for by the presence of more smaller droplets rather than more charge per droplet (Rigit and Shrimpton 2009). In general, results show a relatively constant non-dimensional mean charge level across the diameter classes, despite the variation in spray specific charge between the four sprays. With regards to the r.m.s charge across diameter classes $D/d_{inj} < 1.5$, a clear trend is evident in that sprays with greater specific charges resulted in a greater spread of charge about the mean. In these cases however, due to the scarcity of data available for the largest droplet diameter classes, the r.m.s. droplet charges show greater variations.

During parcel injection, following selection of the droplet diameter, the charge Q_k per real droplet in the k^{th} injected parcel is selected from an assumed normal distribution with specified $\bar{Q}$ and Q' from the profiles in figures 8.8 and 8.9. Directly specifying droplet charge according to this method shall henceforth be referred to as the 'Direct Q-D' method. Critically, charge conservation for the direct Q-D method must be achieved prior the input of the charge-diameter profiles to simulations. This is ensured by multiplying the mean charge levels by a weighting factor W_f, across the range of diameter classes $i = 1$ to N_c, specified in the composite droplet diameter PDF. The weighting

factor is calculated as the ratio of the total charge injected per time-step to the total charge present across each of the diameter classes according to the following equation,

$$W_f = \dot{Q}\Delta t / \sum_{i=1}^{N_c} \bar{Q}_{d,i} \tag{8.37}$$

where $\dot{Q}$ is the charge flow-rate, more commonly referred to as the current.

Given now that mass and charge injected per time-step is conserved within the composite droplet diameter PDF and charge-diameter profiles respectively, for parcels injected during a given time-step, any subsequent adjustments on the relative number of droplets due to mass conservation will automatically correspond with an adjustment of relative charge levels, thus ensuring that charge is conserved.

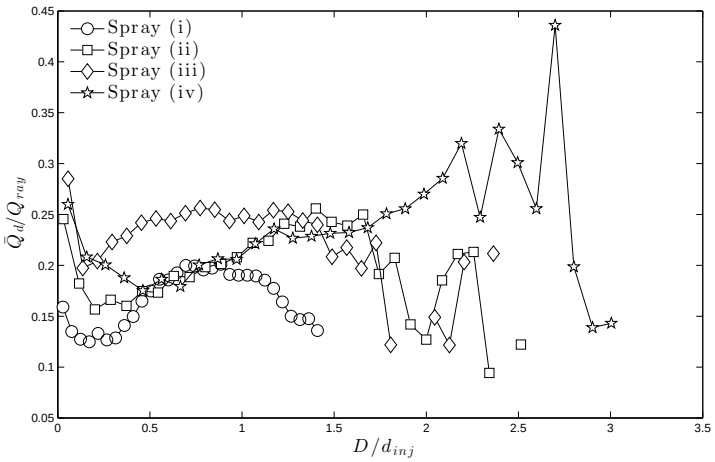

FIGURE 8.8: Mean of the droplet charge normalised by its Rayleigh limit per non-dimensional droplet diameter class, for experimental sprays shown in table 8.1.

"Modelling" of droplet charge follows a different approach whereby the relationship between charge and diameter is quantified as a scaling, droplet relative charge law defined as,

$$\frac{Q_{d,k}}{Q_{d,k+1}} = \left(\frac{D_k}{D_{k+1}}\right)^m \tag{8.38}$$

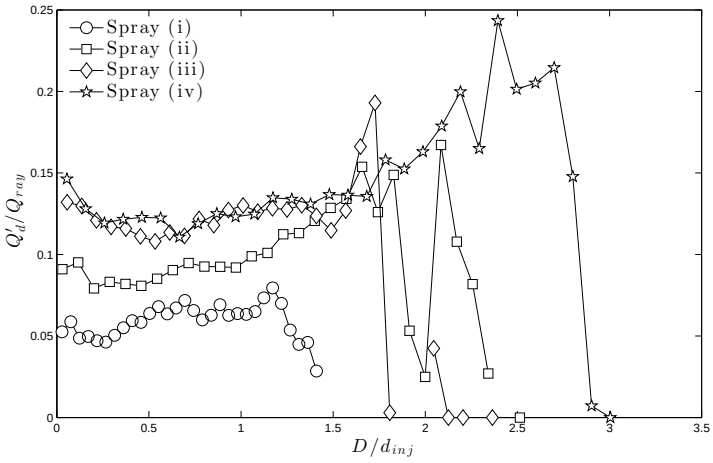

FIGURE 8.9: R.m.s. of the droplet charge normalised by its Rayleigh limit per non-dimensional droplet diameter class, for experimental sprays shown in table 8.1.

Where the constant is taken as $m = 1.8$, (Shrimpton and Laoonual 2006). This allows the total charge injected at any time interval $\dot{Q}\Delta t$, to be expressed in terms of a conserved injected current $\dot{Q}(t)$ such that,

$$\dot{Q}\Delta t = \sum_{k=1}^{K_p} N_{d,k} Q_{d,k} = Q_{d,1} \sum_{k=1}^{K_p} N_{d,k} \left(\frac{D_k}{D_{k+1}} \right)^m \tag{8.39}$$

where K_p is the total number of parcels injected during the time-step. Charge is then defined conservatively without explicitly constraining it to obey any limits. This procedure shall be referred to henceforth as the 'Model Q-D' method.

8.8.3 Preliminary Assessment of Modelled and Direct Q-D Specification Methodology

Briefly the validity of the modelled and direct Q-D methods at specifying droplet charges for computed sprays are examined. Comparison is made between different methods of charge specification against experimental data for spray (i) of table 8.1. For all tests, $10,000$ droplets are injected during a single time-step within the CFD code and subsequent charge and diameter statistics are examined.

At this stage of development, the direct Q-D method specifies only the mean and variances of droplet charges per diameter class. This does not capture the higher order

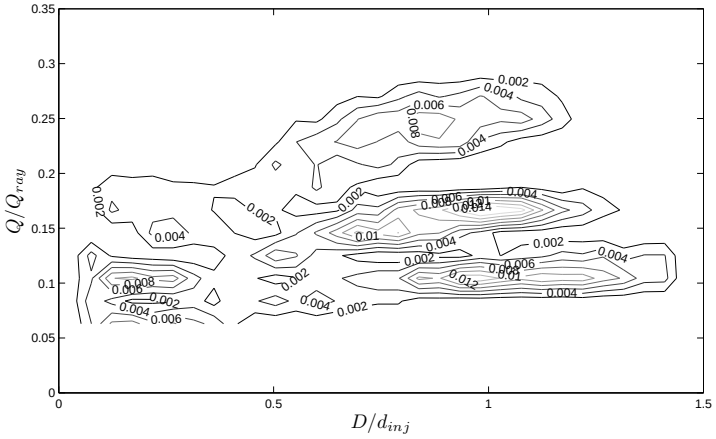

(a) Experimental Data

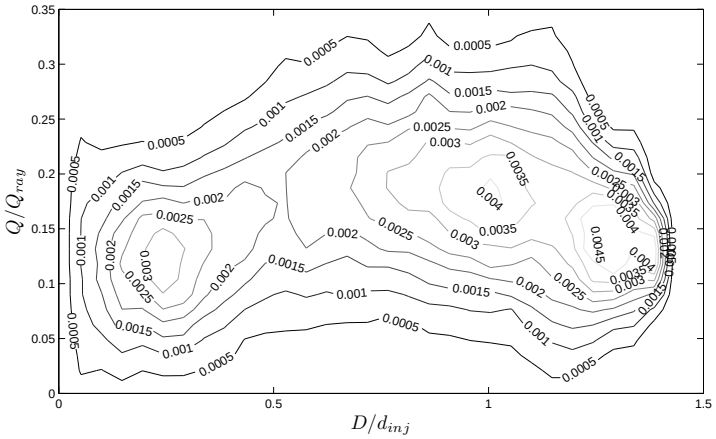

(b) Direct Q-D ($\bar{Q}$ and Q' specified per diameter class)

FIGURE 8.10: Comparison of the droplet Q-D JPDF obtained from experimental data and the approximate JPDF obtained using the direct Q-D method for spray case (i) of table 8.1. Contours indicate levels of equal probability.

moments of the Q-D JPDF such as the skewness and kurtosis. However, with higher order statistics, there is argument as to whether or not these moments are reliable enough for numerical consideration, as they are more sensitive to the quality of experimental data to which they were obtained from. Nevertheless, one can justify the use of the first two statistical moments to approximate to a reasonable degree, the Q-D JPDF present within experiments. To demonstrate this, figure 8.10 shows for spray case (i) of table 8.1, the similarity between the JPDF obtained from experiments and the approximate JPDF obtained using the direct Q-D method.

One could argue that there is still some loss of statistical information but from figure

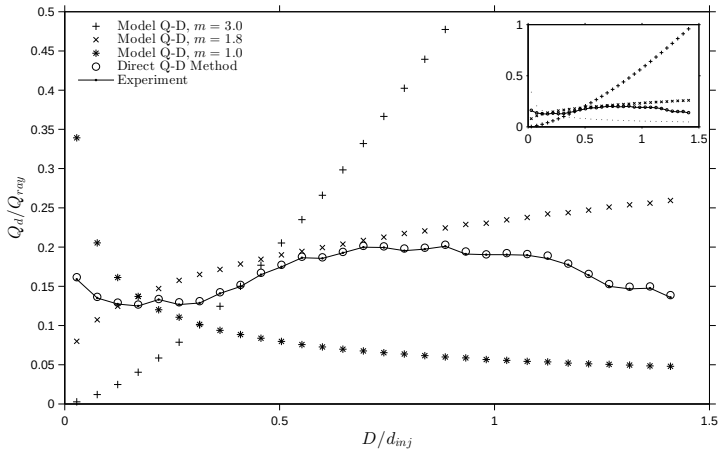

FIGURE 8.11: CFD Code input checks on the variation of mean of the normalised drop charge as a function of normalized droplet diameter class. The chosen test case for charge validation is spray (i) of table 8.1

8.11, the direct Q-D method shows good agreement with the experimental data. One can see that for the modelled Q-D method using an exponent of $m = 1.8$, mean droplet charges are in close agreement with experimental values in the region $0.5 \rightarrow\approx 0.9\ D/d_{inj}$. For $D/d_{inj} > 0.9$ the model starts to over predict the Q-D relationship with increasing divergence up to $D/d_{inj} = 1.4$. This may be attributed to the earlier speculation about the capture of quality for higher order statistical moments obtained from experiments. The region $0.125 \rightarrow\approx 0.5\ D/d_{inj}$ shows reasonable agreement amidst a slight over-prediction to experimental values but below this range, the model starts to under predict droplet charges. Modelled Q-D tests using exponents $m = 3.0$ and 1.0 show no agreements whatsoever with experimental data thus highlighting their unsuitability.

8.9 Numerical Considerations

8.9.1 Boundary Placement

Caution was taken to ensure that boundary placement for the domain did not affect the statistics within the sample space of computed sprays, defined such that it spans all equivalent PDA measurement locations from corresponding experiments. For sprays of Rigit and Shrimpton (2006) and Shrimpton and Yule (1999), PDA measurements spanned the sample space regions $9 \geq z \geq 0cm$, $6 \geq r \geq 0cm$ and $15 \geq z \geq 0cm$,

$7 \geq r \geq 0cm$ respectively. Sprays (i) and (vi) of table 8.1 were chosen as a means to examine the issues of boundary placement upon statistics. For each chosen spray (i) and (vi), four different set-ups were defined for the computational domain. For each subsequent set-up, boundaries (4) and (5) illustrated by figure 8.3, were placed at progressive locations away from the edge of the spray sample space. These placements are listed in table 8.3 along with other relevant parameters defining the computational domain. In table 8.3, set-ups RS1-RS4 and SY1-SY4 correspond to the set-ups used for sprays (i) and (vi) respectively. When the percentage change in computed mean droplet diameters fell to $< 10\%$ between subsequent boundary placements, the set-up was deemed to have a negligible effect upon droplet statistics. Domain set-ups "RS4" and "SY4" were subsequently chosen for the production simulations of sprays (i)-(iv) and sprays (v)-(vi) listed in table 8.1, respectively.

Domain			Region Type, (z, r) cm						Mean % change in	
Set-up	N_z	N_r	Nozzle (2)		Uniform (A)		Expansion (B)		D_{10} at outermost	
			z_1	r_1	z_2	r_2	z_3	r_3	z and r PDA locations.	
RS1	88	49	2.5	1	7.5	4	11.5	6	-	
RS2	96	55	2.5	1	7.5	4	29.5	12	40.5%	6.4%
RS3	98	58	2.5	1	7.5	4	38.5	18	8.0%	1.0%
RS4*	100	61	2.5	1	7.5	4	47.5	24	6.7%	1.0%
SY1	92	50	2.5	1	7.5	4	17.5	7	-	
SY2	92	56	2.5	1	7.5	4	17.5	14	-18.4%	-4.2%
SY3	98	59	2.5	1	7.5	4	32.5	21	33.5%	22.5%
SY4*	100	62	2.5	1	7.5	4	47.5	28	9.5%	3.4%

TABLE 8.3: Summary of mesh parameters used for validations. Starred set-ups correspond to the chosen domain setup used for simulations. N_z and N_r represent the total number of computational cells in axial and radial directions respectively. Both the uniform region and the nozzle region have a cell spacing of 1 mm and the expansion factor for region is ≈ 1.2. Dimensions for the nozzle region were based upon geometric properties of a typical nozzle found in experiments (Shrimpton and Yule 1999; Rigit and Shrimpton 2006).

8.9.2 Stationary Conditions

Preliminary simulations were performed to determine the optimal trade-off between the number of Lagrangian parcels required for injection per time-step, and the computational effort associated with ensuring that enough droplets reside in the domain of interest to obtain reliable statistics. Subsequently, for all sprays examined in this study, the number of droplet parcels injected per time-step was set to 10, and the time-step required was

$\Delta t \approx O(10^{-6})s$. All simulations were found to reach a statistically stationary state after $1s$ of real simulation time, and statistics were recorded every $0.04s$ seconds, to provide instantaneous snapshots of the spray ready for analysis. With these parameters the total number of droplets residing within the domain for any given snapshot was approximately $O(10^4)$. The total runtime for all spray simulations was $6s$ allowing for $5s$ worth of data recording.

8.9.3 Collection of Statistics

As with all CFD simulations, a means by which interpretation of data can be achieved is sought for. Prior to this study, a small set of post-processing tools existed that were limited in their ability to post-process the data output CFD simulation code. These tools were developed extensively over the course of this study, and these tools can now be used to obtain, compare and correlate a wide range of CFD simulation statistics directly against those available from experiments. A brief summary of tool functionalities are given.

- Spatial sampling of droplets for constructing PDFs over single or multiple files
- Spatial sampling of droplets for constructing profiles of droplet diameter and velocity characteristics throughout the spray
- Ability to include relevant experimental data for comparisons where required

These tools were developed as scripts within the MATLAB® numerical software environment.

8.10 Results

In this section, the outcomes of the study are presented with dynamics and characteristics of computed sprays discussed via comparisons with experimentally available data.

Qualitative examination shall serve as a preliminary means to validate whether charged sprays of electrically insulating and semi-conducting liquids can be successfully simulated. Droplet vector plots along with overlaid contours of voltage potential shall be examined in conjunction with spray photographs taken using a $1s$ exposure. Since these photographs were taken only for experiments of Shrimpton and Yule (1999), one can only compare against the simulated sprays that use the Model Q-D method. These comparisons shall provide useful information regarding droplet trajectories and general structure of the spray plume.

For the quantitative comparisons, the spatially resolved statistics available from post-processed simulation data with those directly from PDA measurements are discussed in detail. It should be noted here that due to lack of any observable differences in statistics between sprays (ii) and (iii), spray (ii) is excluded from the results presented herein. Since the interest here lies in the sensitivity of initial conditions upon statistics of the computed sprays, the remaining sprays presented cover a wide enough set of conditions, sufficient for analysis. Sprays (i), (iii) and (iv) are examined, and briefly comments shall address the reliability of using the modelled Q-D method over the direct Q-D method for specification of initial droplet charge. The analysis of computed sprays (v) and (vi) shall provide us with additional knowledge regarding the reliability of the modelled Q-D method in predicting dynamics and characteristics for charged sprays of this type. To conclude the quantitative analysis, estimates of the error for mean droplet diameters and velocities, are summarized for all sprays (i)-(vi).

This section also examines how the mean spatial velocity characteristics of small droplets, classified as those with diameters $< 100\mu m$, vary between model Q-D sprays (i) and (vi), and corresponding experiments. Small droplets typically have large charge-to-mass ratios and are therefore much more sensitive to spray conditions such as the electric field. Sprays (i) and (vi) were selected for this analysis due to the different characteristics present between them. One may recall from earlier in section 8.6, that spray (i) consists of a bi-modal diameter distribution, injected with a low velocity of $10m/s$, whereas spray (vi) consists of a uni-modal diameter distribution injected at a faster velocity of $34m/s$. Ideally one wants to determine the suitability of the model Q-D method for predicting

the dynamics of small droplets in slow and fast sprays respectively. In addition, these sprays come from entirely different experiments so this particular analysis should serve as a means to identify any systematic issues with the modelled Q-D method.

8.10.1 Qualitative Comparisons Between Computed Sprays (v)-(vi) and Experiments

Figures 8.12a and 8.12b show the qualitative differences between sprays (v)-(vi) from experiments of Shrimpton and Yule (1999) and the corresponding modelled Q-D sprays from simulations.

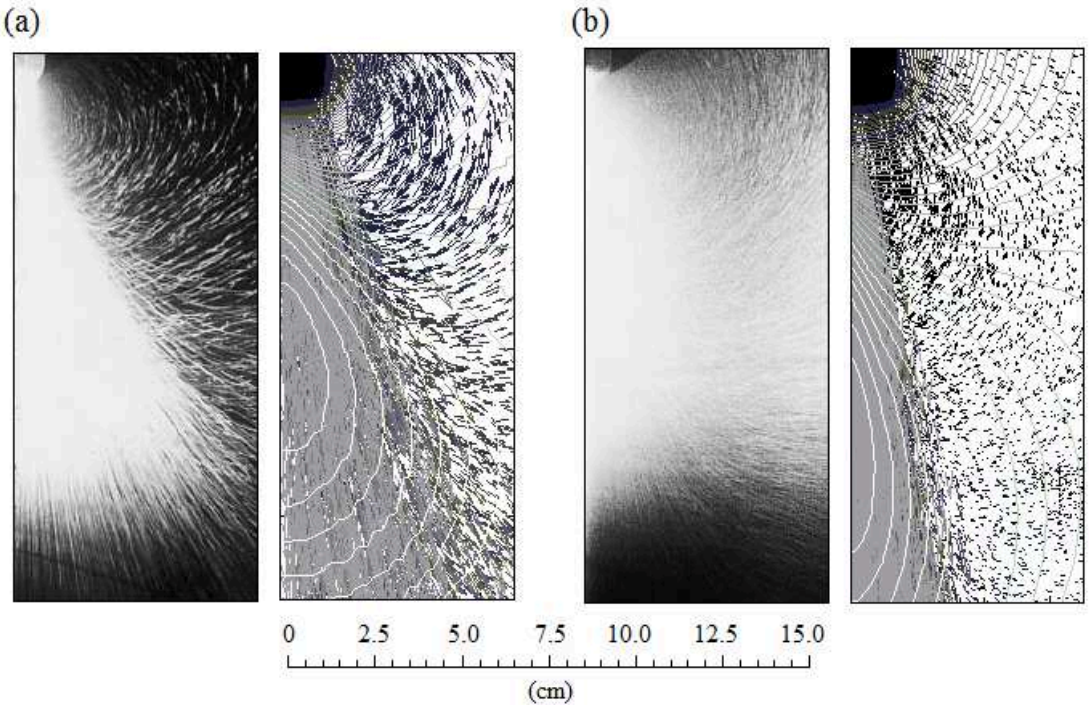

FIGURE 8.12: Qualitative comparisons showing droplet trajectories illuminated from a 1s exposure photograph taken during spray experiments along with droplet vectors and overlaid contours of voltage potential obtained during simulations of corresponding sprays using the modelled Q-D method. Figures a) and b) compare sprays (v) and (vi) of table 8.1 respectively.

For both computed and experimental sprays (v) and (vi), there is clear evidence of droplet recirculation back towards the earthed body of the atomizer. This occurs due to the presence of an electric field in the spray plume, and the tendency of small droplets

with high charge to mass ratios and low inertia, to follow gradients in the voltage potential. The strongest gradients occur near the earthed body of the atomizer indicated by the densely packed contours of voltage potential in figures 8.12a and 8.12b.

For spray (v) of table 8.1, a remarkable similarity can be observed whereby the trajectories of computed droplets follow closely the trajectories highlighted through the photography. Radial deflections of computed droplets from the spray core coincide well with radial deflections of droplets in the experiment. This gives us confidence that the computed electric field is similar to the actual electric field present within the experiment. Evidence of a primary core in the computed spray comes from the spatial density of droplet vectors. Likewise for the experiment, evidence comes from the density of droplet exposure trails. On the other hand for spray (vi) of table 8.1, droplet trajectories in the computed spray show slight disagreements with the experiment. In the lower half of the spray photograph, it appears that trajectories of droplets extend radially and directly outwards from the spray plume. In the computed spray however, it appears that droplets following a similar track reside further downstream by ≈ 100 orifice diameters. In addition, computed droplets deflecting radially nearer the top of the spray plume take a more direct trajectory back towards the atomizer than similarly located droplets from experiment. Together, these observations suggest that the electric field of the computed spray, does not accurately represent the field present within the experiment for spray (vi).

8.10.2 The Direct Q-D vs Modelled Q-D Method vs Experiments

Figure 8.13 highlights the mean droplet diameter profiles for sprays (i), (iii) and (iv) of table 8.1. Away from the spray centreline, profiles for the direct Q-D spray show reasonable agreement with profiles from experiments. However, along and near the spray centreline, there is a slight tendency for direct Q-D sprays to have larger mean droplet diameters than in corresponding experiments. This is likely because of the following reasons. The direct Q-D method specifies initial droplet charge according to a mean and variance and takes into account the observed variability in droplet charge. This permits very small droplets to have little to zero charge present. Small droplets

that have little to zero charge are more likely to remain longer in the spray core, than similarly sized droplets of greater charge. Therefore, an increased small droplet presence in the spray core will reduce the local mean droplet diameter profiles. Also, it should be noted that Rigit and Shrimpton (2006) observed positive skewness in charge levels for experiments of sprays (i)-(iv), giving reasonable evidence to suggest an even greater abundance in the spray core of small droplets with little to zero charges present. This is something not captured within the direct Q-D method and explains why the mean diameter profiles near the spray centreline are larger than profiles from experiment. This effect is even more pronounced for the model Q-D method that specifies only first order moments, preventing any possibility that droplets have little to zero charge present. Figure 8.14 highlights mean droplet diameter profiles for sprays (v) and (vi) of table 8.1. For spray (v), with increasing radial displacement and downstream from the atomizer, profiles for the mean droplet diameter diverge and overestimate the profiles from experiment. For spray (vi) on the other-hand, mean droplet diameter profiles agree with remarkable accuracy to the profiles from experiment, more so than any other spray investigated. This suggests that simulations are more suited to predicting profiles of mean droplet diameter, for charged sprays where large injection velocities present. Because of the large injection velocities present, the effect of the electric field upon the motion of charged droplets is less pronounced, allowing for more dominant effects like droplet inertia to govern the formation of the steady-state spatial mean diameter characteristics.

Figures 8.15 and 8.16 show the spray profiles for the mean axial droplet velocity. It is immediately apparent that across sprays (i), (iii) and (iv) of table 8.1, computed profiles of droplet axial velocity along the spray centreline significantly over-estimate profiles of experiments by a factor of approximately two. It was mentioned earlier in this section, that both direct and modelled Q-D methods over-estimate mean droplet diameter profiles of experiments near the spray centreline, due to the greater presence of large droplets. Generally, larger droplets in the spray plume have greater inertia and their increased presence is likely to bias the mean axial droplet velocity to larger velocities. For computed sprays (i), (iii) and (iv), it appears that with increasing radial displacement, the profiles for mean axial droplet velocity cross profiles of corresponding experiments.

Subsequently, at the outermost radial locations, profiles for the axial droplet velocity of computed sprays, under-estimate those from experiments. This under-estimation is not as severe as the over-estimation near the spray centreline. However, at some locations the axial velocity profiles of the computed sprays are negative, whereas corresponding experimental profiles are not. Due to the presence of small droplets with high charge to mass ratios in the outermost regions of the spray, differences in the electric field between computed and experimental sprays will cause these small droplets to have reversed trajectories. These differences in trajectories show up in statistics of the mean axial and radial droplet velocities. On the other-hand, computed profiles of mean axial droplet velocity for sprays (v)-(vi) are far better in agreement to experiments than sprays (i), (iii) and (iv). There is however a slight over-estimation for spray (v) in the mean axial velocity at outermost radial locations and a slight over-estimation for spray (vi) near the spray centreline, that appears to be more prominent with increasing downstream displacement from the hypothetical atomizer.

Figures 8.17 and 8.18 show the spray profiles for the r.m.s. axial droplet velocities. For sprays (i), (iii) and (iv), experimental profiles shows significant levels of scatter without any distinctive trends. Experimental profiles generally show r.m.s. axial velocities for droplets to be relativity high in the spray core region, compared to lower values nearer the spray periphery. Interestingly, sprays (i), (iii) and (iv) appear to have relativity similar values for r.m.s. axial droplet velocities across their spatial profiles. With regards to the computed profiles, again it is apparent that direct Q-D and modelled Q-D methods result in virtually identical spray profiles. Away from the spray injection location at downstream displacements $z \geq 30mm$, profiles for droplet r.m.s. axial velocities appear to increase from zero near the spray axis, reach a peak or plateau a short distance away radially and then decrease in line with experimental values at the outer edge of the spray peripheries. For sprays (v) and (vi), experimental data for droplet r.m.s. axial velocities was only available for latter. With regards to the computed profiles agreement with experimental data, it appears from profiles that r.m.s. axial velocities are much higher for computed than experimental sprays. For spray (vi), there is evidence in profiles reaching a peak/plateau near the spray core. This is followed by a decrease in r.m.s. values nearer the spray periphery.

Figures 8.19 and 8.20 show the spray profiles for the mean radial droplet velocities. Profiles for all sprays show that droplets move away from the spray centreline until a maximum velocity is reached, at which point the droplets begin to decelerate. The initial increase in radial droplet velocity is caused by the high space charge repulsion forces present in the core of the spray. Due to axisymmetry, the mean radial electric field component and the mean radial droplet velocity at the spray centreline should both be zero. The computed profiles for all sprays obey this requirement giving confidence in the accuracy of the simulations. It also appears that radial droplet velocities in the computed sprays over-predict the radial droplet velocities of the experiment. Despite this disagreement however, the characteristic shape of the velocity profile between computed and experimental sprays remain remarkably similar. There is slight evidence that computed profiles for sprays (v) and (vi) over-predict the profiles of experiments, however for the most part of the spray plume, profiles are well matched. For spray (vi), the initial radial acceleration appears less pronounced than spray (v) which is probably due to the fact that spray (vi) has a large injection velocity present.

Figures 8.21 and 8.22 show the spray profiles for the r.m.s. radial droplet velocities. Near the spray axis and downstream from the atomizer, computed r.m.s. radial velocities for sprays (i), (iii) and (iv), tend to have smaller values compared to experimental profiles. Only for sprays (iii) and (iv) near the spray periphery do computed profiles start to agree with experimental profiles however this is more likely a result of decreased radial droplet velocities at these locations. As before, radial r.m.s. velocities between model and direct Q-D sprays agree well with each another. For sprays (v) and (vi), r.m.s radial droplet velocities tend to show better agreement with experiments near the spray axis. However, only for spray (vi) do the r.m.s profiles continue to agree well with experimental profiles with increasing radial displacement.

To conclude the analysis between direct Q-D and modelled Q-D sprays, percentage errors in D_{10}, $\bar{U}_d$ and $\bar{V}_d$ were calculated for each of the computational sprays according to the form given by equation (8.40) for D_{10}.

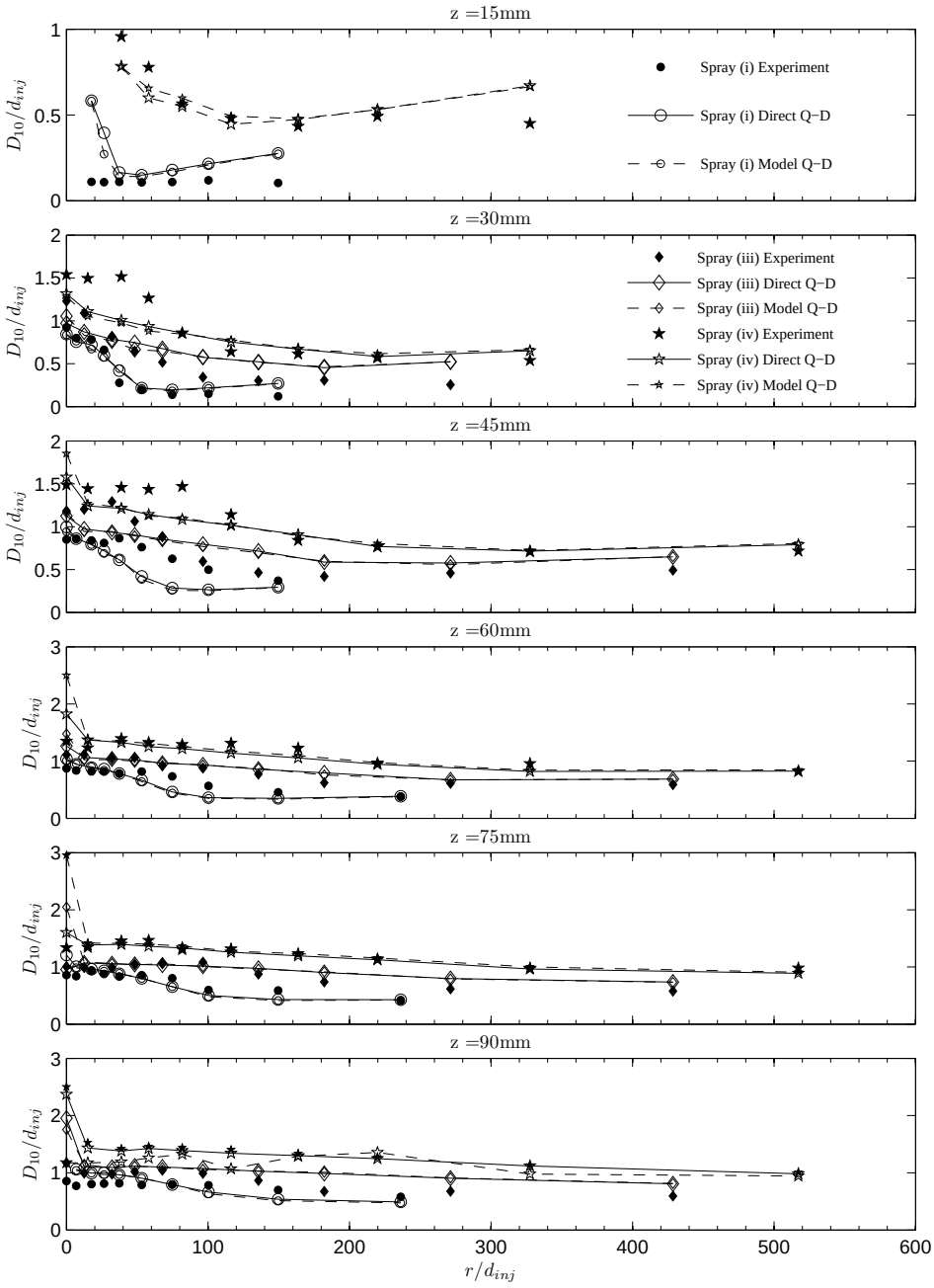

FIGURE 8.13: Profiles of mean droplet diameter D_{10}/d_{inj} for sprays (i), (iii) and (iv) of table 8.1.

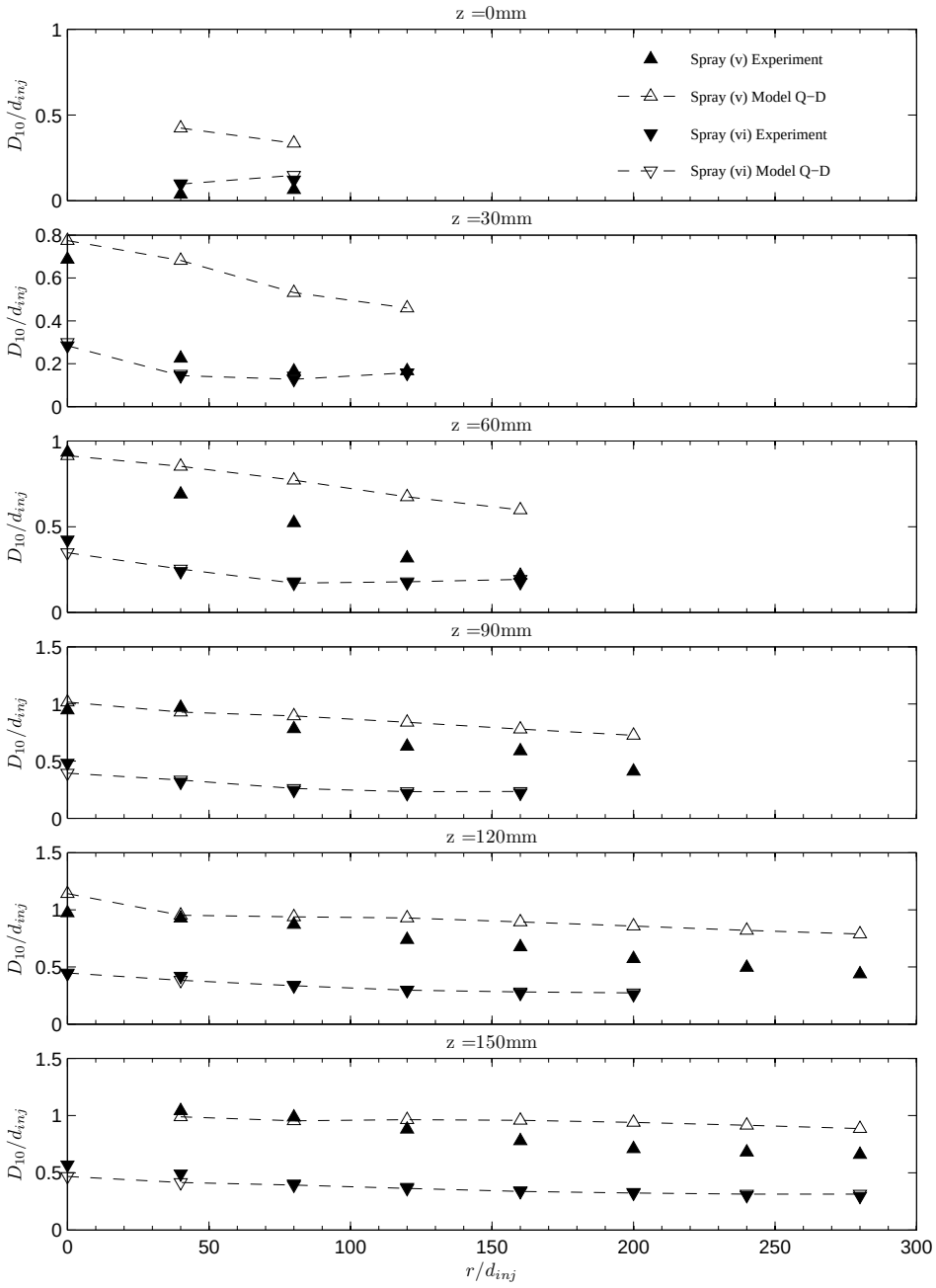

FIGURE 8.14: Profiles of mean droplet diameter D_{10}/d_{inj} for sprays (v)-(vi) of table 8.1.

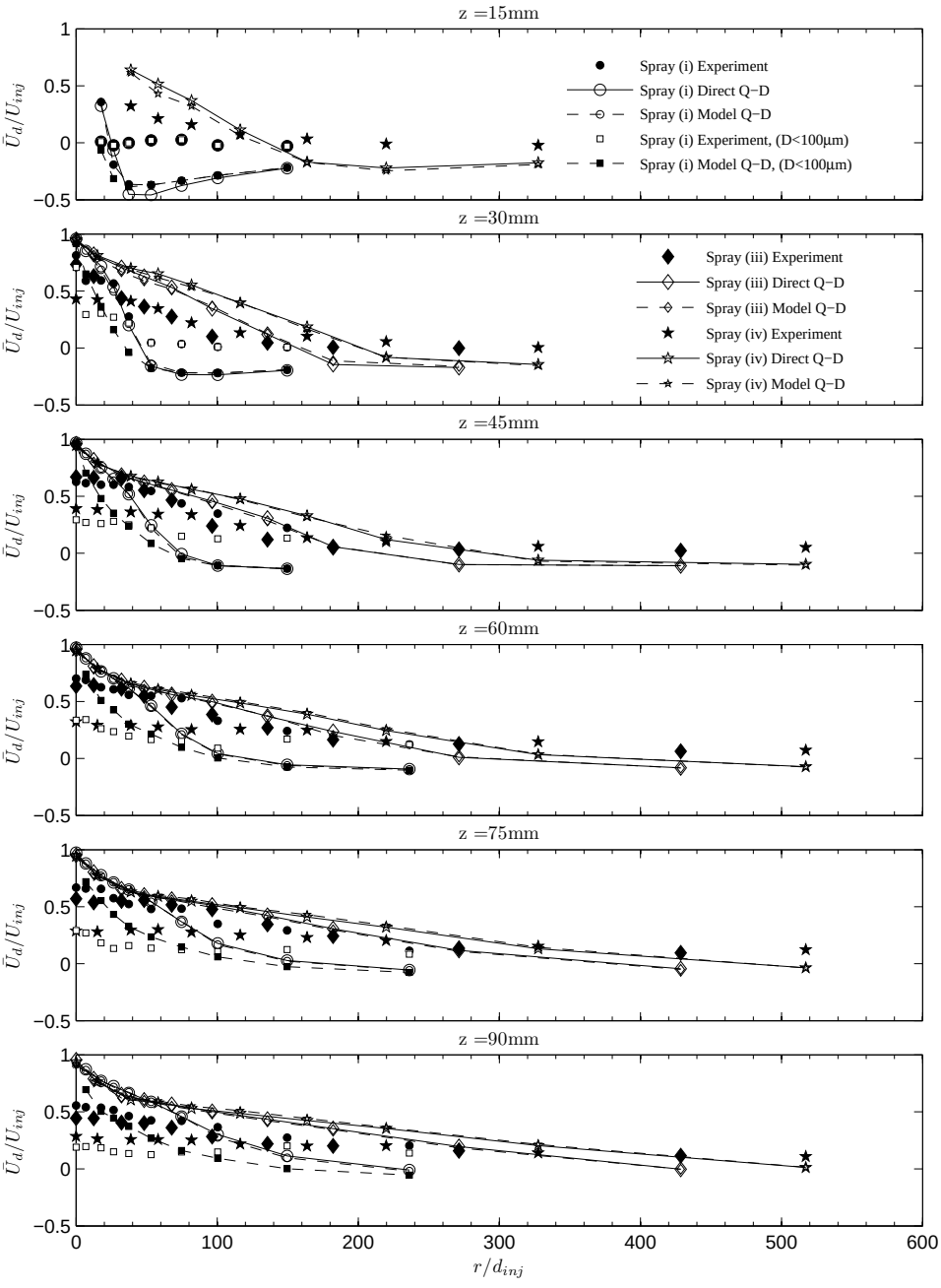

FIGURE 8.15: Profiles of mean droplet axial velocity $\bar{U}_d/U_{inj}$ for sprays (i), (iii) and (iv) of table 8.1.

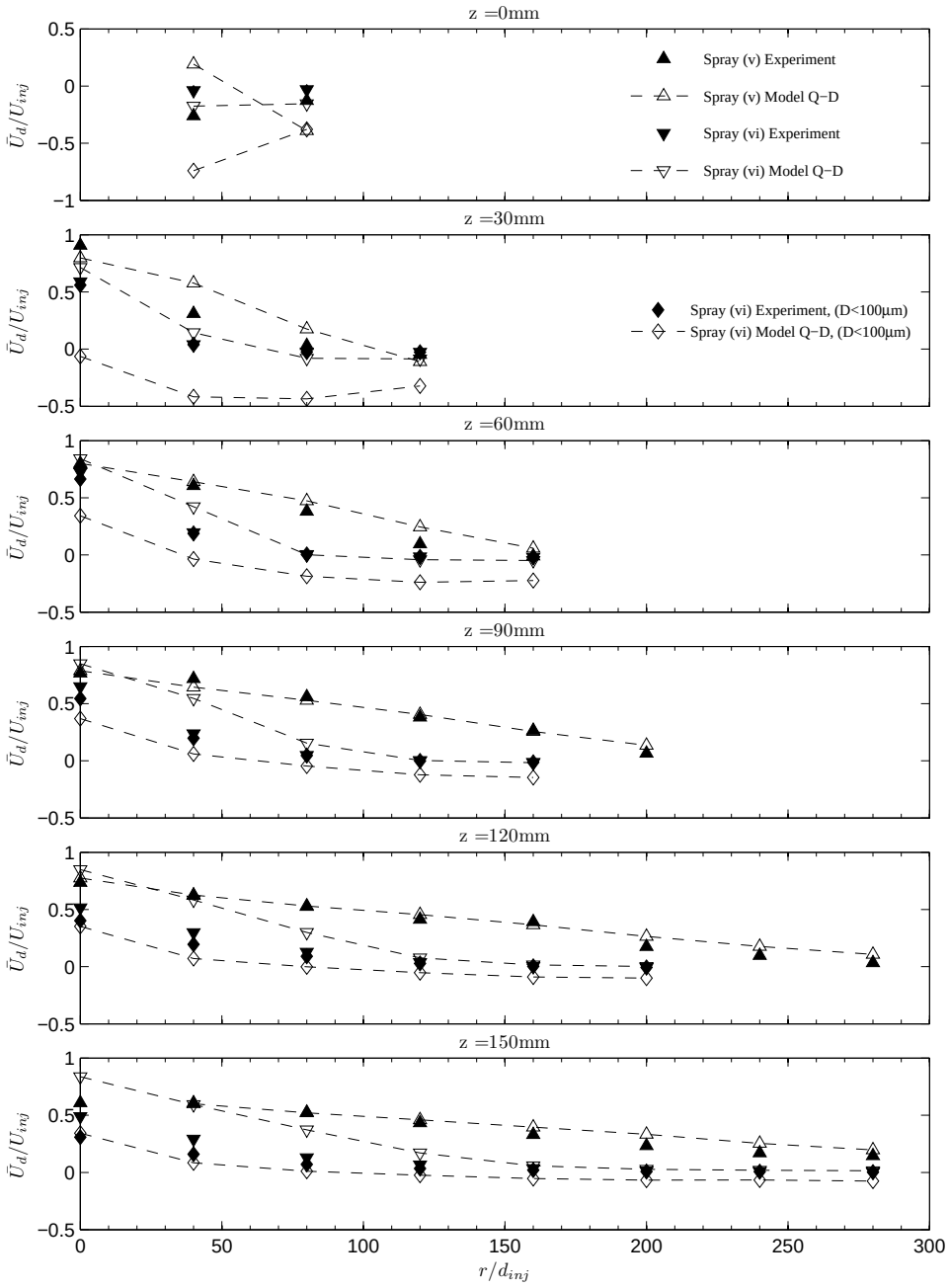

FIGURE 8.16: Profiles of mean droplet axial velocity $\bar{U}_d/U_{inj}$ for sprays (v)-(vi) of table 8.1.

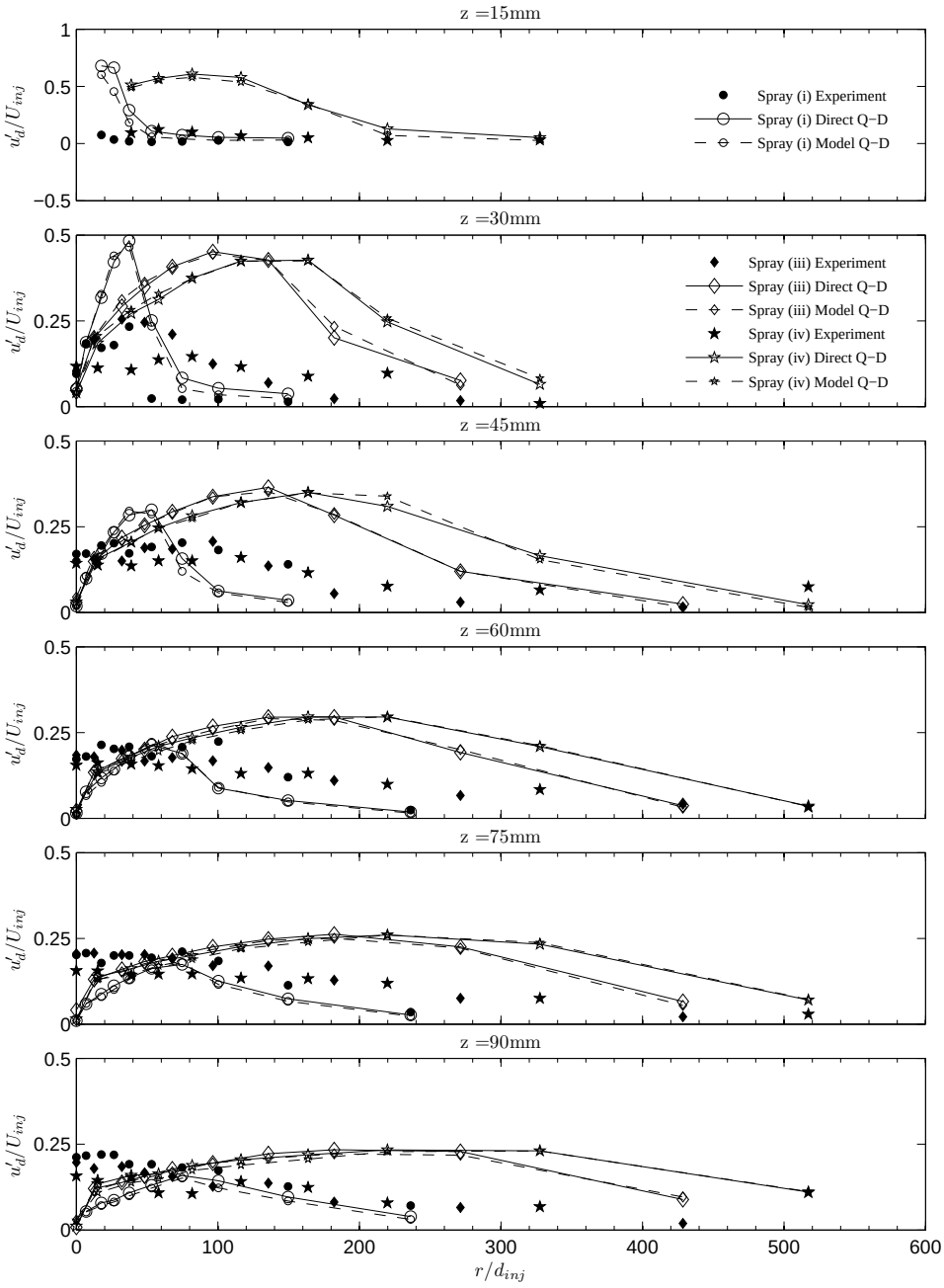

FIGURE 8.17: Profiles of r.m.s. droplet axial velocity u'_d/U_{inj} for sprays (i), (iii) and (iv) of table 8.1.

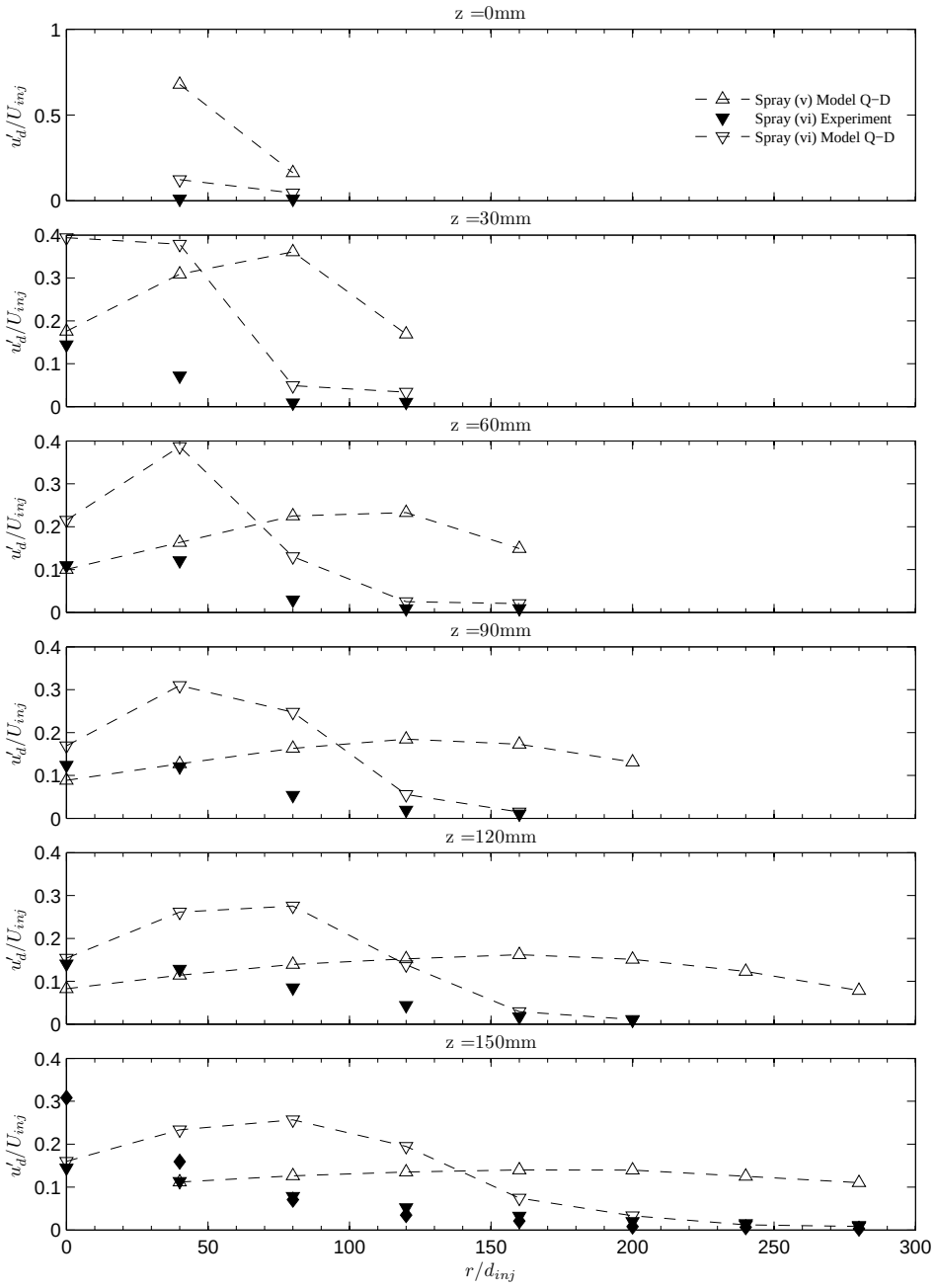

FIGURE 8.18: Profiles of r.m.s. droplet axial velocity u'_d/U_{inj} for sprays (v)-(vi) of table 8.1.

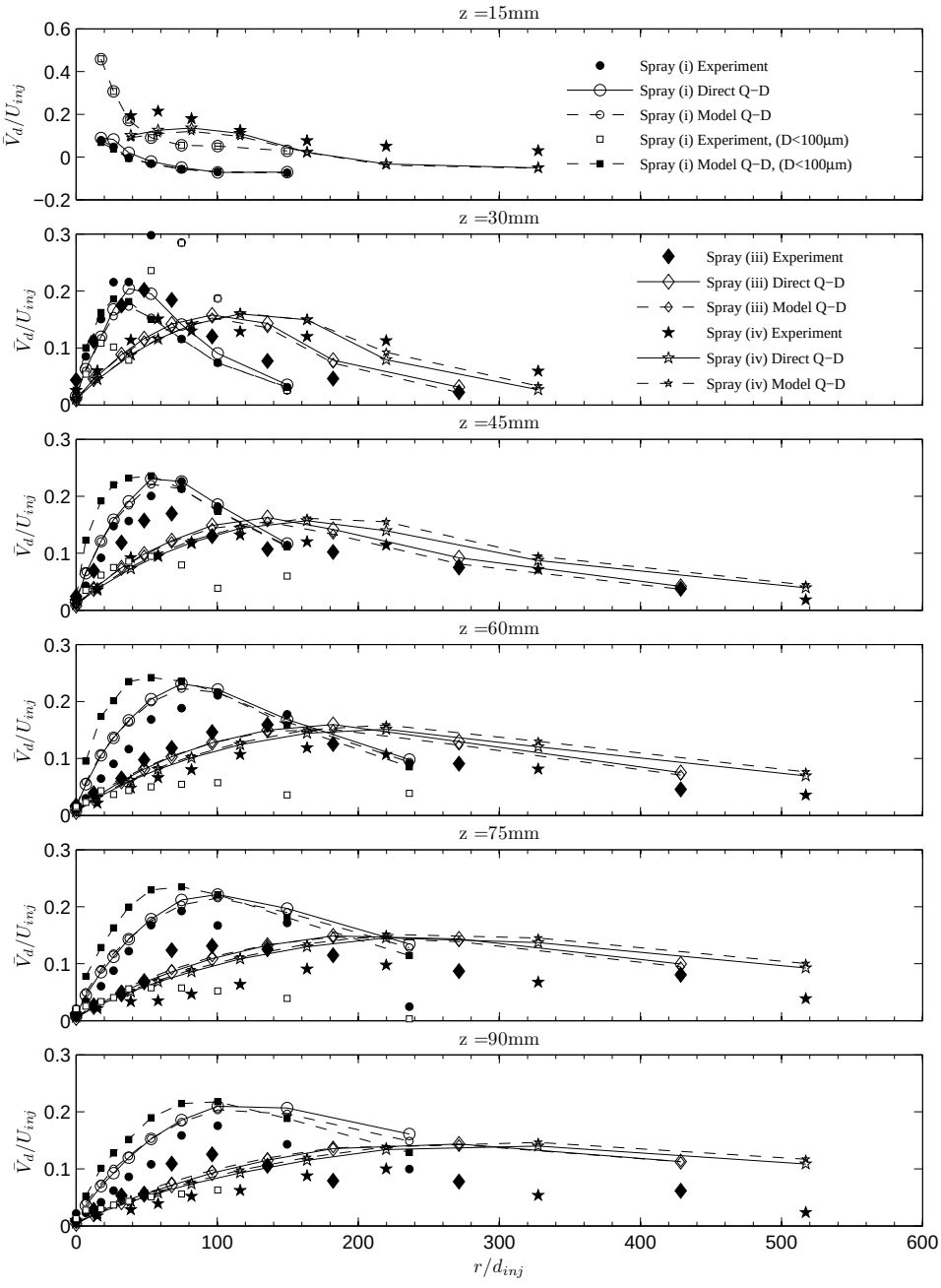

FIGURE 8.19: Profiles of mean droplet radial velocity $\bar{V}_d/U_{inj}$ for sprays (i)-(iv) of table 8.1.

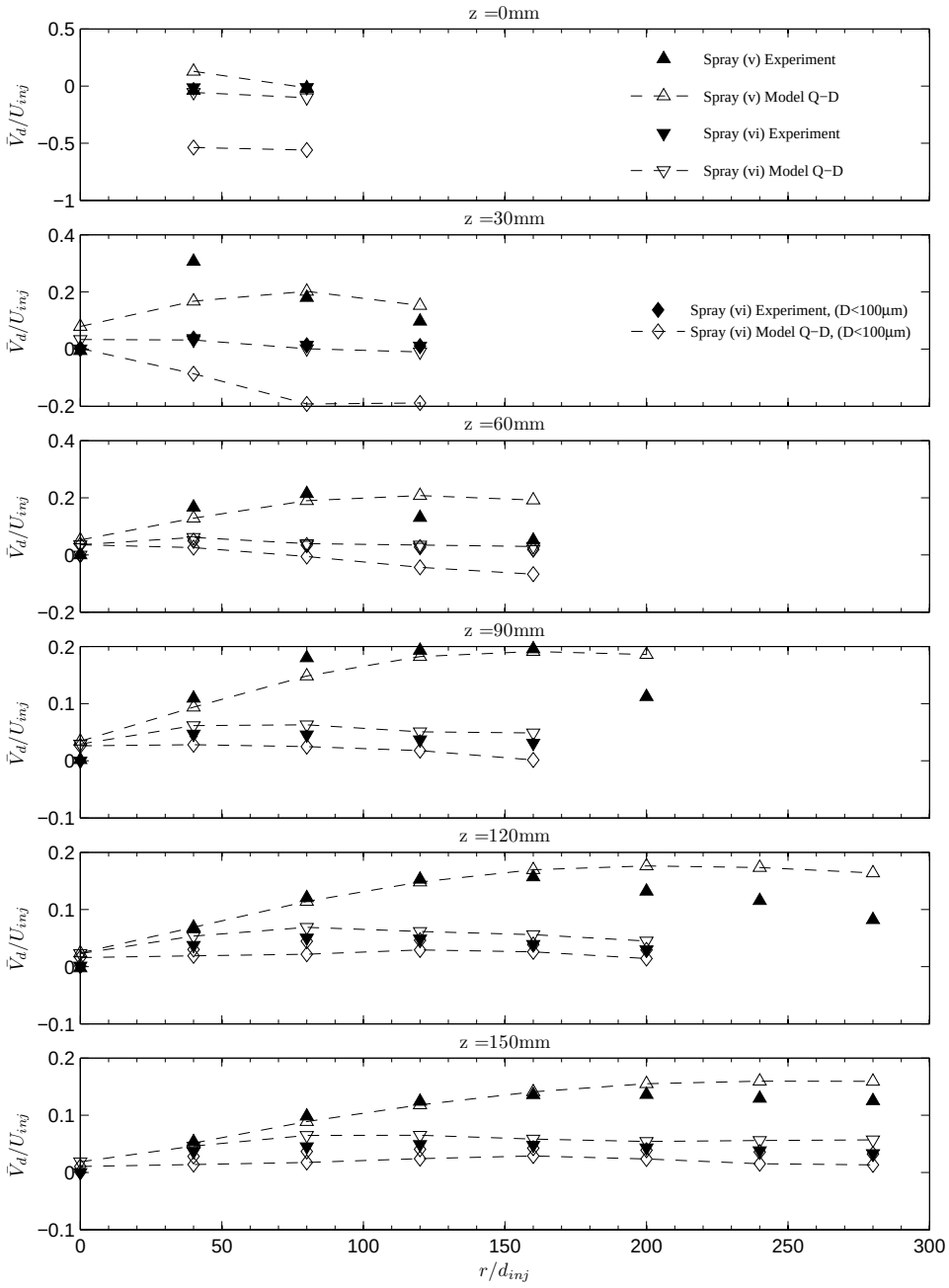

FIGURE 8.20: Profiles of mean droplet radial velocity $\bar{V}_d/U_{inj}$ for sprays (v)-(vi) of table 8.1.

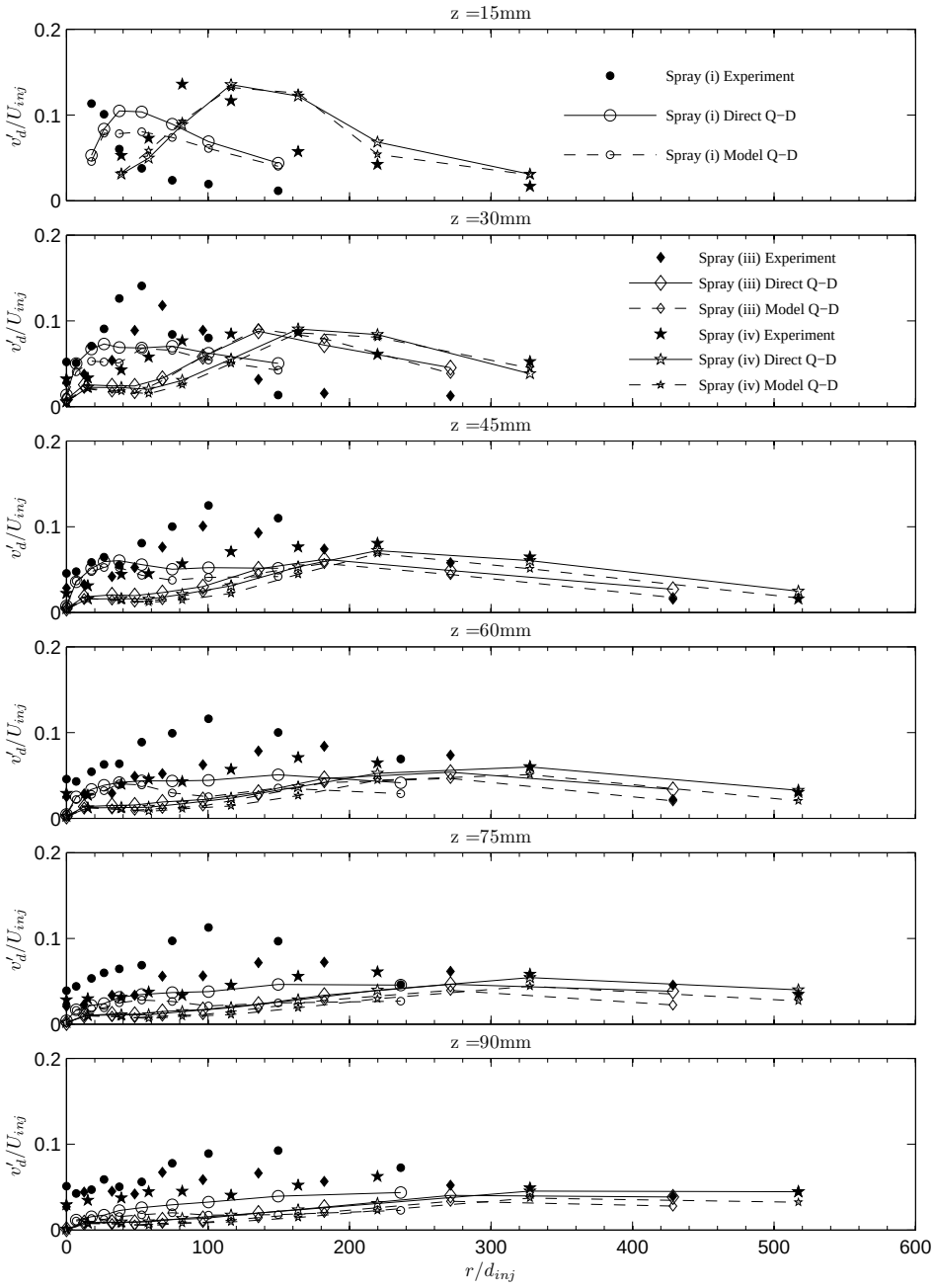

FIGURE 8.21: Profiles of r.m.s. droplet radial velocity v'_d/U_{inj} for sprays (i), (iii) and (iv) of table 8.1.

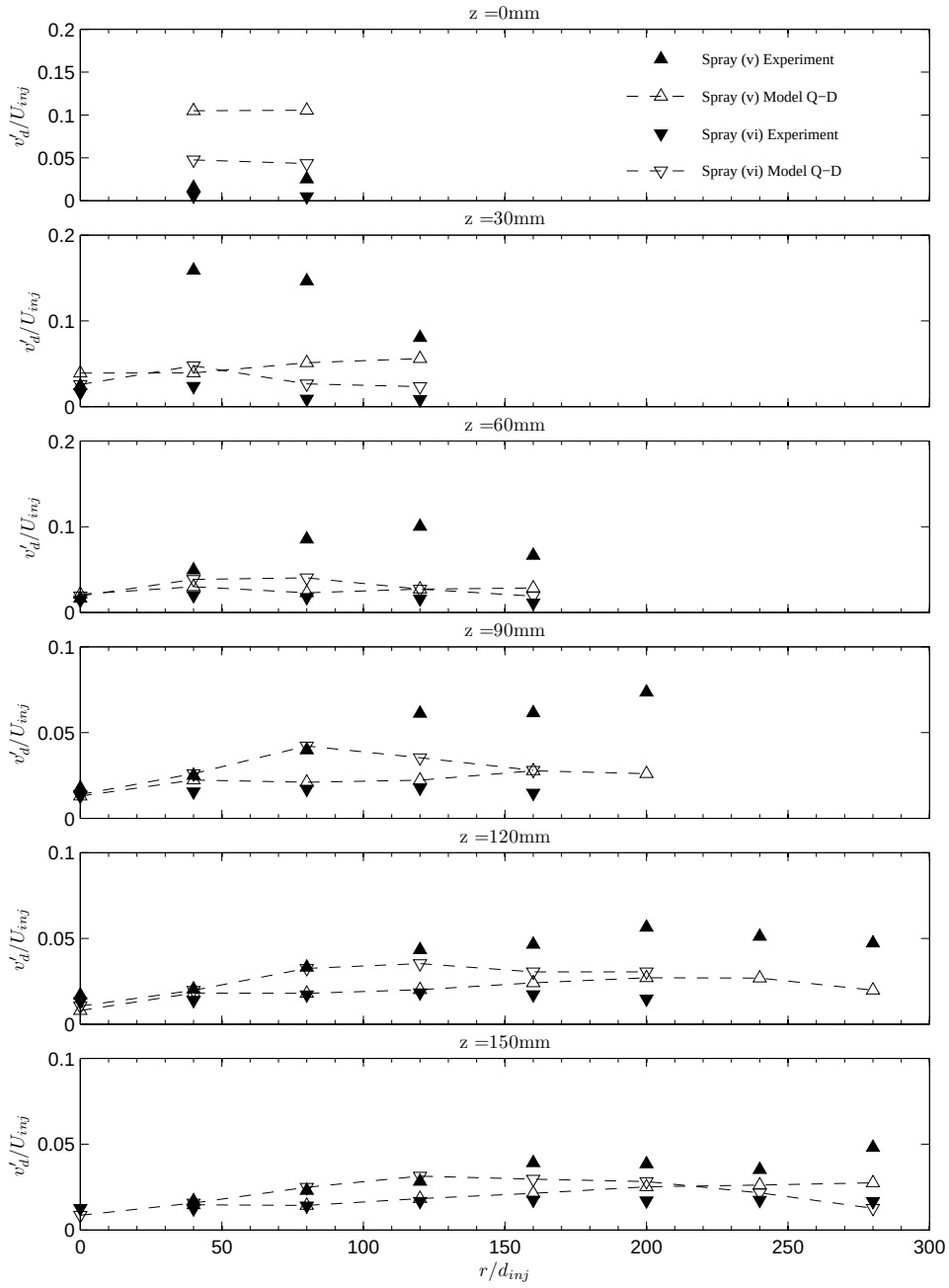

FIGURE 8.22: Profiles of r.m.s. droplet radial velocity v'_d/U_{inj} for sprays (v)-(vi) of table 8.1.

Profile Type	Spray (i) (%)	Spray (ii) (%)	Spray (iii) (%)	Spray (iv) (%)	Spray (v) (%)	Spray (vi) (%)
D_{10}	15.4 (16.0)	6.9 (6.1)	8.1 (5.5)	5.1 (3.1)	34.1	0.8
$\bar{U}_d$	14.6 (13.2)	19.4 (19.0)	18.6 (19.7)	52.5 (53.1)	24.4	73.9
$\bar{V}_d$	12.7 (17.4)	23.0 (29.3)	19.4 (22.6)	26.3 (23.7)	12.9	16.2

TABLE 8.4: Summary of the average percentage relative differences between model Q-D and experimental sprays, where values in brackets correspond to average percentage relative differences between the direct Q-D and experimental sprays.

$$\text{Error } \% = \frac{1}{N} \sum \left[\frac{\left(\bar{D}_{comp} - \bar{D}_{expt} \right)}{\left(\bar{D}_{comp} + \bar{D}_{expt} \right) /2} \right]^2 \times 100 \tag{8.40}$$

In equation (8.40), N represents the number of data points that form the profiles in figures 8.13-8.20. A summary of the percentage errors between the computed and experimental sprays is given in table 8.4.

For sprays (i)-(iv) based on experiments of Rigit and Shrimpton (2006), the percentage estimates of the error between the modelled Q-D sprays and experiments versus the direct Q-D sprays and experiments, agree closely and remain within 10% of one another. This gives us confidence that simulating charged sprays using the modelled Q-D method, is virtually the same as using a direct Q-D method. From a practical standpoint, the model Q-D method is a far easier alternative for specification of initial droplet charge than the direct Q-D method which relies explicitly upon having experimental measurements of spray droplet charges. For all sprays investigated, considering percentage estimates of the error for the modelled Q-D sprays alone, it is clear that profiles of mean droplet diameter are well predicted. For modelled Q-D sprays (i)-(iv), percentage estimates of the error for mean droplet diameter range from 5.1% to 15.4%. Similarly for sprays (v)-(vi), percentage estimates of the error range from 0.8% to 34.1% where it is interesting to note, the spray with the fastest injection velocity is most accurate in the prediction of mean droplet diameter. With regards to the mean axial velocity of droplets, percentage estimates of the error range from 14.6% to the highest of 73.9% corresponding to the spray with the fastest injection velocity, unfortunate considering the accurate prediction of mean droplet diameters for the same spray case. Although only present in a single spray investigated, this may suggest an existence of a trade off

between accurate prediction of mean droplet diameters, and the not so accurate prediction in mean axial droplet velocities. Lastly, percentage estimates of the error for mean radial droplet velocities across the modelled Q-D sprays range from 12.7% to 26.3%.

8.10.3 Analysis of Small Droplet ($D < 100\mu m$) Dynamics Between Modelled Q-D Sprays (i) and (vi), Against Experiments

Figures 8.15 and 8.16 include mean axial velocity profiles for small droplets in sprays (i) and (vi) respectively. In spray (i), the mean axial velocity for small droplets residing near the centreline, is significantly greater in the model Q-D spray than in the experiment. However, with increasing radial displacement from the centreline, the model Q-D profiles decrease in axial velocity and eventually cross over corresponding profiles from the experiment, leading to an under-prediction in mean axial velocities. It is also evident across profiles, that the location where crossover occurs, increases radially with an increase in downstream displacement. A different behaviour is observed for spray (vi) where across profiles, the model Q-D spray under-predicts mean axial velocity for small droplets throughout the spray plume. This under-prediction is most pronounced along the spray centreline and close to the atomizer. Notably, across both model Q-D sprays, mean axial velocity profiles for small droplets cross to negative values unlike the profiles from experiments that remain with positive values tending towards zero with an increase in radial displacement.

Likewise, figures 8.19 and 8.20 include the mean radial velocity profiles of small droplets for sprays (i) and (vi) respectively. In spray (i), evidence shows that downstream from the atomizer, radial velocities for small droplets in the model Q-D spray are significantly greater than in the corresponding experiment. For spray (vi) on the other-hand, small droplets of the model Q-D spray tend to have lower mean radial velocities than in the experiment. Significantly, the radial velocity profiles of spray (vi) at locations z = 0-60mm, are far more negative in values than profiles of the experiment. One may recall that droplet recirculation, indicated by negative values for the radial droplet velocity, occurs due to the strong electric field near the earthed body of the atomizer. An increase in droplet charge will increase the effect that the electric field has on the droplet motion.

This explains why near the atomizer, small droplet mean radial velocities in the model Q-D spray, are far more negative in value than with experiments. Further downstream from the atomizer, at locations $z > 60mm$, mean radial velocity profiles of the model Q-D spray and experiment are far better in agreement with each other. There is also a slight tendency for mean radial velocity profiles of the model Q-D spray, to have smaller velocities than the experiment which appears to be negligible considering the difference in values between profiles.

To summarize these particular sets of results, profiles for mean droplet axial and radial velocities across both computed sprays, suggest that too much charge is being specified for small droplets using the model Q-D method. This subsequently affects the electric field generated by the charged spray, therefore changing the dynamics of droplet motion throughout. With regards to r.m.s velocity profiles, significant disagreements to experimental profiles were evident for all computed sprays. However, despite these disagreements, profiles are able to illustrate a characteristic structure in the dynamics observed across computed sprays.

8.11 Summary

Following analysis of the qualitative and quantitative results, it is evident that general characteristics of a charged liquid spray can successfully be reproduced using the numerical methodology and procedure developed in this study. Percentage estimates of the error for modelled Q-D and direct Q-D sprays remain within 10% of one another. This showed that modelling droplet charge according to a scaling droplet diameter relationship, proves just as reliable as directly using experimentally obtained droplet charge measurements.

Computed mean droplet diameters across the spray plumes showed good agreement with experimentally obtained statistics. The only discrepancies observed was the slight tendency to over-predict mean droplet diameters along spray centrelines. These discrepancies were found to be a side effect of reduced small droplet presence along the spray centreline, subsequently biasing droplet diameters and mean axial velocities to

higher values. This effect was more pronounced for model Q-D sprays than for direct Q-D sprays due to limitations of both methods defining up to first and second order moments respectively for the specification of initial droplet charge. Using the modelled Q-D method, mean droplet diameters appeared to be the most well predicted for the spray with the fastest injection velocity with the percentage estimate of the error remaining less than 1%. This indicates a strong suitability of simulations for predicting characteristics of high speed, $\geq 34m/s$, sprays.

With regards to the dynamics of droplets, mean axial velocity profiles of the model Q-D sprays were generally close in agreement to experiments. However, near the spray centreline the mean axial velocity of droplets was found to be significantly greater than experiments due to bias caused by increased presence of large droplets with high velocities at the spray centreline. Percentage estimates of the error for mean axial velocity range from 14.6% to the highest of 73.9% corresponding to the spray with the fastest injection velocity. With this result for the spray with the fastest injection velocity, it was noted that a trade-off may exist between the accurate prediction of mean droplet diameters and prediction of mean axial droplet velocities in high speed, $\geq 34m/s$, sprays. Further work involving charged high speed sprays should provide closure to such indications.

The most consistent agreement between modelled Q-D sprays and experiments was shown with the mean radial velocity profiles. Percentage estimates of the error ranged from 12.7% to 26.3%. The characteristic shape of the mean radial velocity profiles was successfully reproduced, including the initial droplet acceleration away from the spray core, followed by a deceleration with increasing radial displacement. In addition, comparisons between model Q-D and experimental sprays highlighted the characteristic presence of droplet recirculation back to the earthed atomizer body. Although generally good agreements with experiments were shown, there was also the occasional discrepancy with behaviour. The most likely cause of these discrepancies is due to subtle differences in the Q-D relationship between computations and experiments. Upon closer examination of small droplet dynamics, mean axial and radial velocity profiles indicated that the model Q-D method specifies too much charge for small droplets. Due to the impact of the electric field upon small droplets with high charge-to-mass ratios, variation in the

Q-D relationship induces a lack of, or an increased abundance of small droplets in the spray plume. This subsequently biases mean velocities accordingly. It should also be noted that an interplay exists between the charge specified on all droplets in the spray and the electric field generated from the charged droplets. A change in the droplet Q-D relationship causes a change in the way that the electric field is formed which in turn, changes the spatial statistics for all droplet diameter classes in the spray plume.

Finally, this section briefly highlight some general recommendations to serve as a quick reference set of guidelines for simulating electrostatically atomized dielectric liquid sprays.

- The methodology presented in this paper can be readily extended to encompass 3D spray systems and is suitable for the simulation of free sprays, such as those for simulating paint spraying over earthed surfaces, or enclosed sprays in industrial applications.
- Providing that primary spray conditions are known, such as the injected liquid physical properties, desired mass and charge flow-rates, spray cone angle, initial droplet diameter distribution, and the near-orifice external atomizer geometry, the procedure detailed herein can be successfully used in CFD simulations to predict the characteristics of electrostatically atomized dielectric liquid sprays for low pressure spray systems.
- It should be noted that jet break-up modelling according to the procedure outlined in this paper is suitable for point-plane (Malkawi 2009; Shrimpton and Yule 1999; Rigit and Shrimpton 2006; Kourmatzis and Shrimpton 2012) and plane-plane type, (Malkawi 2009), charge injection atomizers.
- Attention should be made to ensure conservation of injected charge and liquid mass within the CFD simulation.
- Earthed surfaces in the vicinity of the spray plume should be accounted for with appropriately defined boundary conditions.

8.12 Further Work

As far as the aims in this chapter are concerned, the study on low pressure, electrostatically atomised and charged liquid sprays is complete. The only identified area for future work would be the methodology's extension towards other charge injection devices, such as the electrostatic pressure swirl nozzle, (Laryea and No 2004). This could be achieved relatively easily and would only require some procedural changes to the numerical method that defines initial droplet conditions within the computational domain. Whilst it is entirely possible for the modelled charge-diameter relationship to depend on the type of atomizer device used, further experimental work would still be useful to re-affirm such relationship. Although this study is restricted to 2D spray systems, this methodology can be readily extended to encompass 3D spray systems. However, this extension would be something beyond the scope of this thesis.

Nevertheless, further work extending on the knowledge gained from this study is covered within the remaining chapter of this thesis. This extends towards the CFD prediction of charged high pressure spray behaviour, where secondary atomization plays an dominant role in the subsequent characteristics and dynamics of the spray plume.

Chapter 9

Modelling Secondary Atomization in Charged High Pressure Sprays

9.1 Introduction

In chapter 8, computational analysis of charged sprays was restricted to the development and successful validation of a numerical methodology suitable for low pressure spray systems, with typical injection velocities of $< 30m/s$. To extend on this knowledge, this chapter shifts focus to simulations of high pressure charged spray systems, whereby larger droplets in the spray plume disintegrate into smaller droplets through the mechanism known as secondary atomization. Such systems are pertinent to applications like combustion engines, where high pressures are typically required for fuel injection within engine cylinders. From literature, only a select few experiments deal specifically with electrostatic atomization at high injection pressures, (Sehili and Romat 2002; Kourmatzis and Shrimpton 2012; Bankston et al. 1988; Kwack et al. 1989). Yet as far as CFD is concerned, there is still to be any validation that addresses the numerical methodology required for successful simulation of a charged high pressure spray system. This hurdle remains outstanding for developing the idea of applying charge injection technology to improve fuel spray dynamics prior to combustion.

Therefore, the purpose of this particular investigation is to answer the question, *Can simulations successfully account for charged high pressure spray behaviour that includes secondary atomization?*

To address this question, numerical methodologies of selected secondary atomization models within the context of RANS based CFD simulations and experiments of charged high pressure sprays are evaluated.

9.2 Physical Principles of Secondary Atomization

9.2.1 Introduction

Secondary atomization in sprays is predominantly caused by the relative velocity occurring between droplets and their surrounding gas. Droplets moving through a turbulent gas experience velocity and pressure perturbations due to varying aerodynamic forces imposed on their surface. These perturbations act to deform the droplet away from its most stable state governed by its material surface tension. The non-dimensional parameters that characterise the criterion for break up are known as the droplet Weber number We defined by,

$$We = \frac{\rho_f u_{rel}^2 D}{\sigma} \tag{9.1}$$

and the Ohnesorge number Oh,

$$Oh = \frac{\sqrt{We}}{Re} = \frac{\mu_d}{\sqrt{\rho_d \sigma D}} \tag{9.2}$$

In these equations, the surface tension is responsible for the cohesiveness properties of the droplet surface, and dynamic viscosity responsible for the dampening of unstable perturbations. An increase in viscosity essentially corresponds to a slowing down of the droplet deformation process. This allows time for drag forces to react, reducing relative velocities and the potential for the droplet to breakup. If the Weber number for a given

droplet exceeds a critical Weber number We_{crit}, only then will the droplet undergo breakup. According to the review of Faeth (2002), We_{crit} is constant for $Oh < 0.1$ and the effect of dynamic viscosity is negligible. For $Oh > 0.1$, the empirical correlation of Brodkey (1967) may be used.

$$We_{crit} = 12(1 + 1.077Oh^{1.62}) \tag{9.3}$$

9.2.2 Droplet Deformation Prior to Secondary Atomization

Qualitatively, prior to the onset of secondary atomization for $We < We_{crit}$, the droplet experiences a deformation that may be approximated as an oblate spheroid.

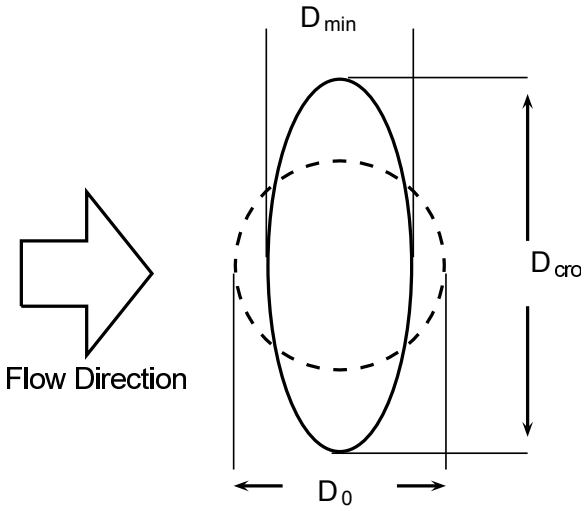

FIGURE 9.1: Diagram of Deformed Droplet

Here the diameters D_0, D_{cro} and D_{min}, correspond to the initial spherical droplet diameter, the cross-stream diameter normal to the flow direction, and the minimum diameter parallel to the flow direction respectfully.

Zhao et al. (2011) showed that at the onset or secondary atomization, droplet deformation was related to the Weber number of the surrounding fluid such that,

$$\left(\frac{D_{\text{cro}}}{D_0}\right)_{\max} = \left(\frac{D_{\min}}{D_0}\right)^{-1/2} = 1 + 0.2We^{0.56}(1 - 0.48Oh^{0.49}) \tag{9.4}$$

For $Oh > 0.1$, the maximum deformation of the droplet at a given Weber number decreases due to slowing of the rate of deformation, which subsequently reduces the droplets relative velocity. Here $(D_{\text{cro}}/D_0)_{\max}$ represents the maximum possible deformation which occurs at the onset of secondary atomization. Considering the effects of droplet deformation on drag characteristics, the correlation by Liu et al. (1993) may be utilised, that approximates drag of a deformed droplet as a linear function of deformation.

$$C_D = C_{D,Sphere}(1 + 2.632y) \tag{9.5}$$

Here $y = 1 - (D_0/D_{cro})^2$ is the non-dimensional displacement of the droplet equator, and $C_{D,Sphere}$ the co-efficient of drag for a sphere.

$$\begin{aligned} C_{D,Sphere} =& \frac{24}{Re}\left(1 + \frac{1}{6}Re^{2/3}\right) && ; Re \leq 1000 \\ =& 0.44 && ; Re > 1000 \end{aligned} \tag{9.6}$$

9.2.3 Regimes of Secondary Atomization

For $We > We_{crit}$, different droplet breakup regimes may be identified, (Faeth et al. 1995). These breakup regimes are shown as a function of Ohnesorge and Weber numbers in figure 9.2, and are typically identified for $Oh < 0.1$ as follows.

- Bag, $12 < We < 20$
- Multi-mode, $20 < We < 80$
- Stripping, $80 < We < 800$
- Catastrophic, $We > 800$

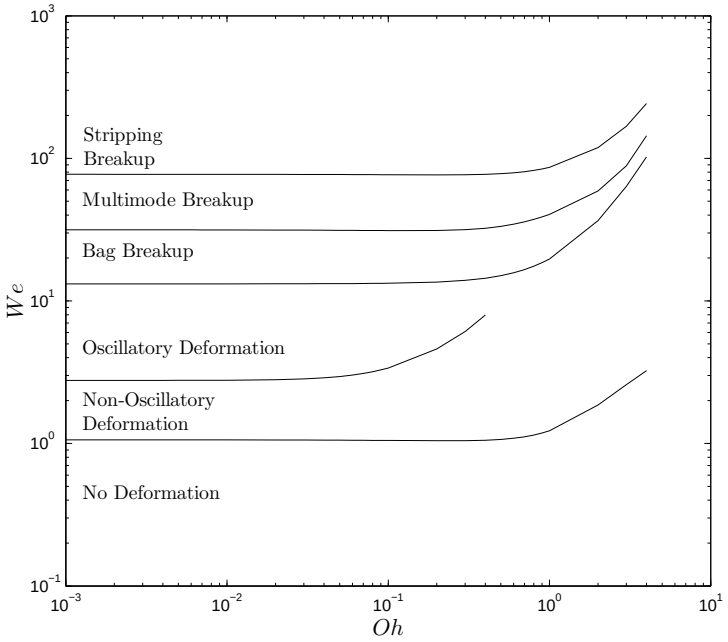

FIGURE 9.2: Regimes of droplet deformation and breakup, (Hsiang and Faeth 1992).

Many authors have reported different ranges of We classifying the aforementioned breakup regimes, but regardless is the fact that as droplet Weber numbers increase, different breakup mechanisms occur, (Guildenbecher et al. 2009). Within the bag regime, the breakup process starts with the the deformation of a droplet into a thin disk shape normal to the flow direction. This is followed shortly after by formation and growth of a ring and bag-like structure, with the bag structure extending towards the downstream direction. Here breakup occurs through subsequent disintegration into smaller droplets. The transition from bag to shear regimes of breakup is covered uniquely by the multi-mode regime, with subdivisions termed bag-plume and plume-shear, with a transition occurring at approximately $We \approx 40$. Droplets that undergo breakup within the bag-plume regime exhibit the same deformation towards formation of ring and bag structure, but with additional presence of a plume structure that points upstream and forms at the tip of the bag, (Dai and Faeth 2001). Distinguishing between bag-plume and plume-shear breakup is the fact that either breakup is caused through disintegration of structures, or the stripping due to shear of the structures respectfully. Typically, shear breakup involves some deflection of the flattened droplet disk periphery towards the downstream direction, with stripping of small droplets occurring from the periphery

of the structure. Lastly for the catastrophic regime, droplets disintegrate into smaller and smaller fragments through Rayleigh-Taylor instabilities (Wang et al. 2010).

9.2.4 Time-scales of Secondary Atomization

Most secondary atomization processes occur over a finite period of time. Experimentally measured time-scales for these processes are typically made non-dimensional using the characteristic droplet deformation time-scale derived by Ranger and Nicholls (1969).

$$\tau^* = \frac{D}{u_{rel}} \left(\frac{\rho_d}{\rho_f} \right)^{1/2} \tag{9.7}$$

The duration for initial droplet deformation t_{ini} is typically a constant $1.6\tau^*$, (Hsiang and Faeth 1992). Beyond such a duration, the droplet is said to undergo breakup that lasts for a finite period of time denoted by t_b. Following a survey on hydrodynamic fragmentation, Pilch and Erdman (1987) devised a set of correlations that characterised the total breakup time of droplets, spanning a wide range of Weber numbers.

$$\begin{aligned}
\frac{t_b}{\tau^*} &= 6\left(We - 12\right)^{-0.25} && ; 12 < We < 18 \\
&= 2.45\left(We - 12\right)^{0.25} && ; 18 < We < 45 \\
&= 14.1\left(We - 12\right)^{-0.25} && ; 45 < We < 351 \\
&= 0.766\left(We - 12\right)^{0.25} && ; 351 < We < 2670 \\
&= 5.5 && ; We > 2670
\end{aligned} \tag{9.8}$$

These correlations form the basis of the Pilch-Erdman secondary atomization model that shall be introduced later in section 9.3.2 of this chapter.

9.2.5 The Effects of Droplet Charge upon Secondary Atomization

9.2.5.1 Maximum Droplet Charge

To encompass the effects of droplet charge within the principles of secondary atomization, one may consider the effect of charge upon the stability of an isolated, electrically charged spherical liquid droplet without the presence of any externally applied electric field. Furthermore, one can assume the free charge is distributed evenly over its surface such that no internal electrical field exists. Firstly, the presence of charge on a droplets surface generates an electric field normal to the surface E_s, such that,

$$E_s = \frac{Q_d}{\pi \epsilon_0 D^2} \tag{9.9}$$

Here the field normal to the droplet surface must remain below the critical field strength E_c of the fluid, comprising the drop and its surrounding continuum such that $E_s < E_c$, (Bailey 1986). If this condition is violated, the droplet will discharge just enough charge from its surface to the surrounding continuum, in order to maintain the surface electric field below this critical field strength. This process is known as coronal discharge, where charge may be lost from the droplet without any formation of breakup products. The diameter of the droplet at this critical field strength is given by,

$$D_c = \frac{8\sigma}{\epsilon_0 E_c^2} \tag{9.10}$$

Typically, for hydrocarbon oils $E_c \approx 10^8 V/m$ which means that for most practical cases considered in this study, the droplet diameter at the critical field strength remains small and in the order of $O(D_c) \approx 1\mu m$. Since D_c is small, modelling coronal discharge[1] is unnecessary.

[1]Coronal discharge is different from electrical breakdown of the fluid that occurs within the nozzle prior to atomization. The two are however related by the critical field strength.

If one assumes that the field normal to the droplet surface is equal to the critical field strength such that $E_s = E_c$, one can combine together equations (9.9) and (9.10), to define a theoretical maximum charge level that a droplet may hold. This is known as the droplet Rayleigh limit[2].

$$Q_{ray} = 4\pi\sqrt{0.5\epsilon_0\sigma D^3} \tag{9.11}$$

In essence it defines the charge level at the point where the effective surface tension goes to zero, and droplet disruption occurs. In reality, the Rayleigh limit is rarely ever reached due to the fact that either electrical, or aerodynamic forces act to deform the droplet away from the perfect electrical and physical symmetry conditions that are assumed. It has been suggested that due to these deviations, the maximum charge on a droplet created via electrostatic atomization is limited in practice to typically 80% of the Rayleigh limit, (Shrimpton 2009). Nevertheless, the process of disruption caused by exceeding the Rayleigh limit at diameters greater than D_c may also lead to Coulomb fission events, whereby a stream of sibling droplets, each carrying with them a fraction of the parent's mass and charge, are ejected from the droplets surface, (Taflin et al. 1989; Gomez 1994; Shrimpton 2009).

9.2.5.2 Charged Droplet Fission

Theoretical analysis performed on charged droplet fission processes have predominately relied upon the minimization of Gibbs free energy technique (Roth and Kelly 1983; Rohner et al. 2004; Shrimpton 2008), using knowledge of parent droplet parameters, and assumptions relating to the formation of a stream of ejected sibling droplets. To model the Coulomb fission process, the relationships given by Gu et al. (2007) and Hunter and Ray (2009) may be used.

[2]An alternative way to derive equation (9.11) is to start from a thermodynamic point of view by considering the total reversible work to increase the area and charge of a free surface, (Cerkanowicz 1981)

$$\frac{f_q}{f_m} = C\sqrt{\frac{\rho_d D_0^3}{8\sigma}}\frac{k}{\epsilon_0 \epsilon_r} \tag{9.12}$$

Here, $f_q = \Delta Q/Q_d$ and $f_m = \Delta m/m_d$ denote the fractional charge and mass lost from the parent to sibling droplets. The empirical constant in equation (9.12) was calculated to be $C \approx 14.78$. This constant was found following numerical tests of equation (9.12) with input parameters from known experimental observations (Shrimpton 2009; Gomez 1994; Taflin et al. 1989), predicting that parent droplets typically lose between 10-18% of their charge, and 1-2.3% of their mass (Taflin et al. 1989). Any number between $n_p = 7$-30 of sibling droplets may eject from the parent droplet during fission (Feng 2001), each with a diameter $\approx 10\%$ of their parents original droplet diameter prior to fission (Taflin et al. 1989). Assuming identical sibling droplets and a uniform variation of ΔQ, Δm, and n_p within experimentally observed ranges, one can subsequently calculate the size and charge held by sibling droplets produced during the Coulomb fission process.

For evaporating droplets whereby mass is lost without any loss of charge from the surface, modelling the Coulomb fission process is essential to ensure that total spray evaporation rates are predicted as accurately as possible. Evaporation rates are promoted in sprays by the increase in number of small droplets, and the subsequent increase in total spray surface area, relative to a spray containing the same volume of liquid across larger droplet sizes. Although evaporation does not occur for high pressure sprays investigated in this study, after numerical tests approximately 2% of spray droplets were found to exceed their Rayleigh limits after aerodynamically induced secondary atomization. Coulomb fission mechanisms were therefore considered negligible for purposes of this study[3].

[3]Without the presence of evaporation, modelling the Coulomb fission processes resulted in significantly over-predicted numbers of small droplet diameters within the spray. For computed sprays where evaporation occurs, one expects that small droplets will quickly disappear due to mass loss to the surrounding continuum.

9.2.5.3 Charge Mobility on Liquid Droplets

Extending on the knowledge regarding electrostatic charge on droplets, an experimental study by Guildenbecher et al. (2009) noted that breakup is not only a function of charge level, but also dependant on the rate of charge movement, (Cloupeau and Prunet-Foch 1990). It was therefore assumed that similar dependencies exist within the principles of secondary atomization. To account for this, all fluids are said to posses a resistivity resulting in a finite rate of charge movement, characterised by the charge relaxation time τ_Q.

$$\tau_Q = \frac{\epsilon_0 \epsilon_r}{k} \tag{9.13}$$

Here ϵ_r is the relative permittivity of the liquid otherwise known as the dielectric constant, and k the electrical conductivity of the liquid measured in Siemens per metre. This charge relaxation time can be made non-dimensional using the characteristic droplet transport time-scale of equation (9.7), yielding the conductivity number k^* which is given by,

$$k^* = \frac{\epsilon_0 \epsilon_r}{k} \frac{u_{rel}}{D} \left(\frac{\rho_f}{\rho_d} \right)^{1/2} \tag{9.14}$$

The conductivity number allows a comparison between the time-scale of charge movement throughout the droplet, to the characteristic breakup time of a droplet undergoing secondary atomization. Therefore, when $k^* \ll t_b^*$, the rate of charge movement is assumed to be much faster than the rate of deformation, such that the charge will re-distribute itself fast enough throughout the droplet, by migrating and spreading uniformly across the droplet surface to achieve a distribution that minimizes electrostatic stresses. In such a scenario, the balance between electrostatic and surface tension forces is assumed to be independent of position on the droplet surface. Alternatively, when $k^* \gg t_b^*$, the rate of charge movement is much slower, and hence assumed to be frozen

throughout the droplet breakup process. Any deformation whether it be prior to or during secondary atomization, may therefore result in a faster breakup process. Guildenbecher et al. (2009) examined this effect, but found no significant impact upon either the initial breakup times, nor total breakup times of charged droplets undergoing secondary atomization. This is not to say a role does not exist, but rather the effect of charge mobility is hidden within existing experimental uncertainties, and the dominant mechanisms associated with aerodynamic induced fragmentation.

9.2.5.4 Effective Surface Tension

For a perfectly conducting droplet, charge is allowed to move freely and infinity fast such that no internal electric field can exist. Perfectly insulating droplets on the other hand have no free charges, therefore any externally sprayed ionic charges, or embedded immobile charges remain fixed upon or within the droplet. In reality, a finite electrical conductivity and charge mobility exists throughout the droplet, providing a transient state whereby the electric field across the droplet continuously varies, and a scenario whereby the surface charge density maybe non-uniform over the droplet surface. In such a scenario, disruption may still occur providing that localised electrostatic disruptive forces are sufficiently large to overcome restorative forces due to surface tension.

To account for electrically charged droplets, one may equate a force balance between the surface tension restorative forces of a spherical droplet associated with inter-molecular cohesion of the liquid, and disruptive forces associated with Coulomb repulsion of electrostatic charge that acts to pull apart a droplet.

$$F^* = 4\pi\sigma D - \frac{Q_d^2}{2\pi\epsilon_0 D^2} \tag{9.15}$$

By dividing equation (9.15) by $4\pi D$, one may then obtain an equation for the effective surface tension.

$$\sigma^* = \sigma - \frac{Q_d^2}{8\pi^2\epsilon_0 D^3} \tag{9.16}$$

This equation is valid within limits, such that as $Q_d \rightarrow 0$, $\sigma^* \rightarrow \sigma$, and as $Q_d \rightarrow Q_{ray}$, $\sigma^* \rightarrow 0$. Subsequently, equation (9.16) may be used in place of σ, appearing in (9.1) and (9.2), to yield corresponding electrostatic Weber We_{e-} and Ohnesorge Oh_{e-} numbers. Usage of σ^*, We_{e-}, and Oh_{e-} can then be incorporated within existing droplet deformation and secondary atomization models.

An increase in surface charge density leads to increased droplet We_{e-} and Oh_{e-} numbers, and at elevated Oh_{e-} numbers We_{crit} also increases. However, the observed breakup modes for droplets that exceed We_{crit} within a given Weber number range remain the same (Guildenbecher and Sojka 2009). With a predicted increase in the dampening of unstable perturbation with increasing Oh_{e-}, there is yet a greater influence of charge on We_{e-} numbers, subsequently increasing the likelihood of secondary atomization. This was validated during an experimental study by Guildenbecher and Sojka (2008), who showed that for highly conductive liquids, use of equation (9.16) leads to a better agreement with the Pilch and Erdman (1987) break-up time correlations, introduced previously in section 9.2.3.

9.3 Modelling Secondary Atomization

Secondary atomization models all attempt to replicate the dynamics, characteristics and physical mechanisms observed throughout different droplet breakup regimes. Many researchers (Chou and Faeth 1998; Reitz and Diwaker 1986; Reitz and Diwakar 1987; Pilch and Erdman 1987) have developed models accounting for these different droplet breakup regimes, all for the purpose of enabling cost-beneficial numerical simulation of secondary atomization phenomena. Most models are based upon observed droplet breakup processes, encompassing a wide range of experimental and practical scenarios. Yet with all models comes the inherent limitation of application robustness. Some models are reliable for low Weber number applications such as the Taylor Analogy Breakup (TAB) model of O'Rourke and Amsden (1987), and others more suitable for high Weber number applications such as the Wave breakup model of Reitz and Diwakar (1987). It is nevertheless convenient, to examine models that are applicable to a wide range of

practical scenarios, yet relatively straightforward with their design and numerical implementation. In this section, breakup models developed by Reitz and Diwaker (1986) and Pilch and Erdman (1987) are examined, where a choice is made as to which model should be used for subsequent CFD investigations regarding charged high pressure sprays.

9.3.1 The Reitz and Diwaker Breakup Model

The Reitz and Diwakar breakup model has been employed in many modern commercial CFD codes and has remained consistent at predicting typical spray penetration characteristics from experiments across the years, (Hiroyasu et al. 1990; Naber and Siebers 1996; Kennaird et al. 2002). The breakup model of Reitz and Diwaker (1986), assumes that primary atomization of the liquid jet and initial droplet breakup dynamics are indistinguishable processes within the dense spray core near the nozzle exit. Primary atomization is typically prescribed by injecting droplets that have a characteristic size equal to the exit orifice diameter of the nozzle, which subsequently breakup due to interactions with the gas phase in which they penetrate.

Droplet breakup is modelled given conditions that define two different breakup regimes. The bag breakup regime occurs when,

$$We = \frac{\rho_f u_{rel}^2 D}{\sigma} > 12 \tag{9.17}$$

and the stripping breakup regime occurs conditionally when,

$$\frac{We}{\sqrt{Re}} > 1.0 \tag{9.18}$$

Here, the Reynolds number of the droplet is calculated according to equation 3.23. Within the bag regime, the lifetime of unstable droplets is assumed to be proportional to the droplets natural frequency as,

$$t_{bag} = C_{bag} \left[\frac{\rho_d D^3}{8\sigma} \right]^{1/2} \tag{9.19}$$

with the co-efficient $C_{bag} = \pi$. For the stripping regime the lifetime of unstable droplets is given as,

$$t_{strip} = C_{strip} \frac{D}{2u_{rel}} \left(\frac{\rho_d}{\rho_f} \right)^{1/2} \tag{9.20}$$

Here different values of the co-efficient C_{strip} have been reported in literature, with typical values ranging $5 - 20$ reported by Reitz and Diwakar (1987), and a value of $\sqrt{3}$ reported by O'Rourke and Amsden (1987). At a given distance downstream from the atomizer, smaller values for the C_{strip} co-efficient result in faster droplet breakup times, smaller stable droplet diameters and subsequently shorter spray core breakup lengths, (Reitz and Diwakar 1987). Typically, commercial CFD software packages assume a default co-efficient of $C_{strip} = 20$.

The numerical procedure for implementing this model is as follows. Firstly, the stability criterion's given by equations (9.17) and (9.18) are checked for each droplet parcel, at each timestep during simulation. If either criterion is met for the duration of the droplet breakup lifetimes given by equations (9.19) and (9.20), then a new droplet size for the parcel is specified according to the characteristic regime of breakup. The size of unstable droplets is allowed to vary continuously in time according to equation (9.21), reflecting the finite time required for the breakup physics to result in a stable droplet with a diameter of D_{stable}.

$$\frac{\mathrm{d}D}{\mathrm{d}t} = -\frac{(D - D_{stable})}{t_b} \tag{9.21}$$

Here $t_b = t_{bag}$ or $t_b = t_{strip}$ depending on the breakup mode occurring. D_{stable} is given by equation (9.22) for the bag regime of breakup, or equation (9.23) for the stripping regime of breakup respectively.

$$D_{stable} = \frac{12\sigma}{\rho_f u_{rel}^2} \tag{9.22}$$

$$D_{stable} = \frac{\sigma^2}{\rho_f u_{rel}^3 \mu_f} \tag{9.23}$$

Finally, the number of real droplets contained within a droplet parcel is updated to conserve liquid mass according to equation (9.24).

$$N_{d,n+1} = N_{d,n} \left(\frac{D_n}{D_{n+1}} \right)^3 \tag{9.24}$$

9.3.2 The Pilch and Erdman Breakup Model

The breakup model of Pilch and Erdman (1987) is solely based on empirical correlations derived from data, following an extensive literature survey on hydrodynamic fragmentation, (Pilch 1981). Since breakup processes occur over a period of time from the onset of secondary atomization, this model allows for the time-dependent, acceleration-induced breakup processes to be more accurately characterised than the model of Reitz and Diwaker (1986).

As before, droplet breakup is said to occur if the droplet Weber number becomes greater than the critical Weber number given by equation (9.3). The Pilch and Erdman (1987) correlations describing the non-dimensional total breakup times $\tau_b^* = t_b/\tau^*$, were presented earlier in section 9.2.4 of this chapter, and given by equation (9.8). In order to calculate numerically the dimensional breakup time of droplets, one can multiply τ_b^* by the characteristic droplet transport time-scale factor of Ranger and Nicholls (1969) given by equation (9.7).

It should be noted that correlations in the Pilch and Erdman model are just empirical fits to collated experimental data. To some extent, distinction is made between the unique regimes of breakup experienced by droplets, and the various correlations governing total droplet breakup times although not explicitly stated by Pilch and Erdman (1987).

Based on improved[4] estimates for average fragment droplet sizes produced in the bag and multi-mode breakup regimes (Wert 1995), the stable droplet diameter D_{stable} is evaluated using the following correlations.

For $12 < We < 18$,

$$D_{stable} = \frac{D_{0.5}}{D_{32}} 0.32 We^{2/3} \left[\frac{4.1}{(We-12)^{1/4}} \right]^{2/3} \frac{\sigma}{\rho_g u_{rel}^2} \tag{9.25}$$

for $18 < We < 45$,

$$D_{stable} = \frac{D_{0.5}}{D_{32}} 0.32 We^{2/3} \left[\frac{2.45(We-12)^{1/2} - 1.9}{(We-12)^{1/4}} \right]^{2/3} \frac{\sigma}{\rho_g u_{rel}^2} \tag{9.26}$$

for $45 < We < 100$,

$$D_{stable} = \frac{D_{0.5}}{D_{32}} 0.32 We^{2/3} \left[\frac{12.2}{(We-12)^{1/4}} \right]^{2/3} \frac{\sigma}{\rho_g u_{rel}^2} \tag{9.27}$$

and for $We > 100$,

$$D_{stable} = We_{crit} \frac{\sigma}{\rho_f u_{rel}^2} \left(1 - \frac{V_c^*}{u_{rel}} \right)^{-2} \tag{9.28}$$

In equation (9.28), V_c^* is the velocity of the fragment cloud post-breakup taking into account the decreasing relative velocity between droplets and the flow field due to changes in droplet acceleration, and is calculated via,

$$V_c^* = u_{rel} \left(\frac{\rho_f}{\rho_d} \right)^{1/2} \left(B_1 \tau_b^* + B_2 \tau_b^{*2} \right) \tag{9.29}$$

[4]These improved correlations were found to overcome the pitfalls in D_{stable} prediction for $We < 100$ originally noted by Pilch and Erdman (1987). These pitfalls were examined as part this study, with details given in section 9.3.3.2. The main issue with the standard Pilch and Erdman D_{stable} correlation, equation (9.28), was the fact that at the onset of secondary atomization at $We \approx We_{crit}$, D_{stable} was predicted to be greater than the diameter of the droplet undergoing physical breakup.

where co-efficients B_1 and B_2 are chosen to fit experimental data (Pilch 1981), and their values taken typically as 0.375 and 0.236 respectively[5]. Use of the relation $D_{0.5}/D_{32} = 1.2$ is also employed throughout equations (9.25)-(9.27), which relates the mass median to the Sauter mean diameter of the droplet fragment cloud post breakup (Simmons 1977). Figure 9.3 illustrates the variation of D_{stable}/D_0 as a function of We predicted by the improved correlations. Selected and most recent experimental observations on stable droplet diameters produced in the bag and multi-mode breakup regimes are included for reference, (Zhao et al. 2011; Chou and Faeth 1998; Dai and Faeth 2001; Kulkarni et al. 2012).

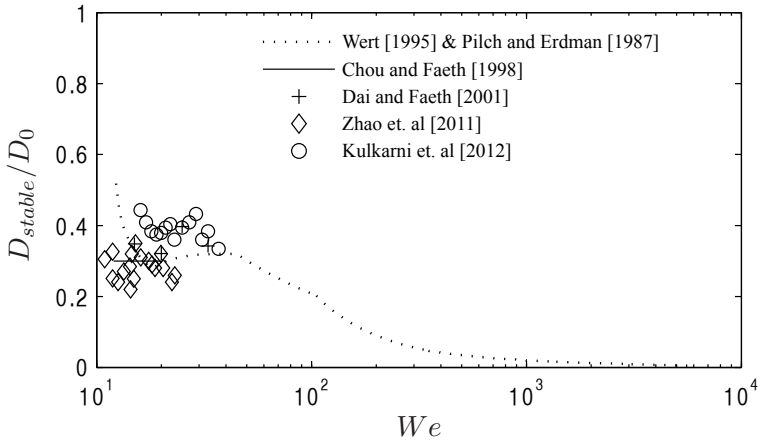

FIGURE 9.3: Influence of We on D_{stable}/D_0 predicted by correlations (9.25)-(9.28)

Lastly, the droplet diameter changes according to equation (9.21), and the number of real droplets contained within a droplet parcel is updated to conserve liquid mass according to equation (9.24).

9.3.3 Evaluation of Secondary Atomization Models

The aim of this section is to provide detailed analysis on modelled secondary atomization behaviour within the context of charged high pressure spray experiments listed in table 9.1. It is important at this stage to evaluate how well fundamentally these models account for the physical processes occurring during breakup, particularly the

[5]It should be noted here that according to Pilch and Erdman (Pilch and Erdman 1987), co-efficients B_1 and B_2 differ depending on whether incompressible or compressible flow is considered. For incompressible flow, co-efficients are in fact taken as 0.375 and 0.227, whereas for compressible flow these co-efficients are taken as 0.75 and 0.348 respectively.

time-dependent formation of breakup products from droplets undergoing secondary atomization.

Firstly, a summary of charged high pressure spray experiments from Kourmatzis and Shrimpton (2012) is introduced, along with a brief discussion on the characteristics of those sprays. Next, predicted total breakup times and stable droplet diameters computed via Reitz-Diwaker and Pilch-Erdman models are presented for a range of priori charge levels. Focus at this stage is on how the breakup models operate numerically, rather than how the models predict characteristics between experiments. An evaluation is then made between computed predictions, and the corresponding experimental evidence documented throughout literature, on the capability of models in predicting breakup behaviour for realistic high pressure sprays. Lastly, justification is made on the chosen model suitable for the subsequent investigation presented in this chapter on charged high pressure sprays.

9.3.3.1 Summary of Experiments

The primary investigation of Kourmatzis and Shrimpton (2012) was to assess the electrical and atomization performance of Diesel fuel spray injected from a plane-plane type, charge injection atomizer at pump pressures ranging from 15 to 35 bar. Such pressures correspond to injection velocities of up to $50m/s$, and due to these high injection velocities present, spray specific charges up to 6 C/m^3, were successfully injected into the spray. Spay specific charges of such had never been achieved prior to experiments of Kourmatzis and Shrimpton (2012), and implications are considered significant in terms of advancing electrostatic atomization technology towards industrial application with real-world high pressure spray systems. The general structure of spray plumes was examined through use of high quality spatial PDA measurements, made on three of the experiments published by Kourmatzis and Shrimpton (2012). A summary detailing the operating conditions of these experiments are listed in table 9.1, along with liquid properties for the Diesel fuel used listed in table 9.2.

Kourmatzis and Shrimpton (2012) attempted to address the effect of charge on the initial liquid jet properties of the spray, considering classical laminar and turbulent jet theory

Case	U_{inj} (m/s)	$\dot{m}$ (kg/s)	Q_v (C/m^3)	Re_j	We_j
1P	37	0.38	6	1943	5750
2P	40	0.41	6	2100	6720
3P	48	0.49	5.5	2520	9677

TABLE 9.1: Operating conditions for charged high pressure spray cases from experiments of Kourmatzis and Shrimpton (2012). For all spray cases, Diesel fuel was used, the orifice diameter d_{inj} was $125\mu m$, and the surrounding gas density throughout the spray was $1.184kg/m^3$.

Property	**Diesel**
Density, kgm^{-3}	840
Dynamic Viscosity, $kgm^{-1}s^{-1}$	0.002
Surface Tension, Nm^{-1}	0.025
Relative Permittivity	2.0
Electrical Conductivity, pSm^{-1}	5.0
Molecular Weight, $kgmol^{-1}$	0.2
Critical Pressure, MPa	1.8
Critical Temperature, K	659
Freezing Temperature, K	277.6

TABLE 9.2: Properties of Diesel fuel at $293K$ unless otherwise stated.

of Schweitzer (1937) and Wu et al. (1995) respectively. By assuming a cylindrically charged jet instead of spherically charged droplet, an effective surface tension of the form shown in equation (9.30) was derived.

$$\sigma^* = \sigma - \frac{Q_d^2 d_{inj}^3}{48\epsilon_0} \tag{9.30}$$

Kourmatzis and Shrimpton (2012) showed that for low levels of injected spray specific charge, usage of equation (9.30) for the prediction of liquid jet breakup length yielded an error of 23% compared to experimental measurements. However, for high levels of injected spray specific charge, usage of equation (9.30) yielded negative values for σ^*, predicting an immediate disintegration of the liquid jet. Unfortunately this fact prevents any prediction on the likely breakup regimes experienced by liquid jets, using classical Re_j vs Oh_j graphs.

The analysis provided by Kourmatzis and Shrimpton (2012) did not cover effects of electrical charge upon secondary atomization performance. However, mention was made as to the existence of secondary atomization via evidence shown in droplet diameter PDFs

obtained from PDA measurements taken along the spray centreline. On this matter, a bi-modal PDF was present at locations closer to the nozzle exit orifice for cases 1P and 2P of table 9.1. With further downstream displacements, the bi-modal PDF peaks for case 1P remained relatively unchanged, whereas for case 2P the peak density present at larger droplet diameters gradually diminished, whilst the peak density present at smaller droplet diameters increased. For case 3P, a uni-modal PDF was observed with a single peak present at small droplet diameters for all sampled downstream displacements. These observations showed that secondary atomization in as an ongoing process, with characteristics unique to the spatial and temporal development of the spray plume.

9.3.3.2 Predicting Breakup Times and Stable Droplet Diameters

To evaluate how well secondary atomization models predict total breakup times and stable droplet diameters, a range of priori values representative of initial spray conditions from experiments listed in table 9.1 are chosen. For each experimental spray, the parameter ranges are as follows;

- Droplet charge Q_d was varied between $0 - 90\%$ of Q_{ray} at intervals of 10% Q_{ray}.
- Initial droplet diameter D_0 prior to breakup was varied between $0 - 200\%$ of d_{inj} at intervals of 8% d_{inj}.
- Relative droplet velocity u_{rel} was varied between $90 - 110\%$ of U_{inj} at intervals of 2% U_{inj}.

Original unmodified Reitz-Diwaker and Pilch-Erdman models were programmed as functions within the MATLAB® environment, taking as an input the numerical values of droplet charge, initial droplet diameter, and relative droplet velocity. Predicted total breakup times and stable droplet diameters after breakup were computed for each combination of parameters. Results from these predictions are plotted as functions of droplet Weber number, utilising an effective surface tension in the form given by equation (9.16)

to account for droplet charge. Total droplet breakup times are reported in their dimensional forms, and stable droplet diameters are reported in their non-dimensional forms, as a ratio against their initial diameter prior to breakup.

Predicting Droplet Breakup Times

Figures 9.4 and 9.5 detail predicted total droplet breakup times as a function of droplet Weber number for Reitz-Diwaker and Pilch-Erdman models respectfully. From figure 9.4, it is evident that only the stripping mode criterion of breakup is met, (i.e. $We/\sqrt{Re} > 1.0$), for all combinations of parameters examined. Experiments performed by Hsiang and Faeth (1992) have distinctly shown that bag breakup occurs for droplets with Weber numbers ranging from 12 to 20, so it is peculiar as to why Reitz and Diwaker (1986) imply use of the criteria $We/\sqrt{Re} < 1.0$ for $We > 12$ to define bag breakup, when clearly the known droplet behaviour observed from experiments contradicts this assumption. Prior to Reitz and Diwaker (1986), Gelfand (1974) noted that breakaway of the liquid surface from the droplet followed only when the condition,

$$\frac{We}{\sqrt{Re}} > A(p) \tag{9.31}$$

was satisfied. Here $A(p)$ was some constant of proportionality determined by,

$$A(p) = 1.5 \left(\frac{\rho_d}{\rho_f}\right)^{1/4} \left(\frac{\mu_f}{\mu_d}\right)^{1/2} \tag{9.32}$$

Usage of equation (9.31) within Gelfand et al. (1974) was found to be in relation to the scenario of droplets subjected to secondary atomization in highly pressurized environments ranging 1-50atm. However, the validity of equation (9.31) was found only to be relevant for droplets with $We \approx 283$, and not droplets spanning other Weber number ranges. It therefore is no surprise that the equivalent criterion used within the Reitz-Diwaker model fails to provide an upper-bound limiting the conditions defining the bag regime breakup. Results shown in figure 9.4 should therefore be treated with extreme scepticism. Nevertheless, total droplet breakup times computed via the Reitz-Diwaker model show no dependency upon classical droplet breakup regimes when distinguished

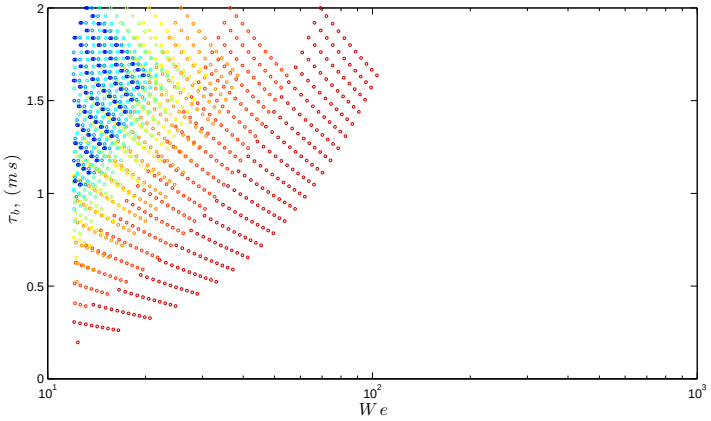

(a)

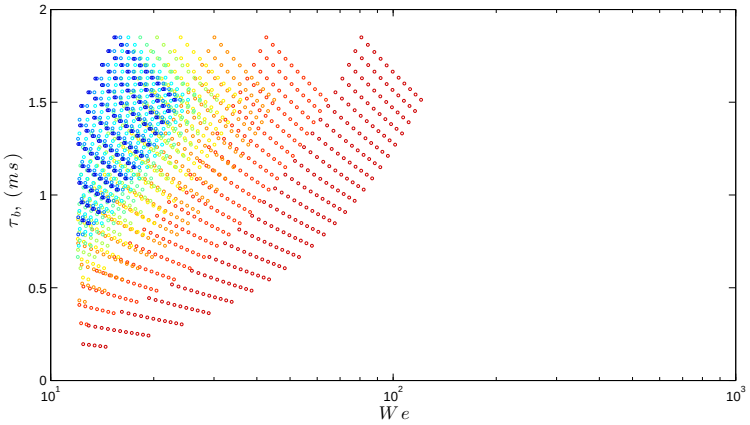

(b)

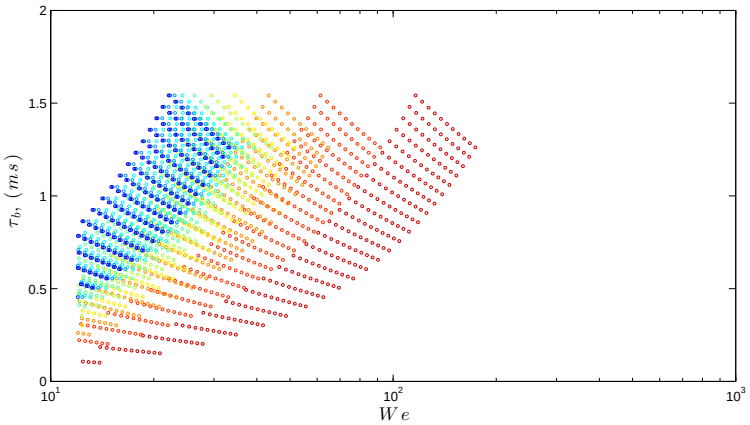

(c)

FIGURE 9.4: Predicted droplet breakup times based upon the Reitz and Diwaker (1986) secondary atomization model, for experimental sprays; a)Case 1P, b)Case 2P and c)Case 3P. Data points ranging dark blue to red correspond to increasing levels of droplet charge.

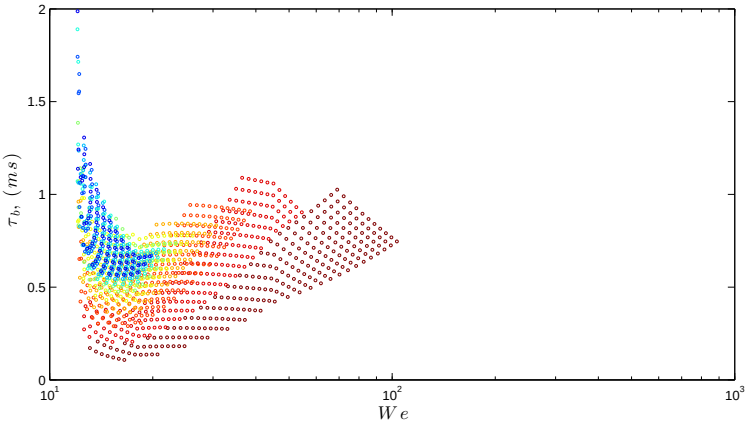

(a)

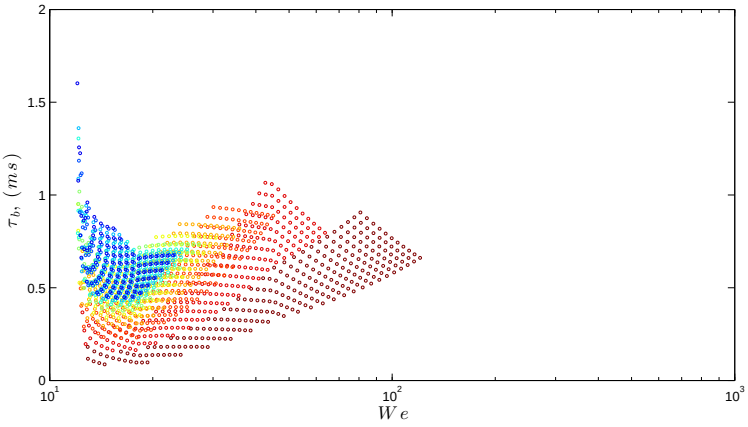

(b)

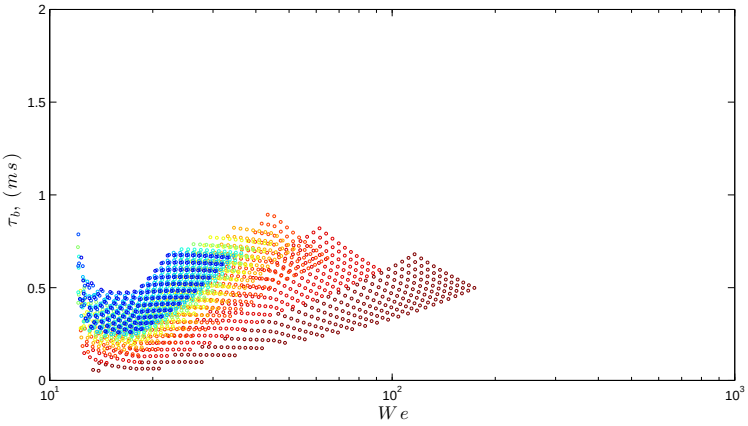

(c)

FIGURE 9.5: Predicted droplet breakup times based upon the Pilch and Erdman (1987) secondary atomization model, for experimental sprays; a)Case 1P, b)Case 2P and c)Case 3P. Data points ranging dark blue to red correspond to increasing levels of droplet charge.

via characteristic droplet Weber number ranges, inherently due to the design of the model itself. From a simple examination of equation (9.20), one can clearly see that the non-dimensional breakup time is calculated solely via $t_b^* = C_{strip}/2$. This highlights a weakness within the model since one would always need to tune C_{strip} so that computed total breakup times match those known from experiments or a real-world spray system. Without data from specific real-world sprays available for comparison, there is no way of knowing how well predicted behaviour for hypothetical sprays will be. With regards to the differences in predicted total breakup times between spray experiments, generally an increase in spray injection velocity results in faster droplet breakup times (relative to fixed droplet diameters and charge levels). It also appears that an increase in droplet charge level has little to no effect upon predicted total breakup times, rather the effect is an increased likelihood that smaller droplets undergo breakup due to subsequently increased Weber numbers.

The problems highlighted within the Reitz-Diwaker model, are not so much an issue within the Pilch-Erdman model. Instead, breakup times are computed from correlations which are based entirely upon experimental observations. In Pilch and Erdman (1987), total breakup times of droplets were classified as a function of their Weber number, and there is some evidence of effort made to classify total breakup times according to specific breakup regimes from the clustering of data observations and the bounds that define the breakup time correlations themselves. In figure 9.5, total breakup times are reported in their dimensional forms to aid in analysis[6]. Between experiments of table 9.1, predicted total breakup times for the Pilch-Erdman model show that for small droplets with Weber numbers $We < 20$, an increase in relative velocity results in faster breakup time. For droplets with Weber numbers $We > 20$, breakup time-scales are typically within the same orders of magnitude. An increase in droplet charge levels is shown to increase droplet Weber numbers, however it is only via the effective surface tension term and Weber number that charge actually modifies predicted total breakup times.

[6] If non-dimensional breakup times were reported instead, one would see a collapse of all data to form the Pilch-Erdman breakup time correlations.

Predicting Stable Droplet Diameters

In this section, analysis is restricted to typical operating conditions of spray case 1P with details listed in table 9.1, since little effect was seen on model performance with regards to stable droplet diameter predictions between experiments.

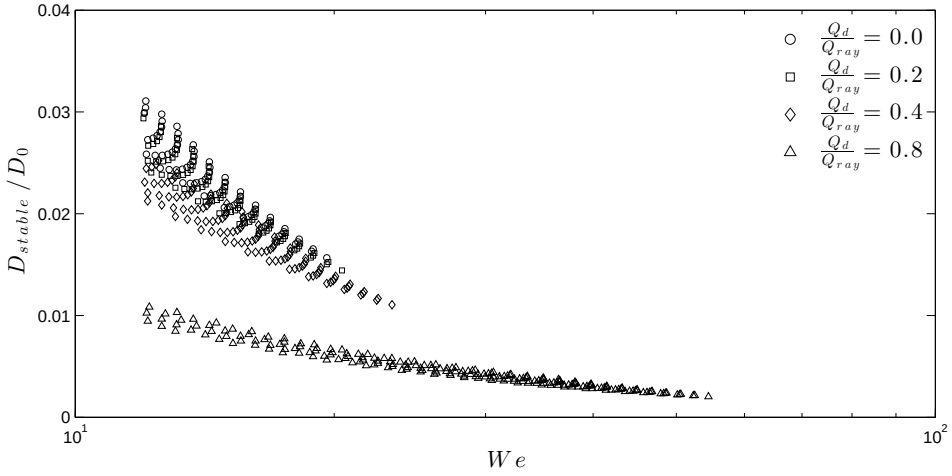

FIGURE 9.6: Stable droplet diameters predicted from the Reitz and Diwaker (1986) secondary atomization model for experimental spray case 1P.

Figures 9.6 and 9.7 show the stable droplet diameters predicted from Reitz-Diwaker and Pilch-Erdman secondary atomization models respectfully. For both models, increasing droplet charge levels relative to fixed initial droplet diameters, and fixed relative velocities corresponds to an increase in droplet Weber numbers and a decrease in predicted stable droplet diameters. Reductions in predicted stable droplet diameters for the Pilch-Erdman model follow the correlations defined by equations (9.28) and (9.29) collectively. Figure 9.7 notably shows that for droplets with Weber numbers below ≈ 20, predicted stable diameters are greater than their initial droplet diameters prior to breakup. Furthermore, examination of figure 9.7 shows an asymptotic solution to a stable droplet diameter that extends to $+\infty$ at the instant breakup occurs at $We \approx 12$. Clearly this is not correct, and highlights the limitation in reliability of the original unmodified Pilch-Erdman secondary atomization model.

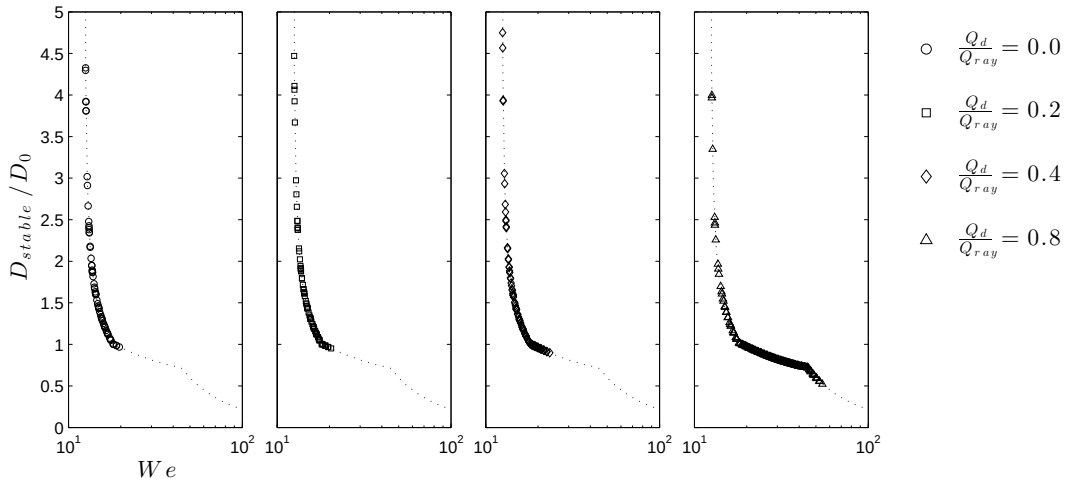

FIGURE 9.7: Stable droplet diameters predicted from the Pilch and Erdman (1987) secondary atomization model for experimental spray case 1P.

For the Wert (1995) modified Pilch-Erdman secondary atomization model, an entirely different picture is seen with regards to model performance whilst predicting stable droplet diameters. As can be seen in figure 9.8, all possible combinations of input parameter values for spray case 1P, fall on the corrected correlation for stable droplet diameters. Most importantly, the singularity at the onset of breakup is captured correctly.

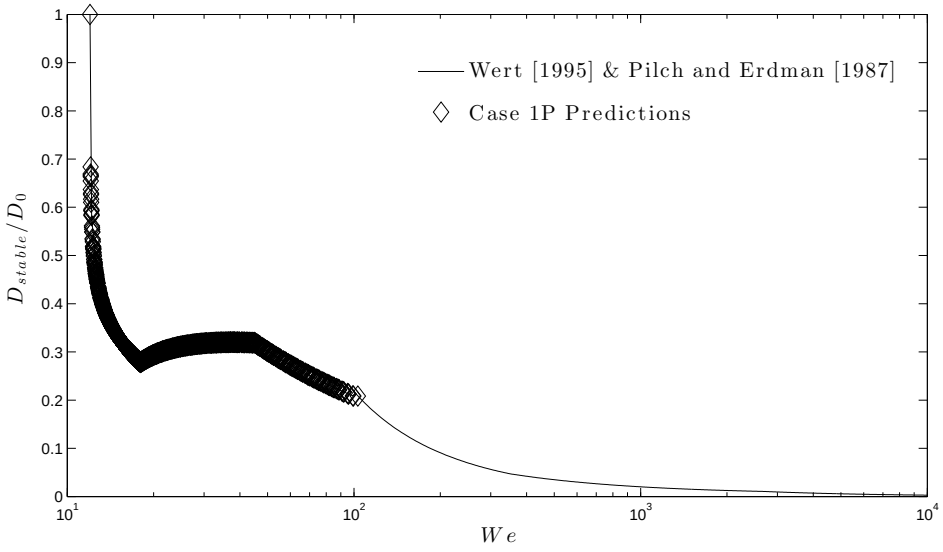

FIGURE 9.8: Stable droplet diameters predicted from the Wert (1995) modified, Pilch and Erdman (1987) secondary atomization model for experimental spray case 1P.

9.3.4 Justification of Chosen Secondary Atomization Model

From the evaluation on secondary atomization models, the original Pilch-Erdman model clearly outperforms the model developed by Reitz and Diwaker (1986). The only fault in the design of the original Pilch-Erdman model, was the prediction of stable droplet diameters for droplets undergoing bag breakup. As noted previously in section 9.3.2, the modified stable droplet diameter correlations of Wert (1995) corrected such faults and the model is now complete, without any requirement to tune for any given practical nor hypothetical spray application. The modified Pilch-Erdman model is therefore chosen for subsequent investigations on charged high pressure sprays presented in this chapter.

9.4 Secondary Atomization Modelling of Charged High Pressure Diesel Fuel Spray Experiments

9.4.1 Introduction

In order to make reliable CFD predictions of charged high pressure sprays, one needs to be certain of the accuracy in numerical methodologies used. Computed sprays are therefore setup to reflect the conditions present within experimental sprays of Kourmatzis and Shrimpton (2012). Statistics from computed sprays are obtained in a similar manner to statistics from experimental spray PDA measurements. This allows for an accurate assessment of model performance and CFD procedures, used to account for initial conditions and characteristics of spray experiments.

In this section the initial conditions of the discrete CFD sprays shall be defined along with a proposed set of high pressure spray simulations to investigate. The results are subsequently presented followed by a discussion on the performance of the Pilch and Erdman breakup model along with recommendations on its usage towards simulating electrostatically atomized charged high pressure sprays.

9.4.2 Initial Conditions

Modelling initial conditions for the discrete phase must be distinguished from the fact that for sprays examined in chapter 8, secondary atomization did not occur. Therefore, modelling of initial conditions was restricted to consideration of only primary atomization dynamics. For high pressure sprays considered in this study, the "big-blob" type model is adopted, (Guildenbecher et al. 2009). Modelling initial conditions now accounts for some primary atomization and all of secondary atomization.

Primary atomization dynamics arise as a consequence of initial liquid jet breakup mechanisms, encompassing the Rayleigh, first, and second wind-induced breakup regimes. Rayleigh breakup is caused by growth of axi-symmetric oscillations appearing on the jet surface. Droplet diameters produced in such a scenario typically exceed the jet diameter. The first wind-induced breakup is caused by an augmentation of surface waves as a result of increased relative velocities between the jet and ambient gas. Breakup typically occurs many jet diameters downstream of the nozzle, with resulting droplet diameters typically the same diameter as the jet. For the second wind-induced breakup regime, droplets are produced via the unstable growth of short-wavelength surface waves, again caused by increased relative velocity. Droplets produced as a consequence have average diameters much smaller than the jet diameter. Atomization of the jet is characterised by the complete disruption of the liquid outflow at the nozzle exit orifice.

Due to large injection velocities present within high pressure sprays, there is inherent difficulty faced by experimentalists in measuring the mean jet breakup length. Based upon findings from earlier analysis in section 8.7, one can justify use of the correlations given by equations 8.27, 8.28 and 8.29 to compute jet breakup lengths for high pressure sprays listed in table 9.1. These correlations were found to be far more reliable in predicting finite mean jet breakup lengths, than those from classical models governing laminar and turbulent jets, which when modified to account for charge using an effective surface tension failed significantly (Kourmatzis and Shrimpton 2012).

The initial velocity of droplets is specified by mean and fluctuating components of the

injection conditions. In addition, knowledge of the half spray cone angle $\theta/2$ for calculating the variation in initial droplet radial velocities is required. In practice, the half spray cone angle for electrically charged sprays is a difficult quantity to measure, primarily due to the fact that droplet trajectories follow parabolic paths. However, if one was to assume that all spray droplets originate at, or near the centre of the liquid jet, one may justify use of the correlation provided by Reitz et al. (1979) and Heywood (1988), to predict spray cone angle. This correlation was chosen for its suitability across most modern Diesel injectors, and is given by equation (9.33).

$$\tan(\theta/2) = \frac{4\pi}{A}\left(\frac{\rho_f}{\rho_d}\right)^{0.5}\frac{\sqrt{3}}{6} \tag{9.33}$$

Here A is a constant depending on the nozzle design, or it may be approximated using,

$$A = 3.0 + 0.28\left(\frac{l}{d_{inj}}\right) \tag{9.34}$$

Subsequently, one may distinguish the trajectories of droplets defined solely by the mean and fluctuating velocities of initial conditions, and trajectories modified by the additional Coulombic repulsion forces acting from other droplets in the spray core. The latter numerics can easily be computed post injection of droplets within the computational domain.

For the next part of the injection procedure, specification of the injected droplet diameter PDF is required. Due to the presence of secondary atomization, it is unreliable to use measured PDFs of droplet diameters. This is because measured PDFs are functions of transient processes occurring during secondary atomization, exhibiting themselves as spatially dependent characteristics within the spray plume. Therefore, initial PDFs for high pressure sprays examined in this study are assumed to take the form of a normal distribution, chosen such that the mean diameter equals the nozzle orifice diameter, with a standard deviation equal to one third of the orifice diameter according to equation (9.35).

$$D_k = d_{inj}\left(1 + \frac{1}{3}RAN_G\right) \tag{9.35}$$

This yields a normally distributed diameter PDF, with diameters ranging from $0 - 2d_{inj}$. This follows in line with the theory of Rayleigh (1879), that the largest unstable wavelength on a liquid jet yields a droplet with diameter $\approx 1.89d_{inj}$, (Lefebvre 1989). Mass conservation of the injected droplet diameter PDF is then ensured using the same methodology as presented in section 8.8.1.

For initial specification of the mean droplet charge, the modelled Q-D method described in section 8.8.1 is used. Additionally, a variation in charge based upon typical values calculated for the standard deviation across diameter classes is applied. From experiments of Rigit (2003), standard deviations in droplet charge vary between 5% and 15% of the Rayleigh limit. In practice for electrostatically atomized high pressure sprays, there is every reason to suggest a relationship exits between droplet charge and diameter, unique to the initial conditions of the spray in question. One can therefore justify use of a methodology that uses the modelled Q-D method to specify an initial mean charge, and a modification that adjusts charge levels with a random variation based on the likely standard deviation of charge levels found for droplets of that particular class size. For all our high pressure sprays, the standard deviation of charge levels across injected droplets was set to equal 10% of the injected droplets Rayleigh charge limit. Charge conservation is ensured using the same methodology presented in section 8.8.2.

9.4.3 Results

Statistics were post-processed from simulated CFD sprays in a similar manner to statistics processed from experimental PDA measurements. Sample control volumes from CFD and experimental measurements were taken at the same downstream and radial locations away from the atomizer orifice. This allows for an accurate assessment of model performance and the CFD procedures employed.

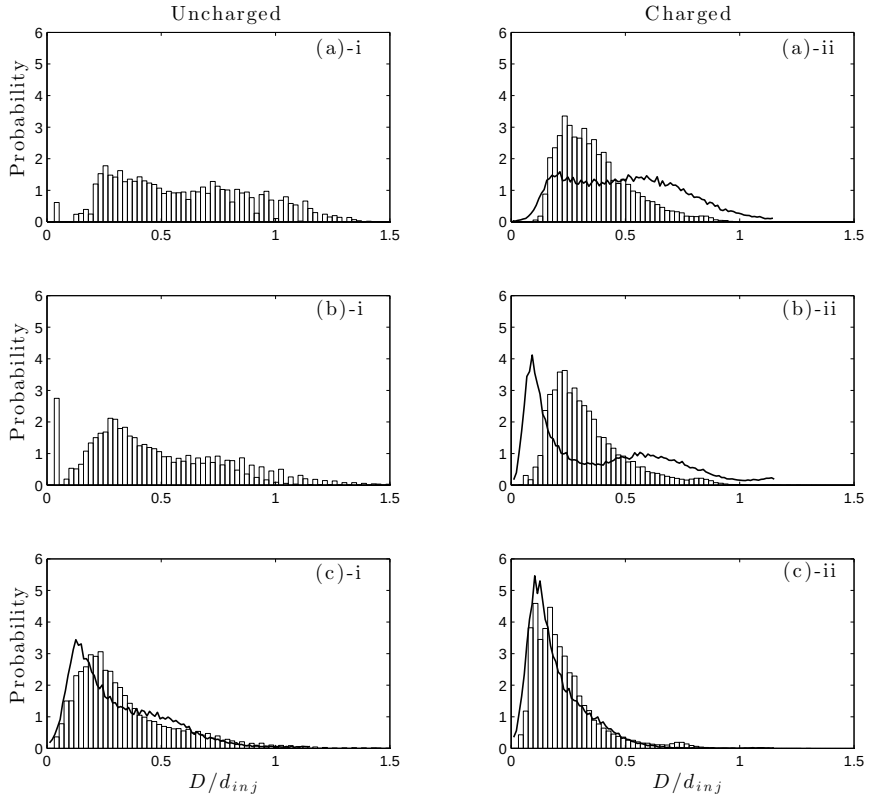

FIGURE 9.9: Histogram PDF measurements obtained from post-processed CFD simulation data for uncharged (i) and charged (ii) high pressure sprays; a) Case 1P, b) Case 2P, and c) Case 3P. Overlaid profiles correspond to experimental spray PDFs. PDFs were sampled along the spray axis downstream from the atomizer at $17cm$ for Case 1P, $15cm$ for Case 3P, and at $12.5cm$ and $17.5cm$ for the uncharged and charged Case 2P respectively.

Figure 9.9 compares droplet diameter PDFs obtained from computed sprays, with available PDFs obtained from experimental spray measurements. With regards to uncharged computed sprays, a distinct evolution from a bi-modal to uni-modal droplet size distribution is observed with increasing spray injection velocity, relative to fixed downstream sample locations. For charged computed sprays, droplet size distributions are predominantly uni-modal, with a single peak for droplet diameters occurring in the range 0.1-$0.25D/d_{inj}$. Furthermore, the tails in these distributions in the direction of increasing droplet diameters tend to show reduced probabilities as spray injection velocities increase. Comparison of PDFs between computed and experimental charged sprays only show reasonable agreement for case 3P. For case 1P, computed results show a uni-modal PDF, whereas the experimental PDF remains bi-modal. A similar behaviour is observed

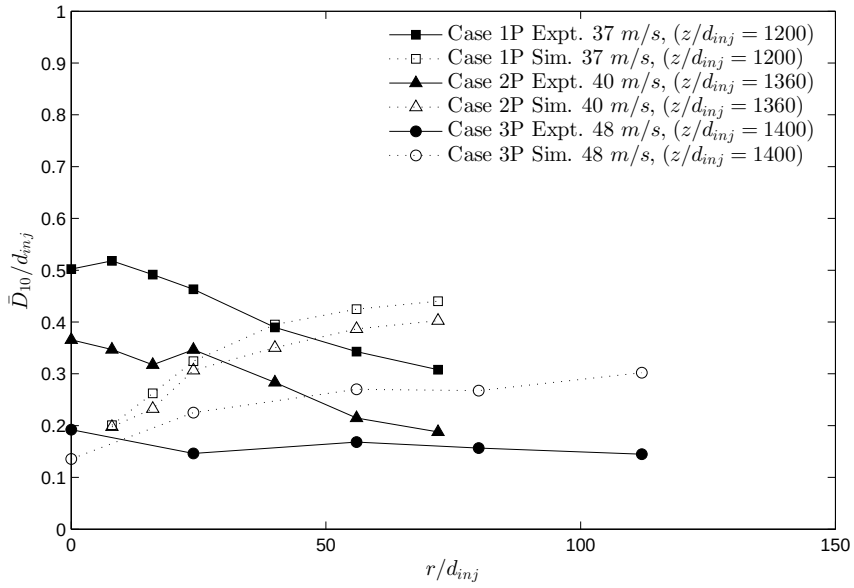

FIGURE 9.10: Mean droplet diameter profiles for charged high pressure sprays 1P, 2P, and 3P of table 9.1.

for case 2P, the only difference being an increase in smaller droplet probability within the bi-modal experimental PDF. These discrepancies are most likely caused by weaknesses in the modelling of dispersion for charged high pressure sprays.

Figure 9.10 show mean diameter profiles of charged spray droplets compared between simulations and experiments. Experimental and computed profiles generally show that small droplet diameters have a dominant presence at the spray centreline. However, comparison between computed and experimental sprays show disagreements. For experimental spray cases 1P and 2P, mean droplet diameters tend to decrease for increasing r/d_{inj}, yet computed spray profiles show the opposite behaviour. The experimental profile for spray case 3P shows a relatively consistent behaviour with mean droplet diameter as radial displacement increases, with $\bar{D}_{10}/d_{inj} \approx 0.15$. For the computed spray case 3P however, consistent prediction in mean droplet diameter only occurs beyond a radial displacement of $r/d_{inj} = 50$, with $\bar{D}_{10}/d_{inj} \approx 0.25$. Near the spray centreline, the mean droplet diameter predicted is $\bar{D}_{10}/d_{inj} \approx 0.15$. This suggests that the radial dispersion of large droplets within computed sprays is more than what is observed in experiments. Unfortunately, experiments of Kourmatzis and Shrimpton (2012) did not

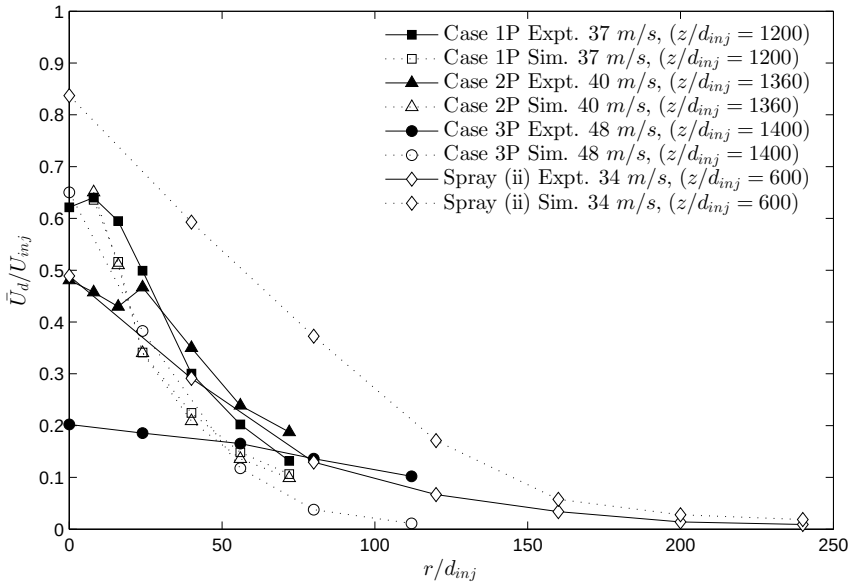

FIGURE 9.11: Mean droplet axial velocity profiles for charged high pressure cases 1P, 2P, and 3P of table 9.1, as well as spray (ii) from Shrimpton and Yule (1999).

obtain information about the radial dispersion characteristics of spray droplets, so the no way of ascertaining the exact cause of observed discrepancies.

Figure 9.11 shows mean axial velocity profiles of charged spray droplets compared between simulations and experiments. Profiles computed for high pressure sprays all show reasonable agreements with experiments, with the exception being case 3P where the computed profile exceeds the experimental profile near the spray centreline by nearly a factor of 3. To explain this behaviour, one can observe in Figure 9.11 that as spray injection velocities increase, the mean velocity of droplets sampled at the spray centreline decreases. An increase in spray injection velocity therefore leads to greater dispersion which adds a radial component to droplet velocities. Our computed profiles do not show evidence of this behaviour. Instead, there is a tendency for computed profiles to exceed experimental profiles near the spray centreline. Nevertheless, for increasing r/d_{inj}, the computed profiles show reasonable consistency in their agreement with experimental profiles. Figure 9.11 also includes an experimental mean axial velocity profile for a $34m/s$ low pressure spray, originally presented as spray (ii) by Shrimpton and Yule (1999), and its computed corresponding profile taken from a recently published CFD study (Amine-Eddine and Shrimpton 2013). Comparing case 1P to spray (ii) up to

$r/d_{inj} = 100$, experimental profiles show reasonable agreement with each another. Furthermore, the computed profile for case 1P agrees well with its own experiment, and that of spray (ii). This gives us confidence that the method used to model secondary atomization within charged high pressure sprays, accounts reasonably well for charged spray behaviour existing in sprays where secondary atomization is not a dominant process. Lastly, the average percentage errors between computed and experimental mean velocity profiles was calculated to be 19.5%, 16.2%, and 27.5% for spray cases 1P, 2P, and 3P respectively.

9.5 Summary

- The physical effects of droplet charge upon the phenomena of secondary atomization has been comprehensively examined, in order to develop a computational framework for simulating high pressure electrostatically atomized dielectric liquid sprays.

- The Pilch and Erdman (1987) secondary atomization model, modified according to improved correlations of droplet fragmentation and breakup developed by Wert (1995), has been found far superior in terms of robustness compared to the secondary atomization model of Reitz and Diwakar (1987). This improved Pilch-Erdman model has also been shown to overcome the pitfalls associated with the original formulation, when predicting stable diameters for droplets undergoing breakup within the bag regime. The main advantage of this new improved model is the fact that no tuning of co-efficients is required whatsoever.

- A numerical methodology has been developed, suitable for predicting the characteristics of high pressure electrostatically charged Diesel fuel sprays. This methodology utilises the charge-diameter distribution model developed earlier in chapter 8, and the Wert (1995) improved Pilch-Erdman secondary atomization model with effective surface tension modifications to account for electrostatic charge presence on spray droplets. Most importantly, this methodology is reliable at predicting secondary atomization processes in both uncharged and charged spray plumes.

- For uncharged computed sprays, sampled droplet diameter PDFs measured between cases show a distinctive evolution from a bi-modal to uni-modal droplet size distribution as the spray injection velocity is increased. For charged sprays, droplet diameter PDFs are predominantly uni-modal, with a single peak in droplet diameters present in the range 0.1-0.25 D/d_{inj}. For the fastest charged high pressure spray, the droplet diameter PDFs between computed and experimental sprays show excellent agreement.

- Droplet diameter profiles of computed sprays appear to show discrepancies in behaviour compared to corresponding experiments. These disagreements suggest that too much radial dispersion occurs for large droplets within computed sprays, subsequently biasing mean droplet diameters to become smaller nearer the spray centreline.

- Droplet axial velocity profiles from computed charged high pressure sprays show reasonable agreement to corresponding experiments, with average percentage errors ranging from 16.2% to 27.5%.

- The results from this investigation highlight the suitability of the CFD methodology presented, for simulating high pressure electrostatically charged fuel sprays, at elevated injection conditions typically employed within automotive and marine Diesel combustion engines.

Chapter 10

Conclusions and Further Work

10.1 Conclusions

The work presented in this thesis concerns a fundamental examination of poly-dispersed and electrically charged particle suspensions two-way coupled to turbulence, and the potential application of using electrical charge on fuel droplets to improve the pre-combustion dynamics and characteristics of sprays internal to Diesel combustion engines. It is hoped that this work will provide a framework for progress in this research area, and future application of presented ideas to alternative industrial technologies. The conclusions from this thesis are summarised as follows:

10.1.1 Poly-Dispersed Particle Suspensions Two-way Coupled to Turbulence

- A fundamental examination of select poly-dispersed particle suspensions two-way coupled with turbulence has been conducted.
- Investigations have found that poly-dispersed suspensions at high mass loading ratios typically attributed to increased attenuation of turbulent kinetic energy, can in certain scenarios attenuate turbulent kinetic energy less so than mono-dispersed suspensions with smaller mass loading ratios.

- Investigations have found that the presence of two size classes within a poly-dispersed suspension, each with an individual mass loading ratio of $\phi_m \approx 0.2$, can counteract the level of turbulent kinetic energy attenuated by the dominant size class with an individual mass loading ratio of $\phi_m \approx 0.5$.

- It has been determined that it is favourable to have a poly-dispersed particle suspension, rather than a mono-dispersed suspension, when one aims to maximise the homogeneity within a turbulent flow field. Furthermore, it has been determined more favourable to have a $\langle St_\eta \rangle_{\mathscr{L}} > 1$ poly-dispersed particle suspension at high mass loading ratio, than a $\langle St_\eta \rangle_{\mathscr{L}} < 1$ suspension at the same mass loading ratio, in terms of the amount of energy required to maintain a homogenised suspension of poly-dispersed particles in a turbulent flow field.

10.1.2 Charged Particle Suspensions Two-way Coupled to Turbulence

- A fundamental examination into the behaviour of electrically charged particle suspensions two-way coupled with turbulence has been conducted.

- It was determined that the presence of electrical charge on $St_\eta = 1$ particles within a suspension, forced particles to reside in turbulence scales non-resonant with their own characteristic time-scales.

- In the presence of gravity, $\langle St_\eta \rangle_{\mathscr{L}} = 1$ particles sufficiently charged to a high enough level were found to fall at a rate slower than their own Stokes settling velocities. This was attributed to the greater spatial homogeneity of charged particles, forcing them to pass through turbulent vortices more so than around turbulent vortices in the flow.

- The presence of electrical charge on particles within a two-way coupled mono-dispersed suspension, was found to attenuate levels of turbulent kinetic energy relative to kinetic energy of an unladen turbulent flow, less so than an uncharged particle suspension. Furthermore, the observed small scale augmentation for charged particle suspensions was not a much as the augmentation observed for identical yet uncharged particle suspensions.

- Investigations determined that the mesoscopic kinetic energy spectra of the particle phase is augmented at large scales, and attenuated at small scales for charged particle suspensions. This behaviour was found to be analogous to the behaviour of turbulent kinetic energy in the scenarios where drag reduction and promotion of fluid transport is achieved using polymer additives within the turbulent flow field. It has thus been determined, that the addition of electrical charge on particles within a suspension residing in a turbulent flow field, will promote large scale transportation of the dispersed phase throughout the flow medium.

10.1.3 Validation of a Droplet Charge-Diameter Distribution Model

- A detailed validation of a previously published droplet charge-diameter distribution model has been conducted, with successful publication of a "first of its kind" academic paper.

- It was determined that modelling droplet charge according to a scaling droplet diameter relationship, was just as reliable as directly using experimentally obtained droplet charge measurements.

- The general steady state behaviour of electrostatically atomized liquid hydrocarbon sprays was successfully reproduced using the numerical methodology and procedure developed in the study. Both qualitative and quantitative results between CFD and experiments showed excellent agreement to one another.

- A general set of recommendations have been presented, providing guidelines for potential future work by industry and academics alike in simulating electrostatically atomized dielectric liquid sprays through RANS based CFD methods.

10.1.4 Modelling Secondary Atomization in Charged High Pressure Sprays

- A thorough review of existing research regarding the effects of droplet charge upon the phenomena of secondary atomization has been undertaken. Underlying physical phenomena such as droplet deformation, regimes of secondary atomization, and

time-scales of secondary atomization processes have been assessed in relation to changes of effective surface tension due to presence of electrical charge on droplets.

- Improved correlations of droplet fragmentation and breakup developed by (Wert 1995) were found to increase significantly the robustness of the (Pilch 1981) secondary atomization model. Prediction of stable droplet diameters and droplet breakup time-scales within regimes was found to match closely with experimental data, without any need for tuning of parameters.

- A numerical methodology has been presented, suitable for predicting the characteristics of high pressure electrostatically charged Diesel fuel sprays. The methodology was found to be reliable at predicting secondary atomization processes for both uncharged and charged spray plumes.

- Close match between CFD results and experiments is obtained for sampled droplet diameter PDFs measured between cases. Agreement is found in the prediction of bi-modal and uni-modal droplet size distributions at selectively sampled sites downstream within the spray plume.

- The results from this investigation highlight the suitability of the CFD methodology presented, for simulating high pressure electrostatically charged fuel sprays, at elevated injection conditions typically employed within automotive and marine Diesel combustion engines.

10.2 Further Work

The scope for further work derived from findings of this thesis remains large. Nevertheless, several avenues for further work are identified as follows;

10.2.1 Fundamental DNS Investigations

- Development of the DNS code should be focused on re-design and parallel scalability. The current design of the code requires particles to be distributed across many cores and slices of computational domain. This design hinders scalability due to the requirement of large MPI over-head requirements. Pencil-like decomposition as well as decomposition across all three spatial dimensions, would significantly help the scalability of code.

- DNS code development could also extend capability to simulation of homogeneous flow scenarios such as shear, axi-symmetric compression, axi-symmetric expansion and plane strain. However, the field of research in that area appears to be saturated, with little progress nor effort being made to solve practical problems. The most plausible area of research progress is a complete database set of closed third-order Eulerian particle stress correlations, (derived from shear, strain, axi-symmetric DNS), for different ranges of particle Stokes numbers, Taylor Reynolds numbers and particle mass loading ratios.

- Investigations regarding two-way coupled poly-dispersed particle suspensions with turbulence, noted difficultly in pinpointing coherent modification of turbulence scales. Poly-dispersity adds a level of complexity to the already difficult phenomena of inertial particle two-way coupling. It is probably more beneficial for future DNS investigations to examine different shapes of poly-dispersed size class distributions specific to a given practical multiphase application, and evaluate how turbulent kinetic energy, dissipation rate and particle kinetic energy statistics are modified as function of different size class distribution parameters.

- Investigations regarding two-way coupled charged particle suspensions with turbulence, identified a very unique behaviour of mesoscopic kinetic energy spectra.

Further work should aim to examine how the presence of charge on particles within a suspension, modifies passive scalar Lagrangian transport across turbulence scales. One would expect based upon research findings presented in this thesis, that passive scalar transport is augmented at large scales of turbulence and attenuated at small scales.

- This thesis has also identified a potential limitation relating to over-saturation of a two-way coupled DNS flow field, by a large number of computational particles with small statistical weights such that $W_p \ll 1$ and $N_c \gg N_p$. Due to artificial smoothing of Eulerian momentum source terms, the assumption of statistical equivalence between the computational ensemble of particles and the physical dispersed phase system considered is raised into question. Specifically, the question being at what point do the dynamics of computational particles start to deviate from the realism of a physical two-way coupled dispersed phase system. Future work should investigate such issue, and ideally provide guidelines on the maximum ratio of N_c/N_p practical for two-way coupled DNS investigations. This ratio should be evaluated based on the ability of the two-way coupled DNS flow field to maintain statistical equivalence between the ensemble of computational particles and the physical dispersed phase system considered, without adversely affecting the modulation of resolved turbulence scales in a non-physical manner.

10.2.2 Practical Application of Electrostatic Charging to Engineering Technologies

- Electrostatic paint spraying is already common for many industrial processes, yet little research exists examining how such processes may benefit economically from CFD of electrostatically atomized liquid sprays. Optimisation of industrial processes would be a main focus for potential utilisation of such a concept.

- Development of a computational procedure successful at predicting behaviour of charged high pressure sprays has its benefits, in terms of ability to evaluate technology processes where secondary atomization plays a dominant role. Further work is still required to investigate the transient behaviour of electrostatically charged high

pressure spray plumes. Additionally, where applications involve droplets charged to a high level close to their Rayleigh limit, further experimental work is needed to identify for different liquid spray compounds, how Coulombic fission plays a role in droplet breakup processes and whether or not such phenomena can or needs to be modelled.

- Combustion in marine Diesel engines is expected to become more efficient with the addition of electrical charge on fuel spray droplets. Further work should incorporate ideas developed in this thesis, and examine the effects of electrostatic charge on pre-combustion dynamics of fuel sprays, on subsequent flame fronts during combustion, and on Soot and NOx formations post combustion.

Appendix A

Averaging Conventions

In this appendix, the averaging conventions used throughout this thesis are defined. The three most common averages used in turbulence modelling research research are the time average, spatial average and ensemble average.

A.1 The Time Average

Time averaging of an arbitrary variable ϕ is denoted by an overbar line, i.e. $\overline{\phi}$. It is most appropriate for stationary turbulence, that is turbulence whose statistics do not vary over time.

$$\overline{\phi}(\mathbf{x}) = \lim_{T\to\infty} \frac{1}{T} \int_t^{t+T} \phi(\mathbf{x}, t) dt \tag{A.1}$$

A.2 The Spatial Average

Spatial averaging of an arbitrary variable ϕ is denoted by $\langle\phi\rangle_{\mathscr{V}}$. It is most appropriate for homogeneous turbulence, whereby statistics remain invariant under translations of the reference frame.

$$\langle\phi\rangle_{\mathscr{V}}(t) = \lim_{V\to\infty}\frac{1}{V}\iiint_V \phi(\mathbf{x},t)dV \tag{A.2}$$

A.3 The Ensemble Average

Ensemble averaging of an arbitrary variable ϕ is denoted by $\langle\phi\rangle_{\mathscr{E}}$. An ensemble average is an average taken from N identical experiments with initial and boundary conditions that differ by a random infinitesimal perturbation.

$$\langle\phi\rangle_{\mathscr{E}}(\mathbf{x},t) = \lim_{N\to\infty}\frac{1}{N}\sum_{n=1}^{N}\phi(\mathbf{x},t) \tag{A.3}$$

A.4 The Density-Weighted Average

The density-weighted (Favre) average is a special form of averaging used in simplifying the formulation of averaged Navier-Stokes equations in variable density flows. Specifically for this thesis, the density weighted average is used to simplify the formulation for averaged mesoscopic particle phase continuity and momentum transport equations. As an example, for the mesoscopic particle phase velocity $\tilde{v}_i$, the density-weighted ensemble average is denoted by

$$\langle\tilde{v}_i\rangle_{\mathscr{F}} = \frac{\langle\tilde{n}_p\tilde{v}_i\rangle_{\mathscr{E}}}{\langle\tilde{n}_p\rangle_{\mathscr{E}}} \tag{A.4}$$

where subscript $\mathscr{F}$ is used to denote the density-weighted (Favre) average.

A.5 The Lagrangian Average

The Lagrangian average of an arbitrary variable ϕ is denoted by $\langle\phi\rangle_{\mathscr{L}}$. The Lagrangian average is an average taken over a population of N_L Lagrangian particles within a given population.

$$\langle \phi \rangle_{\mathscr{L}} = \frac{1}{N_L} \sum_{i=1}^{N_L} \phi^{(i)} \tag{A.5}$$

A.6 The Ergodic Hypothesis

For turbulence that is homogeneous only, the ergodic hypothesis assumes that spatial and ensemble averages are all equal to one another. For turbulence that is stationary, homogeneous and isotropic, the ergodic hypothesis assumes that time, spatial and ensemble averages are all equal to one another.

A.7 Correlations

Averages of products are computed as follows,

$$\overline{u_i u_j} = \overline{(\bar{u}_i + u_i')(\bar{u}_j + u_j')} \tag{A.6}$$

$$= \bar{u}_i \bar{u}_j + \overline{u_i' u_j'} + \overline{\bar{u}_i u_j'} + \overline{\bar{u}_j u_i'} \tag{A.7}$$

$$= \bar{u}_i \bar{u}_j + \overline{u_i' u_j'} \tag{A.8}$$

Noting that the average of a fluctuating quantity is zero by definition.

Appendix B

Summary of Dispersed Phase DNS Data Matrices

Brief summaries noted for the data matrix tables are as follows;

- For one-way coupled DNS parameters, table B.3 shows calculated ϕ_v values, given $N_c = 10^5$, D set by St_η, and $\rho_p = 11300 kg/m^3$. ϕ_v values equalling 10^{-4} could only be achievable at physically unrealistic values of particle density. These densities are shown in table B.4 for reference.

- For two-way coupled DNS parameters, tables B.5, B.6, and B.7 show calculated W_p values, given $N_c = 10^7$. These tables clarify the statistical weights per computational particle to be specified, in order to achieve target mass loading ratios of $\phi_m = 0.2$, 0.5 and 1.0 respectively. The increase in number of computational particles tracked was necessary in order to improve the quality of results presented for two-way coupled DNS investigations presented in chapters 6 and 7 of this thesis.

St_η	$Re_\lambda = 24.27$	$Re_\lambda = 44.65$	$Re_\lambda = 83.37$	$Re_\lambda = 142.47$
0.2	4.46E-02	1.22E-02	2.45E-03	5.38E-04
0.5	1.12E-01	3.06E-02	6.12E-03	1.34E-03
0.8	1.78E-01	4.89E-02	9.79E-03	2.15E-03
1.0	2.23E-01	6.11E-02	1.22E-02	2.69E-03
2.6	5.80E-01	1.59E-01	3.18E-02	6.99E-03
3.0	6.69E-01	1.83E-01	3.67E-02	8.06E-03
5.0	1.12E+00	3.06E-01	6.12E-02	1.34E-02
6.0	1.34E+00	3.67E-01	7.35E-02	1.61E-02
10.0	2.23E+00	6.11E-01	1.22E-01	2.69E-02
20.0	4.46E+00	1.22E+00	2.45E-01	5.38E-02
30.0	6.69E+00	1.83E+00	3.67E-01	8.06E-02
40.0	8.92E+00	2.44E+00	4.90E-01	1.08E-01

TABLE B.1: Table showing calculated particle relaxation time-scales, for both one and two-way coupled prospective DNS cases.

St_η	D/η	$Re_\lambda = 24.27$	$Re_\lambda = 44.65$	$Re_\lambda = 83.37$	$Re_\lambda = 142.47$
0.2	0.02	1.333E-03	6.976E-04	3.123E-04	1.463E-04
0.5	0.03	2.108E-03	1.103E-03	4.937E-04	2.313E-04
0.8	0.04	2.666E-03	1.395E-03	6.245E-04	2.926E-04
1.0	0.04	2.981E-03	1.560E-03	6.982E-04	3.271E-04
2.6	0.06	4.806E-03	2.515E-03	1.126E-03	5.275E-04
3.0	0.07	5.162E-03	2.702E-03	1.209E-03	5.666E-04
5.0	0.09	6.665E-03	3.488E-03	1.561E-03	7.315E-04
6.0	0.10	7.301E-03	3.821E-03	1.710E-03	8.013E-04
10.0	0.13	9.425E-03*	4.933E-03	2.208E-03	1.035E-03
20.0	0.18	1.333E-02*	6.976E-03	3.123E-03	1.463E-03
30.0	0.22	1.633E-02*	8.544E-03*	3.824E-03	1.792E-03
40.0	0.25	1.885E-02*	9.866E-03*	4.416E-03	2.069E-03

TABLE B.2: Table showing calculated particle diameters, for both one and two-way coupled prospective DNS cases. Starred values indicate calculated particle Diameters that are valid only for two-way coupled prospective DNS cases.

St_η	$Re_\lambda = 24.27$	$Re_\lambda = 44.65$	$Re_\lambda = 83.37$	$Re_\lambda = 142.47$
0.2	5.00E-07	7.17E-08	6.43E-09	6.61E-10
0.5	1.98E-06	2.83E-07	2.54E-08	2.61E-09
0.8	4.00E-06	5.73E-07	5.14E-08	5.29E-09
1.0	5.59E-06	8.01E-07	7.19E-08	7.39E-09
2.6	2.34E-05	3.36E-06	3.01E-07	3.10E-08
3.0	2.90E-05	4.16E-06	3.73E-07	3.84E-08
5.0	6.25E-05	8.96E-06	8.03E-07	8.26E-08
6.0	8.21E-05	1.18E-05	1.06E-06	1.09E-07
10.0	1.00E-04	2.53E-05	2.27E-06	2.34E-07
20.0	1.00E-04	7.17E-05	6.43E-06	6.61E-07
30.0	1.00E-04	1.00E-04	1.18E-05	1.21E-06
40.0	1.00E-04	1.00E-04	1.82E-05	1.87E-06

TABLE B.3: Table showing calculated volume fraction ϕ_v levels, for one-way coupled DNS cases where $\phi_m \approx 0$, given $N_c = 10^5$, D set by St_η and $\rho_p = 11300 kg/m^3$. Any ϕ_v values equalling 10^{-4} could only be achievable at physically unrealistic values of particle density, of which are listed in table B.4.

St_η	$Re_\lambda = 24.27$	$Re_\lambda = 44.65$
10.0	16519	-
20.0	33037	-
30.0	49556	13575
40.0	66074	18100

TABLE B.4: Table showing calculated ρ_p values for un-physical, one-way coupled DNS cases. Values of ρ_p are calculated such that $\phi_v = 10^{-4}$ in Table B.3.

St_η	$Re_\lambda = 24.27$	$Re_\lambda = 44.65$	$Re_\lambda = 83.37$	$Re_\lambda = 142.47$
0.2	3.54E-01	2.47E+00	2.75E+01	2.68E+02
0.5	8.96E-02	6.25E-01	6.97E+00	6.77E+01
0.8	4.43E-02	3.09E-01	3.44E+00	3.35E+01
1.0	3.17E-02	2.21E-01	2.46E+00	2.39E+01
2.6	7.55E-03	5.27E-02	5.88E-01	5.71E+00
3.0	6.09E-03	4.25E-02	4.74E-01	4.61E+00
5.0	2.83E-03	1.98E-02	2.20E-01	2.14E+00
6.0	2.15E-03	1.50E-02	1.68E-01	1.63E+00
10.0	1.00E-03	6.98E-03	7.79E-02	7.57E-01
20.0	3.54E-04	2.47E-03	2.75E-02	2.68E-01
30.0	1.93E-04	1.34E-03	1.50E-02	1.46E-01
40.0	1.25E-04	8.73E-04	9.74E-03	9.47E-02

TABLE B.5: Table showing calculated W_p values for prospective two-way coupled DNS cases with the desired mass loading ratio of $\phi_m = 0.2$.

St_η	$Re_\lambda = 24.27$	$Re_\lambda = 44.65$	$Re_\lambda = 83.37$	$Re_\lambda = 142.47$
0.2	8.85E-01	6.17E+00	6.88E+01	6.69E+02
0.5	2.24E-01	1.56E+00	1.74E+01	1.69E+02
0.8	1.11E-01	7.72E-01	8.61E+00	8.37E+01
1.0	7.92E-02	5.52E-01	6.16E+00	5.99E+01
2.6	1.89E-02	1.32E-01	1.47E+00	1.43E+01
3.0	1.52E-02	1.06E-01	1.19E+00	1.15E+01
5.0	7.08E-03	4.94E-02	5.51E-01	5.35E+00
6.0	5.39E-03	3.76E-02	4.19E-01	4.07E+00
10.0	2.50E-03	1.75E-02	1.95E-01	1.89E+00
20.0	8.85E-04	6.17E-03	6.88E-02	6.69E-01
30.0	4.82E-04	3.36E-03	3.75E-02	3.64E-01
40.0	3.13E-04	2.18E-03	2.43E-02	2.37E-01

TABLE B.6: Table showing calculated W_p values for prospective two-way coupled DNS cases with the desired mass loading ratio of $\phi_m = 0.5$.

St_η	$Re_\lambda = 24.27$	$Re_\lambda = 44.65$	$Re_\lambda = 83.37$	$Re_\lambda = 142.47$
0.2	1.77E+00	1.23E+01	1.38E+02	1.34E+03
0.5	4.48E-01	3.12E+00	3.48E+01	3.39E+02
0.8	2.21E-01	1.54E+00	1.72E+01	1.67E+02
1.0	1.58E-01	1.10E+00	1.23E+01	1.20E+02
2.6	3.78E-02	2.63E-01	2.94E+00	2.86E+01
3.0	3.05E-02	2.13E-01	2.37E+00	2.30E+01
5.0	1.42E-02	9.88E-02	1.10E+00	1.07E+01
6.0	1.08E-02	7.51E-02	8.38E-01	8.15E+00
10.0	5.01E-03	3.49E-02	3.89E-01	3.79E+00
20.0	1.77E-03	1.23E-02	1.38E-01	1.34E+00
30.0	9.64E-04	6.72E-03	7.49E-02	7.29E-01
40.0	6.26E-04	4.37E-03	4.87E-02	4.73E-01

TABLE B.7: Table showing calculated W_p values for prospective two-way coupled DNS cases with the desired mass loading ratio of $\phi_m = 1.0$.

Appendix C

The Physical Significance of Statistically Weighted Computational Particles

In Lagrangian-Eulerian simulations the physical dispersed phase system described by equations (3.19) and (3.20) consisting of N_p real particles, is indirectly represented by N_c computational particles. This approach requires the ensemble of computational particles to be statistically and dynamically equivalent to the system of real particles considered for simulations (Février et al. 2005; Garg et al. 2009). Statistical equivalence is defined from the requirement that the particle number density and velocity distribution implied by the computational ensemble, evolves in a manner consistent with the physical dispersed phase system described by equations (3.32), (3.33), and additionally for two-way coupled flows the instantaneous Navier-Stokes momentum equation[1] defined by,

$$\frac{\partial u_i}{\partial t} + u_j \frac{\partial u_i}{\partial x_j} = -\frac{1}{\rho_f}\frac{\partial p}{\partial x_i} + \nu_f \frac{\partial^2 u_i}{\partial x_j \partial x_j} - \frac{1}{\rho_f} f_i \tag{C.1}$$

Computational particles in the Lagrangian framework are represented by point-particles at time t, by $X_{p,i}^{(n)}, V_{p,i}^{(n)}, D_p^{(n)}, W_p^{(n)}$ $n = 1, ..., N_c(t)$. Where $X_{p,i}^{(n)}$ is the position vector,

[1]Since this thesis considers incompressible fluid flows, only the appropriate form is defined here.

$V_{p,i}^{(n)}$ the velocity vector, $D_p^{(n)}$ the diameter, and $W_p^{(n)}$ the statistical weight. Statistical weighting requires that,

$$\sum_{i=1}^{N_c(t)} W_p^{(i)} = \langle N_p(t) \rangle \tag{C.2}$$

such that the summation of statistical weights over all computational particles, equals the expected total number of real particles within the physical system considered. If the number of computational particles equals the number of real particles represented within the system such that $N_c = N_p$, then the statistical weight per computational particle is $W_p = 1$. If on the other-hand $N_c < N_p$, then the statistical weight per computational particle becomes $W_p > 1$. For this scenario it is sometimes more convenient to refer to the computational particle as a parcel containing a number of statistically identical real particles. When $N_c > N_p$, each real particle is instead represented by a finite ensemble of computational particles such that $W_p < 1$. An advantage of this scenario is that a larger number of computational particles with smaller statistical weights, can be used in regions of low particle number density to reduce statistical error induced via any Mesoscopic characterisation of particle phase behaviour, (see section 3.3.1.1). Garg et al. (2009) utilised this scenario to develop numerically converged estimates of the mean inter-phase momentum transfer within a particle-laden lid-driven cavity flow simulation, by using a control algorithm that modifies the computational particle number density. At most, the ratio of computational to physical particle number density permitted within this control algorithm was $N_c/N_p = 2$, performed on a cell by cell basis. It is stressed however, that this control algorithm was implemented only for a one-way coupled flow problem.

For two-way coupled Lagrangian-Eulerian DNS, increasing the number of computational particles such that $N_c \gg N_p$ can present itself with a new type of problem. Saturation of the DNS flow field by a large number of computational particles with $W_p \ll 1$, can adversely lead to artificial smoothing of the Eulerian momentum source field. This is due to the fact that computational particle dynamics are dependent on underlying fluid turbulence, which in itself is affected by momentum sources from computational particles

themselves. Subsequently, it is possible for the assumption of statistical equivalence between computational and physical particles to shift apart from one another in an undesirable manner. This raises the question, as to what point the mesoscopic dispersed phase dynamics start to shift away from the realism of a physical turbulent two-way coupled dispersed phase system. It is perhaps more appropriate to say that in two-way coupled scenarios where $N_c \gg N_p$, the particle system being simulated resembles more of a quasi-dispersed phase. Nevertheless, future work should explore such a question, and provide recommendations to DNS research that specifically examines fundamental effects of two-way coupling between particles and turbulence.

Bibliography

A. H. Abdelsamie and C. Lee. Decaying versus stationary turbulence in particle-laden isotropic turbulence: Turbulence modulation mechanism. *Physics of Fluids*, 24(1): 015106, 2012.

A. H. Abdelsamie and C. Lee. Decaying versus stationary turbulence in particle-laden isotropic turbulence: Heavy particle statistics modifications. *Physics of Fluids*, 25(3): 033303, 2013.

I. Adamczewski. *Ionization, conductivity, and breakdown in dielectric liquids.* Taylor and Francis Ltd, 1969.

T. Agui and M. Nakajima. Drop formation characteristics of electrostatic ink jet using water-based ink. *IEEE Transactions on Electron Devices*, 24(3):262–266, 1977.

C. N. Ahmed and W. Balachandran. Suppression of smoke particles using electrostatic spraying. In *ICLASS-91*, Gaithersburg, 1991.

V. Alipchenkov, L. Zaichik, and O. Petrov. Clustering of charged particles in isotropic turbulence. *High Temperature*, 42(6):919–927, 2004.

A. Aliseda, A. Cartellier, F. Hainaux, and J. C. Lasheras. Effect of preferential concentration on the settling velocity of heavy particles in homogeneous isotropic turbulence. *Journal of Fluid Mechanics*, 468:77–105, 2002.

G. H. Amine-Eddine and J. S. Shrimpton. On simulations investigating droplet diameter-charge distributions in electrostatically atomized dielectric liquid sprays. *International Journal for Numerical Methods in Fluids*, 72(10):1051–1075, 2013.

A. A. Amsden, T. D. Butler, P. J. O'Rourke, and J. D. Ramshaw. Kiva: A comprehensive model for 2d and 3d engine simulations. Technical report, Los Alamos National Lab., NM (USA), 1985.

E. K. Anderson, D. C. Kyritsis, A. P. Carlucci, and A. De Risi. Electrostatic effects on gasoline direct injection in atmospheric ambiance. *Atomization and Sprays*, 17(4): 289–314, 2007.

A. G. Bailey. The theory and practice of electrostatic spraying. *Atomisation Spray Technology*, 2:95–134, 1986.

S. Bakar, A. R. Ismail, and A. Rosli. Comparative performance of direct injection diesel engines fueled using compressed natural gas and diesel fuel based on gt-power simulation. *American Journal of Applied Sciences*, 5(5), 2008.

S. Balachandar and J. K. Eaton. Turbulent dispersed multiphase flow. *Annual Review of Fluid Mechanics*, 42(1):111–133, 2010.

C. P. Bankston, L. H. Back, E. Y. Kwack, and A. J. Kelly. Experimental investigation of electrostatic dispersion and combustion of diesel fuel jets. *Journal of engineering for gas turbines and power*, 110(3):361–368, 1988.

M. S. Bartlett. Statistical estimation of density functions. *Sankhya: The Indian Journal of Statistics, Series A*, pages 245–254, 1963.

J. Bec, L. Biferale, M. Cencini, a. Lanotte, S. Musacchio, and F. Toschi. Heavy particle concentration in turbulence at dissipative and inertial scales. *Physical Review Letters*, 98(8):1–4, 2007a.

J Bec, M Cencini, and R Hillerbrand. Clustering of heavy particles in random self-similar flow. *Physical Review E*, 75(2):025301, 2007b.

M. Boivin, O. Simonin, and K. D. Squires. Direct numerical simulation of turbulence modulation by particles in isotropic turbulence. *Journal of Fluid Mechanics*, 375: 235–263, 1998.

T. Bosse, L. Kleiser, and E. Meiburg. Small particles in homogeneous turbulence: Settling velocity enhancement by two-way coupling. *Physics of Fluids*, 18(2):1–17, 2006.

R. S. Brodkey. *The Phenomena of Fluid Motions*. Addison-Wesley, Reading, WA, 1967.

E. Brunner. Fluid mixtures at high pressures vi. phase separation and critical phenomena in 18 (n-alkane + ammonia) and 4 (n-alkane + methanol) mixtures. *The Journal of Chemical Thermodynamics*, 20(3):273–297, 1988.

E. Calzavarini, M. Kerscher, and F. Lohse, D.and Toschi. Dimensionality and morphology of particle and bubble clusters in turbulent flow. *Journal of Fluid Mechanics*, 607: 13–24, 2008.

A. E. Cerkanowicz. Rayleigh limit for non-stationary charged drops. IEEE Annual Society Meeting, 1981.

J. Chen, C. Meneveau, and J. Katz. Scale interactions of turbulence subjected to a straining-relaxation-destraining cycle. *Journal of Fluid Mechanics*, 562:123–150, 2006.

W. H. Chou and G. M. Faeth. Temporal properties of secondary drop breakup in the bag breakup regime. *International journal of multiphase flow*, 24(6):889–912, 1998.

M. Chrigui. *Eulerian-Lagrangian approach for modeling and simulations of turbulent reactive multi-phase flows under gas turbine combustor conditions*. PhD thesis, TU Darmstadt, 2005.

J. Chun, D. L. Koch, S. L. Rani, A. Ahluwalia, and L. R. Collins. Clustering of aerosol particles in isotropic turbulence. *Journal of Fluid Mechanics*, 536:219–251, 2005.

M. Cloupeau and B. Prunet-Foch. Electrostatic spraying of liquids: Main functioning modes. *Journal of Electrostatics*, 25(2):165–184, 1990.

S. W. Coleman and J. C. Vassilicos. A unified sweep-stick mechanism to explain particle clustering in two- and three-dimensional homogeneous, isotropic turbulence. *Physics of Fluids*, 21(11):113301, 1–10, 2009.

G. Comte-Bellot and S. Corrsin. Simple eulerian time correlation of full-and narrow-band velocity signals in grid-generated, isotropic turbulence. *Journal of Fluid Mechanics*, 48(02):273, 1971.

J. W. Cooley and J. W. Tukey. An algorithm for the machine calculation of complex fourier series. *Mathematics of Computation*, 19(90):297, 1965.

C. Corre, J. Estivalezes, S. Vincent, and O. Simonin. Direct numerical simulation of the motion of particles larger than the kolmogorov scale in a homogeneous isotropic turbulence. 2008 ASME Fluids Engineering Conference, pages 121–128, Jacksonville Florida USA, 2008.

J. M. Crowley, G. S. Wright, and J. C. Chato. Selecting a working fluid to increase the efficiency and flow rate of an ehd pump. *IEEE Transactions on Industry Applications*, 26(1):42–49, 1990.

G. T. Csanady. Turbulent diffusion of heavy particles in the atmosphere. *Journal of Atmospheric Sciences*, 20:201–208, 1963.

Z. Dai and G. M. Faeth. Temporal properties of secondary drop breakup in the multimode breakup regime. *International journal of multiphase flow*, 27(2):217–236, 2001.

A. Dejoan and R. Monchaux. Preferential concentration and settling of heavy particles in homogeneous turbulence. *Physics of Fluids*, 25(1):013301, 2013.

B. J. Devenish, P. Bartello, J.-L. Brenguier, L. R. Collins, W. W. Grabowski, R. H. A. IJzermans, S. P. Malinowski, M. W. Reeks, J. C. Vassilicos, L.-P. Wang, and Z. Warhaft. Droplet growth in warm turbulent clouds. *Quarterly Journal of the Royal Meteorological Society*, 138(667):1401–1429, 2012.

J. K. Eaton. Two-way coupled turbulence simulations of gas-particle flows using point-particle tracking. *International Journal of Multiphase Flow*, 35(9):792–800, 2009.

S. Elghobashi and G. C. Truesdell. Direct simulation of particle dispersion in a decaying isotropic turbulence. *Journal of Fluid Mechanics*, 242(1):655–700, 1992.

S. Elghobashi and G. C. Truesdell. On the two-way interaction between homogeneous turbulence and dispersed solid particles. i: Turbulence modification. *Physics of Fluids A: Fluid Dynamics*, 5(7):1790–1801, 1993.

E. L. Ergene, G. Malkawi, F. Mashayek, and J. S. Shrimpton. Charge injection with multiple blade-plane configurations in a quiescent dielectric liquid. *Dielectrics and Electrical Insulation, IEEE Transactions on*, 17(6):1846–1852, 2010.

E. L. Ergene, A. Kourmatzis, J. Komperda, R. J. Schick, J. S. Shrimpton, and F. Mashayek. Investigation of the electrostatic charge injection method at high hydrodynamic pressures. In *23rd Annual Conference on Liquid Atomization and Spray Systems*, page 8, 2011.

V. Eswaran and S. B. Pope. An examination of forcing in direct numerical simulations of turbulence. *Computers and Fluids*, 16(3):257–278, 1988.

G. M. Faeth. Dynamics of secondary drop breakup rate controlling processes in dense sprays. *Zaragoza*, 9:11, 2002.

G. M. Faeth, L. P. Hsiang, and P. K. Wu. Structure and breakup properties of sprays. *International Journal of Multiphase Flow*, 21:99–127, 1995.

J. Fan, X. Zhang, L. Cheng, and K. Cen. Numerical simulation and experimental study of two-phase flow in a vertical pipe. *Aerosol Science and Technology*, 27(3):281–292, 1997.

J. Feng. Application of galerkin finite-element computations in studying electrohydrodynamic problems. *Journal of Electrostatics*, 51-52:590–596, 5 2001.

Járai-Szabó . S. Ferenc and Zoltán Néda. On the size distribution of poisson voronoi cells. *Physica A: Statistical Mechanics and its Applications*, 385(2):518–526, 2007.

A. Ferrante and S. Elghobashi. On the physical mechanisms of two-way coupling in particle-laden isotropic turbulence. *Physics of fluids*, 15(2):315–329, 2003.

J. H. Ferziger and M. Perić. *Computational methods for fluid dynamics*, volume 3. Springer Berlin, 1996.

J. R. Fessler, J. D. Kulick, and J. K. Eaton. Preferential concentration of heavy particles in a turbulent channel flow. *Physics of Fluids*, 6(11):3742, 1994.

P. Février, O. Simonin, and K. D. Squires. Partitioning of particle velocities in gas-solid turbulent flows into a continuous field and a spatially uncorrelated random distribution: theoretical formalism and numerical study. *Journal of Fluid Mechanics*, 533: 1–46, 2005.

R. Garg, C. Narayanan, D. Lakehal, and S. Subramaniam. Accurate numerical estimation of interphase momentum transfer in lagrangian eulerian simulations of dispersed two-phase flows. *International Journal of Multiphase Flow*, 33(12):1337–1364, 2007.

R. Garg, C. Narayanan, and S. Subramaniam. A numerically convergent lagrangian-eulerian simulation method for dispersed two-phase flows. *International Journal of Multiphase Flow*, 35(4):376–388, 2009.

B. E. Gelfand. The main models of the drops breakup. *Inzenerno Physicheski Journal*, 27(1):120–126, 1974.

K. Gomez, A.and Tang. Charge and fission of droplets in electrostatic sprays. *Physics of Fluids*, 6(1):404–414, 1994.

A. D. Gosman and E. Ioannides. Aspects of computer simulation of liquid-fueled combustors. *Journal of Energy*, 7(6):482–490, 1981.

S. Goto and J. Vassilicos. Sweep-stick mechanism of heavy particle clustering in fluid turbulence. *Physical Review Letters*, 100(5):1–4, 2008.

D. Gottlieb and S. A. Orszag. *Numerical analysis of spectral methods : theory and applications*. Society for Industrial and Applied Mathematics, Philadelphia, 1977.

W. Gu, P. E. Heil, H. Choi, and K. Kim. Comprehensive model for fine coulomb fission of liquid droplets charged to rayleigh limit. *Applied Physics Letters*, 91(6):064104–064104, 2007.

D. R. Guildenbecher and P. E. Sojka. Total time for secondary breakup of electrically charged drops. ILASS 2008, Como Lake, Italy, Sep 2008.

D. R. Guildenbecher and P. E. Sojka. Secondary atomization of electrostatically charged drops. ICLASS 2009, 11th International Annual Conference on Liquid Atomization and Spray Systems, Vail, Colorado USA, July 2009.

D. R. Guildenbecher, C. Lopez-Rivera, and P. E. Sojka. Secondary atomization. *Experiments in Fluids*, 46:371–402, 2009.

J. B. Heywood. *Internal combustion engine fundamentals*. McGraw-Hill, New York, 1988.

H. Hiroyasu, M. Arai, and Society of Automotive Engineers. Structures of fuel sprays in diesel engines. Technical report, Society of Automotive Engineers, 1990.

H. Homann and J. Bec. Finite-size effects in the dynamics of neutrally buoyant particles in turbulent flow. *Journal of Fluid Mechanics*, 651:81–91, 2010.

L. P. Hsiang and G. M. Faeth. Near-limit drop deformation and secondary breakup. *International Journal of Multiphase Flow*, 18(5):635–652, 1992.

J. C. R. Hunt, A. A. Wray, and P. Moin. *Eddies, streams, and convergence zones in turbulent flows*. 12 1988.

H. C. Hunter and A. K. Ray. On progeny droplets emitted during coulombic fission of charged microdrops. *Physical Chemistry Chemical Physics*, 11(29):6156, 2009.

M. Hussaini. Spectral methods in fluid dynamics. *Annual Review of Fluid Mechanics*, 19(1):339–367, 1987.

W. Hwang and J. K. Eaton. Homogeneous and isotropic turbulence modulation by small heavy ($st\sim 50$) particles. *Journal of Fluid Mechanics*, 564:361–393, 2006a.

W. Hwang and J. K. Eaton. Turbulence attenuation by small particles in the absence of gravity. *International Journal of Multiphase Flow*, 32(12):1386–1396, 2006b.

R. I. Issa. Solution of the implicitly discretised fluid flow equations by operator-splitting. *Journal of Computational physics*, 62(1):40–65, 1986.

A. Jankowski, A. Sandel, J. Seczyk, and B. Siemiěska-Jankowska. Some problems of improvement of fuel efficiency and emissions in internal combustion engines. *Journal of KONES Internal Combustion Engines*, 9(3-4):333–356, 2002.

K. Karimi. *Characterisation of multiple-injection diesel sprays at elevated pressures and temperatures*. PhD thesis, School of Engineering, University of Brighton, 2007.

A. Karnik. *Direct Numerical Investigations of Dilute Dispersed Flows in Homogeneous Turbulence*. PhD thesis, 2010.

A. Karnik and J. S. Shrimpton. Destruction of preferential accumulation by lorentz force interactions. In *22nd European Conference on Liquid Atomization and Spray Systems*, volume 15, page 4, 2008.

A. Kaufmann, M. Moreau, O. Simonin, and J. Helie. Comparison between lagrangian and mesoscopic eulerian modelling approaches for inertial particles suspended in decaying isotropic turbulence. *Journal of Computational Physics*, 227(13):6448–6472, 2008.

A. J. Kelly. Low charge density electrostatic atomization. *Industry Applications, IEEE Transactions on*, IA-20(2):267–273, 1984a.

A. J. Kelly. The electrostatic atomization of hydrocarbons. *J. Inst. Energy*, 57(431): 312–320, 1984b.

A. J. Kelly. Charge injection electrostatic atomizer modeling. *Aerosol Science and Technology*, 12:526–537, 1990.

A. J. Kelly. On the statistical, quantum and practical mechanics of electrostatic atomization. *Journal of Aerosol Science*, 25(6):1159, 1994.

D. A. Kennaird, C. Crua, J. Lacoste, M. R. Heikal, M. R. Gold, and N. S. Jackson. In-cylinder penetration and break-up of diesel sprays using a common-rail injection system. *SAE SP*, pages 93–104, 2002.

S. Kondaraju, M. Choi, X. Xu, and J. S. Lee. Direct numerical simulation of modulation of isotropic turbulence by poly-dispersed particles. *International Journal for Numerical Methods in Fluids*, 69(7):1237–1248, 2011.

A. Kourmatzis and J. S. Shrimpton. Turbulent three-dimensional dielectric electrohydrodynamic convection between two plates. *Journal of Fluid Mechanics*, 696:228–262, 2012.

A. Kourmatzis, E. L. Ergene, J. S. Shrimpton, D. C. Kyritsis, F. Mashayek, and M. Huo. High pressure primary charge injection atomization of dielectric liquids. 2011.

V. Kulkarni, D. R. Guildenbecher, and P. E. Sojka. Secondary atomization of newtonian liquids in the bag breakup regime: Comparison of model predictions to experimental data. In *ICLASS 2012, 12th International Conference on Liquid Atomization and Spray Systems, Heidelberg, Germany*, 2012.

J. Kulon, B. E. Malyan, and W. Balachandran. Simultaneous measurement of particle size and electrostatic charge distribution in dc electric field using phase doppler anemometry. *Industry Applications, IEEE Transactions on*, 39(5):1522–1528, 2003.

E. Y. Kwack, L. H. Back, and C. P. Bankston. Electrostatic dispersion of diesel fuel at high back pressures. *Journal of Engineering for Gas Turbines and Power*, 111(3): 578–586, 1989.

S. Lain and M. Sommerfeld. Turbulence modulation in dispersed two-phase flow laden with solids from a lagrangian perspective. *International Journal of Heat and Fluid Flow*, 24(4):616–625, 2003.

G. N. Laryea and S. Y. No. Spray angle and breakup length of charge-injected electrostatic pressure-swirl nozzle. *Journal of Electrostatics*, 60:37–47, 2004.

B. E. Launder and D. B. Spalding. *Mathematical Models of Turbulence*. New York, 1972.

W. Layton, C. C. Manica, M. Neda, M. Olshanskii, and L. G. Rebholz. On the accuracy of the rotation form in simulations of the navier-stokes equations. *Journal of Computational Physics*, 228(9):3433–3447, 2009.

A. H. Lefebvre. *Atomization and sprays*. CRC, 1989.

Y. Ling, A. Haselbacher, and S. Balachandar. A numerical source of small-scale number-density fluctuations in eulerian-lagrangian simulations of multiphase flows. *Journal of Computational Physics*, 229(5):1828–1851, 2010.

Y. Ling, M. Parmar, and S. Balachandar. A scaling analysis of added-mass and history forces and their coupling in dispersed multiphase flows. *International Journal of Multiphase Flow*, 57:102–114, 2013.

A. B. Liu, D. Mather, and R. D. Reitz. Modeling the effects of drop drag and breakup on fuel sprays. Technical report, DTIC Document, 1993.

W. F Lu, W. H. Lai, K. C. Chang, and T. H. Tsai. Turbulence modulation measurements in a charged monodispersed droplet stream. *Chemical Engineering Communications*, 197(2):158–168, 2010.

F. Lucci, A. Ferrante, and S. Elghobashi. Modulation of isotropic turbulence by particles of taylor length-scale size. *Journal of Fluid Mechanics*, 650(1):5–55, 2010.

B. K. Majewski W., Ambs J. Nitrogen oxides reactions in diesel oxidation catalyst. *SAEE transactions*, 104(3):743–753, 1996.

G. Malkawi. *Point-To-Plane and Plane-to-Plane Electrostatic Charge Injection Atomization for Insulating Liquids*. PhD thesis, 2009.

F. Mashayek, F. A. Jaberi, R. S. Miller, and P. Givi. Dispersion and polydispersity of droplets in stationary isotropic turbulence. *International journal of multiphase flow*, 23(2):337–355, 1997.

M. R. Maxey and J. J. Riley. Equation of motion for a small rigid sphere in a nonuniform flow. *Physics of Fluids*, 26(4):883, 1983.

R. Monchaux, M. Bourgoin, and a. Cartellier. Preferential concentration of heavy particles: A voronoï analysis. *Physics of Fluids*, 22(10):103304, 2010.

R. Monchaux, M. Bourgoin, and A. Cartellier. Analyzing preferential concentration and clustering of inertial particles in turbulence. *International Journal of Multiphase Flow*, 40(4):1–18, 2012.

J. D. Naber and D. L. Siebers. Effects of gas density and vaporization on penetration and dispersion of diesel sprays. *SAE paper*, 960034, 1996.

K. P. Nishad. *Modeling and unsteady simulation of turbulent multi-phase flow including fuel injection in IC-engines*. PhD thesis, TU Prints Technische Universität Darmstadt, 2013.

G. Ooms and G. H. Jansen. Particles-turbulence interaction in stationary, homogeneous, isotropic turbulence. *International Journal of Multiphase Flow*, 26(11):1831–1850, 2000.

P. J. O'Rourke and A. A. Amsden. The tab method for numerical calculation of spray droplet breakup. Technical report, Los Alamos National Lab., NM (USA), 1987.

S. Orszag and G. Patterson. Numerical simulation of three-dimensional homogeneous isotropic turbulence. *Physical Review Letters*, 28(2):76–79, 1972.

M. R. Overholt and S. B. Pope. Direct numerical simulation of a passive scalar with imposed mean gradient in isotropic turbulence. *Physics of Fluids*, 8(11):3128–3148, 1996.

R. N. Parthasarathy and G. M. Faeth. Turbulent dispersion of particles in self-generated homogeneous turbulence. *Journal of Fluid Mechanics*, 220:515–537, 2006.

M. Pilch. *Acceleration induced fragmentation of liquid drops*. PhD thesis, University of Virginia, 1981.

M. Pilch and C. Erdman. Use of breakup time data and velocity history data to predict the maximum size of stable fragments for acceleration-induced breakup of a liquid drop. *International Journal of Multiphase Flow International Journal of Multiphase Flow*, 13(6):741–757, 1987.

C. Poelma and G. Ooms. Particle-turbulence interaction in a homogeneous, isotropic turbulent suspension. *Applied Mechanics Reviews*, 59(2):78–90, 2006.

M. Polat, H. Polat, and S. Chander. Electrostatic charge on spray droplets of aqueous surfactant solutions. *Journal of aerosol science*, 31(5):551–562, 2000.

A. Putnam. Integratable form of droplet drag coefficient. *ARS Journal*, 2:2–5, 1961.

A. A. Ranger and J. A. Nicholls. Aerodynamic shattering of liquid drops. *AIAA Journal*, 7(2):285–290, 1969.

Lord Rayleigh. On the instability of jets. *Proceedings of the London Mathematical Society*, 1(1):57–72, 1879.

W. C. Reade and L. R. Collins. Effect of preferential concentration on turbulent collision rates. *Physics of Fluids*, 12(10):2530, 2000.

M. W. Reeks. On the dispersion of small particles suspended in an isotropic turbulent fluid. *Journal of fluid mechanics*, 83(03):529–546, 1977.

R. D. Reitz and R. Diwakar. Structure of high-pressure fuel sprays. Technical report, Fluid Mechanics Dept., GM Research Labs., Warren, MI, 1987.

R. D. Reitz and R. Diwaker. Effect of drop breakup on fuel sprays. Technical report, Society of Automotive Engineers, Inc., Warrendale, PA, 1986.

R. D. Reitz, F. B. Bracco, and Society of Automotive Engineers. On the dependence of spray angle and other spray parameters on nozzle design and operating conditions. Technical report, Society of Automotive Engineers, 1979.

A. R. Rigit. *Performance of a charge injection electrostatic atomizer and spray characteristics.* PhD thesis, 2003.

A. R. Rigit and J. S. Shrimpton. Electrical performance of charge injection electrostatic atomizers. *Atomization and Sprays*, 16(4):401–420, 2006.

A. R. Rigit and J. S. Shrimpton. Estimation of the diameter-charge distribution in polydisperse electrically charged sprays of electrically insulating liquids. *Experiments in Fluids*, 46(6):1159–1171, 2009.

A. Robert. *Fundamental physics underlying polymer drag reduction from DNS of homogeneous shear and isotropic turbulence with the FENE-P model.* PhD thesis, 2010.

R. S. Rogallo. Numerical experiments in homogeneous turbulence. *NASA STI/Recon Technical Report N*, 81:31508, 1981.

T. C. Rohner, N. Lion, and H. H. Girault. Electrochemical and theoretical aspects of electrospray ionisation. *Physical chemistry chemical physics*, 6(12):3056–3068, 2004.

A. M. Roma, C. S. Peskin, and M. J. Berger. An adaptive version of the immersed boundary method. *Journal of Computational Physics*, 153(2):509–534, 1999.

D. G. Roth and A. J. Kelly. Analysis of the disruption of evaporating charged droplets. *Industry Applications, IEEE Transactions on*, IA-19(5):771–775, 1983.

L. Schiller and A. Z. Naumann. A drag coefficient correlation. *Vereines Deutscher Ingenieure*, pages 318–320, 1933.

D. P. Schmidt. Theoretical analysis for achieving high-order spatial accuracy in lagrangian/eulerian source terms. *International journal for numerical methods in fluids*, 52(8):843–865, 2006. ISSN 1097-0363.

P. H. Schweitzer. Mechanism of disintegration of liquid jets. *Journal of Applied Physics*, 8(8):513–521, 1937.

S. J. Scott. *A PDF Based Method for Modelling Polysized Particle Laden Turbulent Flows Without Size Class Discretisation*. PhD thesis, School of Engineering Sciences University of Southampton, 2006.

S. J. Scott, A. U. Karnik, and J. S. Shrimpton. On the quantification of preferential accumulation. *International Journal of Heat and Fluid Flow*, 30(4):789–795, 2009.

M. Sehili and H. Romat. Modification of the size and the velocity of droplets for a diesel oil high speed jet induced by an electric field. In *Electrical Insulation and Dielectric Phenomena, 2002 Annual Report Conference on*, pages 196–199, 2002.

J. S. Shrimpton. *Electrostatic Atomization and Combustion of Hydrocarbon Oils*. PhD thesis, UMIST, 1995.

J. S. Shrimpton. Pulsed charged sprays: application to disi engines during early injection. *International Journal for Numerical Methods in Engineering*, 58(3):513–536, 2003.

J. S. Shrimpton. Modeling dielectric charged drop break up using an energy conservation method. *IEEE Transactions on Dielectrics and Electrical Insulation*, 15(5):1471–1477, 2008.

J. S. Shrimpton. *Charge Injection Systems:Physical Principles, Experimental and Theoretical Work*. Springer, 2009.

J. S. Shrimpton and A. Kourmatzis. Downsizing direct injection spark ignition engines: a timescale analysis. In *Traffic Related Air Pollution and Internal Combustion Engines*, page 33. Nova Science Publishers Inc, 2009.

J. S. Shrimpton and Y. Laoonual. Dynamics of electrically charged transient evaporating sprays. *International Journal for Numerical Methods in Engineering*, 67(8):1063–1081, 2006.

J. S. Shrimpton and A. R. Rigit. Spray characteristics of charge injection electrostatic atomizers with small-orifice diameters. *Atomization and Sprays*, 16(4):421–442, 2006.

J. S. Shrimpton and A. J. Yule. Characterisation of charged hydrocarbon sprays for application in combustion systems. *Experiments in Fluids*, 26(5):460–469, 1999.

J. S. Shrimpton and A. J. Yule. Atomization, combustion and control of charged hydrocarbon sprays. *Atomization and Sprays*, 11(4):365–396, 2001.

J. S. Shrimpton and A. J. Yule. Design issues concerning charge injection atomizers. *Atomization and Sprays*, 14(2):127–141, 2004.

J. Shuen. *A theoretical and experimental study of turbulent particle-laden jets*. National Aeronautics and Space Administration, Lewis Research Center, 1983.

J. S. Shuen, A. S. P. Solomon, G. M. Faeth, and Q. F. Zhang. Structure of particle-laden jets-measurements and predictions. *AIAA journal*, 23(3):396–404, 1985.

H. C. Simmons. The correlation of drop-size distributions in fuel nozzle sprayspart i: The drop-size/volume-fraction distribution. *Journal of Engineering for Power*, 99: 309, 1977.

K. D. Squires and J. K. Eaton. Particle response and turbulence modification in isotropic turbulence. *Physics of Fluids A: Fluid Dynamics*, 2(7):1191, 1990.

K. D. Squires and J. K. Eaton. Measurements of particle dispersion obtained from direct numerical simulations of isotropic turbulence. *Journal of Fluid Mechanics*, 226:1–35, 1991a.

K. D. Squires and J. K. Eaton. Preferential concentration of particles by turbulence. *Physics of Fluids A: Fluid Dynamics*, 3:1169, 1991b.

N. P. Sullivan, S. Mahalingam, and R. M. Kerr. Deterministic forcing of homogeneous, isotropic turbulence. *Physics of Fluids*, 6(4):1612, 1994.

Shivshankar Sundaram and Lance R. Collins. Collision statistics in an isotropic particle-laden turbulent suspension. part 1. direct numerical simulations. *Journal of Fluid Mechanics*, 335:75–109, 1997.

D. C. Taflin, T. L. Ward, and E. J. Davis. Electrified droplet fission and the rayleigh limit. *Langmuir*, 5(2):376–384, 1989.

T. Tanaka and J. K. Eaton. Sub-kolmogorov resolution partical image velocimetry measurements of particle-laden forced turbulence. *Journal of Fluid Mechanics*, 643 (1):177–206, 2010.

G. I. Taylor. Statistical theory of turbulence. *Proceedings of the Royal Society A: Mathematical, Physical and Engineering Sciences*, 151(873):421–444, 1935.

G. C. Truesdell and S. Elghobashi. On the two-way interaction between homogeneous turbulence and dispersed solid particles. ii. particle dispersion. *Physics of Fluids*, 6 (3):1405, 1994.

B. van Poppel. *Numerical methods for simulating multiphase electrohydrodynamic flows with application to liquid fuel injection*. PhD thesis, United States Military Academy, 2010.

H. K. Versteeg and W. Malalasekera. *An introduction to computational fluid dynamics*. Longman Publishing Group, 1995.

P. Walden. Uber organische losungs-und ionisierungsmittel. iii. teil:innere reibung and deren zusammenhang mit dem leitvermorgen. *Z. Phys. Chem*, (55):207–246, 1906.

L. P. Wang and M. R. Maxey. Settling velocity and concentration distribution of heavy particles in homogeneous isotropic turbulence. *Journal of Fluid Mechanics*, 256:27–68, 1993.

Y. Wang, H. W. Ge, and R. D. Reitz. Validation of mesh-and timestep-independent spray models for multi-dimensional engine cfd simulation. *SAE International Journal of Fuels and Lubricants*, 3(1):277–302, 2010.

A. P. Watkins. Three-dimensional modelling of gas flow and sprays in diesel engines. In *Computer Simulation for Fluid-Flow, Heat and Mass Transfer and Combustion in Reciprocating Engines*, pages 193–237, 1989.

M. R. Wells and D. E. Stock. The effects of crossing trajectories on the dispersion of particles in a turbulent flow. *Journal of Fluid Mechanics*, 136:31–62, 1983.

K. L. Wert. A rationally-based correlation of mean fragment size for drop secondary breakup. *International journal of multiphase flow*, 21(6):1063–1071, 1995.

S. Wetchagarun and J. J. Riley. Dispersion and temperature statistics of inertial particles in isotropic turbulence. *Physics of Fluids*, 22(6):063301, 2010.

J. H. Williamson. Low-storage runge-kutta schemes. *Journal of Computational Physics*, 35(1):48–56, 1980.

P. K. Wu, R. F. Miranda, and G. M. Faeth. Effects of initial flow conditions on primary breakup of nonturbulent and turbulent round liquid jets. *Atomization and Sprays*, 5 (2):175–196, 1995.

T. S. Yang and S. S. Shy. Two-way interaction between solid particles and homogeneous air turbulence: particle settling rate and turbulence modification measurements. *Journal of Fluid Mechanics*, 526:171–216, 2005.

X. Yang, X. Zhang, Z. Li, and G. W. He. A smoothing technique for discrete delta functions with application to immersed boundary method in moving boundary simulations. *Journal of Computational Physics*, 228(20):7821–7836, 2009.

P. K. Yeung and S. B. Pope. Lagrangian statistics from direct numerical simulations of isotropic turbulence. *Journal of Fluid Mechanics*, 207(1):531–586, 1989.

P. K. Yeung, S. B. Pope, and B. L. Sawford. Reynolds number dependence of lagrangian statistics in large numerical simulations of isotropic turbulence. *Journal of Turbulence*, 7, 2006.

H. Yoshimoto and S. Goto. Self-similar clustering of inertial particles in homogeneous turbulence. *Journal of Fluid Mechanics*, 577:275–286, 2007.

M. I. Yudine. Physical considerations on heavy-particle diffusion. volume Volume 6 of *Advances in Geophysics*, pages 185–191. Elsevier, 1959.

A. J. Yule, J. S. Shrimpton, A. P. Watkins, W. Balachandran, and D. Hu. Electrostatically atomized hydrocarbon sprays. *Fuel*, 74(7):1094–1103, 1995.

C. X. Zhao, L. He, S. Z. Qiao, and A. P. J. Middelberg. Nanoparticle synthesis in microreactors. *Chemical Engineering Science*, 66(7):1463–1479, 2011.